AAAS

Science

ON THE CUSP

The mathematics that shapes growing rose petals pp. 466 & 520

1 MAY 2025

Your bridge to successful innovation.

NEB's Customized Solutions Team is here to help, and serves as a bridge to the support and resources you need to ensure your success.

Creating the right partnership is essential when pioneering a new life science product. Every aspect of development – technical expertise, reagent optimization, manufacturing scale, turnaround time, reagent quality, and comprehensive logistical support – is vital for achieving your objectives. And in the regulated markets landscape, these challenges magnify, demanding an even more specialized approach.

Your Bridge to Successful Innovation

- Leverage NEB's 50 years of experience in enzymology and reagent manufacturing
- As an extension of your team, we prioritize a deep understanding of your objectives, work with you on an optimal solution, and help to anticipate your future needs
- Benefit from our ISO 9001- and 13485-certified processes and commitment to quality, as well as our GMP-grade* production facility, and specialized lyophilization facility for the highest quality production standards
- Access unparalleled support from our dedicated account managers, program managers, technical scientists and production teams
- We work closely with you on inventory management and global distribution through our network of NEB-owned subsidiaries, to ensure successful commercialization

NEB's Customized Solutions Team will help you access novel products, meet quality specifications, speed time to market, and streamline your supply chain, allowing you to focus more on what matters most — innovation.

Ready to start the discussion? Learn more at
www.neb.com/customizedsolutions.

** "GMP-grade" is a branding term NEB uses to describe products manufactured or finished at NEB's Rowley facility. The Rowley facility was designed to manufacture products under more rigorous infrastructure and process controls to achieve more stringent product specifications and customer requirements. Products manufactured at NEB's Rowley facility are manufactured in compliance with ISO 9001 and ISO 13485 quality management system standards. However, at this time, NEB does not manufacture or sell products known as Active Pharmaceutical Ingredients (APIs), nor does NEB manufacture its products in compliance with all of the Current Good Manufacturing Practice regulations.*

NEW ENGLAND Biolabs®

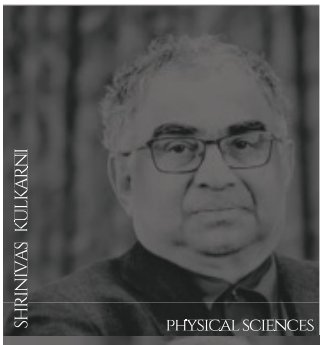

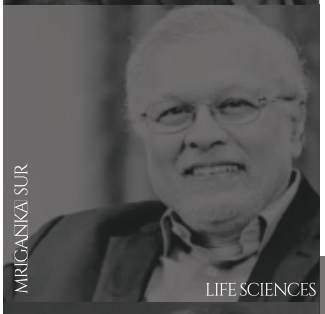

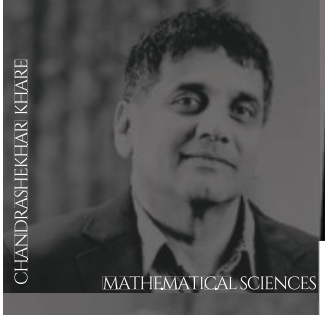

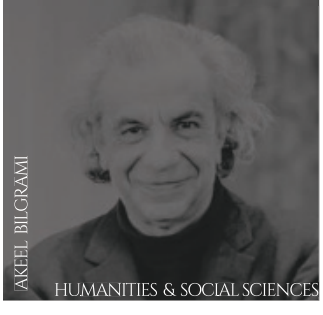

JURY CHAIRS 2025

Infosys Prize

Inspire Progress

NOMINATE NOW

Have a candidate in mind? Please write to us at **ISF@infosys.com**

The Infosys Science Foundation calls for nominations for the Infosys Prize 2025. The Infosys Prize is given for an invention, innovation or distinct achievement.

Nominees must be of Indian origin working anywhere in the world or anyone whose work impacts India and must be 40 years or younger as of November 1, 2025 to be eligible. The nominators will be invited to the nomination council. Self nominations will not be accepted.

You can find the statutes and other criteria for the prize on **www.infosysprize.org**.

CONTENTS

1 MAY 2025 | VOLUME 388 | ISSUE 6746

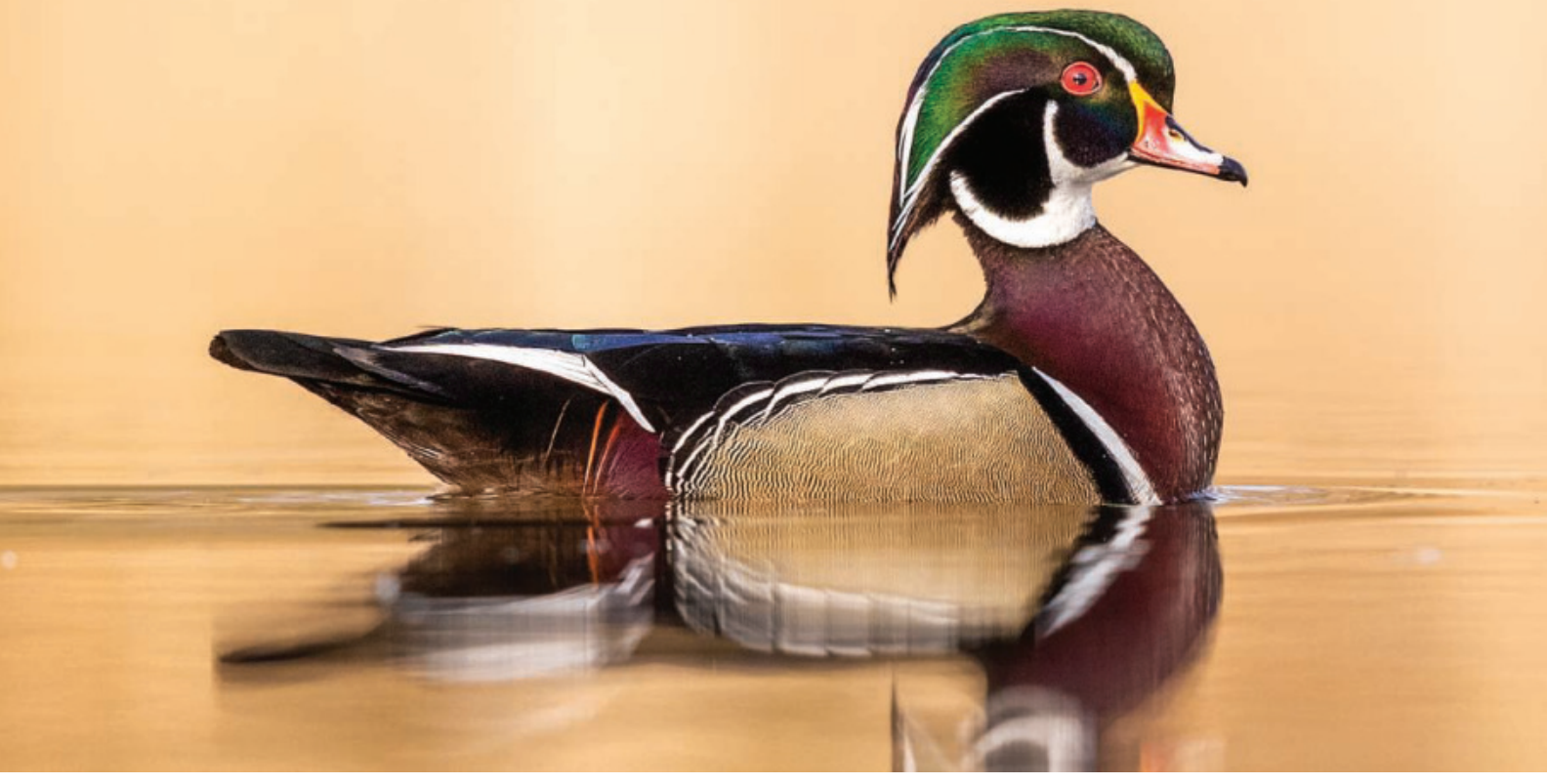

EDITORIAL

NEWS

FEATURES

COMMENTARY

PERSPECTIVES

POLICY FORUM

PHOTO: BRAD IMHOFF/CORNELL LAB MACAULAY LIBRARY

REVIEWS

REVIEW SUMMARY

RESEARCH

HIGHLIGHTS

RESEARCH SUMMARIES

RESEARCH ARTICLES

WORKING LIFE

532

Wood ducks and other birds show varying abundance trends across their ranges.

BOOKS ET AL.

LETTERS

ON THE COVER

A Red Naomi rose blooms with striking, cuspy petal edges—complex shapes that are unlikely to emerge from smooth, symmetric growth. Researchers describe the mathematics that shapes growing rose petals: Growth creates a geometric conflict, forcing petals into forms where the relaxed state cannot be smoothly realized in three-dimensional space without distortion. This frustration shapes the rose's beauty, focusing stress into sharp, elegant edges. See pages 466 and 520.
Photo: Yafei Zhang/Hebrew University of Jerusalem

Science **serves as a forum for discussion of important issues related to the advancement of science by publishing material on which a consensus has been reached as well as including the presentation of minority or conflicting points of view. Accordingly, all articles published in *Science*—including editorials, news, commentary, and book reviews—are signed and reflect the individual views of the authors and not official points of view adopted by AAAS or the institutions with which the authors are affiliated.** *Science* (ISSN 0036-8075) is published weekly on Thursday, except last week in December, by the American Association for the Advancement of Science, 1200 New York Avenue, NW, Washington, DC 20005. Periodicals mail postage (publication No. 484460) paid at Washington, DC, and additional mailing offices.

The title *Science* is a registered trademark of the AAAS. Domestic individual membership, including subscription (12 months): $165 ($74 allocated to subscription). Domestic institutional subscription (51 issues): $2865; Foreign postage extra: Air assist delivery: $135. First class, airmail, student, and emeritus rates on request. Canadian rates with GST available upon request, GST #125488122. Publications Mail Agreement Number 1069624. **Printed in the U.S.A. Change of address:** Allow 4 weeks, giving old and new addresses and 8-digit account number. **Postmaster:** Send change of address to AAAS, P.O. Box 96178, Washington, DC 20090–6178. **Single-copy sales:** $15 each plus shipping and handling available from backissues.science.org; bulk rate on request. **Authorization to reproduce** material for internal or personal use under circumstances not falling within the fair use provisions of the Copyright Act can be obtained through the Copyright Clearance Center (CCC), www.copyright.com. The identification code for *Science* is 0036-8075. *Science* is indexed in the *Reader's Guide to Periodical Literature* and in several specialized indexes.

Science AAAS

EDITORIAL
science_editors@aaas.org

NEWS
science_news@aaas.org

INFORMATION FOR AUTHORS
science.org/authors/science-information-authors

REPRINTS AND PERMISSIONS
science.org/help/reprints-and-permissions

MULTIMEDIA CONTACTS
SciencePodcast@aaas.org
ScienceVideo@aaas.org

MEDIA CONTACTS
scipak@aaas.org

PRODUCT ADVERTISING & CUSTOM PUBLISHING
advertising.science.org
science_advertising@aaas.org

CLASSIFIED ADVERTISING
advertising.science.org/science-careers
advertise@sciencecareers.org

JOB POSTING CUSTOMER SERVICE
employers.sciencecareers.org
support@sciencecareers.org

MEMBERSHIP AND INDIVIDUAL SUBSCRIPTIONS
science.org/subscriptions

MEMBER BENEFITS
aaas.org/membership/benefits

INSTITUTIONAL SALES AND SITE LICENSES
science.org/librarian

Fine print—*Science*'s new look

Beth Rakouskas *and* **H. Holden Thorp**

It's been 11 years since *Science*'s last print redesign. Much has changed since then—in how *Science* is communicated, how readers engage with content, and how *Science* itself is produced.

Even though many readers now access *Science* through digital platforms, including our website, social media, and the *Science*Adviser newsletter, the print issue is still part of the broad reading landscape. Some readers might find the tactile experience more enjoyable than looking at a screen. In thumbing through an issue, readers might find something in a different field they might not have seen otherwise. This is one of the goals of an interdisciplinary journal. A drawback of the online version is that many readers may tend to go to a paper or article of direct interest rather than browsing further afield. We recognize the benefits of publishing a print edition every week so that everyone, whatever their reading habits, can choose a path to (and through) *Science* that works best for them.

We began this redesign by listening, with a survey of those who read the print version of *Science*—from graduate students to retirees. The most important thing we heard was that many readers continue to value the print publication for consuming *Science*.

Developed entirely in-house, this project brought together our staff's editorial and design expertise. The result is a format and arrangement that provides a more cohesive, efficient reading experience not only in print but across all of *Science*'s platforms. The new look is more open—throughout the magazine we removed design elements that cluttered the pages. Photographs, illustrations, graphics, and other visual elements will continue to be striking and informative, and more varied article lengths will accommodate the rich mixture of content types and styles that appeal to *Science*'s broad readership.

On the cover, the *Science* logo now shines at the top, unencumbered by other text. Highlights from the issue will now change position on the cover week to week, depending on the cover image. And starting with this issue, the publication date will be Thursday instead of Friday, matching the online version.

...a format and arrangement that provides a more cohesive, efficient reading experience...

We've rethought the News section to reflect how people now receive breaking news: instantly, on smartphones or other devices. We see the weekly print issue as a channel for deeper, more analytical pieces that will remain fresh days after publication. Accordingly, we've eliminated "News in Brief," a roundup of short news digests drawn mainly from *Science*'s online news site. The new design combines a smaller number of short items with longer stories (formerly "News in Depth") to showcase the best of both.

"Insights" is once again called "Commentary." This name more clearly indicates that in this section, readers will discover views, opinions, and analyses from the global scientific community on matters of broad interest. It also matches how we refer to this type of content on the website and across the *Science* family of journals.

In the Research section, we are "unwrapping" research articles by starting each one at the top of a new page. This change will make print production more efficient, and we think authors will be pleased with the free-standing, discrete appearance of their paper.

We've also added more visual cues to help differentiate the Research, News, and Commentary sections. In this time of political and social disagreements about the principles, practices, and findings of *Science*, we are taking extra care to distinguish scientific findings from scientific opinion. Our goal is, as it always has been, for the magazine to be the best place for scientists and other members of the scientific enterprise to discover what is happening at the leading edge of research, learn about current events in the world that intersect with science, and talk to each other about research interpretations and their implications for society.

We hope *Science* better delivers the content that matters most to you, our readers, including in a form that you can hold in your hands, carry with you, and share with others.

Thanks for reading. □

Beth Rakouskas, Creative Director, *Science* journals. brakouskas@aaas.org; **H. Holden Thorp,** Editor-in-Chief, *Science* journals. hthorp@aaas.org

10.1126/science.ady5490

ANTHROPOLOGY

Radiocarbon dates revise histories of Indigenous societies

New techniques challenge assumptions about Indigenous responses to European contact

LIZZIE WADE

Ten years ago, archaeologist Jennifer Birch thought she had a good handle on when and why Ontario's largest excavated Iroquois village, known as the Jean-Baptiste Lainé Site, was abandoned. Because archaeologists had found few European artifacts there, they figured people deserted the village around 1535, shortly after the first French explorers entered Canada's interior.

But Sturt Manning, a radiocarbon dating expert at Cornell University, saw a way to test that picture. He told Birch that with its wooden architecture and overlapping construction phases, the Jean-Baptiste Lainé Site would be a good candidate for a detailed chronology based on the latest innovations in radiocarbon dating. Birch, now at the University of Georgia (UGA), was stunned by the results: The site was, in fact, occupied between 1590 and 1615, roughly 75 years later than archaeologists thought and nearly a century after European contact. "I was in disbelief for 2 years," Birch remembers, and so were many of her academic peers. "We'd been off by two or three whole generations."

Now, the same technique is rewriting the history of other Indigenous sites along the East Coast of North America, as researchers reported during a session Birch co-organized at the Society for American Archaeology (SAA) meeting in Denver last week. Many of these new histories are challenging conventional wisdom about Indigenous persistence, or the lack thereof, in the face of European contact.

Traditionally, archaeologists have subdivided the history of eastern North American sites based on shifting ceramic styles, as well as the presence or absence of European artifacts. If a site contains objects such as iron blades or glass beads, archaeologists include it in the so-called "historic" period, placing it earlier or later depending on the number of European artifacts. If a site lacks such items, researchers assume it was occupied in the precontact era.

"A lot of us are really frustrated by this arbitrary division of time," says Michelle Pigott, an archaeologist at the University of Tennessee, Knoxville. But in colonial eastern North America, it was often the best archaeologists could do. Radiocarbon dating during this time frame is particularly tricky.

The method works by measuring levels of carbon-14 in organic material such as wood, charcoal, and seeds. Living things absorb the radioactive isotope from the atmosphere, and it gradually decays after death. But turning carbon-14 levels into an age expressed in calendar years requires knowing how much radiocarbon was in the atmosphere when the wood or seed was alive. That baseline fluctuates over time—sometimes substantially, as it did during the 15th through the 17th centuries. For that period, radiocarbon dating can yield possible calendar years that are "wildly different but all completely plausible," says Jacob Holland-Lulewicz, an archaeologist at Pennsylvania State University, resulting in uncertainties of a century or more.

Now, dating experts such as Manning are sharpening the resolution with the help of sophisticated statistical models that incorporate multiple carbon dates from certain kinds of artifacts such as wooden posts or charcoal. Tree rings in those artifacts provide an independent check on the carbon dates, helping archaeologists distinguish which of the statistically pos-

PHOTO: ROBERT RAUSCH/*THE NEW YORK TIMES* VIA REDUX

Archaeologists are revisiting the histories of North American sites, such as those in Ocmulgee Mounds National Historical Park.

sible calendar years is most likely to be correct. The reduced uncertainty brings history into focus, down to just a few decades. "On a generation scale, you can tell a human story," says Erik Marsh, a radiocarbon expert at Argentina's National Scientific and Technical Research Council who applies similar methods in South America.

The new dates are helping answer questions tribal nations have about their own history. Victor Thompson, an archaeologist at UGA, is redating sites in Georgia's Ocmulgee Mounds National Historical Park at the request of the Muscogee (Creek) Nation, whose citizens lived in the region until they were forcibly removed by the U.S. government to Oklahoma in the 19th century. Thompson presented unpublished data showing the Lamar site in Ocmulgee was very likely the Indigenous town known as Ichisi that was visited by Spanish explorer Hernando De Soto in 1540.

Other archaeologists had thought Ichisi was more likely another, nearby site that contains more European artifacts. But the new dates show that a lack of European trade goods doesn't mean a site was precontact. "Just because European stuff exists, that doesn't mean Indigenous people want it. They're not passive recipients," Holland-Lulewicz says.

Many Indigenous communities endured long after archaeologists had assumed. Thompson's new dates show that Muscogee ancestors lived at Lamar well into the 17th century, 100 years after De Soto's visit. Pigott also presented preliminary radiocarbon data suggesting that villages belonging to the Joara society in North Carolina continued to be occupied long after their people destroyed the region's first Spanish fort in 1568.

"People paint the picture that colonization was adopted abruptly—a one-night stay [by a European], and we changed our life completely. And that's just not the case," says RaeLynn Butler, secretary of Culture and Humanities for the Muscogee (Creek) Nation and a discussant at the SAA session.

Improved radiocarbon dates can also free archaeologists from relying on European accounts to shed light on Indigenous people's actions and decisions. At the session, Megan Anne Conger, an archaeologist who works in UGA's radiocarbon dating lab, presented data on two sites where Indigenous people produced beaver pelts in southern Ontario. These sites were assumed to have been occupied after 1580, when the French formally established the North American fur trade. But radiocarbon dates show Indigenous people did not wait for a European decree to reinvent their economy. They were intensively hunting and processing beavers there decades earlier, driving supply before the French formalized their demand.

Harnessing the new dating techniques can be expensive. "Quality control is everything," Manning says. Birch adds that unlike artifact-based chronologies, which are often generalized over entire regions, each carbon-based "microhistory" is unique to a site, and must be "scaffolded together" to construct a larger historical narrative.

Butler emphasized that the highly technical nature of the research can create new barriers between archaeologists and Indigenous communities. "It shouldn't take a tribal historic preservation officer luckily reading a paper to make that connection with the researcher, to share those histories, to strengthen what we know," she said. She also called on archaeologists to connect their new radiocarbon chronologies all the way up to tribal nations in the present day. "Why is it that this [contact] time period is so critical and important?" she said to close the session. "And not necessarily what happened to our people after that?" □

TRUMP TRACKER

HOLD THAT THOUGHT After public and scientific criticism, President Donald Trump's administration on 24 April rapidly reversed course on a landmark study of women's health that the National Institutes of Health (NIH) planned to gut and dropped a key component of a controversial new probe of autism's cause. Last week, the heads of regional centers integral to NIH's Women's Health Initiative said they were told the centers' contracts would end in September. Following an outcry led by senators and celebrity Maria Shriver, a spokesperson for the Department of Health and Human Services (HHS) called that a mistake and said: "We are now working to fully restore funding to these essential research efforts." Separately, NIH Director Jayanta "Jay" Bhattacharya indicated in public comments last week that his agency would set up a registry of individuals with autism, amassing data from sources including private entities, as part of HHS Secretary Robert F. Kennedy Jr.'s project to unravel the condition's causes. There was immediate protest from the autism community and privacy advocates. Days later, HHS declared: "We are not creating an autism registry."

NEW HEADS NIH last week named acting directors for six of its institutes, including the agency's second largest overall, the National Institute of Allergy and Infectious Diseases (NIAID). Influenza researcher Jeffery Taubenberger will lead NIAID after the Trump administration forced out its former director, as well as the other institute heads. Taubenberger's team famously sequenced the virus that caused the 1918 flu pandemic, extracting samples from autopsies of soldiers and an Inuit woman buried in the Alaskan permafrost. All six appointees are experienced NIH employees, and some—including the new acting directors of the Institute on Minority Health and Health Disparities and the Institute of Child Health and Human Development—have already been deputy directors.

REPORT AUTHORS FIRED The Trump administration this week fired the volunteer authors working on the sixth iteration of the U.S. National Climate Assessment, the congressionally mandated report, due later this decade, that guides businesses and states adapting to global warming. The move was not unexpected: Last month, the White House fired technical staff supporting the report. Scientists fear the administration will now try to produce a report downplaying the risks of climate change.

CLIMATE

Hunt for tree rings could yield Africa's first drought atlas

Records could reveal how much humanity has altered Sahel rains **PAUL VOOSEN**

Only a few African tree species preserve a long record of rainfall in their annual rings.

For decades, a climatological mystery has haunted West Africa. In the 1970s and '80s, a vicious drought, perhaps the worst worldwide in the 20th century, struck the region, which includes the Guinea coast and the Sahel savanna, just south of the Sahara Desert. The disaster killed tens of thousands of people in Senegal and other countries and caused a mass migration to cities. But then the drought stopped, and nothing like it has occurred since. Still the question has lingered: Could the great drought return?

Climate researchers led by Edward Cook and Michela Biasutti of Columbia University want to glean an answer from trees, using tree-ring records to create the first comprehensive, multicentury drought atlas for any region of Africa. They're now mounting an arduous search for the few West African trees that capture the whispers of past rainfall in their annual growth. "We want to tell people what to expect in the next few decades," Biasutti says. Climate change will surely affect future droughts, but any forecast requires knowing what happened in the past.

Water-stressed even in normal times, Senegal sorely needs the information, says Ousmane Ndiaye, director general of the African Center of Meteorological Applications for Development and, until recently, director of Senegal's weather service. Ndiaye—who studied climate science at Columbia—devised a seasonal forecast system that uses surface temperatures in the Atlantic Ocean, which strongly influence West African rainfall, to tell farmers whether to plant drought-resilient crops, such as millet, or water-hungry cash crops such as maize or peanuts. But seasonal forecasts aren't enough, he says. "Planning, building roads, managing new cities, those things need information that's long term."

To predict future extremes, climate scientists normally turn to computer models. But those models struggle with the tropics, and West Africa is particularly complex, says Amita Prabhu, a climate scientist at the Indian Institute of Tropical Meteorology. Not only does the nearby Atlantic influence its rains, but so do distant connections with the westerly winds that surround Antarctica, she showed in a paper published earlier this year in *Climate Dynamics*. That coupling, she says, "means that even small shifts in one element can trigger cascading effects on the entire monsoon system, making precise future projections challenging."

In other parts of the world, understanding the natural drought cycle might not require looking back centuries. But West Africa is a special case. Much evidence now suggests the Sahel drought was caused, at least in part, by air pollution from the United States and Europe, Biasutti says. As economies boomed following World War II, coal-fired

PHOTO: MICHELA BIASUTTI

power plants belched sulfur gas, which formed sulfate particles that reflected sunlight and cooled the North Atlantic. The cooling fed the drought by suppressing a natural tendency for the tropical rain bands that form in West Africa's wet season to shift northward. "We have a lot of reason to believe this was going on," she says. But what they don't know is whether such changes can arise unprompted by humanity.

Recorded measurements can't say, because rainfall data for the region are unreliable prior to the 20th century, and spotty even then. The number of weather stations rose in the 1920s, peaked in the 1960s during the end of colonialism, and fell off in the 1990s—a curve very similar to that of sulfates. "It makes it hard to tease that stuff out," says Chris Funk, a climate scientist at the University of California, Santa Barbara.

"Trees will be able to take us further back," Biasutti says. But they aren't an easy source of data either. Many tropical trees are hollow or form rings that do not match up with the swings between wet and dry seasons. But a few African species do seem to produce annual rings. Last month, Biasutti and Cook, joined by Alassane Diouf, a botany graduate student at Cheikh Anta Diop University, spent 2 weeks in Niokolo-Koba National Park, Senegal's largest nature reserve, near its border with Guinea and Mali, where they hoped to find older specimens and extract slender cores of wood from them.

It was not easy going. Temperatures during the day reached 45°C, and on occasion troops of aggressive Guinea baboons chased their SUV. But a park agent who stayed with them to fend off stray hippos or lions—or poachers—learned tree-coring skills and lent a hand. They also shared a camp with French researchers who had been studying Guinea baboons for the better part of 2 decades and knew where to find the five tree species they were targeting. In the end, they collected four cores per tree, and 20 trees of each species.

The drilling yielded one discouraging sign: a gush of water from some specimens when the team removed a core, even though they were working deep in the dry season. "These trees have a way of holding on to water," Biasutti says. That may enable at least some of them to keep growing in the dry season—which might make their rings less sensitive as drought recorders.

Only analysis back in the lab will tell whether the rings do capture a detailed history of drought. If so, Cook will combine the tree records into a map of drought over space and time, using a methodology he has deployed on nearly every other continent. His drought atlases have revealed, for example, long lasting "megadroughts" that struck the Americas regularly from 800 C.E. to 1600 C.E.—showing what a wet anomaly the recent past of the U.S. West has been.

Such a long-term record won't be possible in West Africa, Cook says. "If we can get back to the early 19th century or late 18th century, we would be ecstatic." □

AGRICULTURE

A single gene helps rice handle the heat

Discovery could preserve grain quality and yields as climate change raises temperatures **ERIK STOKSTAD**

Rice plants usually love warmth. But when they start to flower, hot nights can result in meager harvests and chalky grain. So far, breeders have made slow progress in solving these challenges, which are becoming more urgent with climate change.

Now, after searching for more than a decade, researchers in China have found a culpable gene, which they describe this week in *Cell*. They also show that a natural variant of the gene can preserve both yield and rice quality when temperatures rise. "This paper is a major breakthrough," says Argelia Lorence, a plant biochemist at Arkansas State University who studies heat stress in rice. The impact could ultimately be even broader than rice, she notes: The gene is present in other cereals, such as wheat and corn, that suffer similar problems with heat.

Rising temperatures are a major and growing threat to rice production. A landmark 2004 study at the International Rice Research Institute (IRRI) in the Philippines found that yield fell by 10% for every degree Celsius that average nighttime air temperature rose between 1979 and 2003. And nighttime temperatures continue to rise twice as fast as daytime temperatures in many rice-growing areas in Asia and Africa.

In 2012, a team in China began to look for rice varieties that could withstand hotter temperatures. Led by plant geneticist Yibo Li of Huazhong Agricultural University, they planted 533 types of rice in four locations in China where nights have gotten warmer. After harvest, they assessed grain chalkiness by simply counting grains that were white rather than translucent. Two research varieties did particularly well: Chenghui448 and OM1723. By crossing them and tracking genetic markers in the hybrids, the team homed in on a "quality-thermotolerant" gene on chromosome 12, which they named *QT12*.

Further experiments revealed how an overheated *QT12* stirs up trouble and leads to chalky grains. At normal temperatures, three transcription factors that regulate the gene are bound together. Under hotter conditions, one breaks away and binds to the promoter that turns on *QT12*. This change in gene regulation interferes with a crucial cellular organelle called the endoplasmic reticulum, which helps fold proteins and transport molecules. As a result, less protein and more starch get stored in the endosperm, the tissue that makes up the grain. The starch molecules pack together unevenly, which other researchers have shown is the reason the grains look chalky. They also become brittle and likely to break during milling, and the cooked rice tastes pasty.

In future research, Li and colleagues hope to find out how the altered

Rice farmers in Hanoi, Vietnam, plant at night to avoid the summer heat that is increasing across Southeast Asia.

PHOTO: NHAC NGUYEN/AFP VIA GETTY IMAGES

regulation of *QT12* affects yield. One possibility, says Vibha Srivastava, a plant biotechnologist at the University of Arkansas, is that problems in the endoplasmic reticulum disrupt flowering in ways that reduce seed production and therefore yield.

Gene editing provided evidence *QT12* does, in fact, affect quantity as well as quality. The researchers knocked out the gene in a heat sensitive strain of research rice. The modified rice kept its usual yield, whereas unmodified rice bore 58% less grain. That result excites Srivastava because it implies that gene editing—although still challenging to achieve in commercial varieties of rice—could ultimately be used to improve heat tolerance.

Traditional breeding could also do the trick. Li's team identified variations, or alleles, of *QT12* that remain inactive under heat stress. They bred two of these alleles from Chenghui448 into a temperature-sensitive type of rice, called Huazhan, that is widely used in China to create hybrid rice. In field trials, this new strain of Huazhan performed much better under high temperatures, bearing 31% to 78% more grain than regular Huazhan, depending on the location. And only 10% of harvested rice was chalky, compared with 60% from the regular Huazhan.

Li's team also showed protective alleles are not uncommon in the indica subspecies of rice, which fares better in hot conditions than the other important subspecies cultivated in Asia, japonica. By analyzing 4726 rice types from around the world, they found that 18% of varieties have *QT12* heat-tolerant alleles, but none are present in the japonica varieties tested that are adapted for colder climes. Breeders or farmers in lower latitudes may have selected favorable alleles of *QT12*—at some time in the past, without knowing the genetics—to defend their rice harvests from heat.

Srivastava is impressed that a single gene influences two important traits such as quality and yield. "This is a remarkable discovery," she says. Li says his university has signed agreements with major rice breeding companies in China to develop strains with heat resistance. "I hope our paper can be noticed by the majority of breeding workers and actively applied to production," he says. Rice breeder Adam Famoso at Louisiana State University, for one, is interested in trying *QT12* alleles in local varieties. "Let's say we get results like they saw," he muses. "I think it would have a huge impact."

Nese Sreenivasulu, who studies rice quality at IRRI, predicts the findings will turn out to be most beneficial for japonica varieties grown in temperate areas, where current rice crops are particularly sensitive to heat. He suspects that fully protecting indica varieties in the tropics from nighttime temperatures there, which reach up to 30°C, will require more protection than any one gene can muster. Scientists need to keep searching their seed collections, he says: "We need to find extreme tolerant lines." □

IN FOCUS

Moth illusion fools computers

Some animals' optical illusions—for protective camouflage or communication—can trick not just predators and humans, but computers, too. In a study published this week in the *Journal of the Royal Society Interface*, researchers tested whether deep learning artificial intelligence (AI) software was easily fooled by illusory camouflage, which allows an animal to look like something else altogether. Scientists focused on the green fruit-piercing moth, whose patterned green wings mimic a curled leaf, with highlights and shadows making the flat wing appear 3D. Along with images of other camouflaging moths, researchers tested whether the software perceived images of the fruit-piercing moth as a wing or a leaf. Three-dimensional renderings of what the software perceives showed the AI also saw the moth's illusion: A dark spot in the wing's pattern appeared as a shadow on the leaf's underside in the 3D version. The authors say future studies might test the same technique in different light backgrounds to see how the software responds.

PHOTO: SANDID VIA PIXABAY

Containers await shipping at the Port of Baltimore in early April.

PHOTO: SAMUEL CORUM/SIPA VIA AP IMAGES

TRADE POLICY

Tariff war takes toll on labs in China

Scientists face higher prices and import bans on equipment and supplies **RICHARD STONE**

Days after celebrating the publication in *Science* of a paper he co-authored on gene expression in mice, cell biologist Tang Fuchou of Peking University was whiplashed by the deepening trade war between China and the United States. Citing new tariffs imposed by China on U.S. goods, Addgene, a Massachusetts-based nonprofit repository of circular DNA strands called plasmids, last month canceled a contract to supply them to Tang's lab. His team would have to painstakingly construct plasmids itself, delaying a project by months. "It was really frustrating!" he says. Then on 21 April, Addgene agreed to sell Tang the plasmids after all—but at a hefty tariff-driven markup.

The tit-for-tat escalation of tariffs between the world's two biggest economies is afflicting researchers on both sides of the Pacific Ocean. For U.S. scientists, tariffs of 145% on most Chinese imports have meant far pricier reagents, glassware, and other lab essentials from the U.S.'s largest Asian trading partner. In China, elite scientists like Tang are suffering because China has responded to the U.S. moves with a tariff of 125% on all U.S. imports—including high-end instruments and specialty research materials that Chinese firms can't easily supply.

"Tariffs indeed are having a big impact on research in China," says Xiong Bo, a molecular biologist at Zhejiang University. "If this continues for a long time," adds Fan Shaofeng, a research official at Peking University, "it will be greatly detrimental to the development of global science."

In 2024, China imported some $12.5 billion worth of precision instruments from the U.S., according to an 11 April article on the Chinese news site Toutiao. Advanced Hall effect measurement systems, which characterize electrical properties of materials and can cost tens of thousands of dollars, are one example. "It's a critical instrument widely used in semiconductors research," says Zhu Tiejun, a materials scientist at Zhejiang University. One favored system, from Ohio-based Lake Shore Cryotronics, will be far pricier now that it faces a 125% tariff, he says.

Genetics researchers face another hurdle: trade restrictions the Chinese government has placed on Illumina, a prominent U.S. maker of gene sequencers. On 4 February, 3 days after the U.S. slapped an initial tariff of 10% on all Chinese imports, China retaliated with reciprocal tariffs and placed Illumina on its blacklist of "unreliable entities," alleging the California-based firm had engaged in unfair trade practices. A month later, China barred import of Illumina's sequencers.

Chinese labs also depend on U.S. reagents and lab supplies that have been subject to steep markups and supply disruptions. Several major U.S. firms have simply stopped selling antibodies to China, says Chen Ye-Guang, a molecular biologist at Tsinghua University. And he says prices have shot up for U.S.-made restriction enzymes, stem cell–related products, and tissue culture products. "We are seeking replacements and hope that our experiments will not stop," Chen says.

For high-end instruments, few substitutes are available, and Chinese researchers are finding ways to share what they have. According to Deng Huachun, a nanophotonics researcher at the Harbin Institute of Technology, "Some groups have begun using Chinese-made electron microscopes for preliminary experiments." When gunning for publication-quality data they book time on top-of-the-line imports at centralized facilities.

China also has a buffer. Under its 2021–25 national science plan, China's science ministry vowed to

"establish emergency reserves for critical research supplies to ensure stable support for major national projects" and to invest in reagent manufacturing. That response was driven in part by the COVID-19 pandemic, when Chinese labs faced supply shortages. As tensions with the U.S. shot up, many universities and institutes created their own stockpiles of essential reagents and lab materials. The goal was "to reduce China's dependence on imports that put research efforts at risk," notes Denis Simon, a China science policy expert at Duke University.

As Chinese scientific suppliers grow more sophisticated, they are closing the gap with overseas competitors. "Domestic reagent companies have been developing well in China in recent years," Xiong says. The tariff war, he says, is bound to accelerate the trend.

China's efforts to develop the high-end computer chips needed for artificial intelligence (AI) systems could also see a boost from U.S. export restrictions. In 2022, then-President Joe Biden's administration banned sales of Nvidia's top-of-the-line H100 AI chips to China. In response, Nvidia developed a less powerful H20 chip that didn't violate the ban. But last month, President Donald Trump's administration also banned the sale of H20 chips to China.

For the moment, many Chinese firms and researchers have chip stockpiles "which can sustain near-term model training and deployment," says Ray Wang, a Washington, D.C.–based analyst specializing in U.S.-Chinese high-tech competition. The longer term impact hinges partly on how quickly Huawei, China's AI leader, improves the performance of its chips. Huawei's Ascend 910C chip "has performance metrics close to H20," Wang says, though Nvidia chips still have "significant software advantages" that will take time to match.

In the meantime, many Chinese scientists fear both they and their U.S. counterparts will suffer from a prolonged trade war. "The long-term costs to both nations' research ecosystems could be profound," Deng says. □

With reporting by Dennis Normile.

IN FOCUS

Hot chili pepper dance wins Ph.D. contest

University of Helsinki food chemist Sulo Roukka is the winner of this year's "Dance Your Ph.D." contest with an entertaining look at his thesis on humans' perception of food chemicals. The annual *Science* competition invites early-career researchers to interpret their work through movement, offering a bit of fame—and cash prizes, sponsored this year by artificial intelligence company SandboxAQ. Roukka, who took home $2750 for winning both the overall and the chemistry categories, beat out 27 other entries from 16 countries. Shedding a lab coat for a chili pepper–red costume, Roukka interpreted how humans experience food compounds, such as capsaicin in chilies and menthol in mint, by having a team of dancers leap and twirl in his lab and halls and even carry him aloft. See his winning video and others at https://scim.ag/DancePhD2025.

PHOTO: SULO ROUKKA

SCIENTIFIC COMMUNITY

Ecologist blurred professional boundaries, report finds

Thomas Crowther has lost his post at ETH Zürich but denies any misconduct

CATHLEEN O'GRADY

Thomas Crowther, the ETH Zürich ecologist whose rapid rise to prominence brought him intense media coverage, large research grants, and a position advising the United Nations, blurred personal and professional boundaries and broke rules regarding financial compliance and hiring, according to a report the university released last week. The redacted report—which does not name Crowther but describes particulars that match his case—also notes multiple allegations of inappropriate behavior toward employees. Crowther has been denied tenure as a result of the findings and will leave the institution in September when his contract expires, the university has announced.

ETH did not reach a definitive conclusion about some of the interpersonal allegations, Julia Dannath, the university's vice president for personnel development and leadership, said in a 25 April online statement that referred to "an ETH assistant professor." But she says the professor "did not maintain an adequate professional distance from students, doctoral students and staff." Stefan Spiegel, vice president for finance and controlling, said the professor "repeatedly failed to follow internal rules and adequately address conflicts of interest."

In an email to *Science*, Crowther said he "sometimes blurred the lines between friendship and leadership" but that he had not committed any personal misconduct and if university procedures "were inadvertently not fully respected," this was unintentional. He added that he had treated employees with "kindness and respect" and was "deeply saddened" that his approach did not work for some lab members. Members of his lab have written to ETH leadership contesting the findings and complaining of "profound procedural flaws and biased reasoning" in the investigation.

Crowther shot to fame in 2019 with a headline-grabbing *Science* paper reporting that the planet had enough land for an extra trillion trees to be planted, and that doing so could sharply slow climate change. Some scientists criticized the conclusions as simplistic and suggested large-scale tree planting could damage grasslands. Crowther's team issued corrections to the paper,

Thomas Crowther will be leaving ETH Zürich after complaints about the environment in his lab.

PHOTO: FREDERIK VAN DEN BERG

and he clarified that he had never intended to encourage tree planting in open ecosystems.

That and other influential papers helped make Crowther "one of the most high-profile figures in global ecology," says University College Cork ecologist Markus Eichhorn. His work gave rise to the World Economic Forum's Trillion Trees initiative, and Crowther serves as a co-chair of the advisory board to the U.N. Decade on Ecosystem Restoration. But questions about his lab culture began to emerge. A September 2019 profile in *Nature* prompted a social media pile-on drawing parallels to the "toxic culture of Silicon Valley" and pointing out the lack of diversity in the lab. In a profile in *Science* 1 month later, Crowther responded that he was "seriously worried about" diversity and was making an effort to recruit more women. The gender balance in the lab has been at parity for the past 5 years, Crowther says.

In 2023 and 2024, complaints about Crowther's behavior and financial compliance were filed with ETH, the new report says, prompting the university to engage a law firm to investigate. Some of the complaints were reported by Swiss newspaper *Tages-Anzeiger* last year, but it omitted details because of a court injunction prohibiting their publication. The court has partially lifted the injunction, and last week *Tages-Anzeiger* reported details of some complaints, including alleged unwanted approaches to women, which Crowther denies.

The ETH report says some employees describe a "toxic management culture" in the lab, with "sexist and discriminatory comments," pressure to join social events, and "repeated cases of inappropriate behavior towards employees in the context of pranks and games."

The law firm investigated three specific allegations of "inappropriate personal advances," all from past employees. The university concluded that contradictory accounts made the exact details difficult to establish, but said multiple current lab members corroborated the general problem of inappropriate behavior. Although many lab members enjoyed the highly social atmosphere in the lab, the report said, Crowther "displays a leadership style and general behaviour that at least partly contradicts ETH Zürich's values."

In an email to *Science*, Crowther's lawyers wrote that he "welcomes the fact that … the allegations of harassment or other inappropriate behavior [have] been completely dropped." The lawyers argue that "ETH has acknowledged between the lines that the complainants may not always have told the truth." Crowther "never created a toxic culture and behaved appropriately towards all members of ETH."

The university also found Crowther had broken various financial rules, including using ETH funds for public relations advice and legal fees after news of allegations against him broke in August 2024. The university also said a member of Crowther's family was employed in another department while actually working for the Crowther lab, against ETH policy. Crowther says he transferred funds to another ETH lab to pay his sister because she was entitled to grant money from a proposal they had co-written.

Lab manager Emily Clark disputes the claims about Crowther's behavior, saying she never witnessed anything that "would be construed as personal misconduct or harassment." The lab celebrated the diversity of its members and was a close-knit community, she says: "Tom has always been one of the most genuinely inclusive and accepting leaders I've ever worked with."

Dozens of supportive posts on social media describe Crowther as "visionary and kind" and his lab as having a "culture of inclusivity, respect, and unwavering support." Postdoc Lidong Mo said on X it was "the happiest and most supportive environment I have ever worked in." In February, lab members posted an open letter describing their positive experiences there.

Sam Suarez, a former lab employee, welcomes the report, saying it provides "critical clarity" on the case. The university seems to have used the case as impetus to improve its safeguards, she says, but "time will tell" whether its efforts bear fruit.

Crowther would not comment to *Science* about his future or that of his ETH lab. "For now I am focusing on my mental health, and that of my lab members," he says. ETH says it has made arrangements for Ph.D. students in the lab to complete their degrees, but that most other lab members held fixed-term contracts. Clark says the lab is negotiating with the university to extend some of those contracts, but that depending on the outcome, between 25 and 30 employees will lose their jobs, and in many cases will be forced to leave the country. □

IN OTHER NEWS

Still in a baby lull

The U.S. Centers for Disease Control and Prevention released provisional data last week on U.S. births in 2024, showing 3,622,673 new births—just a 1% increase from 2023. The fertility rate remains at only 1.6 total children per woman, which is below the 2.1 fertility rate experts say is needed to sustain a country's population. Globally, the fertility rate may need to be even higher for a steady state. In *PLOS ONE* this week, researchers describe a new model that calculates the necessary global rate by accounting for mortality rates, sex ratios, and the probability of some adults never having children. They found that to avoid a gradual extinction—especially in small, isolated communities that don't tend to interact with outsiders—a population's birth rate may need to climb above 2.7 children per woman. The global fertility rate is now 2.2, according to the United Nations, suggesting birth rates may need to rise if the new study's estimates are correct.

The Chang'e-5 capsule, which landed in Inner Mongolia in late 2020, brought rocks and soil from the Moon back to Earth for the first time since 1976.

PHOTO: TOPPHOTO VIA AP IMAGES

LUNAR SCIENCE

China reveals the foreign scientists who will share its rare lunar samples

Seven research teams in six nations get Moon rocks and soil brought to Earth by the Chang'e-5 mission

DENNIS NORMILE

Five years after its Chang'e-5 mission returned the first samples of soil and rocks from the Moon in nearly 50 years, China has begun to share the precious specimens with select groups of researchers outside the country. Seven institutions in six countries will gain access to tiny shares of the lunar material, the China National Space Administration (CNSA) revealed at a 24 April ceremony in Shanghai. Notably, two institutions in the United States—Stony Brook and Brown universities—are getting samples, even though Chinese researchers have not been able to access NASA's Moon samples because of restrictions imposed by the U.S. Congress.

Those picked to get Chang'e-5's samples feel privileged. "It's honestly a huge honor. Being selected … is both exciting and humbling—especially knowing how competitive the selection process was," says Frédéric Moynier, a cosmochemist at the Paris Institute of Planetary Physics.

When the Chang'e-5 return module landed in the remote grasslands of Inner Mongolia on 17 December 2020, it was carrying 1731 grams of material scooped from the surface and from a 1-meter-deep core drilling. They were the first Moon rocks brought to Earth since the last Soviet Luna mission of 1976. Chinese researchers, often with foreign cooperation, soon began to analyze the trove. In 2023, CNSA also invited proposals from foreign teams, drawing 24 submissions; it quietly informed the winners earlier this year.

Researchers have already published dozens of scientific papers on the samples, which were retrieved from Mons Rümker, an inactive volcano within the Oceanus Procellarum, a vast mare of hardened lava. One surprise is that the material is just 2 billion years old, or about 1 billion years younger than samples retrieved by the U.S. Apollo and Soviet Luna missions. This suggests lunar volcanoes were active more recently than previously thought. And further analyses by Chinese teams have raised the question of what was driving the volcanism in the absence of water and hot radioactive elements to produce subsurface magma.

The foreign scientists now getting samples hope their own unique analytical equipment and expertise will help them answer such questions. Mahesh Anand, a geochemist at the Open University, plans to use a customized instrument to measure isotopes of oxygen that provide hints of where in the Solar System the lunar material originated. "It will help us evaluate the giant impact hypothesis for the origin of the Moon," which proposes that the Moon formed from a collision between early Earth and a Mars-size protoplanet, Anand says.

Moynier says his team is particularly fortunate, getting access to both a sample directly from CNSA and two additional samples that Chinese President Xi Jinping gave to French President Emmanuel Macron in 2023. The CNSA sample is a fragment of basalt, which he says is a rarity in the loose rock that makes up the bulk of the Chang'e-5 samples. Studying the basalt promises a better understanding of the volcanic history of the Moon. And comparing the abundance and composition of volatile elements in this sample and those from Apollo will shed light on the Moon's formation and evolution, Moynier says.

Carsten Münker, a cosmochemist at the University of Cologne who attended the Shanghai ceremony, believes applying his team's analyti-

cal expertise to Chang'e-5 samples will provide hints as to how the lunar magma ocean, a layer of molten rock believed to have covered the Moon's surface shortly after its formation, crystalized into the lunar mantle.

Sharing the samples takes China's embrace of international cooperation in space science to a new level. Many Chang'e-5 papers published so far include international co-authors who helped interpret analytical data produced in Chinese labs. Earlier and later lunar missions, Chang'e-4 and Chang'e-6, each carried four international payloads. Chang'e-6, for example, released a Pakistani CubeSat into lunar orbit that is imaging the Moon's surface. Its lander, the first spacecraft to land on the far side of the Moon, carried a French instrument to study volatile compounds. Chang'e-7, set to launch next year, will have six international payloads.

"I wish that every country would follow in the footsteps of the U.S. and now China" in sharing samples widely, Anand says. With its open, competitive process for access to samples (below), "China is setting a very positive example for scientific cooperation," Moynier adds.

Chang'e-5's samples are providing new insights into the Moon's volcanism and evolution.

PHOTO: TIAN YUHAO/CHINA NEWS SERVICE/VCG VIA GETTY IMAGES

Moynier received his samples last week as he could not attend the signing ceremony. Stony Brook and Brown are still working on final approval of loan agreements, says Stony Brook planetary scientist Tim Glotch. He says they hope to pick up their samples and get to work later this year. (In accordance with a long-standing U.S. congressional ban on using NASA funding for bilateral cooperation with China, the research is being funded by their respective institutions, Glotch says.) The remaining four groups received their samples last week in Beijing.

More samples are on the way. Last year, Chang'e-6 returned nearly 2000 grams of lunar soil, which CNSA says it will also share with foreign teams. Scientists are eager to see what the soil can reveal about the Moon's history. □

U.S. SCIENCE POLICY

NSF director resigns amid cuts to grants and staff reductions

Sethuraman Panchanathan stepped down soon after Trump team started to terminate agency awards **JEFFREY MERVIS**

The scientist President Donald Trump chose during his first term to lead the National Science Foundation (NSF) resigned last week after apparently being unable to stomach the massive changes Trump has imposed on the agency during the first 100 days of his second administration.

"I believe that I have done all I can to advance the mission of the agency and feel that it is time to pass the baton to new leadership," Sethuraman "Panch" Panchanathan wrote in a 24 April letter to the staff. Panchanathan, a computer scientist whom the Senate confirmed to lead NSF in August 2020, leaves 16 months short of the end of the 6-year term.

"I cannot imagine how difficult it must have been trying to protect the NSF, its programs and staff, and the U.S. research community from White House directives and actions that are in conflict with NSF's mission, decades of congressional appropriations, and the law," says Rice University physicist Neal Lane, who led NSF under former President Bill Clinton.

Panchanathan didn't give a reason for his sudden departure, but he could not have been happy with orders from the White House to accept what could be a 55% cut to the agency's $9 billion budget next year and to draw up plans to halve its 1700-person staff. But his resignation letter was the first public indication of his unhappiness. "While NSF has always been an efficient agency," he wrote, "we still took [on] the challenge of identifying other possible efficiencies and reducing our commitments to serve the scientific community even better."

The last straw may have been a decision in mid-April by billionaire Elon Musk's Department of Government Efficiency (DOGE) to terminate up to $2 billion in existing NSF grants. The list appears to have been drawn from a report last fall by Senator Ted Cruz (R–TX) identifying what he said were 3483 "woke science" grants NSF had made to increase diversity in science, foster environmental justice, and study the spread of misinformation on social media. As *Science* went to press, researchers had reported the termination of some 550 awards since the agency's 18 April announcement it would begin to cancel grants.

Before leading NSF, Panchanathan had spent 20 years as a faculty member and then senior research administrator at Arizona State University. When nominated he was also serving on the National Science Board, NSF's presidentially appointed oversight body. His achievements included creating NSF's first new directorate in 30 years, for technology, innovation, and partnerships, and launching 10 regional "engines" that seek to spur economic development.

During his 5-year tenure, Panchanathan worked to build bipartisan ties to congressional leaders, who reciprocated in statements reacting to his resignation. "I thank Dr. Panchanathan for his vision, integrity, and unwavering commitment to U.S. scientific innovation," said Representative Brian Babin (R–TX), who leads the science panel in the House of Representatives.

The top Democrat on the Senate panel that Cruz chairs praised Panchanathan but also pointed a partisan finger at the Trump administration. Its proposal to cut NSF's budget represents "a deliberate dismemberment of America's innovation engine by DOGE" and the head of the White House budget office, Russell Vought, said Senator Maria Cantwell (WA). "Don't blame Panch for stepping down."

Brian Stone, who joined NSF in 2000 as a facilities manager and has spent the past decade as chief of staff to the director, is now acting director. The science board traditionally gives the president a list of potential nominees for director. But the board's leadership is in limbo. Its former chair, computer scientist Dario Gil, left on 21 April because he has been nominated as undersecretary for science at the Department of Energy. The acting chair is chemist Victor McCrary, vice president for research at the University of the District of Columbia. □

PHOTO: ARCHEOSFERA; LABANOF

Dropped into a crypt through manholes, bodies piled up over the course of 60 years.

FEATURES

TALES FROM THE CRYPT

The lives of 17th century Milan's working poor—their health, diet, and drug habits—emerge from thousands of bodies buried under a public hospital

ANDREW CURRY

In 1456, the Duke of Milan established a medical institution dedicated to caring for the city's poor and sick on a scale unprecedented in Europe. Built in the center of medieval Milan, the massive Ospedale Maggiore was soon dubbed Ca' Granda—"Big Factory" in the local dialect. The nickname was a reference to both its scale and its ambition: to heal Milan's working class as efficiently and effectively as possible.

Although churches had sponsored and staffed hospitals since the early Middle Ages, this hospital, funded by the rulers of Milan, was different. Admission was based on lack of income, not religious affiliation. "It's the first secular hospital we know of in Europe," says University of Milan (UNIMI) historian Folco Vaglienti. "That's why people of different ethnicities and religions could be treated. Everybody was welcome."

Ca' Granda's four wings could accommodate thousands of patients at once in a series of specialized wards treating everything from kidney stones and broken bones to tuberculosis (TB). The hospital had its own sewer system, kitchens, ice house, laundry, pharmacies, and chapel.

For 60 years, it also had its own system for disposing of the dead. Between 1637 and 1697, people who died at the hospital were dropped into brick-lined underground vaults below a newly built church. Hospital planners expected the remains to skeletonize quickly, but a cool, moist microclimate slowed decomposition. Bodies accumulated and stank, eventually forcing the hospital to seal off the chambers and begin burying people on the outskirts of town.

More than 300 years later, the tens of thousands of bodies in the crypt are providing scientists with a remarkable record of the poor in 17th century Milan. It's a population and time period about which we know surprisingly little, because archaeologists in Europe haven't paid much attention to how common people lived during the early modern period. "History tells us about politics and war, but nothing about ordinary people," says Mirko Mattia, a bioarchaeologist at UNIMI. "We know more about the commoners

Reading the remains

Information about the habits and health of the working poor in 17th century Milan comes from a vast deposit of bones, teeth, and other remains that accumulated in crypts beneath a hospital, where the dead were interred. Scientists are using an array of forensic and archaeological techniques to decipher the clues.

Graphic by **NOELLE BURGESS**

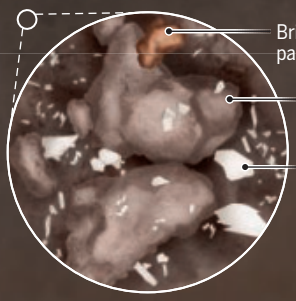

Thanatogenic soil

Decomposed and mummified soft tissue mingled with bone fragments and other material to form an unusual soil-like substance in which larger remains are embedded.

Sex

An individual's sex can be inferred from the **robustness** of structures such as the **supraorbital ridge**, **supraorbital margin**, **mastoid process**, and **nuchal crest**.

Age at death

Skull suture fusion reflects approximate age. The older an individual, the more closed the sutures. **Tooth eruption** canalso indicate age.

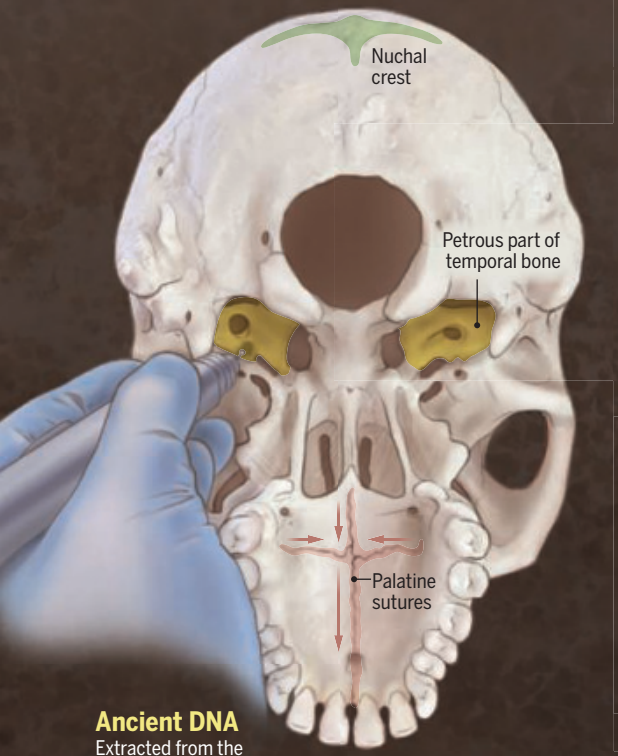

Ancient DNA

Extracted from the petrous part of the temporal bone, **DNA can reveal** an individual's **geographic origin** and **sex**, and **trace population change** over time.

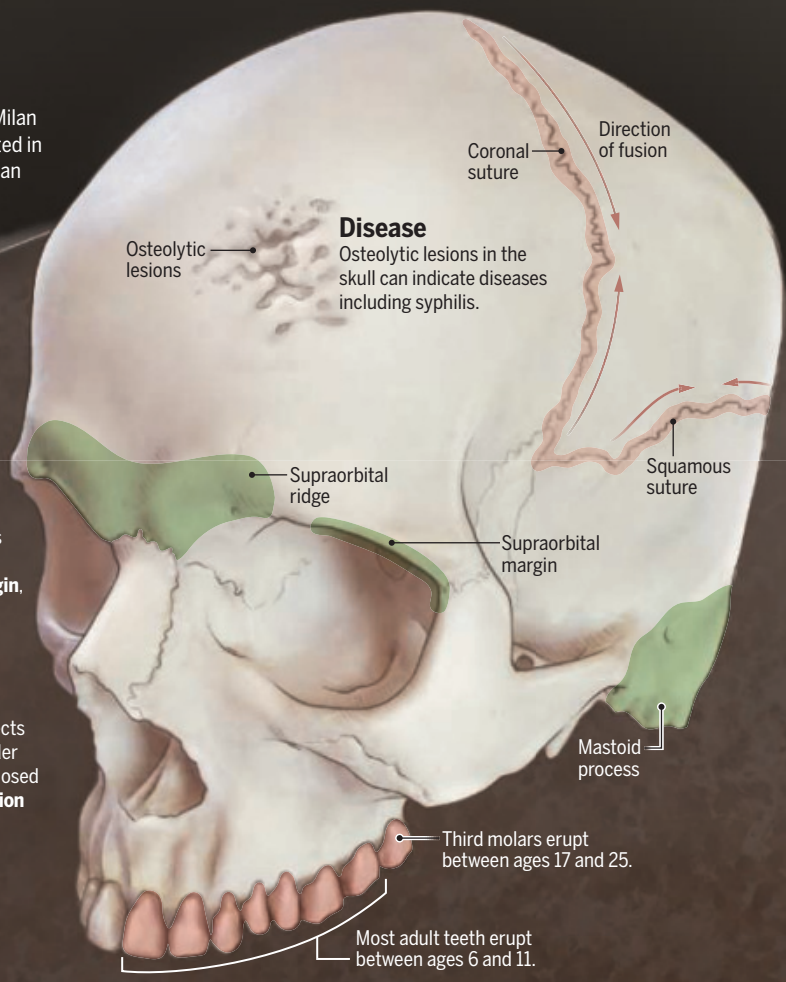

Diet and malnutrition

Lines in the enamel of the teeth, or **linear enamel hypoplasia**, can indicate **stress during growth**, which was common among the poor. **Plant residue** found in plaque can **record diet and herbal remedies**. In 17th century Milan, diets included more legumes such as lentils and broad beans than in Roman times, when barley was more common.

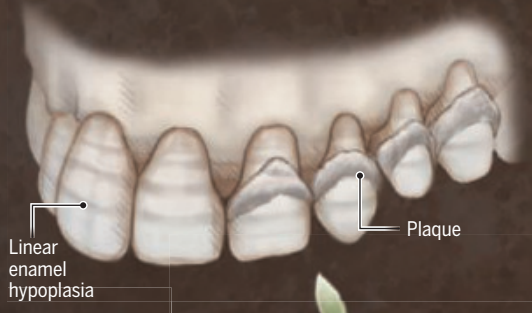

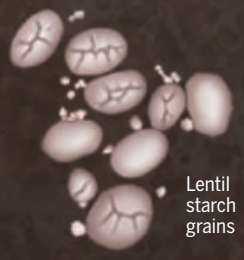

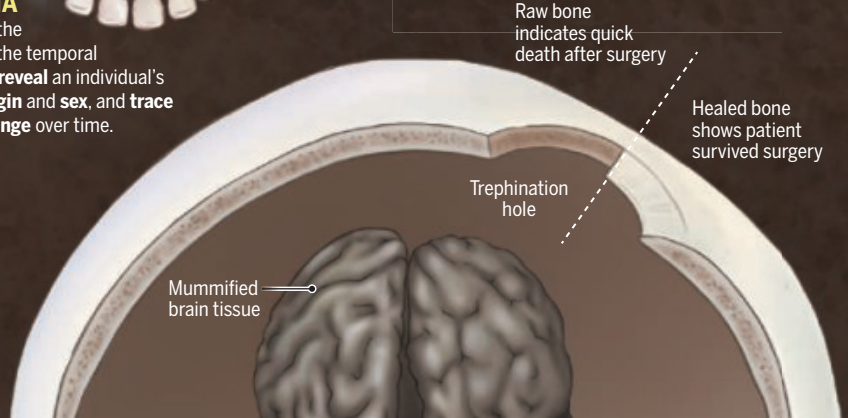

17th century medical treatment

Chemical analysis of **mummified brain tissue** has detected traces of **cannabis, opium**, **coca**, **and mercury**. Some substances may have been used recreationally, others given as medicine. Some skulls had **holes from trephination**, a treatment that can relieve brain pressure after an injury. Healing along the edges indicates whether the individual lived postsurgery.

of ancient Rome than we do about the people of the 17th century."

So far, a team of archaeologists, geneticists, botanists, and specialists in forensic medicine has examined more than 300,000 bones, out of an estimated 2.9 million preserved in the underground vaults. They are applying an array of analyses to the remains, providing a multidisciplinary look at the unnamed people who labored in Milan during a time of turbulent social change. Italian culture is broadly supportive of scientific study of the dead, making it possible to ethically study the remains as part of an effort to understand Milan's past.

"The beauty of a crypt like this is it shows us the history of those individuals, their travels, their activities, their health," says Robert Mann, a forensic anthropologist at the University of Hawaii at Manoa who is not involved with the research. "Finding a sample that large, all in one crypt, that can be dated—all the pieces of the puzzle come together."

The bones, for example, record the injuries and diseases people suffered. Fossilized plaque on teeth contains clues about what they ate, and their DNA hints at the origins of Milan's modern populace. All told, the findings portray a population riddled with illness and malnutrition who found relief in a surprising array of drugs, including coca, newly available from the Americas. They reveal how other plants from the New World, such as the potato, were starting to change the European diet. And from the remains of these forgotten patients, together with detailed death records in the hospital's library, their individual stories are beginning to emerge.

CA' GRANDA'S PRIMARY MISSION was to treat the working people of Milan, then one of Europe's largest cities and a key gateway between Northern Europe and Italy. Behind its colonnaded walkways and wide windows, the sick wards had an assembly line quality, with long rows of beds and regularly spaced toilets. To be admitted, people needed to prove bad luck or illness—not idleness—was preventing them from earning money. "Patients here were the working poor," Mattia says. "The duchy needed workers, and the hospital had to make sure they were cured."

But the limited treatments of the day, from setting bones and surgeries to remove kidney stones to amputation and bloodletting, were often no match for their ailments. (Some, like mercury administered to syphilis patients, may have been worse than the disease.) Because records of patient admissions have been lost, it's hard to estimate the hospital's mortality rate. But by the mid–17th century, "we calculate that 10 to 15 patients died per day," Mattia says. Beginning in 1637, the bodies were slid through manholes into a series of 14 vaulted, brick-lined burial chambers.

The underground water channels that carried sewage and other waste from the hospital ran nearby, and they had an unintended side effect: Along with periodic flooding, they kept humidity high and oxygen low in the burial chambers. Even today, water drips down the sides of the sepulcher walls. "It smells like wet soil down there," says Giulia Tagliabue, a doctoral student at UNIMI whose research focuses on how bodies decompose. The microclimate slowed the decay of the remains, not unlike the conditions that preserve bodies in bogs.

Some of the flesh became mummified or turned into a soaplike substance; the rest slowly putrefied. Accounts from the time report nuns in the chapel above collapsing from the stench. "Everyone in the area suffered," Mattia says. In 1697, Ca' Granda's administrators gave up and sealed the underground chambers. They would remain closed for centuries, aside from brief interludes during an 1848 rebellion and after damage from Allied air raids in 1943.

In 2010, Vaglienti and Cristina Cattaneo, head of UNIMI's Anthropological and Odontological Laboratory, began working with the hospital's archivist to open and study the chambers. Although Italian heritage officials had little interest in the site—it was considered too recent to be of much interest—the team soon realized the remains were a unique source of information. Because the chambers were in use for just 60 years and only used to bury patients from the hospital, they capture a specific slice of Milan's past and population.

It is a portrait composed almost entirely of human remains. Since excavations began in 2018, researchers have recovered a few rings, religious medallions, and crosses, but little else. The lack of clothing remnants, buttons, or buckles suggests the corpses were slipped into the sepulchers naked or wrapped in shrouds.

Bones and teeth recovered from underground vaults hold clues to diet and diseases, and preserved soft tissue reveals 17th century pharmacology.

PHOTO: ARCHEOSFERA; LABANOF

They now form layers of decomposed bodies 1 meter or more deep. Wearing masks and protective suits, the researchers move slowly and carefully through the remains, gathering samples and taking photos of the bone mounds. Computers knit together hundreds of images to create 3D pictures, showing how human remains piled up under the manhole covers above. "Because of the constant input … the bodies themselves create stratigraphic layers," Tagliabue says.

One feature in particular sets the deposit apart from other mass graves. When archaeologists first entered the sepulchers in 2010, they assumed the grayish black soil surrounding the bones meant patients had been buried in a cemetery nearby. Once the flesh had fully decayed, the thinking went, the bodies were exhumed—along with some of the surrounding soil—and placed underneath the chapel, a space-saving practice common in European cemeteries at the time. Tagliabue worked with soil specialists to analyze the material in the crypts, hoping to match it to known locations in the Milan area, like forensic investigators reconstructing a body's movements after a murder.

Under the 400-fold magnification of a scanning electron microscope, the soil samples baffled her. "I'd never seen something like this," Tagliabue says. "Basically, there was no soil in this soil." Chemical analyses were equally odd: "We usually expect lots of mineral components, but that's not the case," she says. "It's not typical of outdoor areas."

Eventually, Tagliabue realized she had something unusual under her microscope—and that researchers had the story of the sepulchers precisely reversed. "The answer is no, it's not soil," she says. Instead, the blackish substance was almost entirely made up of human flesh, with a light sprinkling of brick dust and microscopic bone fragments. (Lead and iridium, likely leftover from 1943 bomb damage, left chemical signatures of their own.) Tagliabue dubbed the substance "thanatogenic anthrosoil," a humanmade soil created by death and decomposition. "It's not similar to anything published in the literature," she says.

The Ospedale Maggiore archives store centuries of patient records, pharmaceutical recipes, medical textbooks, and documents describing the workings of the hospital.

PHOTO: MATTIA BALSAMINI/CONTRASTO VIA REDUX

ON A CHILLY MORNING last fall, buckets of this unique soil were lined up in a vaulted basement below the chapel for close examination and sampling. Fragments of human bones covered in crystallized salts and lime glittered in the dim light, as though dusted with sugar.

Spread out on the table were the knee and foot bones of a long-dead Ca' Granda patient. "What is striking is how much you can extrapolate from an ancient body," Cattaneo says, "and how much you can understand from that about the period they lived in."

During the half-century the crypts were open, epidemics, war, and economic collapse caused tremendous social change all across Europe. Contemporary accounts describe Milan as violent and dangerous, but so far the bones tell a different story. "We have very few signs of interpersonal violence or trauma," Mattia says.

Still, life was tough for the city's 17th century poor. Compared with people living in the Middle Ages, just a few centuries before, the Ca' Granda patients were in worse health, the combined result of repeated famines in the early 1600s and a 1630 plague outbreak that wiped out nearly half the city's population and shattered its economy. The bones record everything from signs of iron deficiency to childhood malnutrition and stress. TB—common enough that an entire wing of the hospital was devoted to treating it—left a mark on many bones, as did syphilis, recently introduced from the New World.

The researchers found other imports from across the Atlantic Ocean as well. When the vaults were first put into use, Europe had been in contact with the Americas for a little more than a century. "Ca' Granda spans a critical moment, which is the discovery of the Americas when Europeans started to introduce crops which later became very important," says UNIMI botanist Marco Caccianiga. But when and how novel crops that now seem synonymous with Italian food—from the tomatoes of marinara sauce to the corn in polenta—were adopted there is unclear. "We have historical records, but they lack detail."

Fossilized dental plaque, scraped from 50 individuals, helped re-

An anonymous 17th century painting depicts Ospedale Maggiore's courtyard, which teems with patients, medical personnel, and visitors. The body borne in the distant funeral procession may be bound for the crypt.

PHOTO: IRCCS FOUNDATION CA' GRANDA HOSPITAL MAGGIORE POLYCLINIC

construct what was on the menu for the poor: mostly Old World grains including wheat, barley, and sorghum, along with rice, millet, and other crops. The plaque also records a surprising newcomer, in the form of potato starch. Contemporary sources describe the South American tuber as poisonous and unpopular. "From history, we know the potato was a plant that came into use very, very slowly," Caccianiga says. "It could be potatoes were more widespread than expected."

Corn—now so widely eaten that the Milanese are sometimes nicknamed "polentoni," or polenta eaters—represents a small fraction of the diet. "We don't see any 'corn revolution' within our time span," Caccianiga says. Another missing crop: the tomato, which was considered deadly for the first few centuries after its introduction and was used only as an ornamental plant. Caccianiga hasn't given up hope that it is absent only because soft fruits are unlikely to be preserved in dental deposits. "Hopefully we can find some undigested tomato skin in the soil," he says.

Other plants told of deprivation. Multiple people in the crypts had spores from horsetails, a rushlike plant, trapped in their plaque. The coarse plant, high in silica, was mostly used to clean pans but contemporary sources refer to people eating it during famine. "Sources mention women who died of hunger with green mouths because they ate grass," Mattia says. "Now we've found the grass."

BECAUSE THE REMAINS include mummified soft tissue, the team can bring to bear analyses more common in crime labs than at archaeological sites. "It's a very different kind of collection," says Mario Zimmermann, a paleoethnobotanist at Boise State University who is not part of the research team. "In terms of complete human materials, it's pretty astonishing what the colleagues in Italy have to work with."

Some of the skulls still contain brain tissue, for example. With both brain and bone to analyze, Gaia Giordano, a forensic toxicologist at UNIMI, could apply toxicology tests used on modern crime victims to see what kinds of drugs were being prescribed—or enjoyed—in the hospital. She's found a wide array of psychoactive substances, including morphine, codeine, noscapine, and papaverine—all derived from the opium poppy. The hospital's detailed pharmacy inventories note some of those drugs, but there is no record of another group of substances, cannabinoids, that Giordano found in multiple bone samples. She thinks patients may have used marijuana recreationally.

In a bigger surprise, Giordano reported last year she had found traces of coca in the preserved brain tissue of nine Ca' Granda patients. It's the earliest known use of the plant outside of South America, predating the first historical mention of coca in Europe by at least 200 years. "Backdating the plant almost 2 centuries in Europe is pretty amazing," Giordano says. "People were probably using it the same way in Milan and South America, as an energy tonic to combat fatigue and hunger."

That, Cattaneo argues, suggests drug use may already have been widespread across Europe. Seventeenth century Milan was well-connected to the rest of the continent. "The fact they were chewing coca in Milan suggests they were chewing in Madrid and Paris, too," she says.

Other lab results have come more slowly. The high humidity that preserved soft tissue, hair, and bones in the underground chambers also degraded genetic material. University of Pavia geneticist Anna Olivieri says her team has been able to recover DNA from only 15 of the two dozen individuals tested so far, an unusually low success rate for samples just a few centuries old.

Still, the genetic information was enough to shed light on the hospital's population. Sex chromosomes

from the initial samples show twice as many men as women ended up in the sepulchers. "Maybe women didn't have equal access to medical care," Olivieri says. Or the skew might indicate men were less likely to survive their stay.

Preliminary analysis shows most of the people she's sampled look genetically similar to the present-day population of Milan, suggesting little immigration in the past 4 centuries. Ancient DNA from earlier periods, collected from graveyards in and around Milan as part of a larger project examining bones from the past 2000 years, tells a different story. "In the Roman period and Middle Ages, there was more genetic diversity," Olivieri says. "Immigration has always characterized our cities, and if people moved to Milan in the modern period it's possible they resembled those already living there."

> **"History tells us about politics and war, but nothing about ordinary people.** **Mirko Mattia,** University of Milan

Together, the bodies tell stories about people rarely remembered. "Historical sources don't tell you everything. Bodies are a more honest representation of who the vulnerable were," Cattaneo says. "I think this is the tip of the iceberg in terms of what forensic science can do to reconstruct history."

A FEW FLIGHTS of stairs up from the shadowy crypt lies another historical trove: the hospital's archives, stored in a series of high-ceilinged, wood-paneled rooms redolent of old paper. Along the walls, 4 kilometers of shelves overflow with bound volumes of patient records, pharmaceutical recipes, medical textbooks, inventories, receipts, and staff records going back 5 centuries. It's all presided over by Ospedale Maggiore archivist Paolo Galimberti, a white-haired historian in a suit and tie who says he's more comfortable in Latin than English.

The hospital's archive is complemented by a unique record known as the Mortuorum Libri, the Book of the Dead, kept across town at the State Archive of Milan. It's a detailed record of every death in the city since 1451, including each person's name and cause of death. Though churches in the Middle Ages often recorded funeral masses, Milan was the first municipality to systematically collect such information for public health purposes. "There's no distinction by sex, age, religion, ethnicity, or wealth," Vaglienti says. "Nobody went forgotten. … It's the first source of its kind that we know of."

The Latin notations include everything from infants who died only a few hours old to a man who survived a fall from his horse only to succumb 9 days later from what an autopsy revealed to be a ruptured kidney. Plague, TB, and syphilis were common causes of death. By carefully noting and tracking such details, Milanese officials hoped to ward off or contain disease outbreaks.

To determine causes of death, the city employed autopsy specialists working at Ca' Granda, in effect the world's first coroners. Given the accuracy of some of his anatomical drawings, Leonardo da Vinci—who lived in Milan in the hospital's early years, about a century before the burial chambers were in use—likely attended Ca' Granda autopsies.

Marks on the exhumed bones suggest autopsies were still going on in the 17th century, and that the hospital staff were performing surgeries. There are signs of sawn-open skulls and amputated limbs. "Doctors got their field training here," Mattia says. "These were the very worst cases."

The book and the bones show Ca' Granda's staff were at the forefront of medical discovery at the time. Separate wards for patients with diseases such as TB showed an awareness of contagion, and the hospital's ample and efficient toilets—one for every two patient beds on the sick wards—were a breakthrough in hygiene. "The knowledge of how to treat and contain contagious illnesses in a period like this, without vaccines or antibiotics, led to medical milestones we're still benefiting from today," Vaglienti says.

In addition to its scientific results, the Ca' Granda research is, in a very literal sense, returning names and faces to the forgotten, Galimberti says. Already, specialists in Cattaneo's forensics lab have reconstructed the faces of several women based on their skeletal remains. In one case, they even guessed at a patient's hairstyle based on skin and hair still present in the sepulcher.

Some of the finds hint at long-lost stories, like a cluster of five 17th century gold coins from Venice, Spain, and France that is among the few artifacts from the crypt. Mattia, who was part of the team that found them, says that because the hospital sold clothes and other possessions of the deceased, it's unlikely that the coins were concealed in someone's pocket or purse. He speculates they were swallowed by a traveling merchant desperate to hide them, who died before they could be retrieved.

Other evidence is more melancholy. Unhealed damage to a woman's pubic bone gives dramatic evidence of a birth gone wrong. And just above a layer of lime, added to the pit in the hopes of accelerating decomposition, Mattia found the bones of a newborn; below that layer, the bones are all of adults. "That tells us the lime was put down just before they opened the hospital to babies," Mattia says. "That was a very sad day."

AS RESEARCH PROGRESSES, distinctive skeletons recovered from the sepulchers—a boy with a broken hip, for example, or a man with dwarfism—might be connected to known cases recorded in the Book of the Dead. "We don't have toe tags on the skeletons, but when the cause of death is peculiar we may be able to connect them," Cattaneo says.

Hanging at the end of a hallway outside the Ospedale's archives, a massive painting by an anonymous 17th century artist captures an imagined moment at the hospital. Doctors, patients, nurses, orphans, and visitors mill about the grassy courtyard; in the background, a funeral procession carries a black-shrouded burden towards the chapel entrance.

In the foreground, a small figure holds out his cap—a likely match for the man whose distinctive bones were found in the crypt. "I know the name of this physician, this dwarf," Galimberti says, leaning in as though greeting old friends. "I know the names of the hospital archivists since the 15th century, the surgeons, the architect who designed the hospital—but I know nothing about the sick people. I can now see those people's faces. It's really amazing." □

eppendorf & Science

PRIZE FOR NEURO BIOLOGY

2024 Winner
Laura Seeholzer, Ph.D.
University of California San Francisco, School of Medicine, USA

For research on airway neuroendocrine cells responding to external threats

Application Deadline
June 15, 2025

Call for Entries 2025

Eppendorf & Science Prize for Neurobiology
The annual Eppendorf & Science Prize for Neurobiology is an international prize which honors young scientists for outstanding neurobiological research based on methods of molecular, cellular, systems, or organismic biology. If you are 35 years of age or younger and doing great research, now is the time to submit an entry for this prize.
It's easy to apply! Write a 1,000-word essay and tell the world about your work.

eppendorf.com/prize

As the winner, you could be next to receive
> Prize money of US$25,000
> Publication of your work in *Science*
> Full support to attend the Prize Ceremony held in conjunction with the Annual Meeting of the Society for Neuroscience in the USA
> 10-year AAAS membership and online subscription to *Science*
> Complimentary products worth US$1,000 from Eppendorf
> An invitation to visit Eppendorf in Hamburg, Germany

eppendorf

Science AAAS

PHYSICS

The mechanics behind the beauty of roses

As rose petals change shape during maturation, they do not follow classical geometrical incompatibility

Qinghao Cui *and* **Lishuai Jin**

An artificial petal mimics how rose morphogenesis is driven by localized stress concentrations.

Nature's artistry in shaping living forms often arises from the delicate interplay between growth and geometry. From the undulating margins of lotus leaves to rippled edges of lily petals, intricate three-dimensional configurations emerge as biological tissues grow unevenly from the initial two-dimensional geometry. For decades, Gauss's Theorema Egregium—a geometrical theory that links intrinsic curvature of a surface to measurements of its distance and angle—has served as the cornerstone for understanding such morphogenesis (*1, 2*). On page 520 of this issue, Zhang *et al.* (*3*) report a distinct mechanism underlying the formation of sharp cusps of rose petals that deviates from this classical incompatibility. This discovery reframes understanding of how geometrical constraints sculpt biological forms and opens new avenues for engineering shape-shifting materials.

Uneven growth in a flat sheet can induce intrinsic curvature, leading to out-of-plane deformation as the material compensates for the curvature mismatch. This geometrical incompatibility between the curvature imposed by growth and the initial flat geometry is the driving force behind many natural patterns. For example, the ruffled edge of a lettuce leaf originates from a mismatch in growth rate between the interior and the edge of the leaf. When the edge grows faster than the interior, the leaf must adopt a wavy shape to compensate for incongruity. This type of morphogenesis, based on Gauss's incompatibility, is often characterized by extended, smooth, periodic undulations or wrinkles and is commonly observed in leaves, petals, and seed pods (*4–6*).

Zhang *et al.* demonstrate that a pronounced change in shape can also occur when the growth is compatible with Gauss's Theorema Egregium. In contrast to the gentle ruffling in many flowers, roses have distinct sharp tips that often appear along the edge of petals. These cusps—the points where two curves meet—are highly localized and almost triangular protrusions. The authors hypothesized that these sharp edges are not driven by classical Gauss's incompatibility, but by a different source of geometrical frustration. Particularly, Zhang *et al.* point to an incompatibility that arises from the inability of surfaces to smoothly accommodate the spatial variation in curvature (see the photos). This violates the Mainardi-Codazzi-Peterson condition, which describes how surface bending must have a smooth transition from one point to another to avoid tearing and unnatural folding in three-dimensional space (*7*). Breaking such compatibility often leads to highly localized stress concentrations and abrupt shape transitions rather than smooth waves that are observed in other natural patterns.

Zhang *et al.* combined elegant experiments with rigorous computational and analytical models to confirm this postulate. Cutting a narrow strip from a rose petal along the radial direction caused the strip to curl. This indicates a built-in curvature in a radial direction. By contrast, strips that were cut along the azimuthal direction remained flat. These observations imply that rose petals are compatible with the flat geometry, which they initially had, but exhibit curvature profiles that cause Mainardi-Codazzi-Peterson incompatibility. These events were also replicated by numerical and theoretical models, further validating the emergence of sharp cusps under such geometrical frustrations.

The findings of Zhang *et al.* relate to the developmental stages of a rose. Young rose petals display smooth edges. As a rose matures, the petals undergo a morphological transition from smooth curves to a polygonal shape with multiple cusps. The number and sharpness of the cusps increase as a rose reaches maturity. Zhang *et al.* replicated the growth process by using a "disc petal"—an elastic petal–shaped sheet with an engineered growth pattern mimicking that of a rose petal. The artificial petal maintained smooth edges until a critical point at which it transitioned to a polygonal shape.

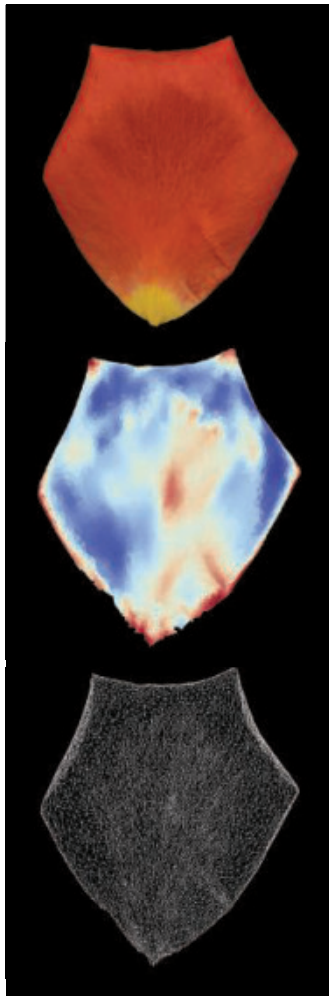

A mature rose petal (top) has sharp edges to accommodate the spatial variation in curvature, which is shown by a contour map (middle; red, convex; blue, concave) and a mesh grid (bottom).

The implications of this discovery go far beyond the mechanism underlying aesthetics. Formation of cusps causes localized stress concentrations, which may influence subsequent growth. This could potentially create a feedback mechanism in morphogenesis in which the petal shape driven by growth affects subsequent evolution. Such a mechanism is consistent with the convex-to-concave transition in cusps of rose petals. Experimentally suppressing cusp formation in a rose petal reverted the shape of the cusp to that of undisturbed tissue (smooth and convex edge), suggesting that mechanical stress is not merely a consequence of development, but an active regulator of biological patterns.

Identifying Mainardi-Codazzi-Peterson incompatibility as a shaping mechanism is not only an important milestone in morphogenesis research but also an inspiration for new designs of shape-morphing materials and structures. The ability to change shape on demand is desired for applications such as soft robotics and deployable spacecraft components (*8, 9*). To date, most design approaches have implicitly relied on the classical Gauss-type incompatibility. For example, spatially embedded pneumatic networks in a flat sheet cause shape changes upon pressurization (*10, 11*), and corrugated sheets enable multistability (simultaneous existence in two or more stable states) and switchable shape morphing (*12*). Leveraging Mainardi-Codazzi-Peterson incompatibility could enable localized, programmable shape changes without requiring large-scale variation in surface distances. And combining Gauss and Mainardi-Codazzi-Peterson incompatibilities could give rise to deformation behaviors that have yet to be seen. □

REFERENCES AND NOTES

1. Y. Klein, E. Efrati, E. Sharon, *Science* **315**, 1116 (2007).
2. U. Nath, B. C. W. Crawford, R. Carpenter, E. Coen, *Science* **299**, 1404 (2003).
3. Y. Zhang, O. Y. Cohen, M. Moshe, E. Sharon, *Science* **388**, 520 (2025).
4. F. Xu, C. Fu, Y. Yang, *Phys. Rev. Lett.* **124**, 038003 (2020).
5. C. Huang, Z. Wang, D. Quinn, S. Suresh, K. J. Hsia, *Proc. Natl. Acad. Sci. U.S.A.* **115**, 12359 (2018).
6. H. Liang, L. Mahadevan, *Proc. Natl. Acad. Sci. U.S.A.* **108**, 5516 (2011).
7. E. Siéfert, I. Levin, E. Sharon, *Phys. Rev. X* **11**, 011062 (2021).
8. L. Jin, M. Yeager, Y.-J. Lee, D. J. O'Brien, S. Yang, *Sci. Adv.* **8**, eabq3248 (2022).
9. Y. Hong *et al.*, *Nat. Commun.* **14**, 4625 (2023).
10. T. Gao, J. Bico, B. Roman, *Science* **381**, 862 (2023).
11. E. Siéfert, E. Reyssat, J. Bico, B. Roman, *Nat. Mater.* **18**, 24 (2019).
12. A. S. Meeussen, M. van Hecke, *Nature* **621**, 516 (2023).

ACKNOWLEDGMENTS

L.J. acknowledges support from a City University of Hong Kong grant (no. 9610696).

10.1126/science.adx1733

Department of Mechanical Engineering, College of Engineering, City University of Hong Kong, Hong Kong, China. Email: lishuai.jin@cityu.edu.hk

IMAGES: ZHANG *ET AL.* (*3*); (OPPOSITE PAGE) YAFEI ZHANG/HEBREW UNIVERSITY OF JERUSALEM

NEURODEVELOPMENT

Searching for partners

Simplifying a three-dimensional search helps neurons find their targets

Yuwei Zhong *and* **Claude Desplan**

During human brain development, billions of neurons need to recognize their partners to form neuronal circuits. To explain this striking specificity, the chemoaffinity hypothesis proposes that neurons bear molecular identification tags (e.g., cell surface proteins) that distinguish them from one another and establish specific connections (*1*). Although this idea has been validated in some cases, given the limited number of cell surface proteins encoded by the genome, it is unlikely that such large numbers of neurons could rely solely on strict chemoaffinity to establish complicated neuronal networks (*2*). This problem might become insurmountable when the neurons have to find their targets in a three-dimensional (3D) environment. On page 538 of this issue, Lyu *et al.* (*3*) report that olfactory neurons in the fruit fly (*Drosophila*) solve this problem by reducing the dimensionality of the search path. These findings could help understand the wiring of the more complex mammalian brain.

During development, neurons use a simple strategy to reduce the number of potential synaptic partners: They divide the search into successive steps. As they extend their processes (long, slender axons and shorter, branched dendrites), neurons initially follow broad attractive or repulsive guidance cues to reach their target brain region. Upon reaching the correct region, neurons must identify synaptic partners from a large pool of potential targets within a 3D space. In both the retina and cortex of vertebrates (*4*), this challenging task is simplified because neuronal processes are organized into distinct layers and columns. This allows neurons to first identify the correct layer and column before selecting their specific synaptic partners. Thus, the choice of potential synaptic partners is largely reduced, enabling interactions through chemoaffinity (*1*) or as a result of proximity (known as Peters' rule) (*5*) to establish the correct connections.

Not all brain structures are layered, however, which means that the same mechanism may not apply to the development of globular brain regions. This is the case in the fruit fly olfactory system, where olfactory receptor neurons (ORNs), which originate from the antennae, must find their individual partners in the globular antennal lobe, the first olfactory processing center in the brain. Each ORN expresses a single type of olfactory receptor on its dendrites, and the axons of all ORNs that express the same olfactory receptor converge onto a specific glomerulus, one of the many small, globular brain regions in the antennal lobe that each respond to one odor. Within each glomerulus, ORNs connect to their specific synaptic partners, known as projection neurons, which convey the olfactory information to higher brain regions for further processing. There are around 50 distinct glomeruli in flies, each innervated by a specific set of ORNs and projection neurons, occupying stereotypic positions within the volume of the antennal lobe (*6*). How do ORNs find their cognate partners that are located within this complex 3D environment?

Lyu *et al.* addressed this gap in knowledge by taking advantage of high-throughput imaging and, more importantly, genetic techniques that enable researchers to simultaneously label and change the gene expression of any single type of ORN or projection neuron. By imaging the antennal lobes in groups of flies at different developmental stages, they followed the paths of projection neuron dendrites and ORN axons. They found that ORN axons use guidance cues to follow specific trajectories along the surface of the antennal lobe until they find their target glomeruli located at the lobe's surface. But what about glomeruli positioned deep within the interior of the antennal lobe? The authors report that ORNs targeting these glomeruli adopt the same strategy of searching along a trajectory on the 2D surface of the antennal lobe. However, in this case, the projection neurons from the interior send dendrites to the surface. These dendrites act as beacons that can be recognized by ORNs. Once the axon of the ORN reaches the dendrites of the projection neuron, the two neurons establish a synaptic connection and retract to the glomerulus inside the antennal lobe (see the figure). Therefore, by simply projecting all 3D glomeruli onto a 2D surface, the search becomes one dimensional—restricted to the predetermined path of the ORN. Of course, this requires an ORN to know exactly which trajectory to follow to encounter the dendrites of its corresponding projection neuron.

If this model is correct, altering ORN trajectories by perturbing axon guidance cues that determine the trajectory should prevent ORNs from establishing correct connections, as they would be unable to encounter their partners. Lyu *et al.* report that this is indeed the case. Furthermore, in the case of interior glomeruli, the dendrites of projection neurons that failed to encounter their presynaptic ORN partners remained on the surface of the antennal lobe in adults, rather than buried inside as they normally would be. The mammalian olfactory system, which is organized in a manner similar to that of flies, uses a comparable mechanism to simplify the synaptic partner search: Instead of being arranged in a 3D structure, all of the thousands of mouse olfactory glomeruli are arranged on one plane during development and in the adult, inherently reducing their di-

Making the right connections

During development of the fruit fly olfactory system, olfactory receptor neurons (ORNs) project from the antenna to the antennal lobe. There they must find the dendrites of specific projection neurons, which extend their dendrites into the antennal lobe to form preglomerular structures at stereotypic positions.

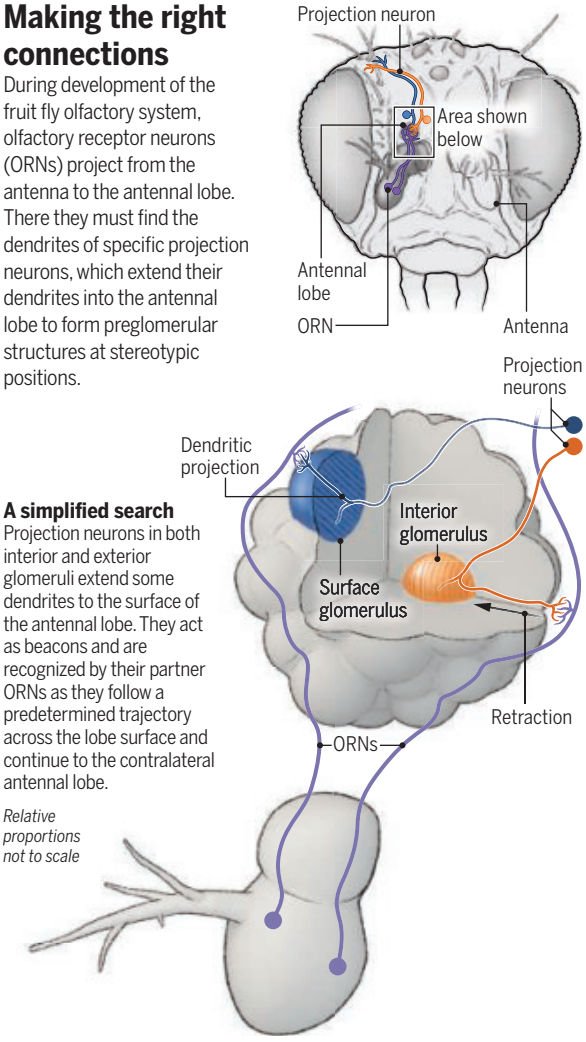

A simplified search
Projection neurons in both interior and exterior glomeruli extend some dendrites to the surface of the antennal lobe. They act as beacons and are recognized by their partner ORNs as they follow a predetermined trajectory across the lobe surface and continue to the contralateral antennal lobe.

Relative proportions not to scale

GRAPHIC: A. FISHER/*SCIENCE*

Department of Biology, New York University, New York, NY, USA. Email: cd38@nyu.edu

mension to 2D (*7*). However, spreading targets on a plane or a layer might not always be an option. This could be the case in the microscopic fly brain, which might not be able to accommodate the space required to spread its glomeruli in two dimensions. Moreover, there are many structures in the mammalian brain that have a 3D, not layered, structure during development, suggesting that the dimensional reduction approach identified by Lyu *et al.* might also apply there.

The study of Lyu *et al.* relied on the use of advanced genetic tools to label (and manipulate the gene expression of) individual types of ORN and projection neuron throughout development. Previous studies noted that ORNs only target the surface of the antennal lobe during development, but an inability to identify and manipulate specific cell types prevented these studies from reaching more definitive conclusions (*8*). Advances in single-cell technologies have since allowed the identification of specific marker genes that are expressed throughout development in many transcriptionally distinct neuronal types (*9*). The promoters of these marker genes can be harnessed to genetically manipulate individual cell types. However, not all cell types can be distinguished by the expression of a single gene. One solution to this problem is to identify pairs of genes that are only coexpressed in one neuronal type. Intersectional genetics approaches (e.g., split-Gal4) can then be used to restrict the expression of target genes only in cells that simultaneously express the gene pairs (*10*, *11*). This was the approach used by Lyu *et al.* However, finding a gene pair with expression that is specific to a single cell type is not always feasible. Another strategy is to use single-cell RNA sequencing and single-nucleus ATAC (assay for transposase-accessible chromatin) sequencing datasets to find regions of open chromatin, which often correspond to enhancers that drive cell type–specific gene expression during development. This allows the identification of more cell type–specific genetic tools that can be combined with intersectional genetics methods (*12*).

Over the past decades, powerful genetic tools in *Drosophila* and vertebrate model organisms have accelerated the understanding of the development and function of different cell types. As technological advances and knowledge of the nervous system deepen, genetic tools with single–cell type resolution will be essential for tackling fundamental biological and developmental questions, for example, how do neurons establish their identity? Further work is also required to establish how neurons form precise synaptic connections and how the resulting neuronal circuits contribute to the behaviors of the organism. □

REFERENCES AND NOTES

1. R. W. Sperry, *Proc. Natl. Acad. Sci. U.S.A.* **50**, 703 (1963).
2. P. Schlegel *et al.*, *Nature* **634**, 139 (2024).
3. C. Lyu *et al.*, *Science* **388**, 538 (2025).
4. J. R. Sanes, S. L. Zipursky, *Neuron* **66**, 15 (2010).
5. A. Peters, M. L. Feldman, *J. Neurocytol.* **5**, 63 (1976).
6. A. Couto, M. Alenius, B. J. Dickson, *Curr. Biol.* **15**, 1535 (2005).
7. P. Mombaerts *et al.*, *Cell* **87**, 675 (1996).
8. W. J. Joo, L. B. Sweeney, L. Liang, L. Luo, *Neuron* **78**, 673 (2013).
9. M. N. Özel *et al.*, *Nature* **589**, 88 (2021).
10. A. del Valle Rodríguez, D. Didiano, C. Desplan, *Nat. Methods* **9**, 47 (2011).
11. Y. D. Chen *et al.*, *Proc. Natl. Acad. Sci. U.S.A.* **120**, e2307451120 (2023).
12. J. Janssens *et al.*, *Nature* **601**, 630 (2022).

ACKNOWLEDGMENTS

The authors thank all members of the Desplan lab, especially B. Sieriebriennikov, N. Özel, R. Rajesh, and Y.-C. Chen, for critical feedback. C.D. aknowledges support from National Institutes of Health grant R01 EY13010.

10.1126/science.adx1186

EVOLUTIONARY BIOLOGY

An uphill grind for wild plant populations

Genetic variation is inadequate for the adaptation of a montane plant to new climates

Sally N. Aitken

The range of temperature and precipitation across which populations remain viable forms the climatic niche for terrestrial life. Many plant (*1*) and animal (*2*) species consist of populations that are locally adapted to their preindustrial climates, with each subgroup tolerating a smaller range of climate conditions compared with the whole species (*3*). Will existing genetic variation be sufficient for the adaptation needed to reverse population decline as climates change (a process known as evolutionary rescue) (*4*)? Can migration from warmer to cooler regions provide the diversity required for climate adaptation (genetic rescue) (*5*)? On page 525 of this issue, Anderson *et al.* (*6*) report that even for the widely distributed species of the rock cress *Boechera stricta* in the United States Rocky Mountains, gene flow from warmer to cooler elevations—possibly facilitated by human intervention—is needed to support future survival of some plants in a warming climate.

Plants have three potential responses if fitness of local genotypes declines with climate warming: adaptation, migration, or extirpation. Predicting this fate requires understanding local adaptation. For this knowledge, transplant experiments in natural conditions are the gold standard. Although analyses of genomic data (*7*, *8*) or of variation in phenotypes in controlled environments can provide more rapid information on population variation, they do not quantify the effects of that variation on growth, mortality, or fitness in nature (*9*). Field-based transplant experiments move genotypes from different origins to experimental gardens in different locations, substituting spatial variation for anticipated temporal changes in climate. This type of experiment provides insights into the potential for, and limitations of, evolutionary and genetic rescue of natural populations under climate change. Such experiments are common with some plants, such as forest trees (*10*), but estimating lifetime fitness for long-lived species is difficult. *B. stricta* is a short-lived, widespread montane perennial plant, making it an ideal model for this type of ecoevolutionary experiment.

Anderson *et al.* planted more than 100,000 *B. stricta* plants in two large experiments. In a reciprocal transplant experiment, genotypes were sourced from, and transplanted to, five different elevations in the Colorado Rocky Mountains. In a provenance transplant experiment, *B. stricta* sampled from a wider geographic range were planted at the same five elevations, and snowpack levels were also manipulated. Populations showed strong local adaptation to both temperature and snowpack, factors that the authors identified as key climate variables. Genotypes originating from close to planting sites had the highest fitness under preindustrial climatic conditions at all five sites.

In current climatic conditions, Anderson *et al.* found that the transplanted populations with optimum performance at mid and high elevations were from source locations that were ~150 to 350 m lower in elevation. At the lowest elevation site, where the warmest, most stressful current conditions occur, phenotypic variation among genotypes was lowest, indicating a reduced capacity for adaptation through natural selection. Under both moderate and high greenhouse gas emissions (reflecting those projected for the period 2071–2100), the authors' modeling predicted that local genotypes would be maladapted at all sites

Department of Forest and Conservation Sciences, University of British Columbia, Vancouver, BC, Canada. Email: sally.aitken@ubc.ca

and that genotypes from the lowest elevation would have the highest fitness, relative to all sources, at almost all sites. In the case of the highest elevation site examined, modeling indicated that for conditions at the end of this century, the optimal genotypes currently occur nearly 800 m lower in elevation.

Results on germination, survival, growth, and fecundity from the transplant experiments allowed Anderson *et al.* to develop evolutionary models that predict where populations would grow, remain stable, or contract under preindustrial, current, and future climates. The models predict that, under current conditions, the lowest elevation site is already demographically unsustainable and populations at the two lowest elevation sites will be extirpated with climate change regardless of genotype, thereby contracting the species range. Other studies have also predicted range contractions at lower elevations for many montane plant species.

The natural movement of pollen or seeds between populations can facilitate genetic adaptation to environments (*11*), but only if the source genotypes are better adapted to the new conditions of the recipient population than local genotypes. For *B. stricta* (and many other species), this would require gene flow upslope from warmer to cooler locations. Anderson *et al.* estimated long-term gene flow rates from genomic data and found that genetic exchange in this mostly self-pollinating species is very low. Furthermore, the authors detected no sign of recent upslope gene flow. They propose that human-assisted gene flow (*12*) would be needed for these populations to be genetically rescued under a changing climate. The capacity for such genetic rescue will be species specific, depending on life history factors such as outcrossing rate and dispersal dynamics, highlighting the need for additional comprehensive ecoevolutionary studies like that of Anderson *et al.*

The impact of climate change on the ranges of terrestrial plants and animals is often predicted using species distribution models that estimate the climatic niche from the current range and then project the future distribution of those conditions under various climate change scenarios (*13*). Anderson *et al.* compared estimates of future population viability, accounting for local adaptation and gene flow, with those from species-level climatic niche projections and found a poor fit between the two predictions. This illustrates the importance of knowledge on local adaptation and gene flow for evaluating both population- and species-level responses to climate change.

The lessons from Anderson *et al.* are sobering with respect to the ability of natural populations to adapt to, and persist under, rapid global warming. Although the capacity for persistence will vary among species and with life history traits, populations cannot persist simply because their locations remain within the overall range of climatic tolerances for that species as a whole. Adequate genetic variation for adaptation to new conditions may not be present or may not be expressed phenotypically under stressful conditions. Even if well-adapted genotypes exist elsewhere in the species range, gene flow may be insufficient to redistribute genetic variation quickly enough. Greenhouse gas emission reductions that slow climate change may provide enough time for adaptation to occur for some species. Human intervention in the form of assisted gene flow among populations could increase the probability of species persisting in a warming climate. □

REFERENCES AND NOTES

1. R. Leimu, M. Fischer, *PLOS ONE* **3**, e4010 (2008).
2. J. Hereford, *Am. Nat.* **173**, 579 (2009).
3. T. Jezkova, J. J. Wiens, *Proc. Biol. Sci.* **283**, 20162104 (2016).
4. G. Bell, *Annu. Rev. Ecol. Evol. Syst.* **48**, 605 (2017).
5. M. Bontrager, A. L. Angert, *Evol. Lett.* **3**, 55 (2018).
6. J. T. Anderson *et al.*, *Science* **388**, 525 (2025).
7. T. Capblancq, M. C. Fitzpatrick, R. A. Bay, M. Exposito-Alonso, S. R. Keller, *Annu. Rev. Ecol. Evol. Syst.* **51**, 245 (2020).
8. B. M. Lind, K. E. Lotterhos, *Mol. Ecol. Resour.* **25**, e14008 (2025).
9. S. M. Wadgymar, M. L. DeMarche, E. B. Josephs, S. N. Sheth, J. T. Anderson, *Annu. Rev. Ecol. Evol. Syst.* **53**, 87 (2022).
10. L. Leites, M. Benito Garzón, *Glob. Change Biol.* **29**, 4711 (2023).
11. T. Lenormand, *Trends Ecol. Evol.* **17**, 183 (2002).
12. S. N. Aitken, M. C. Whitlock, *Annu. Rev. Ecol. Evol. Syst.* **44**, 367 (2013).
13. C. Román-Palacios, J. J. Wiens, *Proc. Natl. Acad. Sci. U.S.A.* **117**, 4211 (2020).

10.1126/science.adx5165

MICROBIOLOGY

A fungal ally wards off liver disease

A metabolite secreted by an intestinal fungus blunts metabolic disease

Lora V. Hooper[1,2,3] *and* **Andrew Y. Koh**[2,4,5]

The human gut is home to trillions of microorganisms, collectively known as the gut microbiota. Most microbiota constituents are bacteria, which produce a diverse array of metabolites that signal to human cells or interact with enzymatic pathways to shape host biology. The microbiota also includes a range of commensal, mutualistic, and pathogenic fungi that, like gut bacteria, produce an abundance of metabolites. However, outside of a few well-studied toxin-producing pathogenic fungi, very little is known about how these fungal compounds interact with host cells to affect health. On page 491 of this issue, Zhou *et al.* (*1*) report a fungal species that resides in the human gut and produces a compound that protects against metabolic disease in mice. The findings point to intestinal fungi as a potentially rich source of beneficial chemical compounds that could be harnessed for human health.

...the fungal microbiome may be a rich, untapped source of compounds with therapeutic potential.

Many intestinal fungi cause disease. For example, *Candida albicans* frequently colonizes the human intestine and causes life-threatening infections in people undergoing cancer therapy or immune suppression for organ and stem cell transplants (*2*, *3*). However, intestinal fungi can also establish symbiotic relationships with hosts, as indicated by the recent discovery that *Kazachstania pintolopesii* stably colonizes the mouse intestine and induces protective immunity against gut pathogens (*4*).

To identify other fungal symbionts in the human intestine, Zhou *et al.* cultured human fecal samples in medium containing nutrients derived from the human gut. The authors then identified fungi by sequencing their DNA. One species—*Fusarium foetens*—was almost universally present in people from different geographic locales and readily grew under culture conditions that mimic conditions of the human gut, such as low oxygen. When inoculated into mice, *F. foetens* stably colonized the gastrointestinal tract without causing injury or invading deeper tissues. These characteristics suggest that *F. foetens* is not merely passing through from the environment but instead is well adapted to the mammalian intestine and leads a symbiotic rather than pathogenic lifestyle. By contrast, other *Fusarium* species can cause opportunistic infections in humans with normal immune systems and life-threatening

invasive infections in immunocompromised individuals (*5*).

Several intestinal fungi, including *C. albicans*, can worsen metabolic disorders, typically by increasing the accumulation of fat in the liver (hepatic steatosis) (*6*). To investigate the effects of *F. foetens* on metabolic disease, Zhou *et al.* used a mouse model of metabolic dysfunction–associated steatohepatitis. This disorder is characterized by fatty liver and liver inflammation and can progress to cirrhosis or liver cancer (*7*, *8*). Similar symptoms can be induced in mice by feeding them a high-fat diet for several weeks (*9*). Unexpectedly, Zhou *et al.* found that *F. foetens* reduced symptoms of steatohepatitis when inoculated into mice. By contrast, inoculation with *C. albicans* failed to protect against this liver condition, suggesting that the effect is species specific.

How does *F. foetens* protect against metabolic dysfunction–associated steatohepatitis? Using an in vitro activity-based assay (*10*), Zhou *et al.* found that *F. foetens* selectively reduced the activity of the enzyme ceramide synthetase 6 (CerS6). CerS6 is expressed in intestinal epithelial cells, where it catalyzes the synthesis of ceramides—an important class of endogenous lipids. Notably, ceramides are exported to the bloodstream and promote the progression of fatty liver disease to metabolic dysfunction–associated steatohepatitis (*11*, *12*). Colonizing mice with *F. foetens* decreased intestinal CerS6 activity and reduced ceramide amounts in both the intestine and the bloodstream, whereas supplementing *F. foetens*–colonized mice with ceramide blunted the beneficial effects on disease progression. Thus, *F. foetens* reduces symptoms by inhibiting ceramide synthesis in the intestine (see the figure).

A resident intestinal fungus protects against metabolic disease

Fusarium foetens, a filamentous fungus that stably colonizes the mammalian gut, secretes a metabolite called *F. foetens* compound 1 (FF-C1). FF-C1 binds to and inhibits ceramide synthetase 6 (CerS6) in the gut epithelium. This reduces ceramide pools in the bloodstream and protects against the development of metabolic dysfunction–associated steatohepatitis in a mouse model. Intestinal symbiotic fungi may be an untapped reservoir of possible therapeutic chemical compounds.

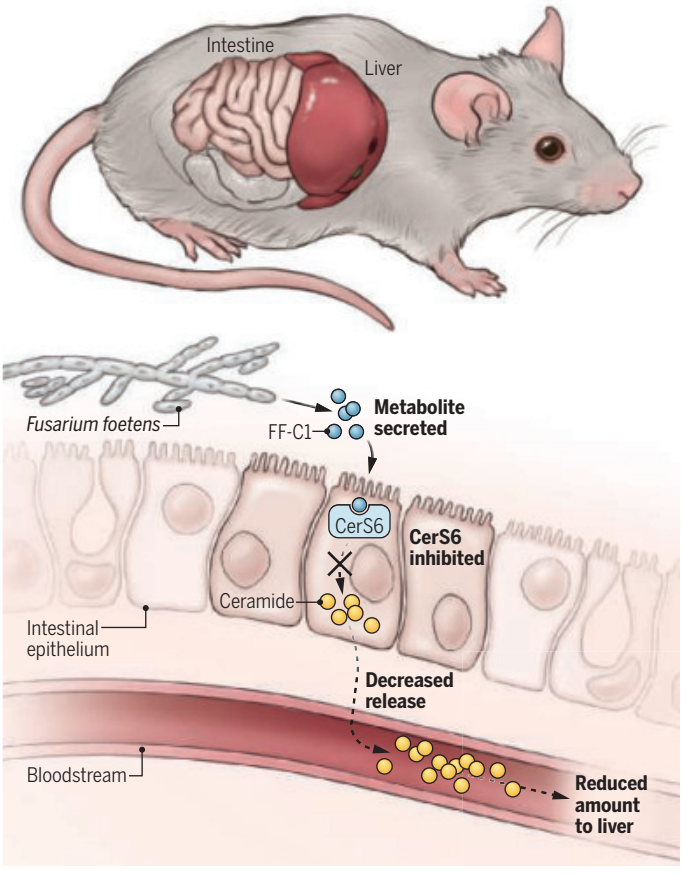

GRAPHIC: N. BURGESS/*SCIENCE*

Investigating the mechanistic basis for this effect, Zhou *et al.* found that *F. foetens* culture medium contains a medley of secreted metabolites and was sufficient to inhibit CerS6 in vitro. Using biochemical fractionation methods to isolate metabolites from the conditioned medium, they found that *F. foetens* compound 1 (FF-C1) bound tightly to CerS6 and inhibited its activity. FF-C1 is a naphthoquinone, a class of aromatic small molecules produced by many fungi (*13*). Administering FF-C1 was sufficient to limit the progression of steatohepatitis in mice, even in the absence of *F. foetens*. This finding opens the door to using FF-C1 to treat metabolic disease, although additional studies are needed to determine whether it is effective against metabolic dysfunction–associated steatohepatitis in humans.

F. foetens has a filamentous morphology, forming a multicellular network of branching hyphae. This was unexpected because studies of *C. albicans* had suggested that adopting a single-cell yeast-like form enabled stable colonization of the mouse intestine, whereas switching to filamentous growth promoted virulence (*14*). However, recent findings provide a more nuanced view in which the yeast form of *C. albicans* thrives in the antibiotic-cleared intestine, but the filamentous form is better equipped for the fully colonized gut ecosystem, where there is bacterial competition for nutrients (*15*). This is attributed in part to candidalysin, a toxin produced by filamentous *C. albicans* that inhibits bacterial competitors. The filamentous morphology of *F. foetens* may confer a similar advantage in the competitive gut ecosystem.

The findings of Zhou *et al.* suggest that the fungal microbiome may be a rich, untapped source of compounds with therapeutic potential. In addition to FF-C1, other compounds were isolated from *F. foetens*–conditioned culture medium that may selectively target different host pathways. It is also likely that other symbiotic fungi in the human gut produce compounds that interact with host pathways to promote health or limit disease. The results from this study should inspire further investigation of the human fungal microbiome to unlock the potential of these microscopic medicinal chemists. □

REFERENCES AND NOTES

1. S. Zhou *et al.*, *Science* **388**, eadp5540 (2025).
2. A. Y. Koh, J. R. Köhler, K. T. Coggshall, N. Van Rooijen, G. B. Pier, *PLOS Pathog.* **4**, e35 (2008).
3. B. Zhai *et al.*, *Nat. Med.* **26**, 59 (2020).
4. Y. Liao *et al.*, *Nature* **636**, 697 (2024).
5. M. Nucci, E. Anaissie, *Clin. Microbiol. Rev.* **36**, e00159-22 (2023).
6. H. Chu *et al.*, *J. Hepatol.* **72**, 391 (2020).
7. A. C. Sheka *et al.*, *JAMA* **323**, 1175 (2020).
8. L. Miao, G. Targher, C. D. Byrne, Y.-Y. Cao, M.-H. Zheng, *Trends Endocrinol. Metab.* **35**, 697 (2024).
9. B. S. Gosis *et al.*, *Science* **376**, eabf8271 (2022).
10. K. Wang *et al.*, *Science* **381**, eadd5787 (2023).
11. E. Hajduch, F. Lachkar, P. Ferré, F. Foufelle, *J. Clin. Med.* **10**, 792 (2021).
12. T. D. Rohrbach *et al.*, *J. Lipid Res.* **60**, 1311 (2019).
13. Y. Kimura, A. Shimada, H. Nakajima, T. Hamasaki, *Agric. Biol. Chem.* **52**, 1253 (1988).
14. J. N. Witchley *et al.*, *Cell Host Microbe* **25**, 432 (2019).
15. S.-H. Liang *et al.*, *Nature* **627**, 620 (2024).

10.1126/science.adx1789

[1]Department of Immunology, University of Texas Southwestern Medical Center at Dallas, Dallas, TX, USA. [2]Department of Microbiology, University of Texas Southwestern Medical Center at Dallas, Dallas, TX, USA. [3]The Howard Hughes Medical Institute, University of Texas Southwestern Medical Center at Dallas, Dallas, TX, USA. [4]Department of Pediatrics, University of Texas Southwestern Medical Center at Dallas, Dallas, TX, USA. [5]Harold C. Simmons Comprehensive Cancer Center, University of Texas Southwestern Medical Center at Dallas, Dallas, TX, USA. Email: lora.hooper@utsouthwestern.edu; andrew.koh@utsouthwestern.edu

BIOCHEMISTRY

Editing proteins inside a cell

Pairs of split protein segments can modify a variety of target proteins in a living cell

J. Trae Hampton *and* **Wenshe Ray Liu**

Programmable gene editing technologies, such as CRISPR, have increased the capacity to study gene functions and to model diseases. These tools can precisely manipulate DNA and RNA at the nucleotide level in both cellular and whole-animal contexts (*1*, *2*). Proteins constitute another primary class of biomacromolecules that forms the basis of genetic information flow and determines the observable traits of an organism. However, no comparable technique is available for directly editing proteins within a cell. On page 487 of this issue, Beyer *et al.* (*3*) report that a pair of split inteins—small protein segments that can undergo a self-sustained protein splicing reaction—enables endogenous protein editing in living mammalian cells. Recently, Hua *et al.* (*4*) also reported the manipulation of folded proteins using the split intein–mediated method. Such direct protein editing creates possibilities for introducing previously unachievable protein functions and their spatiotemporal controls at the cellular level.

Proteins are produced through translation, in which an mRNA orchestrates the assembly of amino acids to form a specific protein. Genetic code expansion can modify proteins during translation by manipulating nucleotide sequences (codons) that encode a specific amino acid arrangement and signal the end of protein synthesis (*5*). Although this approach can introduce functional groups and probes into proteins, it cannot selectively edit specific fragments of proteins after mRNA translation. Protein semisynthesis began in the early 1990s with a native chemical ligation method in which two polypeptide chains were fused to synthesize a protein (*6*). However, side reactions and low efficiency have limited the number of ligations that can be performed. At the same time, protein splicing—the removal of an internal segment from a precursor protein—has been demonstrated in a yeast (*7*).

An intein can catalyze its own removal from a protein's primary sequence without the need for external energy or a cofactor. This reaction is analogous to native chemical ligation, in which a free amino group at the end of a polypeptide chain (N terminus) reacts with a free carboxyl group at another chain end (C terminus), and has been used to modify proteins (*8*). Similarly, a pair of split inteins can join two separately encoded peptides when the complementary intein fragments recognize each other and associate (*9*). This approach improves specificity of the reaction and has produced semisynthetic proteins within cells (*10*). Nevertheless, the split intein–mediated method often requires segments that are exposed near the end of a protein for alteration. Although internal residues have been modified by assembling three separate protein fragments with split inteins, the yield was considerably low (*11*).

Beyer *et al.* used two split intein pairs that do not cross-react with each other to efficiently edit proteins in a mammalian cell. After identifying orthogonal split intein pairs, an amino acid sequence was successfully inserted at a desired location between internal residues of a protein (see the figure). This approach is analogous to DNA transposons—a mobile sequence that can move to a specific location within a DNA—and Hua *et al.* referred to the process as "protein transposition." Beyer *et al.* demonstrated the insertion of various protein fragments into an endogenous protein inside a cell, including noncanonical amino acids (not a standard amino acid); fluorescence tags; and protein sequences bearing nonliving, reactive functional groups, such as an diazirine.

Although protein transposition has been proven versatile, the reaction tends to favor exposed segments or disordered regions of a protein, which limits the site at which the editing can be performed. In addition, the split intein pairs need to be programmed into the DNA sequence that encodes the targeted protein. This alteration could change the activity or subcellular location of a protein before modification. Further development is necessary to alter a protein sequence without the need to integrate split intein fragments into the targeted protein, similar to how CRISPR technology edits DNA.

The studies of Beyer *et al.* and Hua *et al.* expand the range of protein modifications that can be studied in a cellular context. They also open the door to studying time-dependent cellular processes by introducing split intein fragments at a specific time point. Fluorescence tags and functional groups can be selectively inserted to understand how proteins respond to external stimuli in real time. Further, modification of large protein complexes that do not have an exposed end segment for ligation is now possible, as demonstrated by Hua *et al.* Understanding the dynamics of large protein complexes often involves invasive methods, such as the rupturing or staining of a cell. Protein transposition could selectively label large proteins inside a cell without affecting cellular functions. Beyond cell biology, there are many other potential applications of this technique to look for in years to come. □

One-step protein modification

Two orthogonal pairs of split inteins (small protein segments) can guide the insertion of a protein fragment to a specific location between internal residues of a target protein. This method can edit large protein complexes without an exposed residue and endogenous proteins inside a living cell.

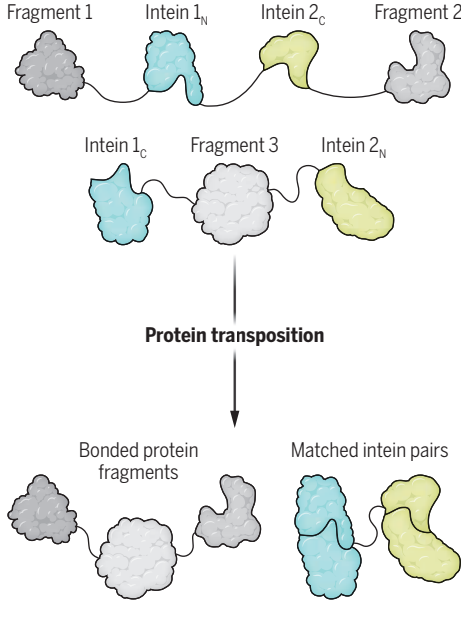

C, with C terminus; N, with N terminus.

GRAPHIC: A. MASTIN/*SCIENCE*

REFERENCES AND NOTES

1. M. Jinek *et al.*, *Science* **337**, 816 (2012).
2. D. B. T. Cox *et al.*, *Science* **358**, 1019 (2017).
3. J. N. Beyer *et al.*, *Science* **388**, eadr5499 (2025).
4. Y. Hua *et al.*, *Science* **388**, 68 (2025).
5. L. Wang, A. Brock, B. Herberich, P. G. Schultz, *Science* **292**, 498 (2001).
6. P. E. Dawson, T. W. Muir, I. Clark-Lewis, S. B. H. Kent, *Science* **266**, 776 (1994).
7. P. M. Kane *et al.*, *Science* **250**, 651 (1990).
8. T. W. Muir, D. Sondhi, P. A. Cole, *Proc. Natl. Acad. Sci. U.S.A.* **95**, 6705 (1998).
9. H. Wu, Z. Hu, X.-Q. Liu, *Proc. Natl. Acad. Sci. U.S.A.* **95**, 9226 (1998).
10. H. Wang, L. Wang, B. Zhong, Z. Dai, *Front. Bioeng. Biotechnol.* **10**, 810180 (2022).
11. J. Shi, T. W. Muir, *J. Am. Chem. Soc.* **127**, 6198 (2005).

ACKNOWLEDGMENTS

The authors acknowledge support from the US National Institutes of Health (grants R35GM145351 and R01CA291968).

10.1126/science.adx5085

Department of Chemistry, Texas A&M University, College Station, TX, USA. Email: wsliu2007@tamu.edu

BIOMEDICAL RESEARCH

Discovery research in physiologically maintained deceased

Expanded research opportunities in deceased humans require ongoing ethical inquiry

Douglas B. Pet[1,2], Brendan Parent[3], Neel S. Singhal[1,2], Claire D. Clelland[1,4]

Deceased humans in whom ventilation and circulation are maintained for a defined period after the declaration of death by neurologic criteria (brain death), referred to here as physiologically maintained deceased (PMD), mimic live human physiology, providing highly valuable research opportunities. Medical research involving PMDs has narrowed translational gaps and ushered in groundbreaking treatments, including the transplantation of gene-edited organs into living human patients (*1*). However, the potential of PMDs remains largely untapped for human therapeutic discovery research. PMDs may be particularly advantageous in discovering and advancing new therapies, such as gene therapies, that are human specific and therefore are limited by nonhuman research models. We envision PMD research as a transformative force for human therapeutic discovery and emphasize the importance of upholding established bioethical standards and pursuing ongoing ethical inquiry to ensure the protection of all stakeholders.

ADVANTAGES FOR DISCOVERY

PMD research has garnered considerable attention in transplantation science as it has enabled quasi–"first in human" studies without posing risk to living patients. In these studies, after declaration of brain death, the deceased were maintained on cardiopulmonary support with mechanical ventilation in a clinical care environment in which physiologic parameters such as heart rate, blood pressure, and electrolyte levels could be monitored and stabilized. Integration of gene editing and bioengineering techniques with PMD-based study designs has helped overcome barriers such as post-transplant organ rejection, as well as vascular and hematologic complications (*1*). Consequently, use of PMDs has facilitated the transition of late-stage technologies into live human application, leading to breakthrough achievements such as genetically modified porcine heart and kidney xenotransplantation in living patients over the past 2 years.

PMD research models, to our knowledge, have not yet been explored for discovering new human drug therapies. However, PMD models hold considerable potential in this area, particularly for identifying human-relevant candidates early in the discovery phase, and otherwise for evaluating new technologies that rely primarily or exclusively on human-specific factors. The traditional therapeutic discovery pipeline progresses from cellular models and small animals (mice and rats) to nonhuman primates, and finally to human trials. Although this approach may suffice for discovery, validation, and de-risking of small molecules, it presents substantial hurdles for testing modern gene therapies such as antisense oligonucleotide, gene replacement, and CRISPR-based gene editing, and their delivery vehicles such as adeno-associated virus (AAV) and lipid nanoparticles (LNPs), which can be highly species specific.

A key shortcoming of this discovery pipeline rooted in animal models is a poor predictive value in identifying successful human therapeutics. For example, distribution and efficacy of AAV (*2*) and LNP (*3*) demonstrate that delivery particles commonly used for gene therapies translate poorly between mice, rats, nonhuman primates, and humans owing to species specificity. In vitro human cellular models are not an alternative, as in vitro delivery does not necessarily predict outcomes in vivo (*4*). In addition, potential genomic off-target effects of gene therapy cannot be accounted for in animal models that do not harbor the human genome. By better mirroring human biology, PMDs bridge critical gaps in the traditional discovery pipeline and help realize the therapeutic potential of advanced gene editing techniques.

> **...this approach may...mitigate risks traditionally borne by human subjects during phase 1 clinical trials...**

Judicious use of PMDs can substantially enhance the scale and efficiency of therapeutic discovery. Techniques such as molecular barcoding enable researchers to analyze vast libraries of biomolecules simultaneously (*3*, *4*) in a single PMD. For example, in one of only two published studies (*5*, *6*) employing a PMD model for discovery research, Arap *et al.* used a phage library of 47,160 labeled peptides to create a detailed molecular map of the human vasculature. Similar methodologies can be extended to gene therapy and nanotechnology research where, bolstered by high-throughput analytical methods, researchers could execute hundreds, if not thousands, of simultaneous head-to-head experiments in a single PMD. Moreover, autopsy and tissue-specific analyses conducted through PMD models offer insights into the biodistribution and physiologic effects across entire molecular libraries.

Research conducted on PMDs may also enhance efficiency and precision in identifying physiologically and therapeutically relevant compounds, notably at the earliest stages of investigation. Researchers may be able to identify and eliminate biomolecules with unfavorable target engagement, immunogenicity, biodistribution, or off-target effects, which may only become evident after the lengthy progression from animal to human trials in traditional pipelines. Consequently, PMD-based models could offer a streamlined pathway to de-risk candidate thera-

[1]Department of Neurology, Weill Institute for Neurosciences, University of California, San Francisco, CA, USA. [2]Department of Neurology, Zuckerberg San Francisco General Hospital, University of California, San Francisco, CA, USA. [3]Division of Medical Ethics, Department of Population Health, NYU Grossman School of Medicine, New York, NY, USA. [4]Department of Neurology, Memory and Aging Center, University of California, San Francisco, CA, USA. Email: claire.clelland@ucsf.edu

peutics, ultimately reducing time and costs associated with candidate therapeutic development. Furthermore, this approach may reduce reliance on nonhuman animal subjects, mitigate risks traditionally borne by human subjects during phase 1 clinical trials, and reduce the number of negative trials. PMD testing has the potential to help researchers identify human-relevant candidates early on, providing better pretrial data on safety, toxicity, and off-target effects, which could reduce the likelihood of harmful impacts on participants during clinical trials, including the risk of exposing them to drugs that are ultimately ineffective. By expediting treatment development and deployment, this refined process has the potential to complement the current discovery pipeline, substantially accelerate human-specific therapies, and benefit patients in need.

ETHICS AND IMPACT

PMD research traverses complex ethical and moral terrain, necessitating a thoughtful approach that protects stakeholders and upholds humane practices (*7*–*9*). Ethical scholarship around organ donation can largely inform PMD-related practices in discovery research as well. However, distinct technical features, risks, and benefits of PMD research, as well as its current obscurity in the public forum, raise critical considerations regarding eligibility, consent, impact on research facilities and personnel, and oversight (detailed below, and see the box).

Eligibility

Priorities regarding eligibility for PMD research are maximizing respect for the deceased, avoiding emotional and/or moral harms to their loved ones, just allocation of donated tissues, and preservation of public trust. In 2005, the North American Consensus Panel on Research with the Recently Dead (CPRRD) convened an interdisciplinary group to provide guidance on research involving the deceased, including but not limited to PMDs. Although acknowledging that PMDs meet legal and physiological definitions of death, the panel emphasized certain "moral obligations" to the recently deceased. The panel's report extended the core bioethical principle of "respect for persons" to the recently deceased, asserting that research practices should respect "the value and dignity of the once-living person." The panel further recommended that researchers treat the deceased in alignment with the individual's life goals and in a manner that upholds their dignity (*9*).

Although autonomy and consent do not directly apply to deceased individuals, researchers should maximize these ethical tenets in their protocols, treating surrogates as extensions of the deceased. Failing to address this issue risks both moral and collateral harm, particularly because of the low public awareness surrounding PMDs. For example, mishandling, misappropriating, or failing to appropriately disclose the procedures in use of PMDs could provoke feelings of violation or disgust among surviving family and members of the public. Such actions could be perceived as a profound breach of respect by medical institutions toward the deceased, whose death carries societal, moral, and ethical importance.

Many individuals who register as organ donors do so solely with transplantation in mind and may not fully consider research uses. Given this ambiguity, it is important to give families the opportunity to make a decision that respects the deceased's wishes and values, and their own comfort with the research goals. Decedents who declined or otherwise objected to donation should be excluded from PMD research (*7*). Exclusion is also warranted if loved ones do not accept the declaration of brain death in the clinical setting (*7, 8*). Consensus around brain death rests at the core of the ethical justification of PMD-based research (*10*). Families who do not accept brain death engage in emotionally difficult conversations with health care providers, making the request for research donation a potential source of additional distress and distrust. To preserve public trust and the integrity of the organ donation system, PMD research frameworks should use current accepted criteria of brain death with adaptive mechanisms to incorporate new criteria as they evolve.

Donor eligibility for transplantation should take precedence over donation for research. Although PMD platforms may lead to discoveries that will benefit future patients, organ donation offers immediate lifesaving benefits. Consensus guidelines published in the US and Canada have stipulated that eligible deceased organ donors be excluded from research enrollment unless the research will not interfere with organ donation or if there is an expressed preference for donation for research over transplantation. Other appropriate exclusions include those for which research participation would interfere with autopsy and those lacking surrogate decision-makers (*9*).

Consent and informed authorization

Despite recent media attention, awareness surrounding PMD research is lacking, and public perceptions of the moral status of PMD-based research remain undefined. If PMD research becomes more prevalent and its use cases diversify, one can anticipate diverse public responses, shaped by cultural beliefs about the definition of death, physical and metaphysical experiences at the end of life, and proper treatment of human remains. Given the sensitive nature of these topics, mishandling or miscommunication concerning PMD-related science has the potential to alienate the public, garnering mistrust toward researchers, clinicians, and institutions. Furthermore, thematic parallels between PMD research and organ donation for transplant mean that such mistrust could discourage voluntary donation, thus jeopardizing the available organ supply and public health efforts. Hence, it becomes imperative that in-

Critical considerations for research

Research involving PMDs can have distinct features, risks, and benefits

General ethical priorities	• Maximize respect for the deceased • Minimize emotional and/or moral harms to decedents' loved ones/next of kin • Preserve public trust

Eligibility for research participation	• Donation for transplant should take precedence over donation for research
	• Decedents should be excluded if:
	  • They had previously declined organ donation or expressed nonacceptance of brain death criteria
	  • Their loved ones/next of kin do not accept the determination of brain death
	  • Research participation will interfere with autopsy

Consent and informed authorization	• An appropriate surrogate decision-maker must be available to provide informed authorization* • Researchers should disclose meaningful and/or influential information about PMD research, including but not limited to the duration of physiological support, handling of PMDs, and return of remains • Those involved in authorization processes should be unaffiliated with the clinical care provided prior to death
Impacts on facilities and personnel	• ICU resources used for PMD research should not detract from the care of living patients • Measures should be taken to minimize biohazard and safety risks to personnel and patients co-occupying facilities where PMD research occurs
Oversight and accountability	• PMD research should be reviewed and approved by Institutional Review Boards (IRBs) or similarly appointed committees†

*In the absence of advanced first-person consent for PMD research from the participant, which we expect to be rare
†Despite the absence of legal requirement in the US, given research participants are deceased

Next of kin will have the most robust opportunity to weigh the decedent's values and wishes in the context of protocol-specific details.

formed consent and authorization procedures for PMD research are not only culturally sensitive but also transparent and safeguard against undue influence and coercion.

According to the "Common Rule" ethical guidelines regarding human subjects research in the US, first-person consent applies to living subjects regarding their informed decision to participate in medical treatment or research. Informed "authorization" has denoted the process by which a decedent's next of kin grants permission for postmortem donation or research enrollment (*8*). For organ donation, organ procurement organizations (OPOs) generally look toward legally designated next of kin for authorization if the deceased's donor status has not been previously documented. However, each US state's anatomical gift act gives legal precedence to advanced registration from the deceased, even when there are objections from next of kin (*11*).

Even though many state registries include research authorization with donor registration, "opt-in" or otherwise generic processes fall short of attaining appropriate consent for PMD research because, owing to its complexity and relative obscurity in the public eye, it likely falls outside of a layperson's understanding when registering as an organ or whole-body donor. First-person consent to PMD research at the end of life would be preferred but is likely to be rare as catastrophic events leading to brain death are often unanticipated. Absent preexisting first-person consent specifically for PMD research, we recommend that PMD research enrollment hinge upon informed authorization from next of kin regardless of donor status, unless it is known that the decedent previously objected to organ donation, which would merit exclusion. Next of kin will have the most robust opportunity to weigh the decedent's values and wishes in the context of protocol-specific details.

Existing ethical guidelines stipulate disclosing pertinent details, which "may be reasonably expected to influence" a decision about research authorization (*7*). For example, the fact the deceased body's heart will be kept beating after brain death may figure critically into a person's decision to donate. Other likely meaningful disclosures would include, but are not limited to, the diseases being studied and potential benefits to science and society, technical descriptions of how deceased bodies are handled and maintained, duration of physiologic support, postmortem medical and surgical procedures, and processes for disposing of remains. We recommend explanations of the latter to address how, when, and whether the return of remains to the decedents' family for burial or other ritual practices would occur.

These and other considerations merit nuanced explanations, as well as the opportunity for next of kin to ask questions to experts familiar with PMD research. Procedures for these discussions will vary based on existing institutional structures and partnerships but should prioritize clear and deliberate communication. Similarly to OPO representatives, those discussing PMD research should be unaffiliated with the clinical care provided prior to death to mitigate any perceived or real conflict. Furthermore, they should be prepared to address not only the technical aspects of PMD research, but the ethical and moral questions it may elicit.

When seeking authorization for any form of PMD research, the potential impact on human health must be framed with uncertainty. The benefits of late-stage studies such as xenotransplant are more immediately accessible by patients. By contrast, the benefits of early-stage therapeutic discovery research are less tangible or proximate, and this may affect the next of kin's decision-making.

Clinical facilities and personnel

PMD research will likely continue to occur in academic hospital intensive care units (ICUs). Researchers must consider the potential impacts on adjacent clinical activities, including the care of living patients, as well as on ICU personnel and workflow. Allocation and funding of intensive care beds, equipment, and staff should be clearly delineated and agreed upon with hospital and ICU leadership. The duration of physiologic maintenance and other ICU-based research activities should be minimized and prespecified to clearly outline resource needs (*9, 10*). Allocation agreements should be transparently communicated to ensure that research does not displace or compete with the care of living patients and to avoid the perception of conflicting priorities.

Open questions regarding staffing and safety should be explored and agreed upon by researchers, hospital leadership, ICU staff, and, in some cases, institutional ethics committees. Some have raised concerns about whether ICU nurses caring for living patients should also manage PMDs or if dedicated personnel are necessary (*7*). Research protocols should elicit and address the concerns of those providing care directly and adjacently to postmortem research participants. Special considerations for biosafety and infection control may be appropriate depending on specific protocols. Institutional bodies specialized in lab safety, which would not typically act within a clinical setting like the ICU, may be prudent to engage for certain PMD-based studies; for example, those involving potentially harmful viral vectors or mutagenic gene therapies (*5*).

Oversight and accountability

Although PMD research poses no direct risk to participants, it carries considerable implications for the family members of the deceased, institutions, and the public. However, because human subjects in the US are defined as living, there is no legal requirement that PMD research be approved by institutional review boards (IRBs). Despite this, and in line with policies of other countries such as Canada (*12*), we join other researchers and ethics scholars (*7, 9, 10*) in voicing the need for systematic review and approval for research involving PMDs by IRBs or similarly appointed committees. Such oversight is crucial for ensuring transparent and ethically sound consent procedures, facilitating responsible collaboration with OPOs, maximizing the scientific value of research, upholding public trust, and addressing evolving clinical and legal policies.

Oversight bodies are needed to broadly weigh the risks and benefits of PMD protocols, considering both scientific and ethical justifications. Requiring robust auditable protocols for informed consent (including timing of family outreach and interactions with OPOs), body donation, specific research procedures, and the disposition of remains will help to ensure respectful treatment of the deceased and proper handling of the body. This will also provide families with crucial assurances and set clear expectations throughout the process. Distinct from those involving live human subjects, "costs" and "risks" of PMD research may be symbolic or indirect. For example, it is ethically prudent to avoid undue disfigurement or desecration of the deceased or cause unreasonable burdens to their families (*13*). Because of its close linkage to the realm of organ transplantation, oversight committees should hold researchers accountable for conducting and conveying ethically informed practices that do not alienate the public or garner doubts around perimortem care or tissue donation. Although all PMD research should be scrutinized for scientific justification, it is possible that some early-stage therapeutic discovery PMD research will be harder to justify than late-stage translational PMD research. Oversight review should pay particular attention in early-stage investigation protocols for strong arguments regarding human specificity of the proposed intervention, lack of alternative models, and importance of the knowledge to be gained.

Institutions or IRBs without experience reviewing postmortem research may seek guidance from specialized bodies such as the Committee for the Oversight of Research Involving the Dead (CORID), which can provide consultations or external reviews on relevant projects. Furthermore, a limited number of guidelines have been proposed regarding ethical frameworks for research involving the recently deceased, including PMDs (*8*–*10*, *13*).

AREAS OF FUTURE STUDY

In exploring the use of PMDs for therapeutic development, further research is necessary to understand how physiological changes (e.g., endocrine, autonomic, and cellular alterations) after brain death may affect experimental outcomes. Routine use of PMDs in drug discovery without a clear understanding of the technical limitations risks not only poor scientific yield, but also ethical violations (owing to lack of scientific justification) and erosion of public confidence. For example, PMD research can provide data on physiologic and molecular effects of interventions over a limited period of time (in most cases, days). Biodistribution of barcoded libraries of delivery vectors is one feasible example that is compatible with this window. The PMD research model will not necessarily be useful for studies over a much longer time horizon (months to years) such as collecting long-term safety data. In addition, PMD research will not replace early-phase clinical trials that rely on monitoring for adverse effects over a longer treatment duration.

Preliminary successes applying PMD research to xenotransplantation suggest the considerable potential for modeling various physiological, immunologic, and therapeutic processes, and initial PMD research should build on this foundation while expanding knowledge about limitations. Other translational challenges include neurotherapeutic research targeting brain tissue; because PMDs do not have cerebral perfusion, such experiments will necessitate the use of anatomical surrogates, such as the spinal cord, which maintains perfusion in brain death (*14*). A deeper understanding of the limitations and opportunities within PMD-based therapeutic discovery research will strengthen its scientific foundation and clarify the types of experiments for which it can offer the most valuable insights.

As new avenues emerge for PMD research, scholarship around ethical, legal, and social implications (ELSIs), as well as community engagement, become increasingly vital to ensuring responsible practices. Thoughtfully weighing risks, costs, and benefits is a core tenet of responsible research and will require dedicated studies exploring both the empirical advantages of PMD-based research and broader ELSI-related topics. Centers engaged in PMD research should be encouraged to conduct ELSI research in parallel, collaborating with others experienced with perimortem issues, including bioethicists, neurointensivists, OPOs, hospital chaplains, and patient advocates.

Future research is needed to compare PMD-based therapeutic discovery research with traditional cell-to-animal-to-human pipelines in terms of cost, efficiency, risks, and biomaterial footprint. Furthermore, to promote inclusiveness in research participation and discourse, the scientific community should seek to understand the priorities and concerns of the public. Studies are needed to assess public views on the role of PMD use in medical research. Limited qualitative data on PMD research suggest that participants' surrogates feel that a research protocol is a reasonable alternative to organ donation regarding honoring their loved one's altruistic wishes (*10*). Further studies involving families who have either authorized or declined the involvement of their loved ones are needed to elucidate hopes, fears, and misconceptions related to PMD research. Broader community engagement, including with religious groups, caregivers, and the elderly, among others, should help capture a diverse range of perspectives on the use and moral implications of PMDs in health research. These endeavors may also help guide best practices for engaging donor representatives. Lastly, understanding the views of clinical staff on their experiences caring for PMDs would help guide hospital policies and improve collaboration (*7*, *15*).

Therapeutic discovery research on donated PMDs that replicate live human physiology offers tremendous potential for advancing science, particularly gene-based therapies, toward lifesaving human treatments. Despite promising potential, history has shown that scientific innovations inevitably bring the potential for new harms. As such, responsible advancement requires careful deliberation and policies that protect the common good. There is a clear need to further establish language, scope, and best practices regarding research practices involving PMDs (*7*, *15*). Broad and publicly engaged ELSI scholarship in this arena will be paramount in charting a responsible path forward. □

REFERENCES AND NOTES

1. N. Moazami *et al*., *Nat. Med.* **29**, 1989 (2023).
2. Q. Huang *et al*., *Science* **384**, 1220 (2024).
3. M. Z. C. Hatit *et al*., *Nat. Nanotechnol.* **17**, 310 (2022).
4. E. L. Han *et al*., *Nano Lett.* **24**, 1477 (2024).
5. W. Arap *et al*., *Nat. Med.* **8**, 121 (2002).
6. B. S. Coller, L. E. Scudder, H. J. Berger, J. D. Iuliucci, *Ann. Intern. Med.* **109**, 635 (1988).
7. B. Parent *et al*., *J. Med. Ethics* jme-2023-109413 (2023).
8. T. Schiff, B, Parent, "Research on the Newly Deceased Following Declaration of Death by Neurologic Criteria" in *Death Determination by Neurologic Criteria*, A. Lewis, J. L. Bernat, Eds. (Springer, 2022), pp. 265–272.
9. R. D. Pentz *et al*., *Nat. Med.* **11**, 1145 (2005).
10. R. D. Pentz, A. L. Flamm, R. Pasqualini, C. J. Logothetis, W. Arap, *Hastings Cent. Rep.* **33**, 20 (2003).
11. National Conference of Commissioners on Uniform State Laws, *Revised Uniform Anatomical Gift Act. §8(a)* (2006).
12. Canadian National Research Council, *Policy for Research Involving Human Subjects*.
13. M. R. Wicclair, *Camb. Q. Healthc. Ethics* **17**, 87 (2008).
14. H. Schneider, F. Matakas, *Acta Neuropathol.* **18**, 234 (1971).
15. N. B. Murphy *et al*., *Can. J. Anaesth.* **70**, 596 (2023).

ACKNOWLEDGMENTS

N.S.S. and C.D.C. contributed equally. C.D.C. acknowledges support from NIH/NINDS K08-NS112330K08, 8NIH Common Fund U19NS132303, U01NS134062, Rainwater Charitable Foundation, Carol and Gene Ludwig Family Foundation, Larry H. Hillblom Foundation, Target ALS, Packard Center, Alzheimer's Association, NACC New Investigator Award, Shupin Fellowship from the UCSF Neurology Endowment, Weill Institute for Neurosciences, and the UCSF Memory and Aging Center. C.D.C. is grateful to N. Sakamoto, J. DiSabato, and the Wolfen Family Foundation. B.P. acknowledges support from NIH/NHLBI R01HL173157-01, NIH/NHLBI R61HL156890-02, The Applebaum Foundation, The Robert Wood Johnson Foundation, and United Therapeutics. B.P. is on the scientific and ethics advisory boards of Procure OnDemand and of Science in Donation and Transplantation. N.S. acknowledges support from VA OSR 1IK2BX005369 and the Marcus Program in Precision Medicine Innovation. C.D.C. is a founder of, with equity in, Ciznor Co., a CNS therapeutics company.

10.1126/science.adt3527

BOOKS ET AL.

ARCHAEOLOGY

Thriving in perilous times

Archaeological evidence shows human societies can reshape themselves in times of crisis **Erle C. Ellis**

Signs of catastrophe are everywhere these days: megafires and massive flooding, dizzying shifts in politics, and alarming infectious disease outbreaks. These challenges of our times might seem to transcend any society's capabilities to navigate them, but that assumption is wrong, according to journalist Lizzie Wade. "Not only have people already confronted almost every possible apocalypse, they have lived through them," she argues in her new book, *Apocalypse*. "All of them."

Forged in the depths of the COVID-19 pandemic, *Apocalypse* dives deep into the latest archaeological research to expose the remarkable adaptations and transformations experienced by human societies that have faced overwhelming adversity throughout history. Fictional narratives featuring firsthand accounts of living through various crises help bring Wade's reporting closer to home. For those struggling to make sense of our troubled times, the book will be very welcome.

Archaeology is at the heart of *Apocalypse*, and it is the real deal—no treasure-hunting Indiana Jones here. The book highlights the innovative science that is rapidly gaining new capabilities to reconstruct the lives of people and places across the planet from the evidence left behind. In nine chapters, each centered on a distinct lesson to be learned from societies that have faced unprecedented challenges, the reader is taken on a fascinating and eclectic tour around the world. Wade delves into the Neanderthal extinction and the submergence of the northern European region known as Doggerland under the North Sea. She describes fire and flooding in Aboriginal Australia, the climatic challenges faced by fishermen and farmers in coastal Peru, and the decline of Harappan India. Her tour includes the Black Plague in Europe, the end of Old Kingdom Egypt, the emergence of the postclassic Maya, European colonization of the Mexica (Aztecs), slavery in St. Croix, and many more harrowing incidents from history.

While this is a book about archaeological discoveries, it is also a book with a message, and the message is often personal. In essence, its teachings might be boiled down to Wade's observation that "learning to see human history through the lens of apocalypse teaches us that our past is a story of survival, transformation, and reinvention."

Throughout her reporting, Wade questions historical narratives that purport to predict upcoming perils. She exposes, for example, Ipuwer's "Admonitions"—a classic Egyptian tale about a dark age brought on by elite decline—as "propaganda" intended to preserve elite power. In this effort, she is in good company with other scholars who have likewise begun examining the deeper history of human experience to "understand who we are and where we came from" [e.g., (*1*)].

Aké, a once thriving city at the heart of the pre-Columbian Maya civilization, was transformed by numerous catastrophes.

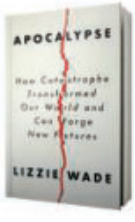

Apocalypse: How Catastrophe Transformed Our World and Can Forge New Futures
Lizzie Wade
Harper, 2025. 320 pp.

Wade aims especially high with the book's final chapter. Here, her synthesis of site-based histories and personal experiences comes to a head with the claim that "apocalypses are also the best chance our societies have for change." Wade's writing in this section is at its most powerful, enticing, and personally impassioned. I found myself convinced, indeed, that "apocalypses are not endings. They are transformations."

Still, readers may justifiably feel that some lessons of the book are built on thin foundations. A chapter on the "apocalypse of colonialism," for example, examines the devastation wrought by the Spanish conquistador Hernán Cortés on the Aztecs during the 16th century. It is a powerful and telling narrative, to be sure, but it fails to capture the full complexity of the destruction caused by European colonialism as other works have (*2*). Likewise, chapter 8 ("How Slavery Created the Modern World") is almost exclusively focused on the story of one plantation in the Caribbean island of St. Croix.

To some degree, those well read on the subject of long-term social change and societal transformation may feel that this book leaves out more than it adds. Some classic works, such as Joseph Tainter's *The Collapse of Complex Societies*, are touched upon, yet other key work seems notably absent. Nor is effort made to address popular misconceptions, such as Jared Diamond's deeply flawed but highly influential misinterpretation of social-ecological catastrophe in Rapa Nui (Easter Island) (*3*). An opportunity is lost to correct the record here, and archaeologists and other experts will likely be left wanting more.

Ultimately, however, this book has the potential to serve well in many roles, including as a text for classes in the environmental humanities, anthropology, and beyond. *Apocalypse* is an inspiring book for challenging times and will be a rewarding read for everyone intrigued by archaeological discovery and the deep history of human social change. □

REFERENCES AND NOTES

1. D. Graeber, D. Wengrow, *The Dawn of Everything: A New History of Humanity* (Farrar, Straus and Giroux, 2021).
2. C. C. Mann, *1491: New Revelations of the Americas Before Columbus* (Knopf, 2005).
3. J. Diamond, *Collapse: How Societies Choose to Fail or Succeed* (Penguin, 2004).

10.1126/science.adw3924

The reviewer is at the Department of Geography and Environmental Systems, University of Maryland, Baltimore County, Baltimore, MD, USA. Email: ece@umbc.edu

SCIENCE AND SOCIETY

Baby's first surveillance technology

From apps to smart cribs, digital tools for parents abound **Veronica Barassi**

Second Life: Having a Child in the Digital Age
Amanda Hess
Doubleday, 2025.
272 pp.

Second Life: Having a Child in the Digital Age, written by journalist Amanda Hess, is a reflective, heartwarming, and detailed memoir that delves into the complexities of pregnancy and early parenthood in a techno-dependent, digitally obsessed society. This, however, is not just another story about digital pregnancy; it is much more. With sharp analysis, sensitivity, and an engaging, accessible style, Hess navigates the uncertainty and the emotional toll of a pregnancy flagged as "abnormal" while providing fascinating insights into our complicated, often absurd relationship with technology—especially when it comes to contemporary parenthood.

The book highlights how technology has become deeply embedded in modern parenting, shaping our behaviors and interactions in ways we rarely question. From obsessive data tracking on pregnancy apps to smart cribs that soothe babies, we have outsourced child-rearing to digital tools—often with questionable results.

Babies and children are rich targets for data-capturing products and services.

A central theme in the book is how these technologies offer a false sense of security, promising parents reassurance while actually increasing anxiety and detachment. Do we really need a pregnancy tracker that offers generic advice and standardizes human experience, especially when navigating a high-risk pregnancy during a global pandemic? Probably not. Do we need an expensive artificial intelligence–powered baby monitor that sends an alert every time our child's breathing pattern shifts? Again, likely not. Hess reflects on the psychological impact of these "homemade panopticon" technologies in family life—how they shape the behaviors and relationships of parents and children. She concludes that for her family, perhaps a $15 audio monitor is the wiser and healthier technological choice.

Divided into 11 chapters that trace the personal journey from before Hess's first pregnancy to the early days with her second child, the book focuses on two different yet interconnected themes. Hess is eager to explore the tech-materiality of early parenthood and its financial and human costs for families. Yet she is also interested in examining the implications of parents' online lives. In doing so, she encourages readers to reflect on the desperate need for reassurance that drives anxious parents toward internet searches, even when doctors explicitly advise "don't Google it." She unpacks the toxic cycle of Instagram comparisons, where the compulsion to document family life not only distracts from real-life moments but also fuels loneliness and inadequacy in others. She shows readers how, instead of fostering genuine connections, social media platforms trap parents in an unhealthy game of mirrors, where curated perfection hunts, bullies, and diminishes everyday life. Even when social media connections provide support—such as in the case of online communities for families of children with special conditions—parents, ultimately, are left alone with dire questions about the implications and consequences of the data that they share online.

In her exploration of social media and contemporary parenthood, Hess does not stop at the surface, she digs into how platforms fuel deep-seated divisions among parents. From "freebirthers" to "trad wives," the digital age has amplified extreme, polarized ideologies about the "right" way to parent. Social media algorithms reinforce these divisions, pushing parents into ideological bubbles where choices about childbirth and child-rearing become almost religious in nature. Medical advice and intergenerational experiences often take a backseat to the pseudoscience and romanticized notions of "natural parenting" propagated in online groups.

Second Life is thus a powerful firsthand account of how digital cultures are distorting and radicalizing parental decision-making. It brilliantly shows that, when it comes to child-rearing, we have become extraordinarily techno-dependent and that this dependency can turn us into anxious, insecure, at times obsessive and extreme parents.

What, then, is the solution? Should we eliminate technology from modern parenthood, disconnect from social media, and embrace a tech-free life? Hess touches on these questions only indirectly, and her answer appears to be no. We do not need to opt out of digital life, but we do need to critically reflect on the kind of parents—and people—these technologies are shaping us into, recognize their false promises, and use them with care and intention.

In her book, Hess blends personal experience with sharp observations, encouraging readers to question how much control technology really gives us—or takes away—and to rethink our relationship with it, but at times, the connection between the author's personal experiences and bigger topics, such as inequality and scientific reductionism, felt underdeveloped. And although Hess mentions concerns about digital surveillance, she does not fully explore what happens to all the data collected on children, leaving some important questions unanswered.

Despite these very minor flaws, *Second Life* is a thought-provoking and powerful book. It offers a very insightful—at times funny, at times infuriating—read for anyone grappling with the challenges of contemporary parenthood. □

10.1126/science.adw8851

The reviewer is at the Institute for Media and Communication Management, University of St. Gallen, St. Gallen, Switzerland, and is the author of *Child Data Citizen: How Tech Companies Are Profiling Us from Before Birth* (MIT Press, 2020). Email: veronica.barassi@unisg.ch

PHOTO: PERFECTLAB/SHUTTERSTOCK

LETTERS

Edited by
Jennifer Sills

Ecologically valuable old-growth forests in the US Pacific Northwest are at risk of increased logging.

PHOTO: MATTHEW G. BETTS

Benefits of onshoring forestry rely on science

US Executive Orders to reduce wood imports (*1*) and ramp up domestic production (*2*) signal a transformation in forest policy. Portrayed as addressing supply chain and national security concerns, these orders have the potential to reduce substantial environmental effects of US-driven wood consumption overseas (*3*). However, achieving overall environmental benefits and resilient wood supply hinges on sustainable domestic forestry on federal lands—a goal endangered by recent firings of federal scientific and technical experts (*4*).

As one of the world's largest wood importers (*3*), the US has substantially influenced logging's environmental impacts abroad through its shifting policies. For example, logging restrictions under the Northwest Forest Plan moved about 1.3 million cubic meters of harvesting from US land into Canada (*5*), driving sharp declines in Canadian old-forest biodiversity and carbon (*6*). Between 2001 and 2015, US agricultural and forestry imports drove range losses of vertebrates that depend on forests internationally at five times the domestic rate (*7*). Judicious onshoring could therefore reduce the considerable climate and habitat effects of US-driven harvesting, including in highly sensitive ecosystems in countries such as Mexico, Vietnam, and Brazil (*3*, *7*, *8*).

However, cuts to evidence-based forestry (*4*) exacerbate threats to the policy's potential environmental benefits and the goal of long-term wood security. Many US forests harbor large carbon stores and threatened species that are vulnerable to increased logging and weakening of environmental regulations (*2*). For example, the Pacific Northwest's rainforests support 5 billion tonnes of irrecoverable carbon (*9*) and remaining populations of the marbled murrelet and the spotted owl (*7*). In addition, intensifying management of federal lands for production risks undermining other ecosystem values and timber's resilience to escalating pest and wildfire threats (*10*). Finally, reduced US demand for responsibly sourced timber abroad could weaken efforts against unsustainable logging worldwide (*11*).

Achieving global socioenvironmental benefits and national wood security is possible through improved management of federal forests. Landscape-scale management that protects old-growth forests (*6*), directs more-intensive harvests toward areas with existing degraded forests, and expands sustainable forestry practices can promote productive, biodiverse, and resilient forests that sustain timber supply (*12*). Reducing waste and promoting long-lasting wood products can further bolster wood security (*8*). However, maximizing long-term productivity, ensuring wildfire resilience, and minimizing environmental harm require evidence-based and socially acceptable management.

Matthew G. Betts[1]*, Jerry F. Franklin[2], Jacob J. Bukoski[1], Z. Burivalova[3], Emily E. Conklin[1], Thomas H. DeLuca[1], Amelia Fitch[1], Austin Himes[4], Rajat Panwar[1], Hannah Sachs[1], R. Alex Wiebe[5], Gianluca Cerullo[1]

[1]Department of Forest Ecosystems and Society, Oregon State University, Corvallis, OR, USA. [2]College of Forest Resources, University of Washington, Seattle, WA, USA. [3]Department of Forest and Wildlife Ecology and the Nelson Institute for Environmental Studies, University of Wisconsin–Madison, Madison, WI, USA. [4]School of the Environment, Washington State University, Pullman, WA, USA. [5]Department of Ecology and Evolutionary Biology, Princeton University, Princeton, NJ, USA. Email: matt.betts@oregonstate.edu

REFERENCES AND NOTES

1. "Addressing the Threat to National Security from Imports of Timber, Lumber" (The White House, 2025); https://www.whitehouse.gov/presidential-actions/2025/03/addressing-the-threat-to-national-security-from-imports-of-timber-lumber/.
2. "Increasing Timber Production and Designating an Emergency Situation on National Forest System Lands" (US Department of Agriculture, Secretary's Memorandum 1078-006, 2025); https://www.usda.gov/sites/default/files/documents/sm-1078-006.pdf.
3. S. Kan *et al.*, *One Earth* **6**, 55 (2023).
4. *Nat. Ecol. Evol.* **9**, 365 (2025).
5. D. N. Wear, B. C. Murray, *J. Environ. Econ. Manage.* **47**, 307 (2004).
6. M. G. Betts, Z. Yang, J. S. Gunn, S. P. Healey, *Glob. Change Biol.* **30**, e17541 (2024).
7. R. A. Wiebe, D. S. Wilcove, *Nature* **639**, 389 (2025).
8. A. Balmford *et al.*, *Science* **387**, 720 (2025).
9. A. Goldstein *et al.*, *Nat. Clim. Chang.* **10**, 287 (2020).
10. W. R. L. Anderegg *et al.*, *Ecol. Lett.* **25**, 1510 (2022).
11. B. Schatz, 118th Congress (2023–2024), "S.3371 - FOREST Act of 2023" (2023); https://www.congress.gov/118/bills/s3371/BILLS-118s3371is.pdf.
12. J. F. Franklin, K. N. Johnson, D. L. Johnson, *Ecological Forest Management* (Waveland Press, 2018).

COMPETING INTERESTS

M.G.B. and J.J.B. have collaborations with federal scientists, including those at the US Forest Service (USFS). M.G.B. has an active research project funded partly by the USFS. A.H. has served on the board of directors for the Consortium for Research on Renewable Industrial Materials, a nonprofit research corporation that provides a scientific database of information for quantifying the environmental impacts of producing and using renewable wood materials.

Published online 17 April 2025
10.1126/science.adx4908

China's pet squirrel trade needs regulation

In recent years, the popularity of pets has increased substantially in China (*1*), and squirrels have emerged as a favored choice among pet lovers (*2*). At least six species of squirrels, including *Sciurus vulgaris*, *Tamias sibiricus*, *Callosciurus erythraeus*, *Tamiops swinhoei*, *Spermophilus dauricus*, and *Marmota himalayana*, are widely bred and traded in China (*2*–*4*), and two species of flying squirrels, *Trogopterus xanthipes* and *Pteromys volans*, are occasionally encountered in pet markets and farms (*2*, *5*). However, the pet squirrel trade has raised conservation, public health, and animal welfare concerns (*2*, *6*). China should take urgent action to implement strict supervision of the pet squirrel market.

Squirrels are routinely trafficked across the natural ecosystem boundaries created by the Yellow River and the Yangtze River. *C. erythraeus*, a species originally distributed in southeast China (*7*), has been found in the Taihang Mountains in northern China (*8*), and the northern squirrels *S. vulgaris* and *T. sibiricus* (*9*) have been widely transported across southern China (*2*, *3*). *S. dauricus* and *M. himalayana*, originally distributed in northern China and the Qinghai-Tibetan Plateau, have been sold to buyers in central and southern China despite potentially serving as vectors for zoonotic disease transmission (*10*).

China's squirrel trade has also alarmed animal welfare advocates. Squirrels are often weaned early. During shipping, food and water shortages, poor packaging, and violent handling lead to high mortality rates (*11*).

Breeding and sales qualification approvals for pet squirrels are strictly controlled in China (*12*), but the subsequent sale process and destination lack effective supervision. The government should formulate more rigorous regulations governing the sale and ownership of squirrels. Sellers should be required to obtain licenses, and laws should require squirrel breeders to adhere to controlled and humane conditions. China should inspect breeding and transport activities more frequently, impose stricter penalties for violations, and use technology to track the movement of squirrels in the pet trade. Finally, the government should restrict the transportation and

The Siberian chipmunk (*Tamias sibiricus*), a type of squirrel, is a popular pet in China.

PHOTO: LI *ET AL.*

trading of squirrels across ecosystem boundaries to prevent further introductions to non-native ecosystems. By implementing these measures, China can ensure that the pet squirrel trade is sustainable, minimize the spread of invasive species and zoonotic diseases, and protect animal welfare.

Yueqin Yang[1], Jishan Xiang[2], Xianfeng Yi[2]

[1]College of Agriculture, Henan University of Science and Technology, Luoyang, China. [2]College of Biological Sciences and Technology, Yili Normal University, Yining, China. Email: yyqhaust@126.com (Y.Y.); yxfeng1975@126.com (X.Y.)

REFERENCES AND NOTES

1. B. Wang, *Guizhou J. Anim. Husband. Veterin. Med.* **47**, 6 (2023) [in Chinese].
2. J. Chen *et al.*, *One Health* **13**, 100269 (2021).
3. L. Deng *et al.*, *Sci. Rep.* **10**, 1026 (2020).
4. L. Deng *et al.*, *BMC Microbiol.* **18**, 37 (2018).
5. X. Liu *et al.*, *Parasite* **31**, 37 (2024).
6. A.V. Weldon *et al.*, *Anim. Welf.* **30**, 169 (2021).
7. N. Tamura *et al.*, *Behav. Ecol. Sociobiol.* **75**, 97 (2021).
8. C. Ji *et al.*, *Chin. J. Wildl.* **42**, 937 (2021) [in Chinese].
9. Z. Liu *et al.*, *Mammal. Biol.* **79**, 247 (2014).
10. V. Nijman *et al.*, *Integr. Zool.* **16**, 820 (2021).
11. C. Warwick, C. Steedman. *Int. J. One Health* **7**, 42 (2021).
12. China Ministry of Forestry, "Measures for the administration of domestication and breeding permits for nationally protected wildlife (2015); https://www.gov.cn/zhengce/2015-04/30/content_5718776.htm.

10.1126/science.adv6576

Deep-sea mining interests cannot shape research

Although understanding deep-sea ecosystems will require decades of additional scientific work (*1*), activation for the first time of the so-called "2-year rule" (*2*) in 2021 has put pressure on the International Seabed Authority (ISA) to rush the creation and adoption of a mining code. Negotiations related to mining in international waters should not be subject to a timeline imposed by commercial interests (*3*). To effectively protect the deep sea, states must take full account of available scientific evidence, including remaining uncertainties and unknowns.

In 2021, the nation of Nauru declared its intent to seek permission to initiate commercial deep-sea mining through Nauru Ocean Resources, Inc., a wholly owned subsidiary of The Metals Company (*4*). The announcement started the clock established under the 2-year rule, part of a 1994 addendum to the 1982 United Nations Convention on the Law of the Sea, which indicated that if mining rules were not set within 2 years of a planned project, then the project could seek authorization under current rules (*2*). When the 2 years expired in June 2023, mining rules were still far from complete, and negotiations continue today (*5*). Most states have expressed their opposition to commercial mining in the absence of exploitation regulations, and the process that the ISA Council should use to evaluate an application in their absence remains unclear (*3*, *6*). Nevertheless, The Metals Company intends to submit its exploitation application on 27 June 2025 (*7*).

The scientific community is under pressure to propose thresholds for "acceptable harm" to ecosystems for the purposes of regulation (*8*), despite the huge gaps in knowledge that remain to be addressed. If thresholds are designed to evolve as mining proceeds and understanding improves (*9*), a lot of damage may be done before the thresholds reflect the actual risks. Although the legacy effects of sediment plumes from small-scale test mining in the late 1970s were recently deemed "relatively limited," tracks left by the mining equipment are still visible, and biodiversity in the mining zone remains depleted (*10*).

Much of the research underway in proposed deep-sea mining areas is geared toward testing mining equipment and assessing its impacts. Too little research has been devoted to a fundamental understanding of the structure and function of those deep-sea ecosystems, including the services that they provide and how to best protect them from disruption. Scientists and funders should reverse these priorities. Policy decisions should be delayed until more evidence is available and should then be based on data, ensuring that marine ecosystems are effectively protected from harm (*11*).

In January, the newly elected ISA secretary-general, Brazilian oceanographer Leticia Carvalho, started her term of office (*12*), offering an opportunity to strengthen the role of science within the organization. State parties should focus on developing a greater understanding of deep-sea ecosystems and their interconnectivity, with the goal of effectively protecting them rather than facilitating deep-sea mining.

Sebastian Losada[1], Mengjiao Wang[2], David Santillo[2]

[1]Greenpeace International, A Coruña, Spain. [2]Greenpeace Research Laboratories, University of Exeter, Exeter, UK. Email: dsantill@greenpeace.org

REFERENCES AND NOTES

1. D. J. Amon *et al.*, *Mar. Policy* **138**, 105006 (2022).
2. Section 1, paragraph 15, of the Annex to the Agreement relating to the Implementation of Part XI of the United Nations Convention on the Law of the Sea, of 10 December 1982 (1994); https://www.un.org/depts/los/convention_agreements/texts/unclos/closindx-Agree.htm.
3. Decision of the Council of the International Seabed Authority relating to the understanding and application of section 1, paragraph 15, of the Annex to the Agreement relating to the Implementation of Part XI of the United Nations Convention on the Law of the Sea, ISBA/28/C/25 (2023); https://www.isa.org.jm/documents/isba-28-c-25/.
4. Republic of Nauru, Office of the President, Letter to the President of the Council of the 26th Session to the International Seabed Authority (25 June 2021); https://www.isa.org.jm/wp-content/uploads/2022/06/NauruLetter-Notification.pdf.
5. C. Pickens *et al.*, *Mar. Policy* **169**, 105967 (2024).
6. Decision of the Council of the International Seabed Authority on a timeline following the expiration of the two-year period pursuant to section 1, paragraph 15, of the annex to the Agreement relating to the Implementation of Part XI of the United Nations Convention on the Law of the Sea, ISBA/28/C/24 (2023); https://www.isa.org.jm/wp-content/uploads/2023/07/2314552E.pdf.
7. The Metals Company, "TMC Announces June 27, 2025 Submission Date for Subsidiary NORI's ISA Application, and Expanded Company Strategy" (12 November 2024); https://investors.metals.co/news-releases/news-release-details/tmc-announces-june-27-2025-submission-date-subsidiary-noris-isa.
8. B. Hitchin *et al.*, *Mar. Policy* **149**, 105505 (2023).
9. D. Leduc *et al.*, *Ocean Coast. Manag.* **255**, 107252 (2024).
10. M. Cuff, "Deep-sea life is still recovering from mining activity 40 years ago," *New Scientist* (24 February 2025); https://www.newscientist.com/article/2469747-deep-sea-life-is-still-recovering-from-mining-activity-40-years-ago/.
11. Article 145, United Nations Convention on the Law of the Sea (Montego Bay, 10 December 1982, in force 16 November 1994), United Nations—Treaty Series 1833, 1-31363 (1982); https://treaties.un.org/doc/Publication/UNTS/Volume%201833/volume-1833-A-31363-English.pdf.
12. International Seabed Authority, press release (2 January 2025); https://www.isa.org.jm/news/leticia-carvalho-assumes-role-as-secretary-general-of-the-international-seabed-authority/.

10.1126/science.adv0340

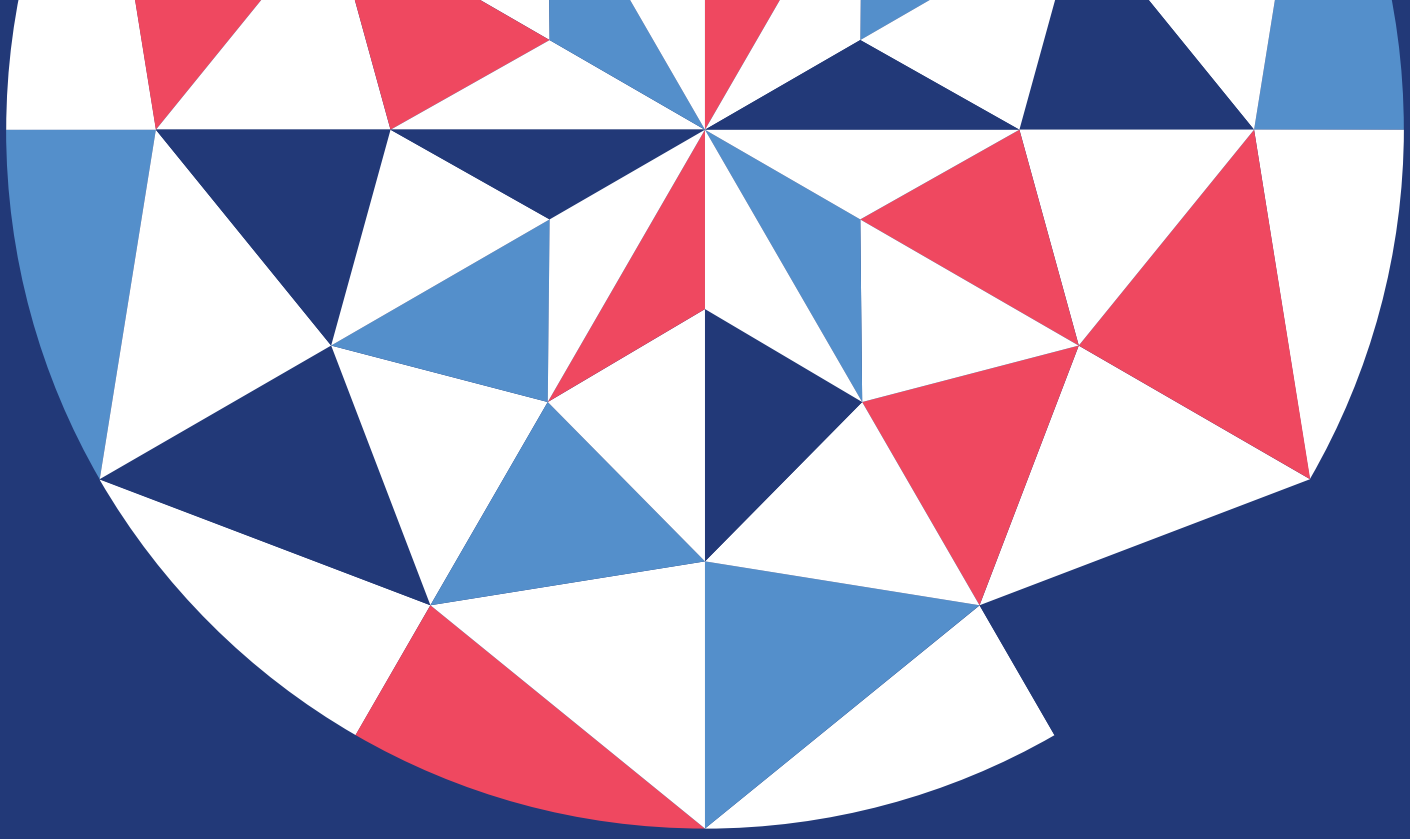

SCIENCE @ SCALE

AAAS | **ANNUAL MEETING**
Phoenix, AZ | February 12–14, 2026

Present your groundbreaking research, lead engaging workshops, and connect with a diverse community of experts.
Be a part of the 2026 AAAS Annual Meeting!

Propose a session or workshop by Tuesday, May 6, 2025
Visit aaas.org/meetings for more information.

REVIEW SUMMARY

CELL BIOLOGY

Stem cells as role models for reprogramming and repair

Magdalena Götz* and Maria-Elena Torres-Padilla*

Full article and list of author affiliations: https://doi.org/10.1126/science.adp2959

BACKGROUND: Stem cells can generate many different cell types, which makes them useful for understanding developmental mechanisms and as a source to replace cells in disease conditions. Developing stem cell therapies takes time, but there are now many clinical trials in progress. Stem cells start everything off from the very beginning of development as totipotent cells that can generate a complete new being. Later in development, pluripotent stem cells (PSCs) that can generate all cells of the body are produced. During further development, tissue-specific stem cells arise and generate progeny that form tissues and organs. The process of differentiation is governed by the surrounding environment (the niche) and the action of specific transcription factors, which are typically lineage restricted. In the adult organism, some tissues and organs are endowed with adult stem cells, which ensure the natural cycles of tissue turnover and homeostasis seen, e.g., in the skin, intestine, and the hematopoietic system. Such adult stem cells can become activated for tissue repair upon injury or degenerative diseases. However, some adult organs do not have a readily available stem cell pool or the pool changes or becomes exhausted during aging. These organs are typically difficult to repair, but using cellular reprogramming inspired by mechanisms of stem cell differentiation can provide a solution.

ADVANCES: Stem cells inspired direct cellular reprogramming because this approach relies on activating developmental fate determinants from tissue-specific stem cells such as those in the muscle or brain or from PSCs. These potent transcription factors are used to instruct cell fate conversion, and this has arisen as a powerful method to generate cells for repair or disease modeling. A foundational discovery in this area is the reversion of somatic cells into a pluripotent state by the so-called Yamanaka transcription factors, which allow the generation of induced PSCs (iPSCs). This discovery has enabled differentiated somatic cells from patients to be reprogrammed to a pluripotent state. In organs without stem cells, natural dedifferentiation or fate conversion can occur, which can be exploited for cellular replacement approaches. Recently, a plethora of reprogramming paradigms have emerged as approaches to repair, and these are now being used to convert cells across germ layers and cell types across a multitude of organs. These experiments have elucidated the mechanisms of cell fate acquisition, conversion, and maintenance and are an advance toward replacing cells in disease conditions. In addition, direct reprogramming has opened entirely unexpected avenues, such as organismal rejuvenation upon transient expression of some of the pluripotency factors in vivo.

OUTLOOK: The number of clinical trials with stem cells or their derivates has increased tremendously in recent years, with many using iPSCs. These approches can enable the use of the patient's own cells as therapeutics. Remarkable progress has been made in bringing stem cell–based methods and stem cell–inspired reprogramming toward clinical testing with promising outcomes, e.g., in diabetes, macular degeneration, epilepsy, and Parkinson's disease. However, therapeutic approaches have also followed unexpected avenues, such as aiming to reprogram cancer cells into antigen-presenting immune cells. Leveraging the knowledge acquired through decades of basic research on the features and functions that characterize stem cells is now enabling the design of unexpected treatment options. These findings, emerging primarily through our understanding of the developmental trajectories that stem cells follow, have guided the choice of strategies deployed in the use and manipulation of isolated stem cells. We anticipate that reprogramming strategies for repair will open new avenues to generate cell types that have not been accessible or replaceable in disease until now. The inspiration from stem cells will hopefully continue to take us into a bright future to foster understanding and discovery of approaches for treatment. □

*Corresponding author. Email: magdalena.goetz@helmholtz-munich.de (M.G.); torres-padilla@helmholtz-muenchen.de (M.-E.T.-P.) Cite this article as M. Götz and M.-E. Torres-Padilla, *Science* **388**, eadp2959 (2025). DOI: 10.1126/science.adp2959

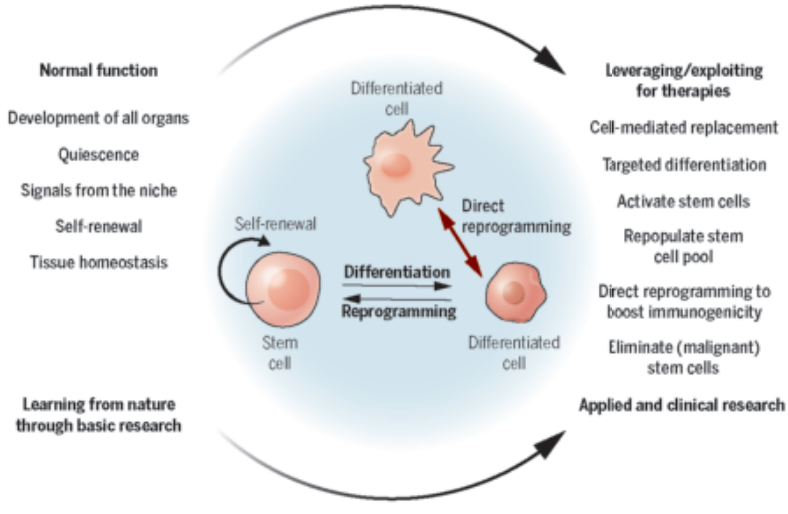

Uses of stem cells in research. Shown are the properties and uses of stem cells during natural development and tissue turnover and in applied and clinical research.

RESEARCH

IN *SCIENCE* JOURNALS

Edited by **Michael Funk**

PHOTO: WANDERLUSTER/ISTOCK PHOTO

PHYSIOLOGY

Pericytes protect brain capillaries from pressure

Increased intraluminal pressure in the brain elicits the constriction of arterioles, which is usually mediated by smooth muscle cells situated in arteriole walls. Ferris *et al.* found that in mouse brains, this role was extended to mural cells called pericytes that reside on the transitional blood vessel segments between arterioles and capillaries (see also the Focus by Earley). The constriction of transitional pericytes in response to increased intravascular pressure required the cation channel TRPC3, which is used in transitional pericytes but not smooth muscle cells. This channel is thus a potential target to alleviate impairments in cerebrovascular flow associated with aging or neurodegenerative diseases. —Wei Wong

Sci. Signal. (2025) 10.1126/scisignal.ads1903

CATALYSIS

Self-regenerating platinum catalysts

Spontaneous platinum dispersion to single atoms was observed for a zeolite containing a low loading of germanium. Hong *et al.* showed that this formed a highly active catalyst for propane dehydrogenation. After prolonged use, the oxidative removal of built-up carbon also redispersed platinum clusters that had formed back to single atoms. This self-regeneration was achieved for more than 110 reaction-regeneration cycles and, unlike commercial platinum-tin catalysts, did not require added chlorine. —Phil Szuromi

Science p. 497, 10.1126/science.adu6907

QUANTUM COMPUTING

Blind quantum computing with color centers

Quantum computers can outperform classical computers at certain tasks and offer

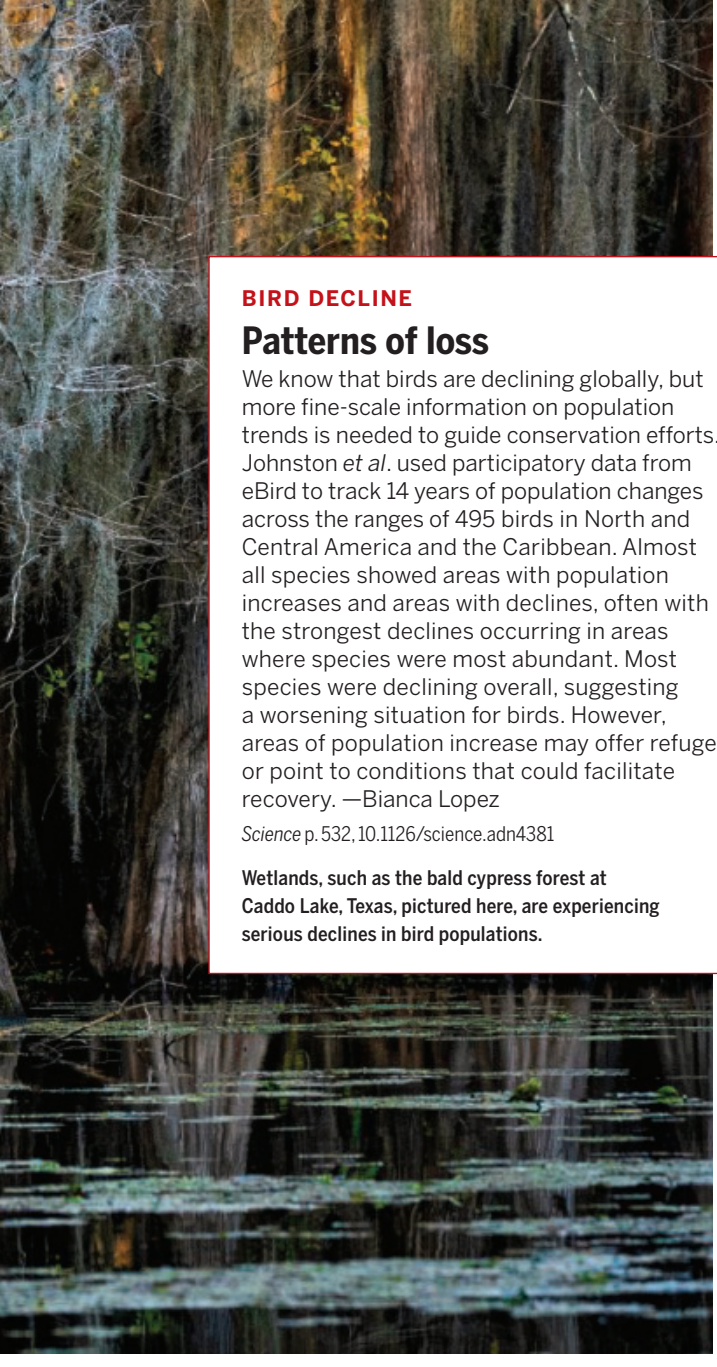

BIRD DECLINE

Patterns of loss

We know that birds are declining globally, but more fine-scale information on population trends is needed to guide conservation efforts. Johnston *et al*. used participatory data from eBird to track 14 years of population changes across the ranges of 495 birds in North and Central America and the Caribbean. Almost all species showed areas with population increases and areas with declines, often with the strongest declines occurring in areas where species were most abundant. Most species were declining overall, suggesting a worsening situation for birds. However, areas of population increase may offer refuge or point to conditions that could facilitate recovery. —Bianca Lopez

Science p. 532, 10.1126/science.adn4381

Wetlands, such as the bald cypress forest at Caddo Lake, Texas, pictured here, are experiencing serious declines in bird populations.

guaranteed security in terms of information communication. However, they are unlikely to be available as individual devices any time soon. Blind quantum computing would allow clients to run their algorithms on quantum servers that are housed in larger facilities without giving away any information about the requested task. Wei *et al*. demonstrate a small-scale blind quantum computing protocol using optically addressable silicon-vacancy centers. Exploiting the nuclear and electronic spin of the centers for storage and manipulation, the authors demonstrate a set of quantum gates and algorithms across their two-node network. This approach is promising for quantum computing over larger distributed networks. —Ian S. Osborne

Science p. 509, 10.1126/science.adu6894

MESOSCOPIC PHYSICS

Electron collisions

Electrons in solids can behave like waves, leading to the development of devices better known from optics, such as interferometers. Chakraborti *et al*. studied electron collisions in a graphene Mach-Zehnder interferometer. By measuring shot noise, the researchers were able to determine the degree of indistinguishability of the colliding electrons. Their findings may lead to improvements in quantum information processing using graphene devices. —Jelena Stajic

Science p. 492, 10.1126/science.adn4622

STRUCTURAL BIOLOGY

Homomeric quaternary RNA structures

Many RNAs fold into complex secondary and tertiary structures that are essential to their biological function. Quaternary structures, formed by the interaction of two RNA molecules, are much rarer. Wang *et al*. used cryo–electron microscopy to elucidate the global structures of four types of RNA molecules capable of homomeric self-assembly. The structures reveal the specific interactions that facilitate the association of two identical RNA molecules and elucidate the mechanisms by which multiple identical RNA molecules assemble to form cage-like structures with hollow centers. The findings demonstrate that the morphology and dimensions of these cages are determined by the number of interaction sites, as well as the shape and flexibility of individual molecules. —Di Jiang

Science p. 545, 10.1126/science.adv3451

OCEANOGRAPHY

Oceans unseen

Despite remarkable improvements in our ability to map the topography of the ocean floor using modern satellite altimetry, such datasets are not as valuable as visual observations for interdisciplinary scientific exploration of the deep ocean. Bell *et al.* reviewed the state of observational science in the deep oceans worldwide and concluded that we have visually observed less than 0.001% of the deep oceans, an area less than one-tenth the size of Belgium. Because oceans cover 66% of our planet's surface, this spatially biased knowledge prohibits a global understanding of deep ocean biogeography and benthic ecosystem functions. —Kip V. Hodges

Sci. Adv. (2025) 10.1126/sciadv.adp8602

TINNITUS

Sound insights

Direct objective measures of aberrant auditory processing disorders such as tinnitus (ringing of the ears) and hypersensitivity to sound (hyperacusis) are difficult to obtain because current measures rely on subjective questionnaires. Smith *et al*. have now identified objective autonomic signatures for chronic tinnitus and auditory hypersensitivity. They found subtle pupil dilation and facial movements elicited by different sounds in individuals with tinnitus and sound hypersensitivity compared with a neurotypical control group. These objective measures were able to predict the individual tinnitus and hyperacusis severity scores of study participants obtained using two standard self-report questionnaires. —Orla Smith

Sci. Transl. Med. (2025) 10.1126/scitranslmed.adp1934

CATALYSIS

Hydrogen boosts selective oxidation

Modification of platinum single-atom sites on cerium dioxide creates hydride-modified and hydroxylated sites, improving reactivity. Yang *et al*. showed that these species formed at Pt^{2+}–Ce^{3+} pair sites on the ceria support after a mild hydrogen reduction at 200°C. The authors observed higher conversion for carbon monoxide oxidation in hydrogen and higher selectivity for propylene in the oxidative dehydrogenation of propane relative to platinum single-site catalysts. —Phil Szuromi

Science p. 514, 10.1126/science.adv0735

Edited by **Corinne Simonti** *and* **Jesse Smith**

DIET

Another reason to eat your veggies

As people approach the age of 50, do their dietary choices at this time still affect their physical health by age 70? Tessier *et al.* collated food frequency questionnaires from more than 100,000 medical professionals across two longitudinal studies. The authors examined their consumption of more than 130 different foods for up to 30 years. They found that healthier diets during adulthood were associated with "healthy aging," that is, reaching age 70 free of cognitive impairments, mental health challenges, hypertension, heart disease, and diabetes. Higher adherence to plant-based diets, nuts, fruits, and whole grains was associated with healthy aging, supporting current widely accepted dietary recommendations. —Ekeoma Uzogara

Nat. Med. (2025)
10.1038/s41591-025-03570-5

PLANT DEVELOPMENT

Layers interact to develop shape

Plant cells are physically connected by cell wall material, meaning that layers of tissue mechanically interact during growth and development. Silveira *et al.* used the *Arabidopsis* anther as a model to understand how inner cell layers affect the tension of the outer epidermis. The authors analyzed growth patterns and inferred the elastic modulus of plant cell walls by imaging combined with finite element methods. They found that anther lobes initiate by softening inner tissue cell walls, and that these cells remain larger than the epidermis, promoting subsequent growth and shape generation. The work clarifies the role of inner tissues in driving plant organ growth and are in contrast to previous assumptions that the epidermis governs tissue expansion. —Madeleine Seale

Nat. Plants (2025)
10.1038/s41477-025-01944-8

NEUROIMMUNOLOGY

Linking inflammation to behavior

Cytokines are released by immune cells to coordinate their inflammatory responses, but these molecules may also modulate the brain. Lee *et al*. found that mice had a subpopulation of neurons that could respond to the proinflammatory interleukin-17 (IL-17) family of cytokines, as well as the anti-inflammatory cytokine IL-10. IL-17A and IL-17C increased the excitability of these neurons and promoted anxiety behavior in mice. By contrast, signals from IL-10 could decrease neuronal firing, suggesting that it might function to decrease anxiety. Thus, signals from proinflammatory cytokines could act to synchronize the immune response with behaviors that are beneficial to fighting infection or preventing the spread of disease, and anti-inflammatory cytokines could decrease as inflammation resolves. —Sarah H. Ross

Cell (2025)
10.1016/j.cell.2025.03.005

LITHIUM CATHODES

Visualizing crack evolution

Nanoscale cracks are widely observed in lithium (Li)-ion battery cathode particles during operation. Understanding their formation, evolution, and resulting influence on Li-ion diffusion is critical for battery optimization but remains challenging. Nam *et al.* investigated this direction using operando scanning transmission soft x-ray microscopy to track the morphological evolution of individual $LiFePO_4$ (LFP) particles, a widely used phase-separating cathode material in industry. Their study reveals that Li-ion insertion at the edges of LFP particles induces strong tensile stress in the core, triggering nanocrack formation. The newly exposed surfaces near the cracks facilitate faster Li-ion (de)insertion compared with the particle edges. This reaction heterogeneity ultimately leads to repetitive crack opening during delithiation (charging) and crack closing during lithiation (discharging). —Jack Huang

ACS Nano (2025)
10.1021/acsnano.4c15960

MECHANICAL METAMATERIAL

Snapping out of the norm

Stretching a rubber band far beyond its elastic limit causes snapping, followed by a large displacement in the same direction as the applied force. In contrast to this common observation is countersnapping, in which a structure responds in a direction opposite to that of the applied force. This unusual behavior has previously only been confirmed theoretically. Ducarme *et al.* experimentally demonstrated countersnapping by designing a modular structure, which consists of three different building blocks with nonlinear mechanical responses. The mechanical metamaterial exhibited a two-step contraction when pulled beyond the critical limit and a soft-to-stiff transition under oscillation. These exotic mechanical responses could be useful for precision actuators and soft robotics. —Sumin Jin

Proc. Natl. Acad. Sci. U.S.A. (2025)
10.1073/pnas.2423301122

SCIENCE AND RELIGION

Moral concerns limit support for science

The first direct evidence of US public beliefs about the morality of scientists can help to explain religious heterogeneity in public support for science. Survey data used by O'Brien and Noy included measures of beliefs about scientists' moral values, such as fairness and compassion. The least skeptical views of scientists' character were reported by agnostics and atheists. To varying degrees, actively religious people were more critical, with conservative Protestants being the most critical. These findings persisted when controlling for various respondent characteristics, such as their scientific knowledge and political ideology. —Brad Wible

Am. Sociol. Rev. (2025)
10.1177/00031224251316904

SLEEP

Birds trade vigilance for rest

Birds exhibit two types of non-REM sleep: symmetric (both brain hemispheres sleeping deeply) and asymmetric (one hemisphere sleeping lightly while the other stays alert). van Hasselt *et al.* investigated how birds balance these sleep modes under increased sleep pressure caused by deprivation. Using high-density EEG on European jackdaws, researchers found that during heightened sleep need, birds prioritize symmetric sleep over asymmetric sleep, sacrificing vigilance to recover from sleep loss. This trade-off highlights the constraints imposed by the need for deep, restorative sleep on the birds' ability to remain alert for potential threats. —Di Jiang

Curr. Biol. (2025
10.1016/j.cub.2025.03.008

RESEARCH ARTICLE SUMMARY

CHEMICAL BIOLOGY

Intracellular protein editing enables incorporation of noncanonical residues in endogenous proteins

Jenna N. Beyer, Yevgeniy V. Serebrenik, Kaitlyn Toy, Mohd. Altaf Najar, Emily Feierman, Nicole R. Raniszewski, Erica Korb, Ophir Shalem*, George M. Burslem*

Full article and list of author affiliations: https://doi.org/10.1126/science.adr5499

INTRODUCTION: The study of proteins in situ in mammalian cells is essential to advance our understanding of eukaryotic cell biology. To study proteins in live mammalian cells, an experimental handle is required to track or control a protein of interest throughout experiments. Often, this requires the addition of amino acids—ranging from relatively small peptides to larger fusion proteins—to the target protein. These tags have revolutionized the study of proteins in cells but have limitations: Tags can influence the properties of target proteins and largely lack temporal resolution for studying dynamic processes. Chemical labels benefit from their small size and diversity beyond genetically encodable residues, yet they remain difficult to apply to proteins in mammalian cells. It is clear that new technologies are needed to label and manipulate proteins in live mammalian cells.

RATIONALE: Motivated by recent advances in chemical biology and gene editing, we envisioned a technology that could enable the posttranslational editing of protein primary sequences inside mammalian cells, including endogenous proteins that best represent native biology. This system would facilitate splicing of an exogenous protein segment into a target protein at a user-defined site, with temporal control and access to useful labels and noncanonical amino acids. To achieve this goal, we designed a system for intracellular protein editing that relies on two pairs of split intein proteins, which individually ligate polypeptide chains. Used in tandem, these split inteins enable the editing of a donor peptide into an acceptor site situated internally within a target protein. The acceptor sequence is inserted into a target protein—either an endogenous protein through genome editing or an exogenously expressed protein. The corresponding donor protein is generated recombinantly, allowing the incorporation of noncanonical amino acids at scale and chemical labeling, if desired. The donor protein is delivered into live mammalian cells and results in the rapid editing of the donor into the target protein.

RESULTS: We first demonstrate a general editing approach, where a generic and minimal donor containing an epitope tag is edited into model proteins calnexin and β-actin. We confirmed the editing of the primary protein sequence using immunoblotting, fluorescence microscopy, and mass spectrometry–based proteomics. Temporal characterization reveals that editing occurs within 10 min of donor protein delivery, which enables experiments on biologically relevant timescales. We demonstrate a sequence-specific mode of editing, where the transcription factor c-Myc and kinase Chk1 are edited nearly tracelessly, enabling time-resolved studies of these dynamic proteins. Further, we show that Chk1 and c-Myc remain functional after editing using proteomic and transcriptomic approaches, which validates our protein editing technology as near-traceless and minimally perturbing.

Additionally, genetic code expansion in *Escherichia coli* was used to encode the noncanonical amino acid and click chemistry handle *p*-azido-phenylalanine (pAzF) into the donor protein before labeling with small molecules. We then edited small-molecule fluorophores or biotin into endogenous calnexin, enabling microscopy and pull-down studies of the endogenous protein without the use of antibodies.

CONCLUSION: Our work establishes a method for editing the primary amino acid sequence of proteins in live mammalian cells. This approach enables the site-specific editing of noncanonical amino acids and useful labels into target proteins, including endogenous proteins. Ultimately, this enables the labeling and manipulation of proteins in a nondisruptive and temporally resolved fashion. This protein editing method represents a useful and widely applicable addition to the repertoire of technologies for studying proteins in mammalian cells, offering the potential to edit, manipulate, and observe nearly limitless target proteins across diverse applications. □

*Corresponding author. Email: shalemo@upenn.edu (O.S.); george.burslem@pennmedicine.upenn.edu (G.M.B.) Cite this article as J. N. Beyer *et al.*, *Science* **388**, eadr5499 (2025). DOI: 10.1126/science.adr5499

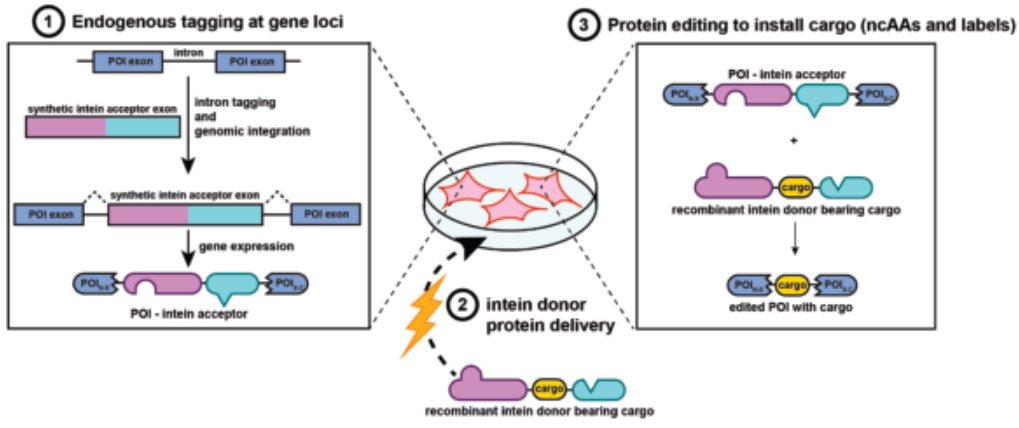

Intracellular protein editing. Intracellular protein editing of an endogenous protein of interest (POI) is enabled by a combination of (1) endogenous gene tagging, (2) delivery of a cargo donor protein, and (3) tandem intein trans-splicing to produce a new polypeptide bearing the cargo. ncAAs, noncanonical amino acids.

RESEARCH ARTICLE SUMMARY

MOLECULAR BIOLOGY

TIGR-Tas: A family of modular RNA-guided DNA-targeting systems in prokaryotes and their viruses

Guilhem Faure†, Makoto Saito†, Max E. Wilkinson†, Natalia Quinones-Olvera, Peiyu Xu, Daniel Flam-Shepherd, Stephanie Kim, Nishith Reddy, Shiyou Zhu, Lilia Evgeniou, Eugene V. Koonin, Rhiannon K. Macrae, Feng Zhang*

Full article and list of author affiliations: https://doi.org/10.1126/science.adv9789

INTRODUCTION: RNA-guided systems allow single proteins (or complexes of proteins) to interact with many different target nucleic acid sequences by varying the portion of the RNA guide that is complementary to the target. In nature, RNA-guided systems have many functions, including prokaryotic adaptive immunity against invading mobile genetic elements (provided by CRISPR systems), gene regulation (provided by various classes of small RNAs), and nucleic acid modification [provided by small nucleolar RNAs (snoRNAs)]. Many of these systems, particularly CRISPR, have been developed into biotechnologies for modifying and modulating the genome and transcriptome and are being used as therapeutics.

RATIONALE: Several new RNA-guided systems have been discovered on the basis of their evolutionary relationship to CRISPR systems. However, many RNA-guided systems remain undiscovered owing to limitations in evolutionary-based searches. To address this, we combined structural mining, sequence profiling, and large-language model clustering techniques to identify RNA-guided systems unrelated to CRISPR.

RESULTS: Starting from the RNA binding domain in *Streptococcus pyogenes* Cas9 (SpCas9), we used comparative structural analysis to search for similar regions. This approach identified the nucleolar protein (Nop) domain, a conserved RNA binding fold present in IS110 recombinases, box C/D small nucleolar ribonucleoproteins (snoRNPs), and Prp31 splicing factors. Further mining uncovered a family of RNA-guided DNA-targeting systems in bacteriophages, archaeal viruses, and parasitic bacteria, which we named tandem interspaced guide RNA (TIGR)–TIGR-associated (Tas) systems.

TIGR-Tas systems are modular both in their guide and effector. The guides, called tigRNAs, are encoded in arrays that contain two spacers (A and B) arranged in tandem and separated either by conserved sequences or secondary structures. Tas proteins all share a Nop domain, but some Tas proteins contain a nuclease domain, whereas others are associated with potential effector proteins. Using cryo–electron microscopy, we resolved the structure of a RuvC nuclease–containing Tas protein, TasR, from *Thermoproteota archaeon isolate LB_CRA_1*. The structure shows that the RuvC domain is largely separate from the core Nop domain, suggesting that it may be replaced with other functional domains in other systems. TasR cleaves DNA by using a distinctive targeting mechanism, wherein the spacers of tigRNAs specify the target by acting in tandem, with spacer A pairing to one strand of the target and spacer B pairing to the other strand. We also find striking similarities in TIGR-Tas systems to box C/D snoRNPs and IS110 RNA-guided transposases, suggesting an evolutionary connection among RNA-guided mechanisms across different domains of life.

CONCLUSION: Their compact and modular structure, tandem guide RNA, and lack of target motif constraints distinguish TIGR-Tas from other RNA-guided systems and may allow for more flexible and precise genome-editing applications. We demonstrate that TasR can edit targeted loci in the human genome, highlighting its potential for further biotechnological development. Although we do not yet know the biological function of TIGR-Tas systems, they may play roles in viral defense or competition, genome regulation, or as-yet-undiscovered processes, and their arrays raise the possibility of an RNA-based memory system. □

*Corresponding author. Email: zhang@broadinstitute.org †These authors contributed equally to this work. Cite this article as G. Faure *et al.*, *Science* **388**, eadv9789 (2025). DOI: 10.1126/science.adv9789

TIGR-Tas systems are modular RNA-guided systems. Comparison of the properties of CRISPR-Cas9 and TIGR-Tas RNA-guided systems.

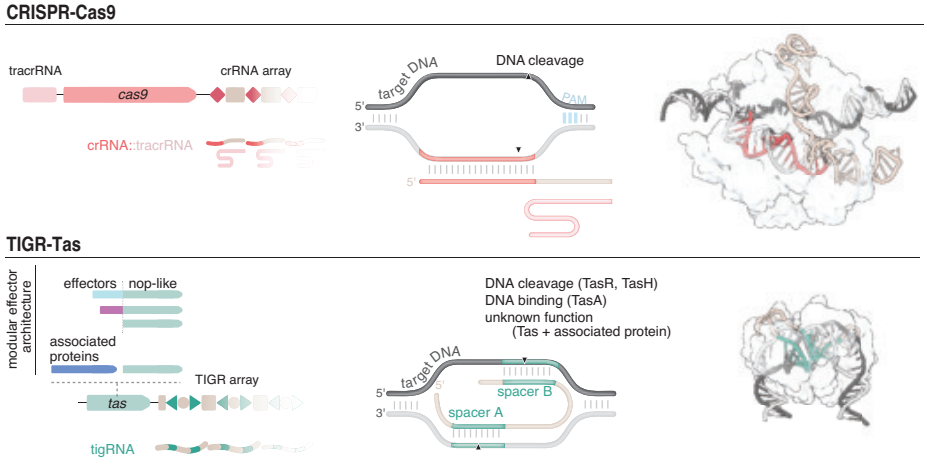

RESEARCH ARTICLE SUMMARY

LIPID SIGNALING

Metabolic signaling of ceramides through the FPR2 receptor inhibits adipocyte thermogenesis

Hui Lin†, Chuanshun Ma†, Kui Cai†, Lulu Guo†, Xuemei Wang†, Lin Lv†, Chao Zhang†, Jun Lin†, Daolai Zhang, Chuan Ye, Tengwei Wang, Shenming Huang, Jifei Han, Zihao Zhang, Junyan Gao, Mingxiang Zhang, Zhao Pu, Fengyang Li, Yongyuan Guo, Xiaojun Zhou, Chengxue Qin, Fan Yi, Xiao Yu*, Wei Kong*, Changtao Jiang*, Jin-Peng Sun*

Full article and list of author affiliations: https://doi.org/10.1126/science.ado4188

INTRODUCTION: Ceramides, comprising a conserved sphingosine base amide linked to a fatty acid chain of variable carbon lengths, are essential cell membrane lipids and metabolic messengers. The increased endogenous ceramides levels are associated with pathological development in various chronic diseases, including but not limited to type 2 diabetes mellitus, obesity, hepatic steatosis, and autoimmune diseases. Historically, ceramide research has focused predominantly on intracellular mechanisms, leaving receptor-mediated transmembrane signaling less explored.

RATIONALE: Recent studies have identified ceramide as a key mediator of interorgan effects that may involve transmembrane signaling. However, whether there are specific membrane receptors that sense ceramides is unknown. Moreover, the signaling mechanisms by which ceramides regulate cells in target tissues, such as adipocytes, remain unclear. We observed that the exogenous application of C16:0 ceramide inhibited fat thermogenesis and decreased intracellular cyclic adenosine monophosphate (cAMP) levels. We therefore hypothesized that a G_i-coupled receptor mediates the acute effects of ceramide in adipose tissue. Unbiased screening of receptors associated with G_i signaling was performed to identify ceramide receptors in adipocytes.

RESULTS: By screening the top 60 G protein–coupled receptors (GPCRs) expressed in adipocytes, we determined that formyl peptide receptor 2 (FPR2), a class A GPCR, is the G_i-coupled ceramide receptor in adipocytes. Fluorescein arsenical hairpin–bioluminescence resonance energy transfer (FlAsH-BRET) sensor assays, activity measurements, and radioligand binding assays revealed a direct interaction between ceramides and FPR2. Further functional characterization of FPR2 deficiency in adipocyte-specific *Fpr2*–conditional knockout mice indicated that the ceramide-FPR2-G_i signaling axis plays a central role in the ceramide-induced reduction in adipose thermogenesis. Additionally, FPR2 recognizes only specific types of ceramides, and receptors that are phylogenetically related to FPR2, such as FPR1 or FPR3, are not activated by ceramides. To reveal the underlying mechanisms, we solved the structures of the C16:0-FPR2-G_{i1}, C18:0-FPR2-G_{i1}, and C20:0-FPR2-G_{i1} complexes through cryo–electron microscopy (cryo-EM). The structures revealed that ceramides bind within the orthosteric ligand pocket of FPR2. The $H102^{3.29}F178^{ECL2}$ hydrophobic motif and the $E89^{ECL1}T177^{ECL2}D281^{7.32}$ polar motif of FPR2 were found to be essential for the recognition of the C=C double bond of the fatty acid chain and the carboxylated sphingoid group of ceramides. Most notably, the back mutants FPR1-$G89^{ECL1}$E and FPR3-$A198^{5.35}$L-$H205^{5.42}$R converted these two receptors from inactive to active in response to ceramide stimulation.

CONCLUSION: Our results revealed that FPR2, a G_i-coupled ceramide receptor, mediates the inhibitory effect on adipocyte thermogenesis by sensing ceramide and decreasing intracellular cAMP levels.

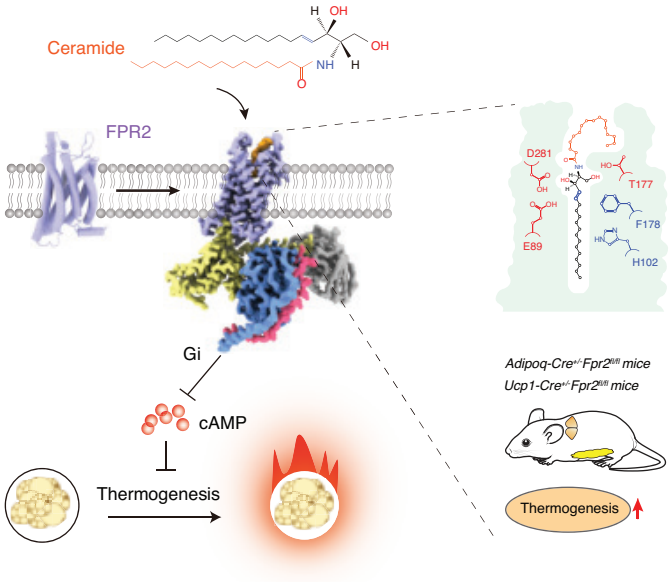

Membrane receptor FPR2 senses ceramides to regulate adipogenic thermogenesis. Ceramide-activated FPR2 in adipocytes stimulates G_i signaling and inhibits adipose thermogenesis. The adipocyte-specific *Fpr2*–conditional knockout mice abolish the inhibitory effects of ceramides. Structural analysis through cryo-EM revealed that FPR2 specifically recognized the C=C double bond and the carboxylated sphingoid group of the ceramide through the $H102^{3.29}F178^{ECL2}$ and $E89^{ECL1}T177^{ECL2}D281^{7.32}$ motifs, respectively. Single-letter abbreviations for the amino acid residues referenced throughout this study are as follows: H, His; F, Phe; E, Glu; T, Thr; D, Asp; A, Ala; L, Leu; R, Arg; G, Gly.

Structural analysis revealed key features of FPR2, including a hydrophobic ligand-binding pocket and polar interaction motifs, that enable the selective recognition of ceramides, particularly C16:0, C18:0, and C20:0, while excluding very-long-chain or unsaturated ceramides. The identification of FPR2 as a selective ceramide receptor not only provides a foundation for developing targeted therapies for obesity and related metabolic disorders associated with elevated plasma ceramide levels but also suggests that the interaction of ceramides with membrane receptors may play important roles in ceramide biology. □

*Corresponding author. Email: sunjinpeng@sdu.edu.cn (J.-P.S.); jiangchangtao@bjmu.edu.cn (C.J.); kongw@bjmu.edu.cn (W.K.); yuxiao@sdu.edu.cn (X.Y.) †These authors contributed equally to this work. **Cite this article as H. Lin *et al.*, *Science* 388, eado4188 (2025). DOI: 10.1126/science.ado4188**

RESEARCH ARTICLE SUMMARY

CELL BIOLOGY

Interphase cell morphology defines the mode, symmetry, and outcome of mitosis

Holly E. Lovegrove*†, Georgia E. Hulmes†, Sabrina Ghadaouia, Christopher Revell, Marta Giralt-Pujol, Zain Alhashem, Andreia Pena, Damian D. Nogare, Ellen Appleton, Guilherme Costa, Richard L. Mort, Christoph Ballestrem, Gareth W. Jones, Cerys S. Manning, Ajay B. Chitnis, Claudio A. Franco, Claudia Linker, Katie Bentley, Shane P. Herbert*

Full article and list of author affiliations: https://doi.org/10.1126/science.adu9628

INTRODUCTION: Tissue formation requires the concerted coordination of diverse cellular processes. For example, the major shifts in cell shape that define tissue architecture frequently occur concomitant with the asymmetric cell divisions that generate tissue heterogeneity. Tight spatiotemporal coupling of distinct morphogenetic events is thus critical to achieving robust tissue assembly.

RATIONALE: In addition to sculpting tissue form, cell shape remodeling also plays a fundamental role in the control of cell division. Upon mitotic entry, metazoan cells typically adopt a spherical shape following global reorganization of the interphase cytoskeleton. This mitotic rounding both promotes high-fidelity segregation of genetic material and generation of equally sized daughters that symmetrically partition most nongenetic cellular components. Thus, modulation of mitotic rounding would represent an elegant means to switch cells from a symmetric to asymmetric division outcome. However, whether cells have the capacity to tune the extent of their mitotic rounding and how this would influence mitotic symmetry and/or daughter identity remains unclear. Moreover, whether prior shifts in interphase cell morphology have any impact on the extent of mitotic shape remodeling or symmetry of division remains unexplored. We hypothesized that, if shifts in interphase cell morphology can indeed affect mitotic shape remodeling, this could explain the close coupling of morphogenetic shape change with the switches in the symmetry of division observed during tissue building.

RESULTS: To investigate the codependence of interphase and mitotic cell shape dynamics, we exploited single-cell morphometric analyses of tissue formation in multiple contexts, including blood vessel and neural crest development. These analyses revealed that stereotyped shifts in pre-mitotic cell morphology act as conserved instructive cues that tune the mode, symmetry, and outcome of mitosis. We identified that distinct shifts in mesenchymal-like cell morphology switch cells to an "isomorphic" mode of division, which uncharacteristically evades mitotic rounding and preserves pre-mitotic cell morphology throughout division. Using a combination of micropatterning tools and in vivo live imaging, we revealed that preservation of asymmetries in interphase cell morphology during division also resulted in the maintenance of asymmetric distributions of key signaling factors. Specifically, we found that during isomorphic divisions, Rab4-positive recycling endosomes and their fate-determinant cargo were asymmetrically inherited, thereby generating daughters of differing identities.

CONCLUSION: These observations uncovered dynamic modulation of the extent of mitotic rounding as a previously unknown trigger for asymmetric cell division. In contrast to the current view, this data suggests that mitotic cell rounding is far from a universal feature of mesenchymal-like cell division and is often elegantly tuned by pre-mitotic cell morphology. Moreover, we identified that cells exploit this phenomenon to functionally couple shifts in interphase shape to the induction of distinct daughter cell identities and behaviours, thereby directing tissue assembly. Thus, morphogenetic cell shape change not only sculpts tissue form but concomitantly generates the cellular diversity underpinning tissue building. Considering that most mesenchymal-like cells exhibit equivalent shape dynamics during tissue remodeling, including metastatic cancer cells, instructive cues encoded in interphase morphology are likely an underappreciated and conserved modulator of mitotic symmetry and cell state heterogeneity in diverse tissue contexts. □

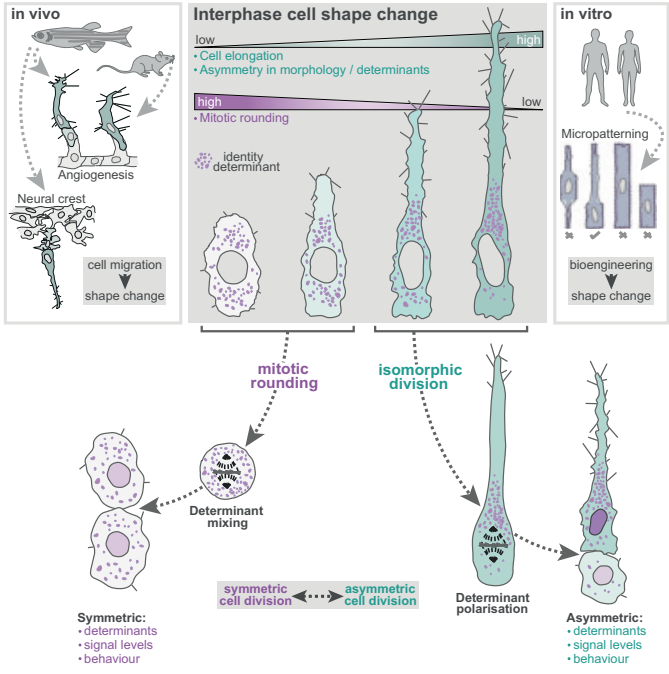

Shifts in interphase cell morphology tune the mode and symmetry of mitosis. Elongation of cells as they migrate in vivo, or upon micropatterning in vitro, switches cells to a newly defined isomorphic mode of division. In isomorphic divisions, cells uncharacteristically retain pre-mitotic asymmetries in morphology and fate determinant positioning throughout mitosis. Consequently, isomorphic division fundamentally couples interphase shape change to induction of symmetric cell divisions.

*Corresponding author. Email: shane.herbert@manchester.ac.uk (S.P.H.); holly.lovegrove@manchester.ac.uk (H.E.L.) †These authors contributed equally to this work. Cite this article as H. E. Lovegrove *et al.*, *Science* **388**, eadu9628 (2025). DOI: 10.1126/science.adu9628

RESEARCH ARTICLE SUMMARY

GUT FUNGI

A symbiotic filamentous gut fungus ameliorates MASH via a secondary metabolite–CerS6–ceramide axis

Shuang Zhou†, Meng Li†, Pengcheng Wang†, Chenghao Guo, Jinxin Zhang, Xi Luo, Yu-Chen Fan, En-Qiang Chen, Xingshun Qi, Jinjun Chen, Lechi Ye, Hai-Yang Yuan, Wen-Bing Yin, Kai Wang*, Ming-Hua Zheng*, Yanli Pang*, Jie Qiao*, Changtao Jiang*

Full article and list of author affiliations: https://doi.org/10.1126/science.adp5540

INTRODUCTION: Components of the gut microbiota are known to be associated with human metabolic diseases. Of microbial factors that influence human health, gut bacteria are the most highly relevant for metabolic diseases. Although fungi are increasingly recognized as important members of the gut community, the role of fungal symbionts in host health and diseases and the underlying molecular mechanisms are still unknown. Optimizing culture techniques and medium composition for gut fungi is essential for understanding intestinal microecology and will yield deeper insights into host-gut microbiota cross-talk.

RATIONALE: To identify the role of fungal gut symbionts, we developed a culture method based on in situ fecal environment incubation. We used this system to show that the filamentous fungi *Fusarium* spp. can acclimate to an anaerobic environment and establish stable colonization in mice. We discovered that this fungus was internationally ubiquitous in sequencing data of human feces. Hence, we investigated whether gut fungi play a role in host disease and particularly in metabolic dysfunction–associated steatohepatitis (MASH) progression in mouse models.

RESULTS: We designed a fungal isolation chip (FiChip)–based optimized in situ cultivation system for gut fungi (FOCUS-G), which helps obtain more unartificial and uncultured fungi. Using FOCUS-G, we systematically isolated 2137 fungal strains from fecal samples of volunteers from five different geographical areas within China. Using oxygen adaptability tests for gut fungal isolates, we characterized *Fusarium* spp. as a group of intestinal filamentous fungi that can acclimate to the anaerobic conditions that prevail in the colon. An analysis of internal transcribed spacer (ITS) data from global intestinal fungal studies confirmed that *Fusarium foetens* is commonly found in the gut of various human populations. We showed that the colons of germ-free and specific pathogen–free mice could be colonized by *F. foetens* with a single oral gavage.

We found that *F. foetens* gavage improves MASH progression in mice by altering ceramide metabolism through the inhibition of CerS6, a key enzyme in the ceramide biosynthetic pathway. We validated the role of CerS6 in *F. foetens*–mediated amelioration of MASH in mice by intestinal-specific *Cers6* deletion and overexpression.

We used chromatographic analyses to show that *F. foetens* produces a secondary metabolite, FF-C1, that inhibits CerS6 activity through direct, noncompetitive binding. We showed that FF-C1 improves MASH progression and disease outcome in $Cers6^{fl/fl}$ mice but not in $Cers6^{\Delta IE}$ mice.

CONCLUSION: We developed a culture method based on in situ fecal environmental incubation and identified *Fusarium* spp. as a group of intestinal filamentous fungi that can acclimate to an anaerobic environment. *F. foetens* colonization reverses MASH progression in mouse models through a secondary metabolite FF-C1, which inhibits intestinal CerS6 to reduce serum levels of ceramides. Collectively, our findings provide a deeper insight into the biology of host-commensal fungi interactions and indicate that a fungal secondary metabolite can influence clinically relevant host metabolic pathways, offering an investigative strategy for improving the therapeutic management of such diseases. □

*Corresponding author. Email: jiangchangtao@bjmu.edu.cn (C.J.); jie.qiao@263.net (J.Q.); yanlipang@bjmu.edu.cn (Y.P.); zhengmh@wmu.edu.cn (M.-H.Z.); wangkai@bjmu.edu.cn (K.W.) †These authors contributed equally to this work. **Cite this article as S. Zhou *et al.*, *Science* 388, eadp5540 (2025). DOI: 10.1126/science.adp5540**

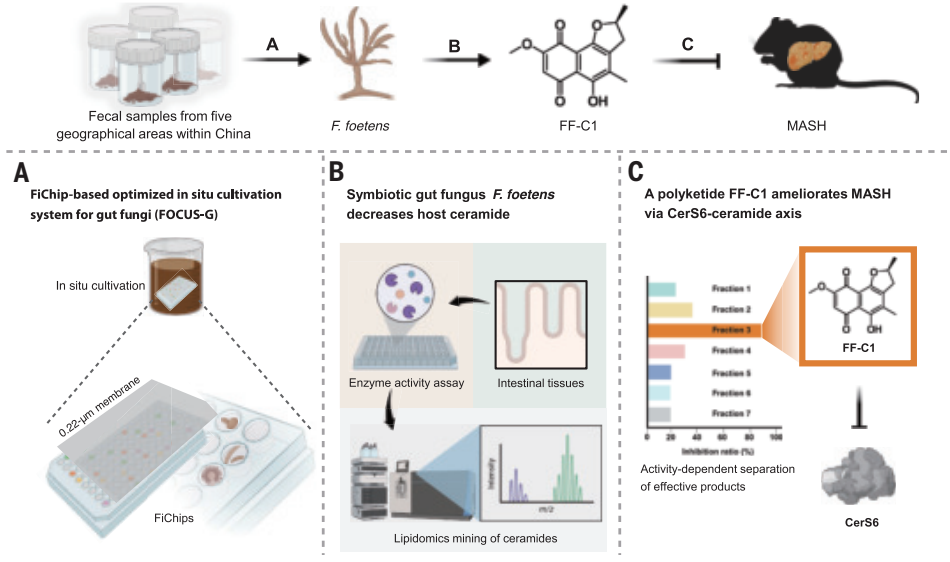

Identification of gut fungi–mediated regulation of host metabolic disease. Identification of gut fungi is important to clarify their roles in health and disease. (**A**) FOCUS-G identified *Fusarium* spp. as symbiotic fungi that can acclimate to anaerobic conditions found in the host colon. (**B** and **C**) Intestinal tissue enzyme-activity analysis and bioactive-guided separation showed that *F. foetens* reverses metabolic dysfunction–associated fatty liver (MAFL)–MASH progression by producing the secondary metabolite FF-C1, which inhibited intestinal CerS6 activity and reduced serum levels of ceramides in mice.

MESOSCOPIC PHYSICS

Electron collision in a two-path graphene interferometer

H. Chakraborti[1]†, L. Pugliese[1]†, A. Assouline[1]‡, K. Watanabe[2], T. Taniguchi[2], N. Kumada[3], D. C. Glattli[1], M. Jo[1]§, H.-S. Sim[4]*, P. Roulleau[1]*

The collision of two electrons at a beam splitter provides a method for studying their coherence and indistinguishability. Its realization requires the on-demand generation and synchronization of single electrons. In this work, we demonstrate the coherent collision of single electrons, generated by voltage pulses, in a graphene Mach-Zehnder interferometer. By measuring shot noise resulting from the collisions, we unveil fundamental characteristics of colliding electrons, highlighting the complementarity between the indistinguishable and distinguishable parts of their wave functions. The former is manifested through fermionic Hong-Ou-Mandel destructive interference, whereas the latter is discerned through double-winding Aharonov-Bohm interference in the noise. The interference visibilities of around 60% enable comprehensive quantum state tomography. Our findings may place coherent operations involving flying qubits within reach in graphene.

Coherent manipulation of single particles enables us to explore their wave nature and exploit it for quantum information processing. In particular, the scattering of single particles at beam splitters is a fundamental building block for generating single-particle or multiparticle interferences (*1*–*3*), providing valuable insights into the quantum statistics of identical particles, such as bosons, fermions, and anyons (*4*–*11*), as well as quantum entanglement among them (*12*). When two indistinguishable electrons collide at a beam splitter, antibunching occurs (*13*, *14*), manifesting as the fermionic analog of the Hong-Ou-Mandel (HOM) effect (*4*). This effect results from the fermionic statistics, where the wave functions of two identical fermions satisfy $\Psi(1,2) = e^{i\theta_s}\Psi(2,1)$ with $\theta_s = \pi$, when the positions of the fermions are exchanged. This collision process can be extended to dynamical generation of orbital entanglement and subsequent detection of its quantum nonlocality (*12*). Furthermore, the collision process is a key element of a quantum state tomography (*15*). In this protocol, a target electron wave packet collides with a small coherent field consisting of electron-hole pairs, and the target state is reconstructed from two-electron interference involving exchange between the target electron and the electron-hole pairs. Demonstrating the collision of two electrons is therefore a milestone in the realization of "flying qubits" for electron quantum optics, where a propagating single-electron wave packet carries information encoded in its orbital degree of freedom. This requires electron sources (*13*, *16*) emitting coherent single-electron wave packets, precise control of the emission energy and timing, manipulation of a beam splitter, and measurement of collision states through shot noise. Additionally, it demands ballistic channels for wave packet propagation that are robust against noise and decoherence. Recently, there have been advancements in electron Mach-Zehnder or Fabry-Perot interferometers in graphene (*17*–*21*). These cutting-edge interferometers showed single-particle Aharonov-Bohm interference persisting even at high electron temperatures of 2 K and voltages of 1 mV, which suggests that graphene is a promising platform for flying qubits.

In this work, we report a two-electron collision in a two-path interferometer. We integrate on-demand manipulation of dynamical electron excitations, an electronic Mach-Zehnder interferometer (MZI), and detection of the fermionic HOM interference in a graphene quantum Hall device. The dynamical electron excitations are generated by applying voltage pulses simultaneously to a pair of electrical contacts, with precise control of the time delay between the pulses. These excitations propagate along quantum Hall edge channels and collide at the MZI. The resulting fluctuations of electrical current or shot noise, measured as a function of the time delay and the magnetic flux enclosed by the MZI, unveil the following fundamental aspects of two-electron collision.

The noise shows the HOM oscillation as a function of the time delay. It exhibits a minimum value at zero time delay, when the two excitations simultaneously reach the MZI. The minimum results from a destructive two-electron interference, a consequence of the fermionic exchange statistics and the indistinguishability between the two colliding excitations; the minimum value is independent of the magnetic flux enclosed by the MZI. By contrast, when the time delay is such that the two excitations are maximally distinguishable, the HOM noise shows a maximum. The maximum value depends on the flux in the MZI and shows $h/2e$ Aharonov-Bohm oscillations, where h is the Planck constant and e is the electron charge. This single-electron interference results from the distinguishable part of the colliding excitations, and the $h/2e$ oscillations indicate "double winding" of an electron around the Aharonov-Bohm flux that happens with the help of an auxiliary hole when the electron is detected in the noise—a two-particle observable. The HOM and $h/2e$ oscillations offer the witness of the full (two-particle and single-particle, respectively) coherence structure of the collision. Finally, we demonstrate the quantum state tomography of a Leviton (a clean electron excitation carrying no extra electron-hole pairs), further underlining the potential of our graphene setup for quantum information processing.

HOM experiment

The sample used is a monolayer graphene quantum Hall pn junction (Fig. 1A). A global graphite gate and a metallic top gate (top G) on the right half of the sample allow us to independently tune the filling factors on the left and right halves. In the n (left half) and p (right half) regions, the filling factors are set to $\upsilon_N = 2$ and $\upsilon_P = -2$, respectively. As a result, in each of the p and n regions, two channels flow along the top physical edge of the graphene sample from a source contact toward the pn interface; another pair of channels flows along the bottom edge from the pn interface toward a drain contact. Along the pn interface, four channels copropagate. Two side gates, SG_1 and SG_2, positioned at the top and bottom intersections between the pn interface and the physical edges, respectively, serve as (top and bottom) beam splitters (*18*). Tuning the filling factors υ_1 and υ_2 underneath the gates controls the transmission and reflection of the channels between the p and n sides. When $\upsilon_1 = 2$ and $\upsilon_2 = 0$, only the top beam splitter operates, allowing an electron moving along the top edge of the n (p) region to be transmitted to the p-side (n-side) channel of the pn interface with probability T_1; no transmission happens between the n and p sides at the bottom intersection. Conversely, when $\upsilon_1 = 0$ and $\upsilon_2 = 2$, only the bottom beam splitter operates with a transmission probability T_2. The electron spin is preserved in the beam splitting (*17*, *18*). When $\upsilon_1 = \upsilon_2 = 2$, both beam splitters partially transmit, leading to the formation of a MZI (*18*, *19*).

[1]SPEC, CEA, CNRS, Université Paris-Saclay, CEA Saclay, Gif sur Yvette Cedex, France. [2]National Institute for Materials Science, 1-1 Namiki, Tsukuba, Japan. [3]NTT Basic Research Laboratories, NTT Corporation, 3-1 Morinosato-Wakamiya, Atsugi, Japan. [4]Department of Physics, Korea Advanced Institute of Science and Technology, Daejeon, South Korea. ***Corresponding author. Email: hssim@kaist.ac.kr (H.-S.S.); preden.roulleau@cea.fr (P.R.)** †These authors contributed equally to this work. ‡Present address: CNRS, Institut Néel, Grenoble, France. §Present address: Department of Physics, Kyungpook National University, Daegu, South Korea.

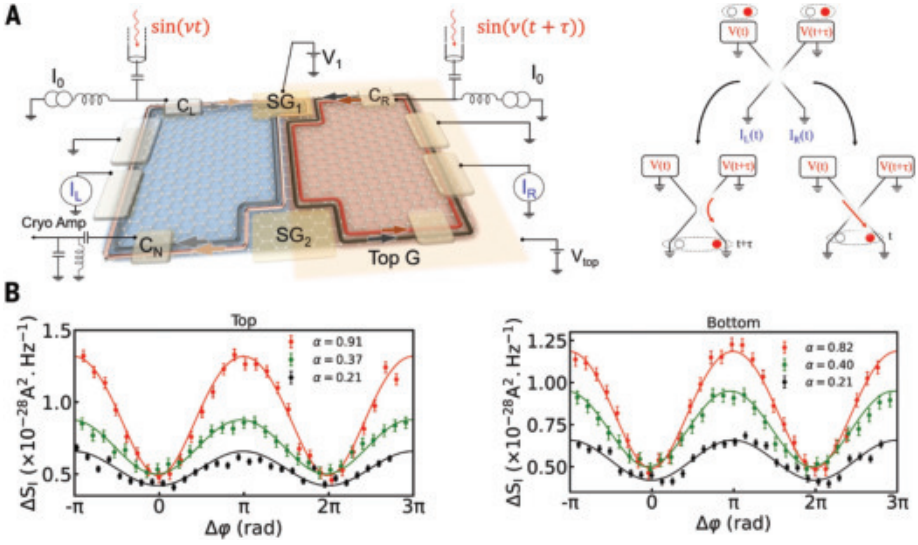

Fig. 1. HOM experiment in the single beam splitter configuration. (**A**) (Left) Schematic representation of the sample in the bipolar regime ($\upsilon_N = 2$, $\upsilon_P = -2$) set by the global back and right top gates. The filling factors below the upper and lower side gates (SG_1 and SG_2) are set to $\upsilon_1 = 2$ and $\upsilon_2 = 0$, respectively. Two sine pulses with a time delay τ collide on the top beam splitter. (Right) Indistinguishability of colliding excitations. In the top panel, electron-hole pairs are emitted from the left and right sources with a time delay τ. In the bottom left (right) panel, the pair from the right (left) source is split at the beam splitter into a hole moving to the left drain and an electron to the right drain. When $\tau = 0$ (i.e., $\Delta\varphi = 0$), the two pairs are fully indistinguishable because they arrive at the beam splitter at the same time. Then, the scattering events in the bottom left and right panels cannot happen simultaneously because of a destructive two-particle interference (Pauli exclusion). When the delay is the largest ($\Delta\varphi = \pi$), the two pairs are the most distinguishable because their wave function overlap at the beam splitter is the smallest. The events in the two bottom panels occur independently, involving the distinguishable parts of the wave functions. (**B**) Shot noise as a function of the delay time ($\Delta\varphi$) when electron-hole pairs collide at either the top beam splitter (left) or bottom beam splitter (right), for frequencies of 5 (in red), 9 (in green), and 15 GHz (in black). The experimental results (filled dots) agree with theoretical curves (solid lines) (*24*).

We first consider $\upsilon_1 = 2$ and $\upsilon_2 = 0$, where only the top beam splitter operates. We apply sinusoidal voltage pulses $V_L(t) = V_{ac}\cos(2\pi\nu t)$ and $V_R(t) = V_{ac}\cos(2\pi\nu t + \Delta\varphi)$ to the left (C_L) and right (C_R) contacts, respectively, with the relative phase $\Delta\varphi = 2\pi\nu\tau$, where ν represents the excitation frequency and τ denotes time delay between the two pulses. The resulting photo-created electron-hole pairs flow from each contact to the pn interface. They undergo collision and partitioning at the top beam splitter, generating autocorrelation shot noise $S_I = 2\int dt\left\langle \delta I_N(t+t_0)\delta I_N(t_0)\right\rangle$ of the electrical currents I_N measured at a drain contact C_N. Here, $\delta I_N(t) \equiv I_N(t) - \left\langle I_N(t_0)\right\rangle$ is the current fluctuation and $\langle\cdots\rangle$ denotes an average over time t_0. The left panel of Fig. 1B shows the shot noise at frequencies of $\nu = 5$, 9, and 15 GHz for different photon numbers $\alpha = eV_{ac}/h\nu$ at 20 mK. It oscillates with the relative phase $\Delta\varphi$. As expected, similar oscillations are observed at $\upsilon_1 = 0$ and $\upsilon_2 = 2$, where only the bottom beam splitter operates so that the photo-created electron-hole pairs collide and then are partitioned at the bottom beam splitter (Fig. 1B, right). The oscillatory behavior results from the two-particle fermionic HOM interference. It agrees with the theoretical expression of the HOM noise at finite temperature (*22*, *23*)

$$S_I^{HOM} = S_I^0 F(\Delta\varphi), F(\Delta\varphi) = \sum_{l=-\infty}^{+\infty}\left[l\coth\left(\frac{l}{2\theta_e}\right) - 2\theta_e\right]J_l^2\left[2\alpha\sin\left(\frac{\Delta\varphi}{2}\right)\right] \quad (1)$$

The factor $S_I^0 = 2\frac{2e^2}{h}D(1-D)h\nu$ represents the characteristic scale of the photo-assisted shot noise, where the factor 2 accounts for the two channels at each physical edge of the p and n regions, and $D = T_1$ for $\upsilon_1 = 2$ and $\upsilon_2 = 0$, whereas $D = T_2$ for $\upsilon_1 = 0$ and $\upsilon_2 = 2$. $\theta_e = k_B T_e/h\nu$, where T_e is the temperature and k_B is the Boltzmann constant, l is the number of absorbed or emitted photons, and J_l is the Bessel function.

The oscillation of the noise S_I^{HOM} as a function of $\Delta\varphi$ exhibits its minimum value (the HOM dip) when the time delay τ is zero (i.e., $\Delta\varphi = 0$). This results from the destructive two-electron interference by the indistinguishability of the two colliding excitations. At $\Delta\varphi = 0$, the two excitations, one generated by $V_L(t)$ at the left source C_L and the other by $V_R(t)$ at the right source C_R, arrive at the beam splitter at the same time so that they are fully indistinguishable in their collision (Fig. 1A, right). They cannot occupy the same outgoing state after the collision owing to the Pauli exclusion principle. As a result, their antibunching always occurs (namely, one of them moves to the n side after the collision, whereas the other moves to the p side), resulting in no noise. By contrast, the noise reaches its maximum value (the HOM peak) when $\Delta\varphi = \pi$. In this case, the two excitations are the most distinguishable because their wave functions have the smallest overlap in the collision. The distinguishable parts of the wave functions are free from Pauli exclusion, and they undergo single-particle scattering at the beam splitter, which is probabilistic and hence generates noise. At intermediate $\Delta\varphi$, the two excitations are partly indistinguishable, resulting in an intermediate value of the noise. Therefore, the dependence of the noise on $\Delta\varphi$ serves as a witness of the two-particle coherence of the collision. In Fig. 2B, we observe that the noise S_I^{HOM} does not drop to zero. This offset of S_I^{HOM} (~5.10^{-29} A^2/Hz) is attributed to heating by the ac signal, which generates thermal noise [further details are available in the supplementary materials (*24*)]. We note that when only $V_L(t)$ is applied [i.e., $V_R(t)$ is turned off], the noise follows the photo-assisted shot noise formula, which is identical to Eq. 1 except for the replacement of the last factor $J_l^2\left[2\alpha\sin\left(\frac{\Delta\varphi}{2}\right)\right]$ with $J_l^2(\alpha)$ (*25*).

HOM effect in the MZI

We next consider the MZI formed at $\upsilon_1 = 2$ and $\upsilon_2 = 2$, where both the top and bottom beam splitters operate (*17*, *18*). The channels along the top and bottom physical edges in the p and n regions serve as the input and output channels of the MZI, respectively, whereas the n-side and p-side channels running along the pn interface constitute the two MZI arms. At the top beam splitter, the n-side (p-side) input channels are scattered into the p-side (n-side) MZI arm with the transmission probability T_1 and into the n-side (p-side) MZI arm with the reflection probability $R_1 = 1 - T_1$. Inside the MZI, there is no scattering between the arms. At the bottom beam splitter, the interface channels are scattered into the output channels with the transmission T_2 and reflection $R_2 = 1 - T_2$ probabilities similarly to the top beam splitter. The two beam splitters and the two arms enclose a magnetic flux that induces the Aharonov-Bohm phase φ_{AB}. Figure 2A shows the h/e Aharonov-Bohm oscillation of the transmission through the MZI for $T_1 \approx T_2 \approx 0.5$, obtained by standard low-frequency lock-in measurement.

Next, we study the HOM effects in the MZI by applying the sinusoidal voltage pulses to the sources C_L and C_R while measuring the shot noise at the drain C_N. To observe the HOM effect, conditioned by the indistinguishability of the input states, the powers applied to the

sources must be precisely equal. To ensure this condition, we tuned the powers individually and measured the Aharonov-Bohm oscillation of the excess shot noise (defined as the shot noise difference with and without the sinusoidal voltage pulses) by applying the sine pulse voltage to either C_L (Fig. 2B) or C_R (Fig. 2C) (*25*). By comparing the measured oscillation with theory (*24*, *26*), we confirmed that the voltages applied to the two sources have the same amplitude. Next, the sine voltage pulses are applied to both sources with the relative phase $\Delta\varphi$, and the resulting Aharonov-Bohm oscillations of the shot noise are measured. At $\Delta\varphi = 0$, the noise exhibits its minimum value (HOM dip), as in Fig. 1B. In this case, no Aharonov-Bohm oscillation is observed (Fig. 2D). By contrast, at $\Delta\varphi = \pi$, the noise has the maximum value (HOM peak) and exhibits $h/2e$ Aharonov-Bohm oscillations.

These observations agree with our theory for the MZI (*24*)

$$S_I^{\text{HOM-MZI}} = S_I^{0,\text{MZI}} F(\Delta\varphi), S_I^{0,\text{MZI}} = 2\frac{2e^2}{h} T_{\text{MZI}}(1-T_{\text{MZI}})h\nu$$

where $T_{\text{MZI}} = R_1T_2 + T_1R_2 + 2\sqrt{R_1T_1R_2T_2}\cos\varphi_{\text{AB}}$ is the transmission probability through the MZI. This equation is valid when the MZI arms have equal length (*18*, *19*) and the two sources have the same value of $\alpha = eV_{\text{ac}}/h\nu$, as in our case. It has the same form as Eq. 1 but with replacement of the photo-assisted shot noise scale S_I^0 by $S_I^{0,\text{MZI}}$. Equation 2 shows that the noise vanishes at $\Delta\varphi = 0$, $F(\Delta\varphi = 0) = 0$ and that no Aharonov-Bohm oscillation happens at $\Delta\varphi = 0$. By contrast, at $\Delta\varphi \neq 0$, the colliding particles are partly distinguishable, resulting in the $h/2e$ Aharonov-Bohm oscillation of the noise, which is described by $T_{\text{MZI}}(1-T_{\text{MZI}}) = (1-\cos 2\varphi_{\text{AB}})/8$ at $T_1 = T_2 = 0.5$. We observed that the $h/2e$ Aharonov-Bohm oscillation is more visible when the colliding particles are more distinguishable with $\Delta\varphi$ closer to π, whereas the destructive two-particle interference of the fermionic HOM effect becomes stronger when the particles are more indistinguishable with $\Delta\varphi$ closer to 0. This represents the complementarity between the two-particle HOM interference and the single-particle $h/2e$ Aharonov-Bohm interference. This complementarity is maximally evident in our MZI with equal arm lengths, where the indistinguishability of the colliding particles at the top beam splitter remains unchanged at the bottom beam splitter. This fermionic complementarity can be compared with other fundamental complementarities (*27*–*29*), such as those between single-particle and two-particle interferences.

We describe a simple picture for the findings. We consider a case of $\Delta\varphi = 0$, where two electrons—one injected from C_L and the other from C_R—simultaneously arrive at the MZI, or a case of $\Delta\varphi = \pi$, where only the electron from C_L arrives at the MZI (the other from C_R is ignored because it does not arrive at the MZI). In these cases where C_L emits an electron $\left[\text{i.e.,}\left\langle c_L^\dagger c_L\right\rangle = 1\right]$, the noise $S_I^{\text{HOM-MZI}} \propto \left\langle c_N^\dagger c_N c_N^\dagger c_N\right\rangle - \left\langle c_N^\dagger c_N\right\rangle^2$ at C_N is expressed as

$$S_I^{\text{HOM-MZI}} \propto \left\langle t^* c_L^\dagger r c_R r^* c_R^\dagger t c_L\right\rangle = T_{\text{MZI}}(1-T_{\text{MZI}})\left\langle c_L^\dagger c_L\right\rangle\left\langle c_R c_R^\dagger\right\rangle \quad (3)$$

Here, $c_{L/R/N}^\dagger$ is the operator creating an electron in a state of $C_{L/R/N}$ and obeys $c_N = tc_L + rc_R$, with the scattering amplitudes t and r in the MZI satisfying $|t|^2 = T_{\text{MZI}}$ and $|r|^2 = 1 - T_{\text{MZI}}$. Equation 3 shows that the noise vanishes at $\Delta\varphi = 0$, where $\left\langle c_L^\dagger c_L\right\rangle = 1$ and $\left\langle c_R^\dagger c_R\right\rangle = 1$ $\left[\text{i.e.,}\left\langle c_R c_R^\dagger\right\rangle = 0\right]$. This is caused by the antibunching of the two injected electrons that are fully indistinguishable in the MZI when $\Delta\varphi = 0$. By contrast, the noise exhibits the $h/2e$ Aharonov-Bohm oscillation of $S_I^{\text{HOM-MZI}} \propto T_{\text{MZI}}(1-T_{\text{MZI}}) = (1-\cos 2\varphi_{\text{AB}})/8$ at $\Delta\varphi = \pi$, where $\left\langle c_L^\dagger c_L\right\rangle = 1$ and $\left\langle c_R^\dagger c_R\right\rangle = 0$ $\left[\text{i.e.,}\left\langle c_R c_R^\dagger\right\rangle = 1\right]$. The term $\cos 2\varphi_{\text{AB}}$ results

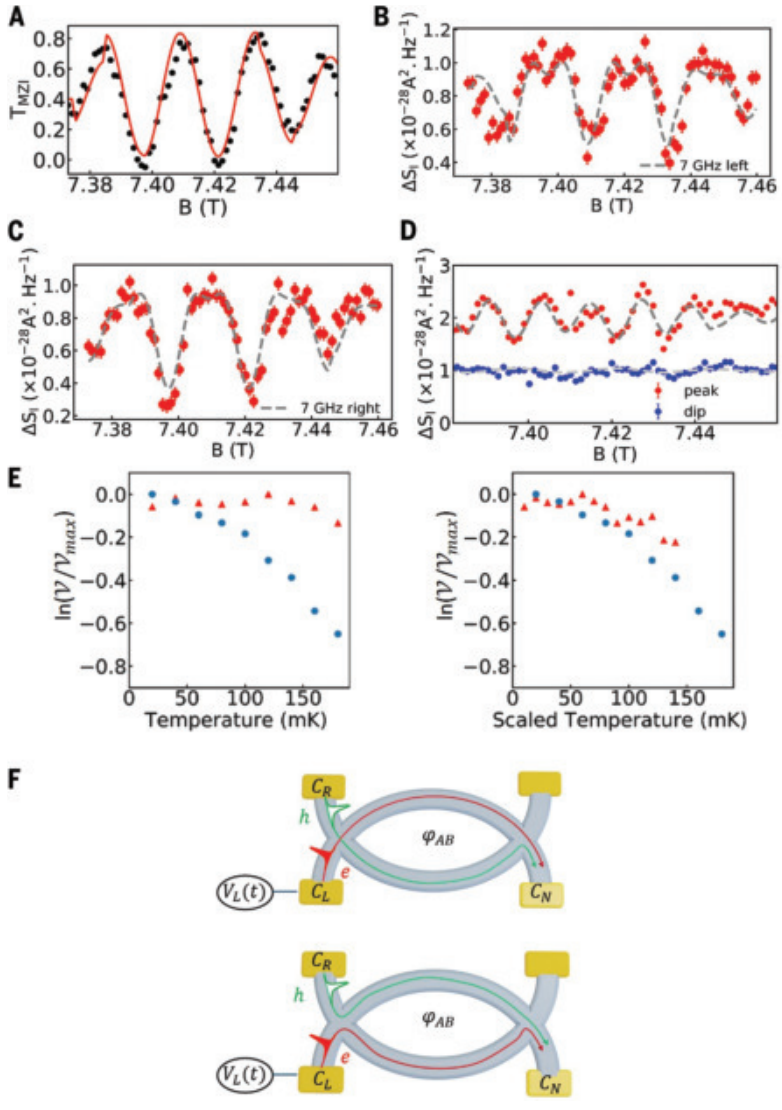

Fig. 2. Noise in the Mach-Zehnder configuration. (**A**) Transmission (T_{MZI}) of the MZI (dots) as a function of the magnetic field. The solid curve shows the theoretical result (*24*). (**B** and **C**) Excess shot noise $S_I^{\text{HOM-MZI}}$ (red dots) as a function of the magnetic field for the 7-GHz sine pulse excitation applied on either the left source (B) or the right source (C). The dashed curves show the theoretical fits (*24*). (**D**) The excess shot noise $S_I^{\text{HOM-MZI}}$ as a function of the magnetic field for the sine pulse applied on both sources with $\Delta\varphi = 0$ (blue dots; HOM dip) and $\Delta\varphi = \pi$ (red dots; HOM peak). The offset noise for $\Delta\varphi = 0$ is caused by the thermal noise (*24*). The dashed curves are the theoretical fits (*24*). (**E**) (Left) Aharonov-Bohm interference visibilities $\mathcal{V}$ of the measured transmission T_{MZI} (red triangles) and the noise $S_I^{\text{HOM-MZI}}$ (blue dots) as a function of temperature T. The decrease of the visibility with temperature is more pronounced for the interference of $S_I^{\text{HOM-MZI}}$. $\mathcal{V}_{\text{max}}$ is the maximum value of the visibility. (Right) The decay of the interference visibility of the noise $S_I^{\text{HOM-MZI}}$ is redrawn with the scaled temperature $T_s = 2T$, whereas that of the transmission T_{MZI} is drawn with $T_s = T$. The two decay curves become nearly identical, which suggests that the interference length scale is two times as large for the noise. (**F**) Schematic illustration of the double winding, which results from an interference between process (i) (bottom) and process (ii) (top). The injected electron (depicted by the red full peak) and the auxiliary hole (the green empty peak) follow the red and green trajectories, respectively.

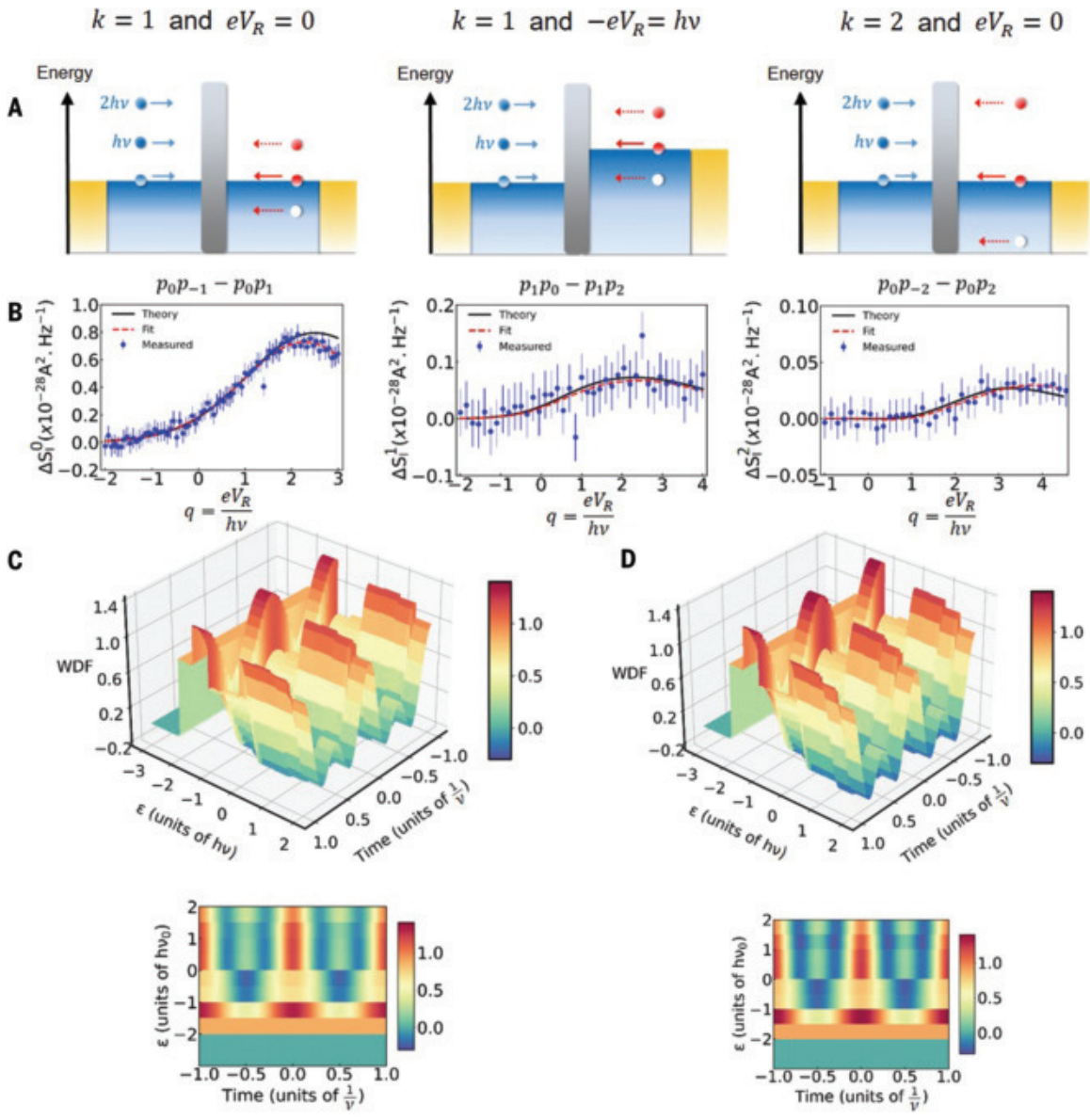

Fig. 3. Tomography of the 2*e* Leviton. (**A**) Schematic representation of the tomography protocol: Lorentzian pulses are applied at frequency ν on the left ohmic contact to generate Levitons in the Fermi sea (shown in blue). For the tomography protocol, the Lorentzian pulse is engineered with three harmonics (*26*). The Levitons are described by a coherent superposition of plane waves (blue dots) of energy $hm\nu$ (with $m = 0, 1, 2, \cdots$) induced by the Lorentzian pulses. A small ac local oscillator is applied at frequency $k\nu$ on the right contact to generate an ac voltage $V_{LO}(t) = \eta_{LO}\left(\frac{h\nu}{e}\right)\cos\left[2\pi k\nu(t-\tau)\right]$ superimposed to a dc voltage V_R. The resulting fermion field is a superposition of plane waves of energy $-eV_R$, $-eV_R \pm hk\nu$ describing electron-hole pairs (red and empty dots). The Levitons and the fermion field collide at a beam splitter (vertical gray bar). (Left) $k = 1$ and $V_R = 0$. In this configuration, cross terms $p_0p_{-1} - p_0p_1$ are computed. (Middle) $k = 1$ and $-eV_R = h\nu$ for computing of $p_1p_0 - p_1p_2$. (Right) $k = 2$ and $V_R = 0$ for computing of $p_0p_{-2} - p_0p_2$ (*24*). (**B**) $\Delta S_i^{k=0}$ with $V_R = 0$ (left), $\Delta S_i^{k=1}$ with $-eV_R = h\nu$ (middle), and $\Delta S_i^{k=2}$ with $V_R = 0$ (right) as a function of $q = eV_R / h\nu$. The measurement allows for the computation of the energy density matrix. (**C**) Reconstructed Wigner distribution function (WDF) from the tomography measurement. The two-dimensional color plots are shown to better display the region of negative values of the Wigner distribution function. (**D**) Theoretical Wigner distribution function in the energy/time basis (*24*).

from the interference between processes (i) and (ii) (Fig. 2F). In (i), the electron injected from C_L moves along the left arm of the MZI, and an auxiliary (or virtual) hole, describing the condition of $\left\langle c_R^\dagger c_R \right\rangle = 0$ that the electron state injected from C_R is unoccupied, moves along the right arm of the MZI. This process is equivalent with an "anticlockwise" winding of an electron around the Aharonov-Bohm flux enclosed by the MZI and gains the phase factor of $e^{i\varphi_{AB}}$. In (ii), the electron moves along the right arm, whereas the auxiliary hole moves along the left arm. This gains the phase factor of $e^{-i\varphi_{AB}}$ by a clockwise winding of an electron around the flux. The interference between (i) and (ii) involves the net phase factor of $e^{2i\varphi_{AB}}$ by a double winding of an electron around the flux. The double winding effectively happens in the noise with the help of an auxiliary hole because the noise is a two-particle observable. It differs from the multiple winding in a Fabry-Perot interferometer or a quantum ring (*20*, *21*).

We next analyze the single-particle coherence of the collision. The $h/2e$ Aharonov-Bohm oscillation at $\Delta\varphi = \pi$ in Fig. 2D can be fitted with Eq. 2 using $\alpha = eV_{ac} / h\nu$. In the left panel of Fig. 2E, the visibility of the $h/2e$ Aharonov-Bohm oscillation—defined as $\mathcal{V} = S_{max} - S_{min}$ with the maximum (S_{max}) and minimum (S_{min}) values of the noise—is shown as a function of temperature T_e from 20 mK to 300 mK and compared with the visibility of the h/e Aharonov-Bohm oscillation of T_{MZI} extracted from

the data in Fig. 2A. The temperature dependences of the two visibilities are well aligned if the temperature for the noise visibility is scaled up by a factor of 2 (Fig. 2E, right). The factor 2 reflects the fact that the noise is associated with the double winding around the magnetic flux as described above, involving twice the MZI arm length ($S_I^{\text{HOM-MZI}} \sim e^{-2L/L_\varphi}$, with L the arm length and L_φ the single-particle coherence length); the interference involving the double winding experiences twice as much decoherence as the single winding. Such scaling is explained by a decoherence model based on intrachannel Coulomb interactions (*19*). In this model, the single-particle visibility follows a universal curve with scaled temperature LT/L_0 by the MZI arm length L (L_0 is a reference length). In graphene, the Coulomb interaction between the colliding electrons and several decoherence sources such as interchannel interactions are suppressed owing to the close proximity of metallic gates, which screen the interactions and freeze decoherence below ~350 mK for the arm length of 1.5 μm (*19*). The suppression is crucial for manipulating the collision states and observing the complementarity.

Quantum state tomography of a Leviton

The excellent coherence observed in our setup underscores its potential for quantum information processing. A natural application of the collision is the full reconstruction of a quantum state or quantum state tomography (*15*, *30*). We perform the tomography of a Leviton (*13*) with charge $2e$ at $\upsilon_1 = 2$ and $\upsilon_2 = 0$ (where only the top beam splitter is operated). The overall process unfolds as follows: A series of the Levitons are injected from C_L by applying Lorentzian voltage pulses $V(t)$ with frequency ν. Simultaneously, a low-intensity fermionic field, which is a coherent superposition of electron-hole pairs, is injected from C_R by applying a small ac voltage $V_{LO}(t) = \eta_{LO}\left(\frac{h\nu}{e}\right)\cos\left[2\pi k\nu(t-\tau)\right]$ superimposed to a dc voltage V_R with amplitude $\eta_{LO} \ll 1$, frequency $k\nu$ (an integer multiple of the Leviton frequency ν), and time delay τ referred to the Leviton emission time. The Levitons and the fermionic field collide at the beam splitter, generating antibunching effects. By measuring the resulting shot noise, the Wigner distribution function $W(t,\varepsilon) = \int_{-\infty}^{\infty} d\delta\rho(\varepsilon+\delta/2, \varepsilon-\delta/2)e^{-i\delta t/\hbar}$ of the Leviton is reconstructed.

We next provide the details of the tomography (*15*). The energy density matrix $\rho(\varepsilon,\varepsilon')$ of the Leviton is expressed as $\rho(\varepsilon,\varepsilon'\neq\varepsilon) = \sum_k \delta(\varepsilon'-\varepsilon-kh\nu)\tilde{\varphi}^*(\varepsilon+kh\nu)\tilde{\varphi}(\varepsilon)$ for the periodic injection of the Levitons, where δ is the Dirac delta function, $\tilde{\varphi}(\varepsilon)$ is the Fourier transform of the Leviton wave function $\varphi\left(t-\frac{x}{v_F}\right)$ at position x and time t, and v_F is the velocity. The wave function product $\rho_{l,l+k} \equiv \tilde{\varphi}^*(\varepsilon+kh\nu)\tilde{\varphi}(\varepsilon)$ for the energy domain $lh\nu < \varepsilon < (l+1)h\nu$ is written as $\rho_{l,l+k} = -\sum_{m=-n}^{l} p_m p_{m+k}$ for the Leviton of charge ne (in our case, $n = 2$) (*24*). Here, p_m is the amplitude of the Leviton wave function component generated by absorption ($m > 0$) or emission ($m < 0$) of m photons thanks to the Lorentzian voltage $V(t)$. It equals the Fourier coefficient of the phase factor by the voltage, $\exp\left[-i\frac{e}{\hbar}\int_o^t V(t')dt'\right] = \sum_m p_m e^{-i2\pi m\nu t}$. To obtain $p_m p_{m+k}$, we measured the noise difference ΔS_I^k between the cases with the ac voltage $V_{LO}(t)$ turned on and off. The extraction of $p_m p_{m+k}$ from the noise uses the theoretical expression (*24*) of $\frac{\Delta S_I^{k\neq 0}}{S_I^0} = \eta_{LO}\cos(2\pi k\nu\tau)\sum_m |m-q|\left(p_m p_{m-k} - p_m p_{m+k}\right)$, with $q = eV_R/h\nu$ for $k \neq 0$. This describes collision between the plane waves of energy $mh\nu$ (with $m = 0, 1, 2, \cdots$) forming the Levitons and the plane waves of energy $-eV_R$, $-eV_R \pm hk\nu$ forming the fermion field (Fig. 3A), which is the underlying mechanism of the tomography. By changing q for k = 0,1,2, we extract relevant $p_m p_{m+k}$ (Fig. 3B), compute $\rho_{l,l+k}$ using them, and reconstruct the Wigner distribution function (Fig. 3C). The result agrees with the theoretical prediction (Fig. 3D). Through the implementation of this method, we gain a deeper understanding compared with the conventional HOM measurement that only yields the wave function overlap between the colliding electrons.

Discussion and outlook

Our work opens a door to coherent operations of flying qubits for entanglement (*12*) and two-particle quantum state tomography (*31*). Moreover, these reference experiments can be extended to anyonic excitations, enabling on-demand manipulation (*22*), measurement of anyonic statistical phases (*32*), and braiding operations.

REFERENCES AND NOTES

1. Y. Ji *et al.*, *Nature* **422**, 415–418 (2003).
2. P. Roulleau *et al.*, *Phys. Rev. B* **76**, 161309 (2007).
3. I. Neder *et al.*, *Nature* **448**, 333–337 (2007).
4. C. K. Hong, Z. Y. Ou, L. Mandel, *Phys. Rev. Lett.* **59**, 2044–2046 (1987).
5. M. Henny *et al.*, *Science* **284**, 296–298 (1999).
6. W. D. Oliver, J. Kim, R. C. Liu, Y. Yamamoto, *Science* **284**, 299–301 (1999).
7. R. C. Liu, B. Odom, Y. Yamamoto, S. Tarucha, *Nature* **391**, 263–265 (1998).
8. H. Bartolomei *et al.*, *Science* **368**, 173–177 (2020).
9. J.-Y. M. Lee *et al.*, *Nature* **617**, 277–281 (2023).
10. P. Glidic *et al.*, *Phys. Rev. X* **13**, 011030 (2023).
11. M. Ruelle *et al.*, *Phys. Rev. X* **13**, 011031 (2023).
12. P. Samuelsson, M. Buttiker, *Phys. Rev. B* **71**, 245317 (2005).
13. J. Dubois *et al.*, *Nature* **502**, 659–663 (2013).
14. E. Bocquillon *et al.*, *Science* **339**, 1054–1057 (2013).
15. T. Jullien *et al.*, *Nature* **514**, 603–607 (2014).
16. G. Fève *et al.*, *Science* **316**, 1169–1172 (2007).
17. D. S. Wei *et al.*, *Sci. Adv.* **3**, e1700600 (2017).
18. M. Jo *et al.*, *Phys. Rev. Lett.* **126**, 146803 (2021).
19. M. Jo *et al.*, *Nat. Commun.* **13**, 5473 (2022).
20. C. Déprez *et al.*, *Nat. Nanotechnol.* **16**, 555–562 (2021).
21. Y. Ronen *et al.*, *Nat. Nanotechnol.* **16**, 563–569 (2021).
22. I. Taktak *et al.*, *Nat. Commun.* **13**, 5863 (2022).
23. V. S. Rychkov, M. L. Polianski, M. Buttiker, *Phys. Rev. B* **72**, 155326 (2005).
24. See the supplementary materials.
25. A. Assouline *et al.*, *Science* **382**, 1260–1264 (2023).
26. P. P. Hofer, C. Flindt, *Phys. Rev. B* **90**, 235416 (2014).
27. G. Jaeger, A. Shimony, L. Vaidman, *Phys. Rev. A* **51**, 54–67 (1995).
28. D. Kaszlikowski, L. C. Kwek, M. Zukowski, B.-G. Englert, *Phys. Rev. Lett.* **91**, 037901 (2003).
29. P. Busch, C. Shilladay, *Phys. Rep.* **435**, 1–31 (2006).
30. C. Grenier *et al.*, *New J. Phys.* **13**, 093007 (2011).
31. P. Samuelsson, M. Büttiker, *Phys. Rev. B* **73**, 041305 (2006).
32. J.-Y. M. Lee, C. Han, H.-S. Sim, *Phys. Rev. Lett.* **125**, 196802 (2020).
33. P. Roulleau, Electron Collision in a Two-Path Graphene Interferometer, data set, Zenodo (2025).

ACKNOWLEDGMENTS

We thank F. Parmentier for his help in fabrication, L. Bernabeu and S. Lee for discussion in the early stage of the work, and M. Kuiri for his help on the manuscript. **Funding:** This work was funded by the ERC starting grant COHEGRAPH 679531 (P.R.), by the EMPIR project SEQUOIA 17FUN04 cofinanced by the participating states and the European Union's Horizon 2020 program (P.R.), by ANR EQUBITFLY (P.R.), by Horizon-EIC-2022-Pathfinderopen project FLATS (P.R.), and by Korea NRF through the SRC Center for Quantum Coherence in Condensed Matter (grant no. RS-2023-00207732) (H.-S.S.). **Author contributions:** H.C., L.P., A.A., and P.R. performed the experiment. H.C., L.P., A.A., N.K., D.C.G., H.-S.S., and P.R. analyzed and discussed the data. T.T. and K.W. provided the boron nitride layers. H.-S.S. and P.R. wrote the manuscript with input from all coauthors. H.-S.S. developed the theory. M.J. fabricated the device with input from A.A. and P.R. P.R. designed and supervised the experiment. **Competing interests:** The authors declare no competing interests. **Data and materials availability:** Data and code are available on Zenodo (*33*). **License information:** Copyright © 2025 the authors, some rights reserved; exclusive licensee American Association for the Advancement of Science. No claim to original US government works. https://www.science.org/about/science-licenses-journal-article-reuse

SUPPLEMENTARY MATERIALS

science.org/doi/10.1126/science.adn4622
Materials and Methods; Supplementary Text; Figs. S1 to S3; Table S1; References (*34*, *35*)
Submitted 11 December 2023; accepted 13 March 2025
10.1126/science.adn4622

CATALYSIS

A self-regenerating Pt/Ge-MFI zeolite for propane dehydrogenation with high endurance

Huizhen Hong[1,2]†, Zhikang Xu[2]†, Bingbao Mei[3]†, Wende Hu[4]†, Paolo Fornasiero[5], Chuanming Wang[4], Tinghai Wang[1,2], Yuanyuan Yue[1,2], Tiesen Li[1,2], Chen Yang[1], Qingyan Cui[1], Haibo Zhu[1]*, Xiaojun Bao[2]*

Supported noble metal cluster catalysts are typically operated under severe conditions involving switching between reducing and oxidizing atmospheres, causing irreversible transformation of the catalyst structure and thereby leading to permanent deactivation. We discovered that various platinum (Pt) precursors spontaneously disperse in a germanium-MFI (Ge-MFI) zeolite, which opposes the Ostwald ripening phenomenon, producing self-regenerating Pt/Ge-MFI catalysts for propane dehydrogenation. These catalysts reversibly switch between Pt clusters and Pt single atoms in response to reducing reaction and oxidizing regeneration conditions. This environmental adaptability allows them to completely self-regenerate over 110 reaction and regeneration cycles in propane dehydrogenation, and they exhibited unprecedented sintering resistance when exposed to air at 800°C for 10 days. Such spontaneous metal dispersion in a Ge-MFI zeolite is a robust and versatile methodology for fabricating various rhodium, ruthenium, iridium, and palladium cluster catalysts.

Supported noble metal clusters (<1 nm) used in industrial catalysis (*1*) are often subjected to severe conditions that switch between reducing and oxidizing environments (often for catalyst regeneration), such as in propane dehydrogenation (PDH) and naphtha reforming. However, these cycles often cause irreversible structural transformation of metal clusters (*2*–*10*) that gradually form into larger sintered metal particles, leading to catalyst deactivation. Self-regenerating metal catalysts that reversibly alter their structures in response to varying atmospheres can address this problem. For example, Pd and Pt supported on perovskite used as exhaust treatment catalysts can self-regenerate (*11*–*17*) and thus substantially prolong the catalyst's operational lifespan. However, the practical application of this kind of catalyst is hindered by its insufficient catalytic activity, which is attributed to the low surface area of perovskite (*18*, *19*).

We focused on self-regenerating PDH catalysts for propylene production (*20*–*31*). The commercial Pt-Sn/Al_2O_3 catalyst for PDH undergoes numerous regenerations of the deactivated catalyst in which high-temperature oxidation in air removes coke. This process results in Pt sintering. To recover the active nanostructure (*20*, *32*, *33*), Cl_2 must be co-fed with O_2 to redisperse the large particles into clusters, and this oxychlorination treatment causes environmental pollution and reactor corrosion. Moreover, the use of chloride creates unfavored acid sites arising from the formation of chloride alumina (Al_2O_3-Cl), giving rise to side reactions that reduce propylene selectivity (*34*, *35*).

Despite substantial progress in the development of durable Pt catalysts for PDH aimed at producing a revolutionary PDH technology (*20*, *21*, *36*), the state-of-the-art catalysts still lack environmental adaptability. They lose catalytic performance after several reaction and regeneration cycles (table S1), so their total lifetime is inadequate for industrial expectations.

In this context, we report that Pt supported on Ge-MFI zeolite catalysts demonstrates extraordinary self-regeneration and maintains its catalytic performance after 110 reaction and regeneration cycles in PDH. Our study provides a new methodology for environmentally adaptable catalysts that maintain performance during gas and temperature cycling conditions.

Metal interactions with Ge-MFI zeolite

We discovered that a Ge-MFI zeolite can efficiently trap metal species. The Ge-MFI was synthesized using a hydrothermal method, with ~0.42 wt % Ge incorporated into the zeolite framework. The trapping of Pt by Ge-MFI was directly illustrated by the interparticle transfer of Pt from SiO_2 to Ge-MFI, which is similar to the phenomenon observed for Pt on ceria support (*37*). In our experiment, Pt/SiO_2 was physically mixed with Ge-MFI and subsequently aged in air at 700°C (fig. S1). Transmission electron microscopy (TEM) images revealed 40 to 80 nm Pt particles on the surface of SiO_2 (Fig. 1, A and B, and fig. S2). After aging, these Pt particles were no longer observed (fig. S3, A to D). Scanning transmission electron microscopy (STEM) images (Fig. 1, C and D, and fig. S3, E to H) showed that Pt clusters had formed within the channels of Ge-MFI. Pt/SiO_2 showed quite low propane conversion (~2.4%) in PDH (fig. S4). The aging of the mixture significantly enhanced propane conversion to ~42.2%, primarily due to the formation of highly active Pt clusters. These findings indicate that Pt transferred from SiO_2 and dispersed in Ge-MFI, as depicted in Fig. 1E.

We then explored a top-down strategy for synthesizing Pt/Ge-MFI catalysts. We performed thermal-oxidative aging on an as-synthesized Pt/Ge-MFI (with Pt particles of 2 to 5 nm) through wet impregnation, a physical mixture of Pt particles (~300 nm) and Ge-MFI, and a physical mixture of H_2PtCl_6 particles (~600 nm) and Ge-MFI (Fig. 1, F, J, and N, and figs. S5 to S7, respectively). In all instances, the initial large Pt species were not observed after aging (Fig. 1, G, H, K, L, O, and P, and fig. S8). STEM characterization showed that these Pt species redistributed into clusters located within the 10-membered ring channels of the Ge-MFI zeolite (Fig. 1, I, M, and Q, and fig. S9). This spontaneous redispersion of Pt also occurred in Pt@Ge-MFI synthesized through the in situ encapsulation method.

After the thermal-oxidative aging, large Pt particles (Fig. 1R and fig. S10, A and B) transformed into small clusters in Ge-MFI (Fig. 1, S to U, and fig. S10, C to F). A spontaneous dispersion of Pt in Ge-MFI (Fig. 1V) that opposed the Ostwald ripening effect occurred. We characterized the four different synthesized Pt/Ge-MFI catalysts using x-ray diffraction (XRD) and N_2 adsorption techniques (fig. S11 and table S2) and confirmed that they were crystalline microporous materials.

We then explored whether other heteroatom-containing MFI zeolites, including Sn-MFI, Zn-MFI, In-MFI, Ga-MFI, and purely siliceous MFI, could trap Pt. We supported ~2 to 5 nm Pt nanoparticles on these zeolites using the impregnation method (fig. S12), followed by thermal-oxidative aging at 700°C. However, Pt redispersion did not occur, and the aging caused Pt agglomeration, resulting in the formation of large Pt particles ranging from 50 to 100 nm (fig. S13). Thus, Ge atoms in the MFI framework played a critical role in the trapping of Pt species and their redispersion into zeolite channels.

[1]State Key Laboratory of Fluorine & Nitrogen Chemicals, College of Chemical Engineering, Fuzhou University, Fuzhou, China. [2]Qingyuan Innovation Laboratory, Quanzhou, China. [3]Shanghai Synchrotron Radiation Facility, Shanghai Advanced Research Institute, Chinese Academy of Sciences, Shanghai, China. [4]State Key Laboratory of Green Chemical Engineering and Industrial Catalysis, China Petrochemical Corporation, SINOPEC Shanghai Research Institute of Petrochemical Technology Co., Ltd., Shanghai, China. [5]Department of Chemical and Pharmaceutical Sciences, Center for Energy, Environment and Transport Giacomo Ciamician, University of Trieste, ICCOM-CNR Trieste Research Unit and Consortium INSTM Trieste Research Unit, Trieste, Italy. ***Corresponding author. Email: haibo.zhu@fzu.edu.cn (H.Z.); baoxj@fzu.edu.cn (X.B.)** †These authors contributed equally to this work.

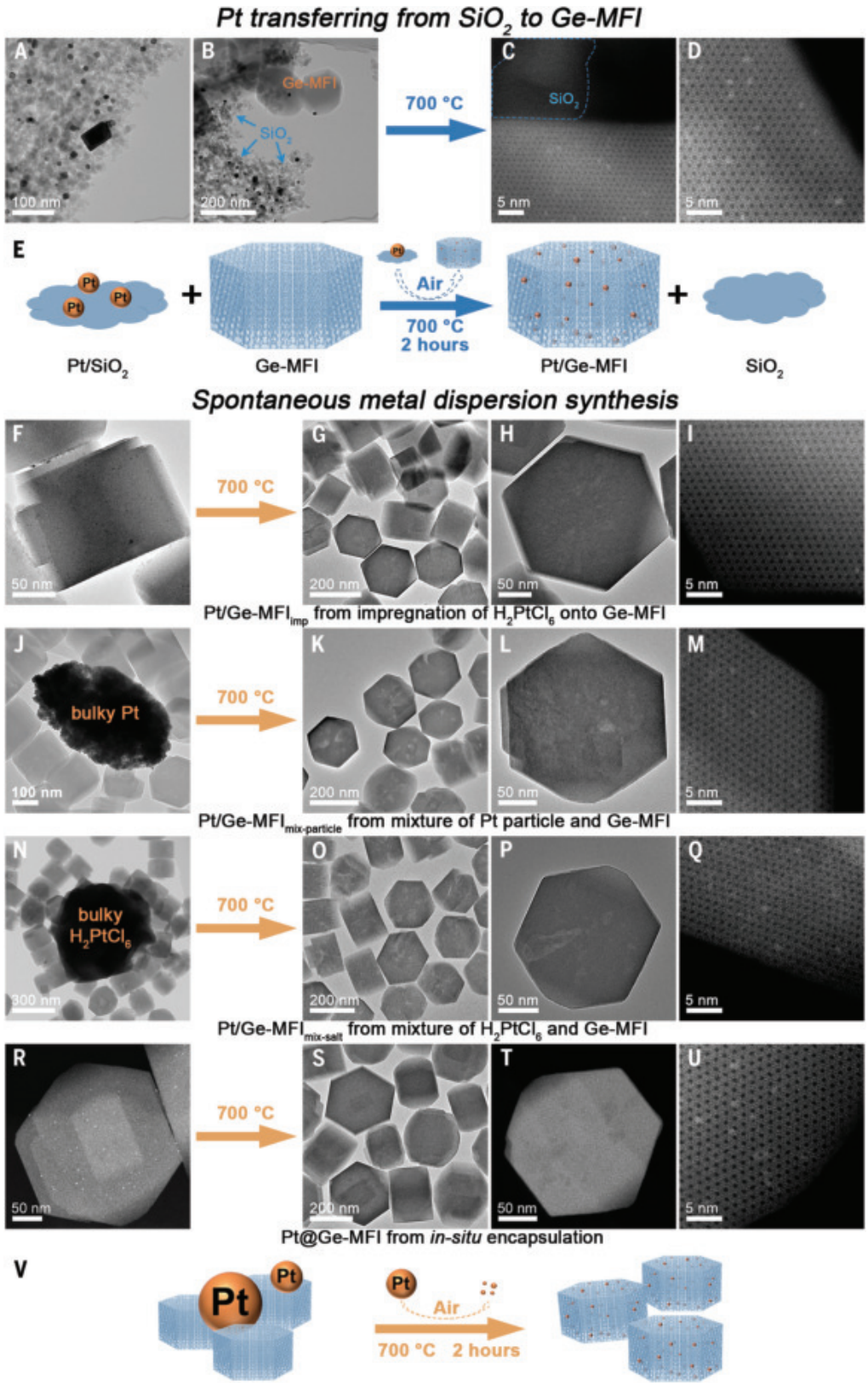

Fig. 1. Synthesis of Pt/Ge-MFI catalysts through spontaneous dispersion of Pt species. (**A** to **D**) TEM images of a mixture of Pt/SiO_2 and Ge-MFI [(A) and (B)] and high-angle annular dark-field scanning transmission electron microscopy (HAADF-STEM) images of the mixture after aging [(C) and (D)]. (**E**) Illustration of Pt transferring from SiO_2 to Ge-MFI. (**F** to **H**) TEM images of $Pt/Ge\text{-}MFI_{imp}$ before (F) and after [(G) and (H)] aging. (**I**) HAADF-STEM image of aged $Pt/Ge\text{-}MFI_{imp}$. (**J** to **L**) TEM images of a mixture of Pt particles and Ge-MFI before (J) and after [(K) and (L)] aging. (**M**) HAADF-STEM image of the aged $Pt/Ge\text{-}MFI_{mix\text{-}particle}$. (**N** to **P**) TEM images of a mixture of H_2PtCl_6 and Ge-MFI before (N) and after [(O) and (P)] aging. (**Q**) HAADF-STEM image of the aged $Pt/Ge\text{-}MFI_{mix\text{-}salt}$. (**R**) HAADF-STEM image of as-synthesized Pt@Ge-MFI. (**S** to **U**) TEM (S) and HAADF-STEM [(T) and (U)] images of Pt@Ge-MFI after aging. (**V**) Illustration of the spontaneous dispersion of Pt species in Ge-MFI. The aging was conducted at 700°C in air for 2 hours.

Propane dehydrogenation studies

The self-regeneration ability of the four Pt/Ge-MFI catalysts was assessed in PDH, which was performed under demanding conditions: 100% propane as the feed, a high-weight hourly space velocity (WHSV) of 9.5 $hours^{-1}$, and a temperature of 585°C. The propane conversion reached ~42% and the propylene selectivity was ~98%. The conversion was marginally below the equilibrium conversion (43.5% at 585°C) that could be obtained with WHSV below 5.0 $hours^{-1}$ (fig. S14). However, this conversion surpassed the ~32% typically achieved in industrial processes (*38*).

The high propane conversion accelerated the coking rate in catalysts, thereby facilitating an efficient evaluation of their self-regeneration performance. Scanning electron microscopy, thermogravimetric analysis, and Raman spectroscopy (figs. S15 and S16) confirmed the formation of coke in the spent catalysts. TEM characterization suggested that the sintering of Pt clusters did not occur during PDH (fig. S17), so coke formation was the primary cause of deactivation.

After 12 hours of PDH, the spent catalysts were subjected to a regeneration treatment in air at 600°C for 2 hours to remove the coke (*39*, *40*). The catalytic performance of these four catalysts could be fully restored for at least 50 cycles of reaction and regeneration, with the propane conversion and propylene selectivity remaining consistent after each self-regeneration (Fig. 2, A and B, and figs. S18 to S20). This result encouraged us to intentionally extend the reaction and regeneration beyond 100 cycles in a representative sample of Pt@Ge-MFI, and the assessment results showed that its catalytic performance remained completely intact after 110 cycles (Fig. 2B and fig. S21).

After 50 or 110 cycles of reaction and regeneration, these four catalysts were studied by XRD, TEM, and N_2 adsorption techniques (figs. S22 to S25). The characterization results showed that their crystalline

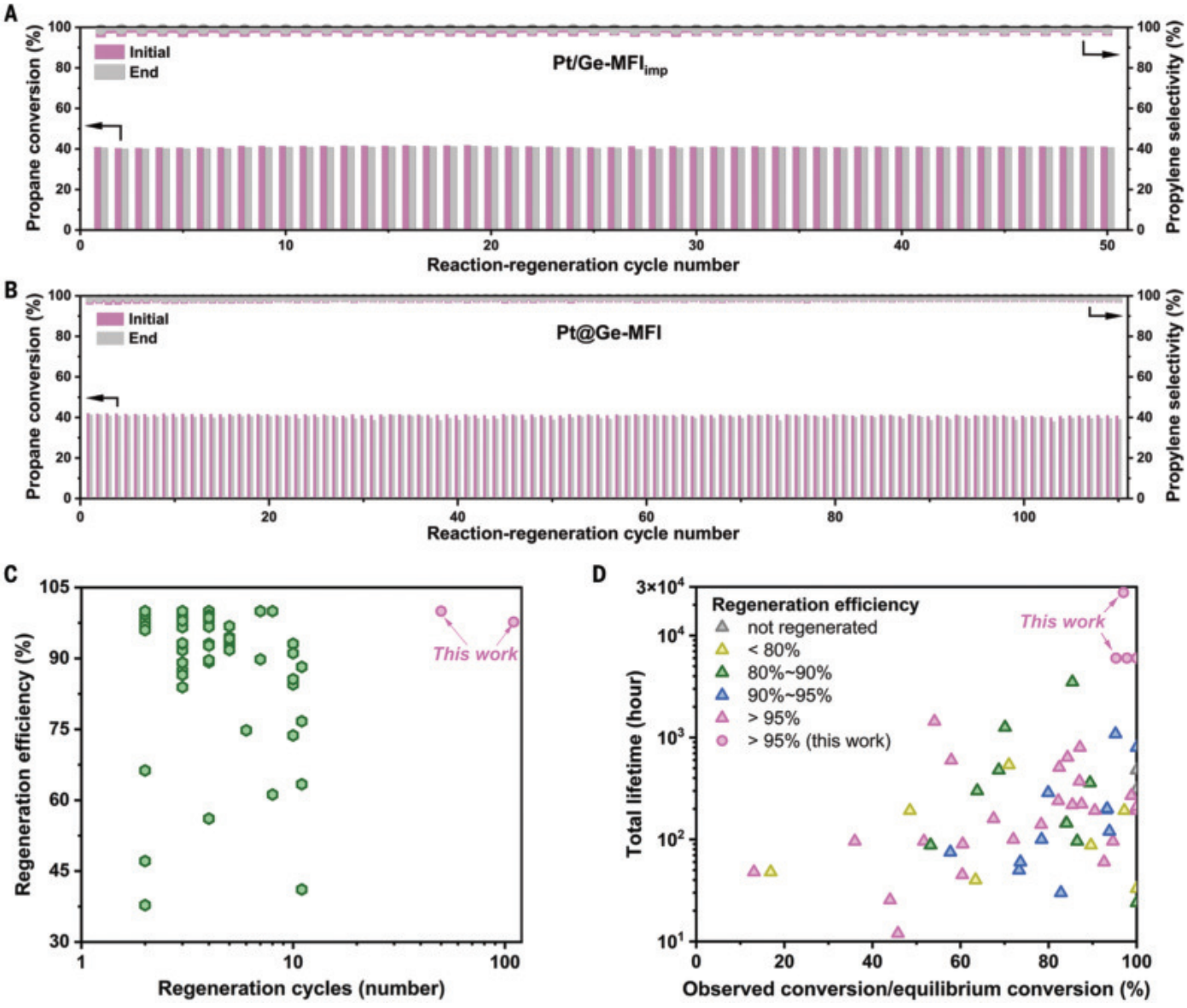

Fig. 2. Self-regeneration performance of Pt/Ge-MFI catalysts in PDH. (**A** and **B**) The propane conversion and propylene selectivity of Pt/Ge-MFI$_{imp}$ (A) and Pt@Ge-MFI (B) catalysts after 50 or 110 reaction and regeneration cycles of PDH. Reaction conditions were as follows: atmospheric pressure, 100% C_3H_8, WHSV 9.5 $hours^{-1}$, temperature 585°C, and reaction time 12 hours. Regeneration conditions were as follows: air atmosphere and temperature 600°C. (**C** and **D**) Comparison of the regeneration efficiency with different regeneration cycles (C) and the expected total lifetime of our catalysts with those of reported catalysts (D) (for detailed data, see table S1).

structure and micropores were well retained, and thus steam produced in the regeneration process did not destroy their structures. Typically, the Pt/Ge-MFI$_{imp}$ catalyst could also be regenerated effectively even under ultrahigh WHSVs of 80.0 and 100.0 hours^{-1} for 20 consecutive cycles (fig. S26), which further validated its exceptional regeneration capability.

In our examination of the industrial counterpart, the Pt-Sn/Al_2O_3 catalyst, the rapid declines in both propane conversion and selectivity were observed in PDH (fig. S27). Additionally, this catalyst was incapable of regeneration by air calcination, with its performance substantially decreasing after only three cycles. We made a detailed comparison of the regeneration capability between our catalysts and state-of-the-art catalysts from recent reports, as shown in table S1 and Fig. 2C, which demonstrates that our catalysts had the highest level of regeneration capability.

In the industrial PDH process, Pt-based catalysts are conventionally regenerated every 5 to 7 days. We further tested the self-regeneration of our catalysts over a long period of 5 to 10 days under a high propane conversion of ~42%. This long duration resulted in the formation of heavy and graphitic coke, which is challenging to remove in the regeneration step. Nevertheless, despite the demanding test protocol, these catalysts completely self-regenerated during PDH (fig. S28). The anticipated lifetime of the representative Pt@Ge-MFI catalyst was at least 3 years (lifetime = single-pass reaction time × number of regenerations), assuming regeneration every 10 days for a total of 110 cycles. This long-expected lifetime is much higher than those found in previous reports (Fig. 2D) and highlights the potential of these catalysts for industrial implementation.

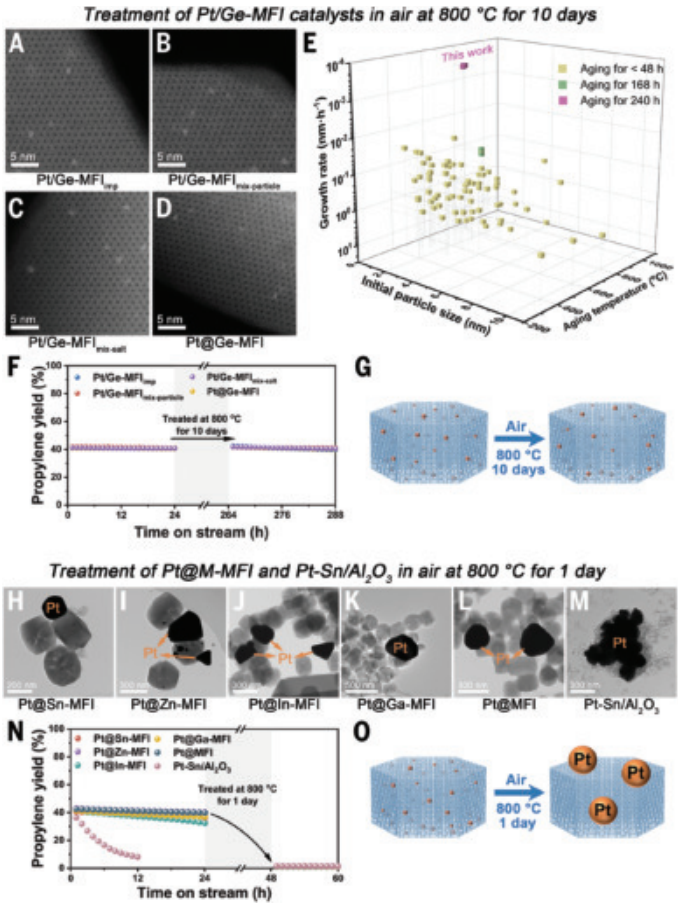

Fig. 3. Evaluation on thermal-oxidative stability of catalysts. (**A** to **D**) HAADF-STEM images of the Pt/Ge-MFI$_{imp}$ (A), Pt/Ge-MFI$_{mix-particle}$ (B), Pt/Ge-MFI$_{mix-salt}$ (C), and Pt@Ge-MFI (D) catalysts after treatment at 800°C in air for 10 days. (**E**) Comparison of the thermal stability of our catalysts with those of reported catalysts (for details, see table S3). (**F**) Propylene yield of Pt/Ge-MFI catalysts before and after treatment at 800°C in air for 10 days. (**G**) Illustration of thermal-oxidative treatment of Pt/Ge-MFI catalysts. (**H** to **M**) TEM images of reference catalysts (Pt@Sn-MFI, Pt@Zn-MFI, Pt@In-MFI, Pt@Ga-MFI, Pt@MFI, and Pt-Sn/Al_2O_3) after treatment at 800°C in air for 1 day. (**N**) Propylene yield of reference catalysts before and after treatment at 800°C in air for 1 day. (**O**) Illustration of the structural change of reference catalysts in the thermal-oxidative process.

We ascribed the self-regeneration of these catalysts to the ultrahigh thermal-oxidative stability of Pt species within Ge-MFI. To validate this hypothesis, we implemented a severe treatment protocol that exposed these catalysts to air at 800°C for 10 days, followed by reduction for TEM characterization and PDH. These four catalysts exhibited thermal-oxidative stability under these conditions. No sintered Pt particles were observed in the TEM characterization (fig. S29), and STEM analysis confirmed that Pt clusters remained intact within the channels of the MFI zeolite (Fig. 3, A to D, and fig. S30). Thus, these metal cluster catalysts remained stable in air at 800°C for 10 days, and their stability surpassed those of the reported catalysts (Fig. 3E and table S3). Correspondingly, their catalytic performance was unaffected after such severe treatment, as shown in Fig. 3, F and G, and fig. S31.

In contrast to the Pt/Ge-MFI catalysts, Pt catalysts supported on other hetero-atomic MFI zeolites, which were prepared using impregnation and in situ encapsulation methods, showed low thermal-oxidative stability. Previous investigations suggested that these catalysts had improved sintering resistance during PDH in a reductive atmosphere; however, they exhibited instability during regeneration in an oxidative atmosphere (*41*–*44*). Treatment of these catalysts in air at 800°C for 1 day resulted in the formation of large Pt particles of 400 to 500 nm (Fig. 3, H to L, and figs. S32 to S34). Similarly, the industrial counterpart, Pt-Sn/Al_2O_3, also showed low thermal-oxidative stability. After 1 day of thermal-oxidative treatment, the original ~1 nm Pt nanoparticles coalesced into quite large agglomerates of ~600 nm (Fig. 3M and fig. S35). Subsequent PDH assessments indicate that these treated catalysts suffered from severe deactivation, with the propylene yield approaching zero (Fig. 3N and figs. S36 and S37).

We attributed the instability of these reference catalysts under thermal-oxidative conditions to their inadequate ability to retain PtO_2 species. PtO_2 has a markedly lower melting point compared with metallic Pt: 450°C versus 1755°C, respectively (*45*). At elevated temperatures in an oxidative environment, highly volatile PtO_2 forms and cannot be firmly retained by these supports. Consequently, the Ostwald ripening process occurs, leading to sintering (Fig. 3O) (*46*).

Structural studies

We used operando x-ray absorption fine structure (XAFS) spectroscopy (fig. S38), in combination with in situ Fourier transform infrared (FTIR) spectroscopy of CO adsorption, in situ x-ray photoelectron spectroscopy (XPS), and TEM techniques, to track the structural evolutions of Pt/Ge-MFI in the reaction and regeneration process. The experiment protocol followed a closed-loop sequence: activation in H_2 (stage I) → PDH (stage II) → calcination in air (stage III) → postreduction in H_2 (stage IV), as shown in fig. S39.

The structure of Pt/Ge-MFI remained consistent in stages I, II, and IV under reductive conditions, as evidenced by the x-ray absorption near-edge structure (XANES) and extended x-ray absorption fine structure (EXAFS) spectra of the Pt L_3-edge (Fig. 4, A and B, and fig. S40), which remained similar across these three stages. The XANES white-line intensity approximated that of the Pt foil reference, signifying the formation of metallic Pt. The presence of metallic Pt was further corroborated by the XPS spectrum shown in Fig. 4C.

The nature of metallic Pt was deduced from the EXAFS fitting results (fig. S41 and table S4). Specifically, the Pt–Pt bond with a low coordination number of ~4.0 suggested the formation of small

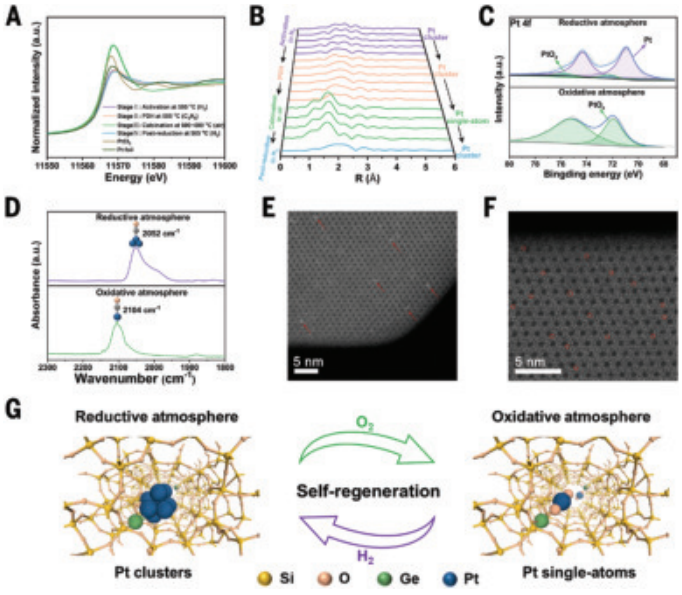

Fig. 4. Operando and in situ spectroscopy for tracking the self-regeneration of Pt/Ge-MFI in PDH. (**A** and **B**) Normalized Pt L_3-edge XANES spectra (A) and k^2-weighted Pt L_3-edge EXAFS spectra (B) collected during the reaction and regeneration process. (**C** and **D**) In situ Pt 4f XPS spectra (C) and in situ CO-adsorbed FTIR spectra (D) of Pt/Ge-MFI after treatment in a reductive or oxidative atmosphere. (**E**) HAADF-STEM image of the Pt/Ge-MFI catalyst after reduction (red arrow denotes the Pt cluster). (**F**) HAADF-STEM image of the Pt/Ge-MFI catalyst after thermal-oxidative aging (red cycle denotes the Pt single atom). (**G**) Illustration of the self-regeneration of Pt/Ge-MFI in PDH.

Pt clusters. Furthermore, the detection of Pt–O and Pt–Ge bonds indicated that Pt clusters were chemically anchored onto the Ge-MFI zeolite. In the FTIR spectrum of CO adsorption, the band at 2052 cm^{-1} further confirmed the presence of Pt clusters (Fig. 4D). The Pt clusters within the zeolite channels were directly visible using STEM (Fig. 4E and fig. S42). The dimensions of the Pt clusters were estimated based on the EXAFS fitting results (for calculation details, see table S5), indicating that each cluster comprises about eight Pt atoms with a size of ~0.60 nm. Note that the Pt_8 structure represents the average configuration rather than the exact structure of the Pt clusters; however, the properties and insights obtained from this model can be generalized to describe the behavior of Pt clusters with varying atomicity.

Upon oxidative regeneration of Pt/Ge-MFI in stage III, there was an increase in the XANES white-line intensity (Fig. 4A and fig. S40), suggesting the formation of oxidized Pt species. The white-line intensity was stronger than that of the $PtCl_2$ reference, implying that the Pt species remained in a high oxidation state. The XPS spectrum shown in Fig. 4C further confirmed the formation of oxidized Pt species. EXAFS spectra revealed the presence of only Pt–O and Pt–O–Ge scattering paths, with no evidence of Pt–Pt and Pt–O–Pt scattering paths, strongly indicating the formation of atomically dispersed Pt single atoms (*47*). The distinct peak at 2104 cm^{-1} in the FTIR spectrum of CO adsorption (Fig. 4D) further supported the presence of Pt single atoms (*48*). The Pt single atoms within Ge-MFI were directly observed in STEM (Fig. 4F and fig. S43). We deduce that the oxidative regeneration resulted in a transformation of Pt clusters into Pt single atoms.

The XANES and EXAFS spectra of the Ge K-edge were also measured during the reaction and regeneration process (figs. S44 and S45). The XANES spectra closely resembled that of the GeO_2 reference in the entire process, indicating that Ge predominantly existed as Ge(IV), even under the reductive conditions. The EXAFS fitting results for the Ge K-edge are presented in figs. S46 and S47 and table S6. The identification of Ge–O and Ge–O–Si bonds, along with the absence of a Ge–O–Ge scattering path, confirmed that Ge atoms were incorporated into the MFI framework.

The results of H_2 temperature-programmed reduction and NH_3 temperature-programmed desorption in fig. S48 further substantiate the incorporation of Ge into the MFI framework. Ge atoms in zeolite framework play a key role in stabilizing Pt single atoms and Pt clusters. The detection of a Ge–O–Pt bond with a coordination number of 1.1 in the oxidative step confirmed the anchoring of Pt single atoms onto Ge atoms through Pt–O–Ge linkages. The formation of a Ge–Pt bond with a coordination number of 0.2 to 0.4 in the PDH and reduction steps verified that Pt clusters were also anchored on the Ge atoms. Recent studies showed that silanol nests are responsible for trapping the metal species in zeolite structure (*29*, *30*, *49*). However, the results of the in situ FTIR measurement shown in fig. S49 is evidence that Pt species were not captured by silanol nests.

The characterization results showed that these catalysts dynamically reconfigure structure in response to atmospheric changes (Fig. 4G). During the PDH under reductive conditions, Pt existed as clusters comprising about eight atoms. When exposed to the oxidative atmosphere for regeneration, these Pt clusters dispersed into isolated Pt single atoms anchored on Ge atoms within the zeolite framework. In the subsequent reduction step, these Pt single atoms reassembled into Pt clusters. This reversible switch between Pt clusters and Pt single atoms was demonstrated in four cycles of reaction and regeneration, as shown in figs. S50 and S51. This environmental adaptability allowed the catalysts to completely self-regenerate during the PDH operation.

Finally, we conducted comprehensive investigations to elucidate the dispersion behavior and underlying mechanism of H_2PtCl_6 spontaneously dispersing in Ge-MFI for producing Pt/Ge-MFI (figs. S52 to S63 and tables S7 and S8). The operando XAFS results revealed that the dispersion process of H_2PtCl_6 was similar to the self-regeneration process of Pt/Ge-MFI. Aging the mixture of H_2PtCl_6 and Ge-MFI in air at high temperature induced a gradual decomposition of H_2PtCl_6 into PtO_2. The volatile PtO_2 was subsequently captured by Ge atoms in the zeolite framework, which follows the atom-trapping mechanism, as reported previously (*37*). Such capture resulted in the formation of Pt single atoms within the Ge-MFI channels (fig. S62, A to C). Subsequent reductive treatment facilitated the transformation of the Pt single atoms into Pt clusters, producing a supported Pt cluster catalyst (fig. S62, D to F).

Theoretical studies

Periodic density functional theory calculations were performed to address the thermodynamics of the reversible transformations between the Pt_8 cluster and the Pt single-atom motif in the Ge-MFI zeolite. PtO_2 is likely the atomic motif after the redispersion of the Pt_8 cluster (fig. S64). The fully atomic redispersion to the PtO_2 motif was exothermic by 1.08 eV, and an energy of at least 1.50 eV was required to strip the atomic PtO_2 motif from the Pt_8 cluster in the initial stage. The thermodynamic plot indicated that such a fully atomic redispersion process became feasible under lower temperatures, higher O_2 pressures, or both as a result of the entropy effect (Fig. 5A). The reclustering of the individual PtO_2 motif into the Pt_8 cluster occurred quite readily, because it was exothermic by >3.0 eV for each motif under all simulated reductive conditions (fig. S65).

Ab initio molecular dynamic (AIMD) simulations of 100 ps at 973 K were performed to address the effect of the framework Ge atom in MFI zeolite on the stability of the Pt_8 cluster and the individual PtO_2 motif. The Ge atom exhibited more significant stabilization effect on the PtO_2 motif than on the Pt_8 cluster. The individual PtO_2 motif was severely restricted near the Ge atom in the Ge-MFI zeolite during AIMD simulation, and the Pt–O–Ge moiety was well preserved, whereas the PtO_2 motif diffused more freely in Si-MFI, Sn-MFI, Zn-MFI, and Ga-MFI zeolites (Fig. 5, B to F).

The results were further confirmed by mean square displacement analysis (Fig. 5G). In the case of the motion of Pt_8 cluster, the MFI

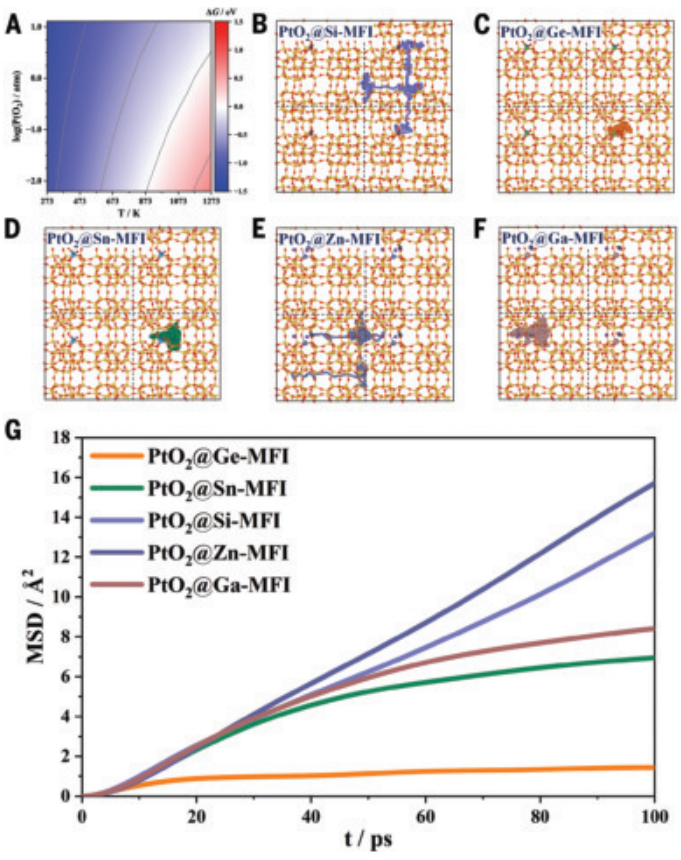

Fig. 5. Theoretical calculation on the self-regeneration process. (**A**) Plot of dispersion free energy with temperature and O_2 pressure from the Pt_8 cluster to the individual PtO_2 motif in Ge-MFI. (**B** to **G**) Motion trajectories [(B) to (F)] and mean square displacements (G) of the Pt atom in single PtO_2 motif in Si-MFI, Ge-MFI, Sn-MFI, Zn-MFI, and Ga-MFI zeolites from AIMD simulations for 100 ps at 973 K.

channels in both Ge-MFI and Si-MFI zeolites imposed obvious confinement, although the framework Ge atoms exhibited an additional stabilization effect on the Pt cluster, particularly Pt atoms close to Ge atoms (fig. S66). The stabilization of the zeolite matrix on the individual PtO_2 motif after dispersion of the Pt cluster is thus pivotal for the design of sintering-resistant zeolite-based catalysts.

Discussion

The spontaneous metal dispersion in Ge-zeolites establishes a robust and universal methodology for fabricating various noble metal cluster catalysts. The scalability of this approach was demonstrated by a successful kilogram-scale production of Pt/Ge-MFI (figs. S67 and S68), indicating promising potential for industrial application. Furthermore, Rh, Ru, Ir, and Pd cluster catalysts supported on Ge-MFI and Ge-beta were also successfully synthesized (figs. S69 and S70). Rh/Ge-MFI, Pt/Ge-beta, and Rh/Ge-beta also demonstrate cluster dispersion and reformation during the reaction and regeneration cycles in PDH, as shown in figs. S71 to S73. This research will pave the way for the design and application of catalysts that can maintain activity during gas and temperature cycling conditions.

REFERENCES AND NOTES

1. B. C. Gates, *Chem. Rev.* **95**, 511–522 (1995).
2. T. W. Hansen, A. T. Delariva, S. R. Challa, A. K. Datye, *Acc. Chem. Res.* **46**, 1720–1730 (2013).
3. S. Hu, W. X. Li, *Science* **374**, 1360–1365 (2021).
4. E. D. Goodman, J. A. Schwalbe, M. Cargnello, *ACS Catal.* **7**, 7156–7173 (2017).
5. S. E. Wanke, P. C. Flynn, *Catal. Rev., Sci. Eng.* **12**, 93–135 (1975).
6. Y. Dai, P. Lu, Z. Cao, C. T. Campbell, Y. Xia, *Chem. Soc. Rev.* **47**, 4314–4331 (2018).
7. J. Lu *et al.*, *Science* **335**, 1205–1208 (2012).
8. M. Cargnello *et al.*, *Science* **337**, 713–717 (2012).
9. J. A. Farmer, C. T. Campbell, *Science* **329**, 933–936 (2010).
10. L. Nie *et al.*, *Science* **358**, 1419–1423 (2017).
11. Y. Nishihata *et al.*, *Nature* **418**, 164–167 (2002).
12. M. Helmer, *Nature* **418**, 138 (2002).
13. M. Kothari *et al.*, *Nat. Chem.* **13**, 677–682 (2021).
14. G. Centi, *SmartMat* **1**, e1005 (2020).
15. H. Tanaka *et al.*, *Angew. Chem. Int. Ed.* **45**, 5998–6002 (2006).
16. M. B. Katz *et al.*, *J. Am. Chem. Soc.* **133**, 18090–18093 (2011).
17. S. Hou *et al.*, *Nat. Commun.* **12**, 5917 (2021).
18. C. Lin *et al.*, *ACS Catal.* **9**, 7318–7327 (2019).
19. X. Mao, C. Lin, G. W. Graham, R. J. Gorte, *ACS Catal.* **10**, 8840–8849 (2020).
20. S. Chen *et al.*, *Chem. Soc. Rev.* **50**, 3315–3354 (2021).
21. J. J. H. B. Sattler, J. Ruiz-Martinez, E. Santillan-Jimenez, B. M. Weckhuysen, *Chem. Rev.* **114**, 10613–10653 (2014).
22. Y. Ma *et al.*, *Nat. Catal.* **6**, 506–518 (2023).
23. L. Zeng *et al.*, *Science* **383**, 998–1004 (2024).
24. R. Almallahi, J. Wortman, S. Linic, *Science* **383**, 1325–1331 (2024).
25. S. Chen *et al.*, *Science* **385**, 295–300 (2024).
26. W. Wang *et al.*, *Science* **381**, 886–890 (2023).
27. R. T. Hannagan *et al.*, *Science* **372**, 1444–1447 (2021).
28. H. Yan *et al.*, *Science* **371**, 1257–1260 (2021).
29. D. Zhao *et al.*, *Nature* **599**, 234–238 (2021).
30. R. Ryoo *et al.*, *Nature* **585**, 221–224 (2020).
31. A. H. Motagamwala, R. Almallahi, J. Wortman, V. O. Igenegbai, S. Linic, *Science* **373**, 217–222 (2021).
32. K. Morgan, A. Goguet, C. Hardacre, *ACS Catal.* **5**, 3430–3445 (2015).
33. G. Ren *et al.*, *J. Catal.* **429**, 115276 (2024).
34. J. Liu *et al.*, *Appl. Surf. Sci.* **368**, 233–240 (2016).
35. H. Zhang, H. Wan, Y. Zhao, W. Wang, *Catal. Today* **330**, 85–91 (2019).
36. M. Sun, Z. Hu, H. Wang, Y. Suo, Z. Yuan, *ACS Catal.* **13**, 4719–4741 (2023).
37. J. Jones *et al.*, *Science* **353**, 150–154 (2016).
38. C. Li, G. Wang, *Chem. Soc. Rev.* **50**, 4359–4381 (2021).
39. Z. Lian, C. Si, F. Jan, S. Zhi, B. Li, *ACS Catal.* **11**, 9279–9292 (2021).
40. E. E. Wolf, F. Alfani, *Catal. Rev., Sci. Eng.* **24**, 329–371 (1982).
41. L. Liu *et al.*, *Nat. Catal.* **3**, 628–638 (2020).
42. Q. Sun *et al.*, *Angew. Chem. Int. Ed.* **59**, 19450–19459 (2020).
43. L. Luo *et al.*, *Nano Lett.* **24**, 7236–7243 (2024).
44. Y. Wang, Y. Suo, X. Lv, Z. Wang, Z. Y. Yuan, *J. Colloid Interface Sci.* **593**, 304–314 (2021).
45. M. Rahmati, M.-S. Safdari, T. H. Fletcher, M. D. Argyle, C. H. Bartholomew, *Chem. Rev.* **120**, 4455–4533 (2020).
46. S. Ma, Z. P. Liu, *Nat. Commun.* **13**, 2716 (2022).
47. X. Li *et al.*, *Nature* **611**, 284–288 (2022).
48. K. Ding *et al.*, *Science* **350**, 189–192 (2015).
49. L. Liu *et al.*, *Science* **383**, 94–101 (2024).

ACKNOWLEDGMENTS

We appreciate use of the hard x-ray spectroscopy beamline (BL20U1), the user experiment assist system, and the Chinese Academy of Sciences-Shanghai Synchrotron Radiation Facility for data collection. **Funding:** This work was supported by the National Key R&D Program of China (grant 2021YFA1500302), the National Natural Science Foundation of China (grants 22478076, 22221005, 22408208, 22178062, 21878050, U23A20113, and U22B6011), the Industrial Joint Fund of Qingyuan Innovation Laboratory (grant 00422001), the 111 Project (grant D17005), the Foundation of State Key Laboratory of Coal Conversion (grant J21-22-620), and the European Union (project HORIZON-WIDERA-2021-ACCESS-03-01, grant 101079384). **Author contributions:** H.H. and Z.X. performed the catalyst preparation, characterization, and catalytic tests. C.W. and W.H. performed the theoretical simulations and wrote the corresponding sections of the paper. P.F. and C.W. provided helpful discussions on catalytic performances, catalyst structures, and comparisons with the commercial catalyst. B.M. participated in the XAFS characterizations. T.W., Y.Y., T.L., C.Y., and Q.C. participated in catalyst synthesis and characterization. H.Z. and X.B. designed the study, analyzed the data, and wrote the paper. **Competing interests:** H.Z., X.B., H.H., and Z.X. are inventors listed on Chinese patents 202510244888.1, 202510243450.1 and 202510243295.3 filed by Fuzhou University, which cover the Pt/Ge-MFI catalysts reported in this paper. The authors declare no competing interests. **Data and materials availability:** All data are available in the manuscript or the supplementary materials.

SUPPLEMENTARY MATERIALS

science.org/doi/10.1126/science.adu6907
Materials and Methods; Figs. S1 to S73; Tables S1 to S8; References (*50–134*)

Submitted 18 November 2024; resubmitted 5 February 2025; accepted 7 March 2025; published online 10 April 2025

10.1126/science.adu6907

QUANTUM SIMULATION

Coherent evolution of superexchange interaction in seconds-long optical clock spectroscopy

William R. Milner[1]*, Stefan Lannig[1], Mikhail Mamaev[1,2], Lingfeng Yan[1], Anjun Chu[1,2], Ben Lewis[1], Max N. Frankel[1], Ross B. Hutson[1], Ana Maria Rey[1,2], Jun Ye[1]*

Scaling up the performance of atomic clocks requires understanding complex many-body Hamiltonians to ensure meaningful gains for metrological applications. Here we use a degenerate Fermi gas loaded into a three-dimensional optical lattice to study the effect of a tunable Fermi-Hubbard Hamiltonian. The clock laser introduces a spin-orbit coupling spiral phase and breaks the isotropy of superexchange interactions, leading to XXZ-type spin anisotropy. By tuning the lattice confinement and applying imaging spectroscopy, we map out favorable atomic coherence regimes. We transition through various interaction regimes and observe coherent superexchange, tunable through on-site interaction and site-to-site energy shift, affecting the Ramsey fringe contrast over timescales >1 second. This study lays the groundwork for using a three-dimensional optical lattice clock to probe quantum magnetism and spin entanglement.

Optical lattice clocks are advancing studies of fundamental physics, metrology, and quantum simulation (*1*–*7*). By controlling all external perturbations to the ground and metastable "clock" state, each one of the confined atoms becomes a pristine, two-level system. With clock precision limited fundamentally by quantum projection noise (*8*), a natural approach for improving clock performance is to probe the largest possible number of atoms combined with the longest possible coherence time. However, in a densely packed sample of atoms, outstanding challenges remain, including maximizing the coherence time for clock precision and evaluating systematic effects for clock accuracy. Often it is desirable to minimize atomic interactions to enhance single-particle coherence and control systematic effects. At the same time, as the understanding of these interactions becomes more sophisticated, we can engineer a large, coherent spin ensemble with interaction precisely controlled to introduce and optimize quantum coherence, correlation, and entanglement to advance the frontier of quantum metrology (*9*–*12*).

With the ease of geometry tunability, optical lattices provide a versatile platform to confine large numbers of atoms and control their interactions and motion. Over the past two decades, progress in clock precision (*13*, *14*) has been largely advanced by the study and control of interactions in one-dimensional (1D) optical lattice clocks. The corresponding interaction dynamics are well described by a collective spin model (*15*, *16*) that includes both on-site *p*-wave interactions and off-site *s*-wave interactions. The latter are induced by the spin-orbit coupling (SOC), arising from a mismatch between clock wavelength and lattice spacing (*17*, *18*), which lifts the indistinguishability between spin-polarized fermions on neighboring lattice layers. Systematic exploration of this 1D spin model identified a confinement depth at which the combination of *s*- and *p*-wave interactions suppressed detrimental mean-field density shifts (*1*, *19*). Introducing a three-dimensional (3D) lattice confinement for scaling up the density (*20*) allows further increase of strength of the elastic and inelastic collisions to the point of strongly suppressing all *p*-wave interactions and making *s*-wave interactions spectroscopically resolvable (*21*). Optimizing the atomic coherence times for best clock performance requires balancing lattice-induced Raman scattering and motional dephasing at deep and shallow lattice depths, respectively (*22*). This study explores different lattice confinement regimes to characterize the impact of higher-order interaction effects, arising from virtual tunneling, on the atomic coherence.

3D lattice spin model

In a 3D lattice filled with a degenerate Fermi gas of spin-polarized ^{87}Sr atoms in the motional ground state (*23*), the system can be modeled with the Fermi-Hubbard Hamiltonian in which ground and excited state atoms on the same lattice site interact through the Hubbard interaction parameter U, and motion is captured by a tunneling parameter t. In the unity filled limit, a Mott-insulating regime emerges at $U \gg t$, atomic motion is restricted, and atoms interact only through virtual second-order tunneling processes that induce spin-exchange couplings between nearest-neighbor atomic spins known as superexchange (*24*–*26*). The physics of superexchange is central in describing magnetic phenomena such as antiferromagnetism (*27*, *28*) and is believed to play a role in superconductivity (*29*). Several ultracold atom experiments have used optical lattices to explore low-temperature bosonic ferromagnetic and fermionic antiferromagnetic correlations induced by superexchange (*30*–*37*), as well as some nonequilibrium superexchange-driven quantum dynamics in local density probes (*38*–*40*). With the goal of achieving optimal and scalable clock performance at a unity filled 3D lattice, understanding and controlling the effects of superexchange on collective spin dynamics become necessary (*20*, *21*). The current work using seconds-long Ramsey spectroscopy on tens of thousands of atoms directly probes the coherent nature of superexchange interaction, thus strengthening our understanding of interaction regimes that are favorable for robust quantum coherence and entanglement.

Here we load a degenerate Fermi gas of ^{87}Sr atoms into a 3D lattice with tunable confinement to explore the 3D lattice spin model. The interaction effects on spin coherence between the ground and metastable clock state are directly recorded on Ramsey fringes, which are modulated by coherent superexchange interactions. These experimental observations are well captured by an anisotropic lattice spin model (XXZ plus antisymmetric exchange terms), which breaks the Heisenberg SU(2) symmetry of the Fermi-Hubbard physics because of the SOC induced by the clock laser (*17*, *18*, *41*, *42*). Such interactions can also be directly used for the generation of large-scale quantum entanglement over the entire 3D lattice system (*43*–*45*).

The experimental schematic is depicted in Fig. 1A. After evaporation, we confine the atoms in a retroreflected, cubic lattice operating at the magic wavelength of $\lambda_{magic} = 813$ nm with lattice constant $a \approx 407$ nm (*20*). Beginning with a nuclear spin–polarized Fermi gas with a reduced temperature $T/T_F \approx 0.2$, where T_F is the Fermi temperature, the atoms are adiabatically loaded into the ground band of the 3D lattice (*20*, *23*). In the deep lattice, the initial state is nearly a band insulator with a peak filling of one atom per lattice site (*4*, *46*). The lattice depth $(V_\perp)$ of the transverse (horizontal with respect to gravity) confinement is tuned independently from the depth of the vertical confinement (V_z) by adjusting the optical power in the corresponding lattice beams. Our two-level spin system is established between the ground $^1S_0$ ($|g\rangle$) and metastable electronic "clock" state $^3P_0$ ($|e\rangle$). We coherently drive the clock transition $|g, m_F = -9/2\rangle \leftrightarrow |e, m_F = -9/2\rangle$

[1]JILA, National Institute of Standards and Technology and University of Colorado, Boulder, CO, USA. [2]Center for Theory of Quantum Matter, University of Colorado, Boulder, CO, USA.
*Corresponding author. Email: william.milner@colorado.edu (W.R.M.); ye@jila.colorado.edu (J.Y.)

at $\lambda_{clk} \approx 698$ nm with a vertical laser beam using an optical local oscillator locked to an ultrastable silicon cavity (*47*).

Ramsey spectroscopy

After loading the lattice, we put the atoms into a superposition of $|g\rangle$ and $|e\rangle$ and perform Ramsey spectroscopy. For detection, in situ absorption imaging along the vertical direction is used and ~100 photons per atom are scattered over a 1-μs pulse duration with minimal blurring compared to the diffraction-limited point-spread function of 1.3 μm (*4*, *46*). Two images of the ground and clock state atoms, their numbers denoted N_g and N_e, are taken to determine the excitation fraction $p_e = N_e / (N_e + N_g)$. For a chosen region of interest P_A of our imaged density distribution, we record the local excitation fraction $p_e^A = N_e^A / \left(N_e^A + N_g^A\right)$. This is shown in Fig. 1A, where the excitation fractions are evaluated in spatially separate regions P_1 and P_2 to determine both the Ramsey fringe contrast C and relative atomic coherence using imaging spectroscopy (*48*).

To evaluate atomic coherence that is related to clock performance at different lattice confinement, we measure the Ramsey fringe contrast for varying dark time T. An XY8 sequence consisting of eight π pulses along the two orthogonal rotation axes in the equatorial plane of the Bloch sphere is used to remove single-particle dephasing as depicted in Fig. 2A (*49*, *50*). To decouple the atomic coherence measurement from the finite atom–light coherence time (~3 s) (*47*), the phase of the final Ramsey π/2 pulse is randomized. Parametric plots of the excitation fractions from concentric regions P_1 and P_2 ($P_1 < 6$ μm and 6 μm $< P_2 <$ 12 μm with respect to the trap center) are used to determine the contrast as shown in Fig. 2B . These parametric plots show ellipses, where a maximum likelihood estimator determines the ellipse contrast and jackknifing is used to extract 1σ (standard deviation) error bars for all Ramsey contrast measurements (*48*). The system is sufficiently homogeneous in the spatial regions P_1 and P_2 that the contrast is approximately the same (*51*). No statistically significant phase shift between P_1 and P_2 is measured, indicating that the XY8 pulse sequence largely removes any spatially varying frequency shift.

As a function of dark time T, a stretched exponential function $C_0 e^{-(T/T_2)^\alpha}$ is fit to the Ramsey contrast to extract a T_2 coherence time for $T > 1$ s in order to reject fast transient oscillatory dynamics. For $V_\perp = 0$, we expect different timescales between inter- and intrasite interactions, leading to Gaussian decoherence. We extract a single value $\alpha = 1.38$ by minimizing the combined χ^2 for all measurements for $V_\perp = 0$. For all other measurements with $V_\perp > 0$, we set $\alpha = 1$ when fitting T_2. The extracted quality factor $Q = \pi C_0 T_2 \nu$ is plotted in Fig. 2C, where ν is the clock transition frequency ≈429 THz. We identify three principal regimes: (i) In the 1D lattice regime with no transverse confinement, the longest coherence times are observed; here, the growth of spin excitations caused by on-site and nearest-neighbor interactions is minimized (*1*, *15*, *19*). However, inelastic on-site p-wave collisions between excited state atoms during the Ramsey dark time lead to a strong loss in atom number with a $1/e$ lifetime of <5 s at the density used in this experiment [see fig. S6 in (*51*)]. In contrast, the atom lifetime in a strong transverse lattice is about 19 s. This renders the 1D limit less favorable for clock operation at high density. (ii) With deep transverse confinement, where the average superexchange coupling strength $\bar{J}_{SE}/h \gtrsim 1$ Hz, coherent superexchange dynamics are observed on the Ramsey fringe contrast over a timescale of seconds (Figs. 3 and 4). Here, the system consists of individual tubes, and each atom acts as a spin-½ particle that interacts with its vertical neighbors. As previously reported (*22*), the deep 3D lattice regime (iii), where $\bar{J}_{SE}/h \ll 1$ Hz, reveals a limit on the coherence time primarily due to Raman scattering of lattice photons on e atoms. This motivates us to investigate the spin dynamics in the intermediate 3D confinement regime (ii) as potential operating conditions for future 3D lattice clocks. The dark times in this study ($T < 16$ s) are short compared to both the $^1S_0$ lattice lifetime and vacuum lifetime (*51*).

During the Ramsey interrogation time, the atoms interact via the Fermi-Hubbard model presented in Fig. 1B (*52*). For our fermionic atoms, Fermi statistics forbids two spin-aligned atoms from populating the same lattice site within the ground band. Thus, in the dense limit with one atom per site, only atoms in opposite electronic states can tunnel along the vertical direction z with rate t_z/h and interact with on-site interaction $U = \frac{4\pi\hbar^2}{m} a_{eg-} \int |W(\mathbf{r})|^4 d^3\mathbf{r}$. These interactions are determined by the s-wave scattering length $a_{eg-} = 69.1(0.9) a_B$ between antisymmetric electronic states (*16*, *21*), and the 3D, single-particle Wannier function $W(\mathbf{r})$ is determined by the lattice confinement. Along the vertical direction, the atoms also experience both the linear gravitational potential and the confinement from the Gaussian transverse lattice beams, leading to an energy offset ΔE_j between adjacent vertical lattice planes indexed by j (*53*). The clock laser is also launched along the

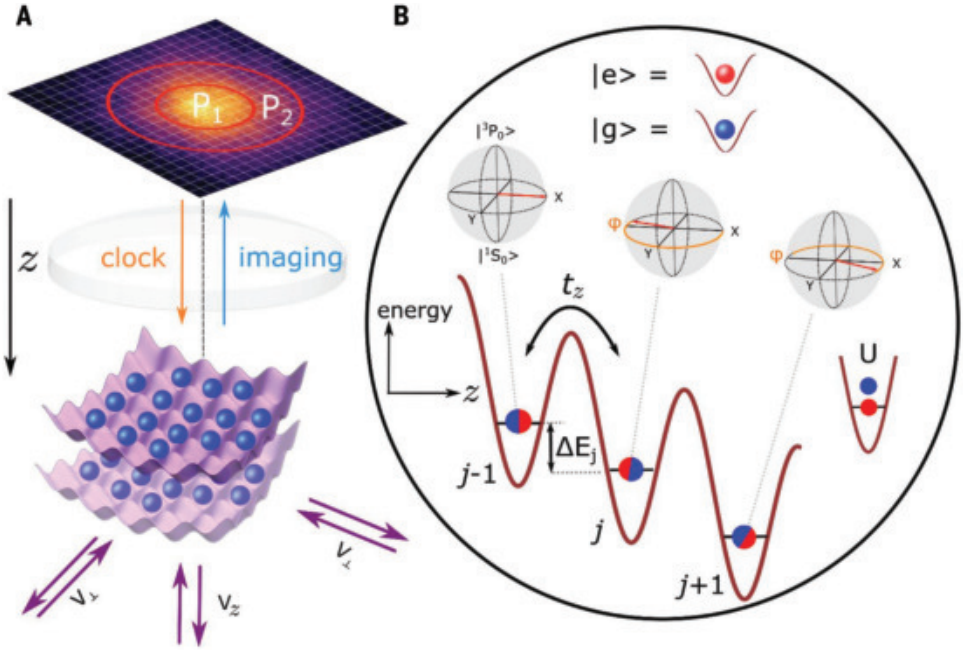

Fig. 1. Experimental setup and interaction model. (**A**) Ultracold fermions are confined in the ground band of a 3D optical lattice with tunable confinement. Lattice depths can be independently varied by changing the optical power of retro-reflected beams in the transverse direction $V_\perp$ or vertical direction V_z. In situ imaging allows spatially resolved interactions and dephasing by imaging spectroscopy (*48*). (**B**) Dynamics are described by the Fermi-Hubbard model with tunneling t_z, interaction energy U, and a site-to-site energy shift ΔE_j from the lattice Gaussian confinement. Atoms along the z axis on sites indexed $j-1$, j are initialized in a superposition state of the ground state $|g = {}^1S_0\rangle$ and the metastable electronic state ("clock" state) $|e = {}^3P_0\rangle$, with spin-orbit coupling arising from the phase advancement φ of the clock laser between lattice sites. Dephasing of the coherence is proportional to an effective superexchange rate: $4t_z^2 U / \left(U^2 - \Delta E_j^2\right)$.

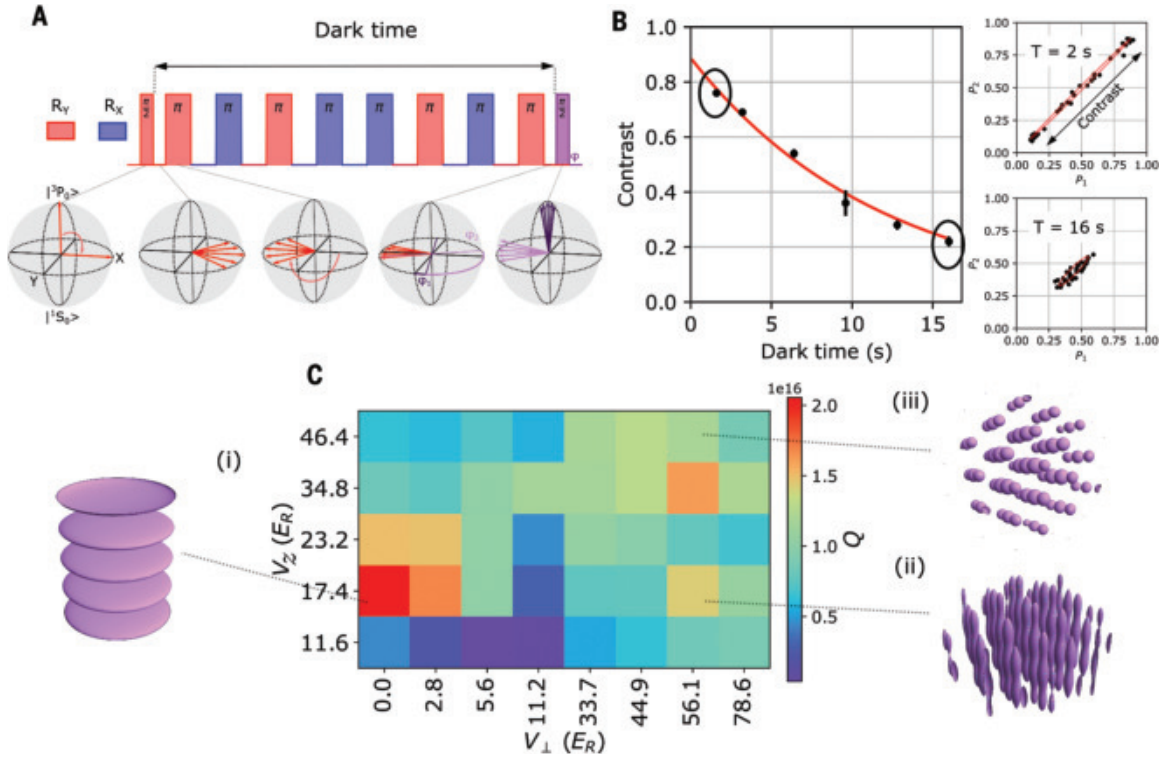

Fig. 2. Coherence time measurement. (**A**) Ramsey spectroscopy is used to study the coherence time. An XY8 pulse sequence is used to mitigate single-particle dephasing. The dephasing and rephasing of individual spins are depicted on the Bloch sphere during the echo sequence. For the final $\pi/2$ pulse, two choices of the randomized phase $\varphi_{1,2}$ are shown (light and dark purple) to illustrate the spread of resulting excitation fractions in individual realizations. (**B**) To determine the coherence time T_2, the contrast decay is fit to a stretched exponential $C(T) = C_0 e^{-(T/T_2)^\alpha}$ as a function of dark time T. Insets: The contrast is determined by parametric plots of excitation fractions in regions P_1 and P_2 of the ensemble as depicted in Fig. 1. Error bars are 1σ (standard deviation) obtained from jackknifing. (**C**) The quality factor $Q = \pi C_0 T_2 \nu$, where $\nu \approx 429$ THz, is plotted over a wide range of transverse and vertical confinement, where $E_R = h^2/8ma^2 \approx h \times 3.5$ kHz is the lattice photon recoil energy. Two candidate regimes are identified to investigate further: the weak or zero transverse confinement regime (i), where the longest optical lattice clock T_2 times have been reported (*1*); and regime (ii), where fast initial contrast decay is observed owing to superexchange interactions. The deep 3D lattice regime (iii) was studied on this platform in (*22*), where the coherence time is limited by Raman scattering of lattice photons.

vertical direction, setting a spin rotation axis that advances by a phase of $\varphi = 2\pi a/\lambda_{clk} \approx 7\pi/6$ between neighboring vertical lattice planes, thus inducing SOC (*17*, *22*) as depicted in Fig. 1B. This SOC phase is crucial in facilitating the generation of distinguishable spin states that enable tunneling and with it a path for on-site interaction U and superexchange.

Superexchange interactions

The superexchange oscillations, observed in the 3D confinement regime of our experiment with $V_z < V_\perp$ [regime (ii) in Fig. 2C], can be understood from a simple double-well model describing two atoms (spin $s = 1/2$) on two adjacent lattice sites $j = 0,1$ along the z lattice direction. The Ramsey spectroscopy protocol initializes the atoms in a superposition state $|\psi_{init}\rangle = (|g_0\rangle + |e_0\rangle)/\sqrt{2} \otimes (e^{-i\varphi/2}|g_1\rangle + e^{+i\varphi/2}|e_1\rangle)/\sqrt{2}$. Crucially, owing to the differential laser phase φ, aside from a global phase this initial state is an admixture of the spin triplet and singlet states, with $|\psi_{init}\rangle \sim e^{-i\varphi/2}|g,g\rangle + e^{i\varphi/2}|e,e\rangle + \cos(\varphi/2)(|g,e\rangle + |e,g\rangle) + i\sin(\varphi/2)(|g,e\rangle - |e,g\rangle)$. At half-filling and in the strongly interacting limit $U \gg t_z$, superexchange interactions arising between neighboring spins, $J_{SE}\hat{\mathbf{s}}_0 \cdot \hat{\mathbf{s}}_1$, introduce an energy shift for the singlet state, which translates to a phase difference $J_{SE}T$ compared to the triplet states during the coherent evolution time T. Here $\hat{\mathbf{s}}_j = (\hat{s}_j^X, \hat{s}_j^Y, \hat{s}_j^Z)$, with $\hat{s}_j^\ell$ referring to spin-1/2 matrices describing atoms on sites j in the lab frame.

More formally, we rotate into a "spiral" frame where the initial state is uniform (all atoms in the same superposition state) and the site-dependent laser phase φ is absorbed into the spin operators across the lattice, $\hat{s}_j^\pm = \hat{\tilde{s}}_j^\pm e^{\pm ij\varphi}$, $\hat{s}_j^Z = \hat{\tilde{s}}_j^Z$. Thus, we obtain a superexchange spin Hamiltonian in the spiral frame

$$\hat{H}_{SE} = \sum_j J_{SE}(j)\left[\frac{1}{2}\left(e^{i\varphi}\hat{s}_j^+\hat{s}_{j+1}^- + H.c.\right) + \hat{s}_j^Z\hat{s}_{j+1}^Z\right] \quad (1)$$

The superexchange interaction strength is $J_{SE}(j) = 4t_z^2 U/\left(U^2 - \Delta E_j^2\right)$, which is inhomogeneous owing to the local potential difference between adjacent sites ΔE_j, including gravity and the lattice Gaussian confinement. Furthermore, the spiral phase makes this spin Hamiltonian go beyond conventional superexchange interactions in optical lattices, as it exhibits exchange-symmetric XXZ-style anisotropy and an antisymmetric spin exchange term (*51*). Observables such as atomic coherence reveal collective quantum dynamics on timescales of the averaged $\bar{J}_{SE}$ over the ensemble, which is tuned by controlling the inhomogeneity and the lattice depth.

In Fig. 3, A and B, we show the contrast decay as a function of dark time for $V_\perp > V_z$, finding a clear oscillatory feature on timescales of the superexchange rate $\bar{J}_{SE}$. For these measurements, V_z is fixed to $17.4E_R$ at which $t_z \approx h \times 14.2$ Hz, where $E_R = h^2/8ma^2 \approx h \times 3.5$ kHz is the lattice photon recoil energy. $\bar{J}_{SE}$ is tuned by varying $V_\perp$ between 19.7 and $67.4E_R$, thus varying U/h from 1.2 to 2.3 kHz. In the $V_\perp \gg V_z$ regime, the system is composed of isolated vertical tubes along z as shown in Fig. 2C . We assume that all atoms within each tube are pinned in place even for non-unity filling, because the local potential difference is much stronger than tunneling ($\Delta E_j \gg t_z$). We further

assume that every uninterrupted chain of neighboring atoms within a given tube undergoes evolution under the superexchange Hamiltonian $\hat{H}_{SE}$. Their evolution is independent of other chains, and the contrast is an average over all chains. The curves in Fig. 3, A and B, show numerical predictions averaging over the full 3D system using calibrated experimental parameters and an optimized temperature, and include the overall slow decay in contrast reported in Fig. 2C, which find good agreement with the measurements. The extracted temperatures in the lattice indicate that our experiments operate at a central filling fraction of ≈0.5 ground-band atoms per lattice site.

To extract the superexchange rates, we vary $V_\perp$ and fit the experimentally measured contrast decay to the function $C_{SE}(T) = Ae^{-T/T_2} + B\cos(2\pi fT)e^{-T/T_{osc}} + D$. In Fig. 3C, the measured oscillation frequencies f are first compared to results derived from the same full many-body Hamiltonian used to generate the theory curves in Fig. 3, A and B (empty red squares). Here, the oscillation frequencies are extracted in the same way as for the measurement data. Additionally, we are also using a simplified theoretical model that averages over contributions of two-site pairs (blue line), which is expected to be valid for low-to-intermediate filling fractions, where long chains are unlikely. This calculation includes higher-order interaction effects such as bond-charge corrections to the tunneling rate t_z (*51*). The agreement with both theoretical models is excellent for intermediate $V_\perp$ between 22.5 and 45 E_R. For the deepest $V_\perp$, the experimentally measured rate appears to be higher frequency. Numerical calculations suggest this could arise from additional interaction inhomogeneity or light-scattering effects (*54*) that favor higher-frequency contributions. At shallow $V_\perp < 20E_R$, where $V_\perp \approx V_z$, our theoretical approximation of isolated vertical tubes breaks down and in-plane interactions become relevant. In Fig. 3D, the dark times of the contrast decay data are rescaled by the calculated superexchange rate from the two-site model (blue line in Fig. 3C). The rescaled data collapse to a single curve, reflecting the underlying superexchange dynamics in all measurements. This is also in agreement with a more general theoretical model that attempts to capture the effects of finite temperature and trap inhomogeneity without explicitly invoking experimental details. Instead, the superexchange couplings and chain lengths are randomly sampled from probability distributions that aim to capture the experimental parameters and inhomogeneity (*51*). We do not expect perfect rescaling owing to varying $J_{SE}(j)$ inhomogeneity caused by a change in lattice curvature as a function of $V_\perp$.

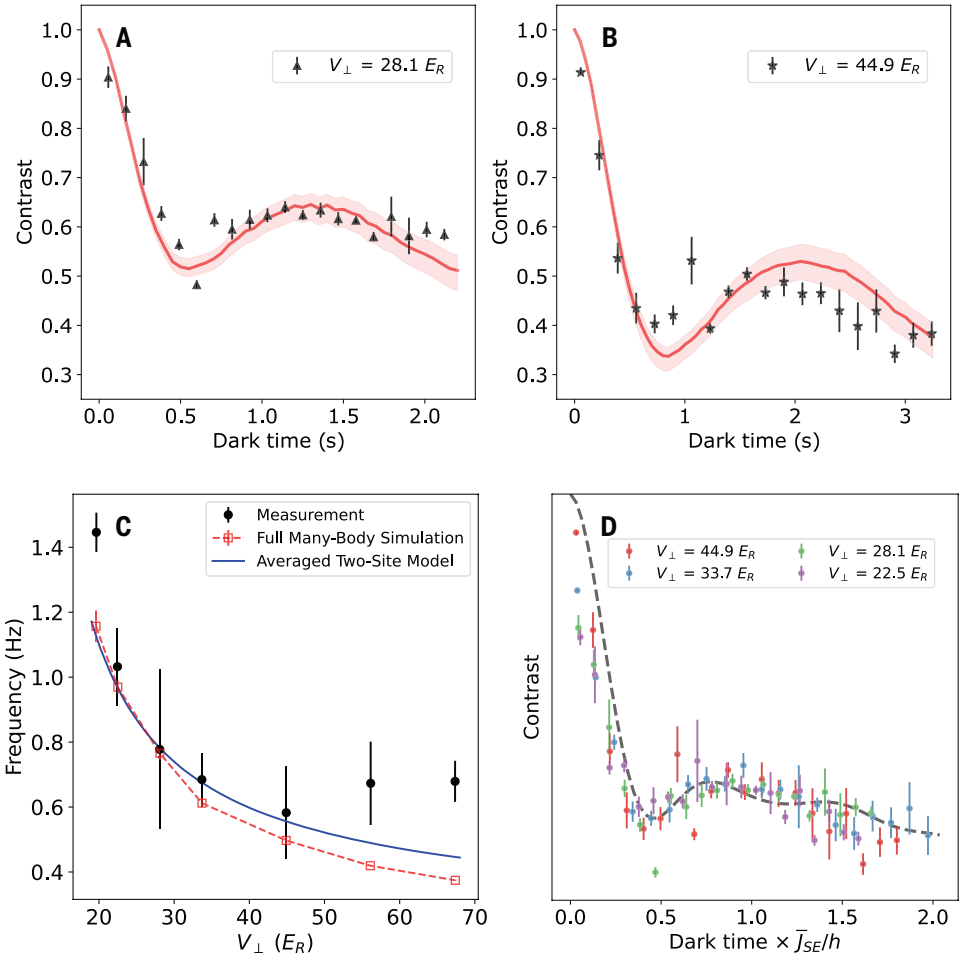

Fig. 3. Observing superexchange interactions. Ramsey contrast decay is studied in a 3D lattice at fixed $V_z = 17.4\,E_R$ and thus t_z, while $V_\perp$ is varied between ~70 and 20 E_R primarily modifying U. Decay curves at (**A**) $V_\perp = 28.1\,E_R$, and (**B**) 44.9 E_R, are plotted. Error bars are 1σ (standard deviation). Red lines are calculated averaging contrast decay in 1D chains initialized from a thermal distribution of the 3D cloud with fitted temperatures of 350(14) nK for $V_\perp = 28.1\,E_R$ and 322(17) nK for $V_\perp = 44.9\,E_R$ (*51*). The error bands stem from the uncertainty on the temperature and T_2. (**C**) Fitted contrast oscillation frequencies (black points) are compared to the fit results obtained from the full simulations as shown in (A) and (B) (red empty squares) and calculated superexchange frequency (blue line) including bond-charge corrections to t_z, which averages the expected oscillations with local ΔE_j and U along the imaging direction. Error bars are 1σ (standard deviation) uncertainty of the fitted frequency. (**D**) Contrast curves approximately collapse when dark times are rescaled by the calculated oscillation frequency (blue line in Fig. 3C). A simple simulation sampling spin chains with different lengths and coupling strengths (gray dashed line) is overlaid.

Controlling superexchange interactions

To study the properties of the interactions further, we vary the lattice filling and the energy offsets ΔE_j of the local lattice tilt in Fig. 4. First, the fraction of atoms participating in superexchange is reduced by imprinting holes in the lattice. Beginning with maximum filling, before Ramsey spectroscopy, a variable clock laser pulse area is used to shelve atoms in e with spatially uniform probability, and subsequently the remaining g atoms are removed with resonant light at 461 nm (Fig. 4A). The ensuing contrast decay as a function of the total atom number N is plotted in Fig. 4B . The oscillation amplitude, reflecting the fraction of atoms participating in superexchange, is strongly decreased as N is reduced owing to the increasing number of holes. Because of the reduced filling fraction at the wings of the atom cloud, this effect is also observed when choosing the region of interest to be an annulus and increasing its radius compared to P_2 [fig. S4 in (*51*)].

As the position of the atoms in the combined potential of gravity and the lattice confinement is shifted vertically, the site-to-site energy shift ΔE_j, and consequently the superexchange interaction strength, is strongly modified. We precisely move the cloud position at the micrometer scale (*51*). Figure 4D displays the resulting oscillations for several values

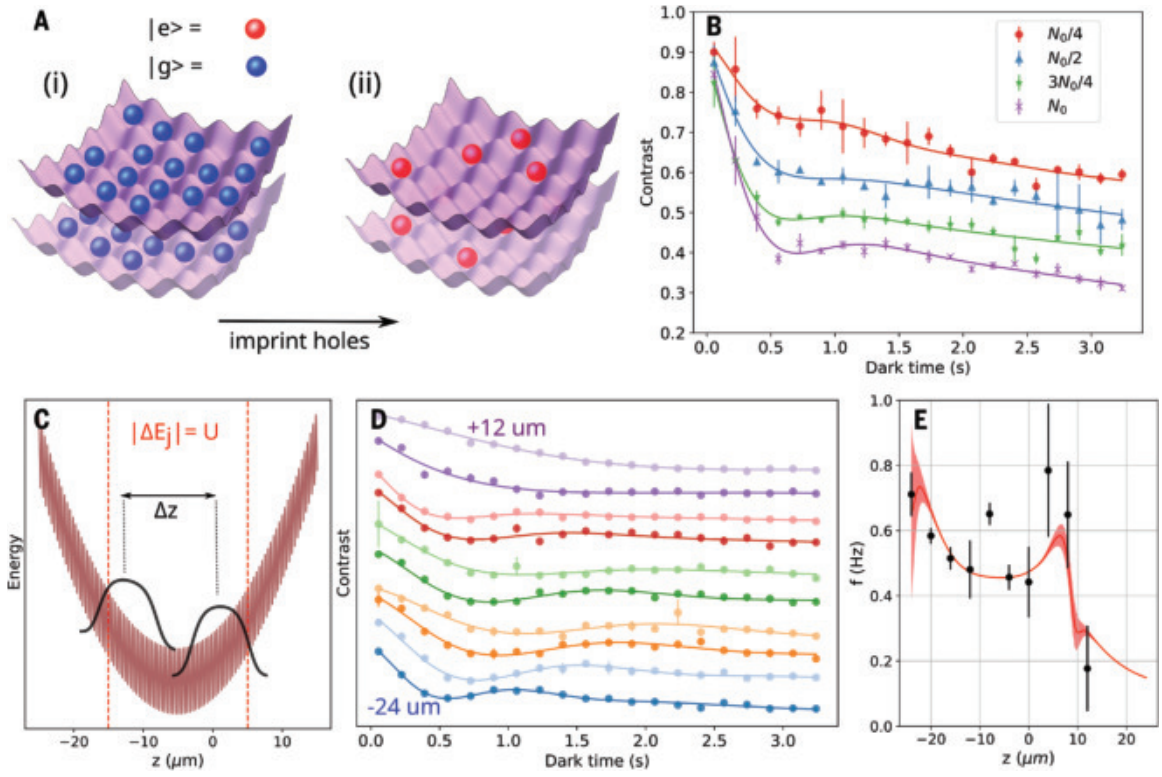

Fig. 4. Controlling superexchange interactions. All measurements presented here are performed at trap depths $V_z = 17.4\,E_R$ and $V_\perp = 44.9\,E_R$. (**A**) The fraction of atoms participating in superexchange is modified by reducing the filling fraction by uniformly adding holes. In (i), the initial state is a highly filled sample of ground state atoms. Next, atoms are placed in a superposition state with tunable pulse area. Light resonant with $|^1S_0\rangle$ is turned on to imprint holes, with the remaining atoms in $|^3P_0\rangle$ as shown in (ii). (**B**) The contrast decay as the clock pulse area and thus total atom number N is reduced compared to the initial atom number N_0. The solid lines shown in (B) and (D) are fits using the model $C_{SE}(T)$ provided in the main text. Error bars are 1σ (standard deviation). (**C**) The superexchange coupling is modified by changing the position of the atoms in the lattice potential, which varies the site-to-site energy shift ΔE_j. Representative density distributions for the cloud at different positions are given by black solid lines. At the positions indicated by vertical red lines, tunneling becomes resonant and strongly enhances the local $J_{SE}(j)$. However, averaged over the whole cloud, this only slightly modifies the oscillation frequencies. (**D**) Oscillations in contrast at different vertical positions z; curves are shifted vertically according to z position. (**E**) These measured oscillation frequencies are compared with a heuristic superexchange simulation (red line) of the Ramsey contrast (*51*).

of the cloud position z. We compare the oscillation frequency with the simplified simulation averaging over two-site pairs in Fig. 4E (red line), similar to the blue line shown in Fig. 3C. Averaging the Ramsey signal along the z-direction during imaging strongly suppresses the effect of locally enhanced $J_{SE}(j)$, where $U = \Delta E_j$. The asymmetry of the background trap gradient around $z = 0$ leads to a reduction in the oscillation frequency at large z where $\Delta E_j > U$. The frequency of the simulation shows qualitative agreement with the measured oscillation.

Discussion and outlook

Superexchange interactions are identified as an important systematic effect that degrades the precision of optical lattice clocks operating with high filling at timescales $h/\bar{J}_{SE}$. For clock metrology, we can either reduce the magnitude or control the form of the superexchange interactions to enhance clock performance. For example, we can increase the lattice constant a sufficiently to reduce the tunneling rate to a negligible value (*22*). Alternatively, a variable lattice spacing can be used to make a commensurate with λ_{clk} to achieve $\varphi \bmod 2\pi = 0$. Without SOC ($\varphi \bmod 2\pi = 0$), the isotropic Heisenberg Hamiltonian $\sum_j J_{SE}(j)\hat{\mathbf{s}}_j \cdot \hat{\mathbf{s}}_{j+1}$ is recovered, and any coherent spin state becomes an eigenstate accumulating only a trivial global phase.

Collective superexchange interactions can also be used to produce spin entanglement for quantum enhanced sensing (*45*). A promising parameter regime for implementing this strategy is around region (i) identified in Fig. 2C . Although in the 1D limit with $V_\perp = 0$ we obtain the maximal value of the coherence time T_2, the amount of usable entanglement in this regime is limited (*15*) owing to the presence of strong p-wave loss. However, we observe that the transition from pancakes to "waffles" by introducing a weak transverse corrugation of $V_\perp \gtrsim 5E_R$ strongly reduces the atom loss by increasingly localizing the atoms in the transverse directions (*51*). Thanks to the lack of clock-induced SOC within each waffle, the in-plane superexchange leads to isotropic Heisenberg interactions, which feature energy gaps between sectors with different total spin length. Thus, by reducing single-particle inhomogeneities via potential shaping or layer selection (*55*), the superexchange interactions investigated in this work can not only energetically lock the atoms in collective spins across all horizontal planes but also subsequently couple and entangle them through the SOC-induced XXZ interaction along the vertical direction.

REFERENCES AND NOTES

1. T. Bothwell *et al.*, *Nature* **602**, 420–424 (2022).
2. A. Aeppli, K. Kim, W. Warfield, M. S. Safronova, J. Ye, *Phys. Rev. Lett.* **133**, 023401 (2024).
3. S. Kolkowitz *et al.*, *Phys. Rev. D* **94**, 124043 (2016).
4. R. B. Hutson, W. R. Milner, L. Yan, J. Ye, C. Sanner, *Science* **383**, 384–387 (2024).
5. Boulder Atomic Clock Optical Network (BACON) Collaboration, *Nature* **591**, 564–569 (2021).

6. N. Nemitz *et al.*, *Nat. Photonics* **10**, 258–261 (2016).
7. W. F. McGrew *et al.*, *Nature* **564**, 87–90 (2018).
8. W. M. Itano *et al.*, *Phys. Rev. A* **47**, 3554–3570 (1993).
9. E. Pedrozo-Peñafiel *et al.*, *Nature* **588**, 414–418 (2020).
10. J. M. Robinson *et al.*, *Nat. Phys.* **20**, 208–213 (2024).
11. W. J. Eckner *et al.*, *Nature* **621**, 734–739 (2023).
12. J. Franke *et al.*, *Nature* **621**, 740–745 (2023).
13. E. Oelker *et al.*, *Nat. Photonics* **13**, 714–719 (2019).
14. A. D. Ludlow, M. M. Boyd, J. Ye, E. Peik, P. O. Schmidt, *Rev. Mod. Phys.* **87**, 637–701 (2015).
15. M. J. Martin *et al.*, *Science* **341**, 632–636 (2013).
16. X. Zhang *et al.*, *Science* **345**, 1467–1473 (2014).
17. S. Kolkowitz *et al.*, *Nature* **542**, 66–70 (2017).
18. S. L. Bromley *et al.*, *Nat. Phys.* **14**, 399–404 (2018).
19. A. Aeppli *et al.*, *Sci. Adv.* **8**, eadc9242 (2022).
20. S. L. Campbell *et al.*, *Science* **358**, 90–94 (2017).
21. A. Goban *et al.*, *Nature* **563**, 369–373 (2018).
22. R. B. Hutson *et al.*, *Phys. Rev. Lett.* **123**, 123401 (2019).
23. L. Sonderhouse *et al.*, *Nat. Phys.* **16**, 1216–1221 (2020).
24. L.-M. Duan, E. Demler, M. D. Lukin, *Phys. Rev. Lett.* **91**, 090402 (2003).
25. M. Lewenstein *et al.*, *Adv. Phys.* **56**, 243–379 (2007).
26. S. Trotzky *et al.*, *Science* **319**, 295–299 (2008).
27. E. Manousakis, *Rev. Mod. Phys.* **63**, 1–62 (1991).
28. A. Auerbach, *Interacting Electrons and Quantum Magnetism* (Springer, 2012); https://link.springer.com/book/10.1007/978-1-4612-0869-3.
29. P. A. Lee, N. Nagaosa, X.-G. Wen, *Rev. Mod. Phys.* **78**, 17–85 (2006).
30. D. Greif, T. Uehlinger, G. Jotzu, L. Tarruell, T. Esslinger, *Science* **340**, 1307–1310 (2013).
31. R. A. Hart *et al.*, *Nature* **519**, 211–214 (2015).
32. M. Boll *et al.*, *Science* **353**, 1257–1260 (2016).
33. L. W. Cheuk *et al.*, *Science* **353**, 1260–1264 (2016).
34. A. Mazurenko *et al.*, *Nature* **545**, 462–466 (2017).
35. M. Takahashi, *Thermodynamics of One-Dimensional Solvable Models* (Cambridge Univ. Press, 2005); https://www.cambridge.org/core/books/thermodynamics-of-onedimensional-solvable-models/B74C2EB63A89A1E5D7347EE48E4AFD6C.
36. S. Taie *et al.*, *Nat. Phys.* **18**, 1356–1361 (2022).
37. M. Gall, N. Wurz, J. Samland, C. F. Chan, M. Köhl, *Nature* **589**, 40–43 (2021).
38. R. C. Brown *et al.*, *Science* **348**, 540–544 (2015).
39. P. N. Jepsen *et al.*, *Nature* **588**, 403–407 (2020).
40. H. Sun *et al.*, *Nat. Phys.* **17**, 990–994 (2021).
41. M. Mamaev, I. Kimchi, R. M. Nandkishore, A. M. Rey, *Phys. Rev. Res.* **3**, 013178 (2021).
42. P. N. Jepsen *et al.*, *Nat. Phys.* **18**, 899–904 (2022).
43. P. He *et al.*, *Phys. Rev. Res.* **1**, 033075 (2019).
44. T. Hernández Yanes *et al.*, *Phys. Rev. Lett.* **129**, 090403 (2022).
45. M. Mamaev, D. Barberena, A. M. Rey, *Phys. Rev. A* **109**, 023326 (2024).
46. W. R. Milner, L. Yan, R. B. Hutson, C. Sanner, J. Ye, *Phys. Rev. A* **107**, 063313 (2023).
47. D. G. Matei *et al.*, *Phys. Rev. Lett.* **118**, 263202 (2017).
48. G. E. Marti *et al.*, *Phys. Rev. Lett.* **120**, 103201 (2018).
49. T. Gullion, D. B. Baker, M. S. Conradi, *J. Magn. Reson.* **89**, 479–484 (1990).
50. J.-R. Li *et al.*, *Nature* **614**, 70–74 (2023).
51. See supplementary materials.
52. T. Esslinger, *Annu. Rev. Condens. Matter Phys.* **1**, 129–152 (2010).
53. P. Lemonde, P. Wolf, *Phys. Rev. A* **72**, 033409 (2005).
54. M. Foss-Feig, K. R. A. Hazzard, J. J. Bollinger, A. M. Rey, *Phys. Rev. A* **87**, 042101 (2013).
55. A. L. Gaunt, T. F. Schmidutz, I. Gotlibovych, R. P. Smith, Z. Hadzibabic, *Phys. Rev. Lett.* **110**, 200406 (2013).
56. W. R. Milner *et al.*, Coherent evolution of superexchange interaction in seconds long optical clock spectroscopy, Data and code, Dryad (2024); https://doi.org/10.5061/dryad.qv9s4mwq5.

ACKNOWLEDGMENTS

We thank A. Aeppli, Z. Hu, J. Hur, D. Kedar, K. Kim, M. Miklos, J. M. Robinson, Y. M. Tso, W. Warfield, and Z. Yao for useful discussions. We thank A. M. Kaufman and N. D. Oppong for careful reading of the manuscript and for providing insightful comments. **Funding:** Funding for this work is provided primarily by the DOE Center of Quantum System Accelerator and by NSF QLCI OMA-2016244, NSF JILA-PFC PHY-2317149, Va. Bush Fellowship, AFOSR FA9550-24-1-0179, and NIST. B.L. acknowledges funding from the Lindemann Trust and S.L. from the Alexander von Humboldt Foundation. **Author contributions:** The experiment was performed by W.R.M., S.L., L.Y., B.L., M.N.F., R.B.H., and J.Y. The theory model was developed by M.M., A.C., and A.M.R. All authors contributed to data analysis and writing of the manuscript. **Competing interests:** The authors declare no competing interests. **Data and materials availability:** Experimental data and analysis code are archived at Dryad (*56*).

SUPPLEMENTARY MATERIALS

science.org/doi/10.1126/science.ado5987
Materials and Methods; Supplementary Text; Figs. S1 to S6; Table S1; References (*57*, *58*)

Submitted 9 February 2024; resubmitted 17 July 2024; accepted 13 March 2025

10.1126/science.ado5987

QUANTUM COMPUTING

Universal distributed blind quantum computing with solid-state qubits

Y.-C. Wei[1]†, P.-J. Stas[1]†, A. Suleymanzade[1]†*, G. Baranes[1,2]†, F. Machado[1,3], Y. Q. Huan[1], C. M. Knaut[1], S. W. Ding[4], M. Merz[5], E. N. Knall[4], U. Yazlar[1,6], M. Sirotin[1,2], I. W. Wang[1], B. Machielse[4,7], S. F. Yelin[1], J. Borregaard[1,7], H. Park[1,8], M. Lončar[4], M. D. Lukin[1]*

Blind quantum computing is a promising application of distributed quantum systems, in which a client can perform computations on a remote server without revealing any details of the applied circuit. Although the most promising realizations of quantum computers are based on various matter-qubit platforms, implementing blind quantum computing on matter qubits remains a challenge. Using silicon-vacancy (SiV) centers in nanophotonic diamond cavities with an efficient optical interface, we demonstrated a universal quantum gate set consisting of single- and two-qubit blind gates over a distributed two-node network. Using these ingredients, we performed a distributed algorithm with blind operations across our two-node network, proving a route to develop blind quantum computation with matter qubits in distributed, modular architectures.

Quantum computers are expected to outperform their classical counterparts for certain problems (*1*), while the no-cloning theorem of quantum mechanics offers routes to information-theoretic security (*2*), as harnessed in quantum key distribution (*3*, *4*). Blind quantum computing (BQC) has the potential to combine these two concepts, allowing a client with limited quantum capabilities to utilize remote, powerful servers with information-theoretic privacy (*5*–*10*). The realization of BQC requires the exchange of quantum information between physically separated parties through flying qubits, for example, photons. BQC was first experimentally explored with all-photonic platforms, including generating cluster-state resources for blind protocols (*11*–*14*).

The ability to locally manipulate quantum information via matter qubits offers scalable ways for generating larger entangled resources (*15*–*18*). Moreover, recent progress in quantum computing with matter-based platforms, including neutral atoms (*19*, *20*), superconducting qubits (*21*, *22*), trapped ions (*23*, *24*), semiconductor quantum dots (*25*), and solid-state defects (*26*, *27*) makes it timely to explore whether BQC can be realized on such matter-based quantum systems. Matter-based BQC requires high-fidelity matter-photon entanglement, in which photons travel to clients to mediate quantum gates applying on the matter qubits (*28*, *29*). This approach critically depends on the availability of efficient optical interfaces—a challenge for matter-based quantum platforms, which are typically not optimized for this purpose. Other challenges include scaling up the number of qubits; the distributed quantum computing architecture provides a natural solution for systems with matter-photon interfaces (*3*, *30*–*32*). Although a matter-photon implementation of blind rotations has been recently demonstrated (*15*), several key ingredients for matter-based BQC, including a universal blind gate set and blind operations on distributed matter resources, have not yet been experimentally explored.

Silicon-vacancy (SiV) centers integrated in diamond nanophotonic cavities (*33*–*36*) provide an efficient matter-photon interface, making them suited for BQC applications. In this study, we report the first experimental implementation of a universal gate set for matter-based BQC, including distributed blind operations, using a two-node SiV-based quantum network.

BQC architecture with SiV spin qubits

The goal of BQC is for a client to perform a computation on a server without revealing the applied quantum circuit (Fig. 1A, top left). A way to fulfill this requirement for arbitrary algorithms is to compose the entire circuit from universal blind cells with a periodic pattern (Fig. 1B) (*6*, *8*, *29*, *37*). The client uses such a universal blind cell to apply any desired quantum operations in the universal gate set, including arbitrary single-qubit rotations and a two-qubit gate. However, the client's choice of operation is indistinguishable to the servers, making the quantum logic hidden from the servers. A universal blind cell can be implemented from two subunits: one-qubit blind gates (1QBG) and two-qubit blind gates (2QBG) (supplementary materials section 1). The 1QBG allows the client to execute any arbitrary single-qubit operations from the universal gate set, whereas 2QBG allows the client to choose between applying a maximally entangling two-qubit gate and applying a nonentangling gate. For both 1QBG and 2QBG, the client's choice of operation is unknown to the servers (Fig. 1B). The implementation of 1QBG and 2QBG completes a universal gate set for BQC.

We use an SiV-based two-node quantum network (*33*) as a backbone for our BQC implementation. The network consists of two physically separated nodes and a photonic measurement apparatus, acting as two distributed servers and a client, respectively (Fig. 1A). The servers use spin qubits as computational resources, and blind gates are applied through matter-photon entanglement generated locally by servers. The photons, which are part of the resulting entangled resource, are sent to the client for measurements. These measurements define the gate logic applied on the spin qubits while preserving secrecy.

Each server node consists of an SiV center coupled to a nanophotonic cavity. Selectively implanting the ^{29}Si isotope creates a two-qubit register: one electron spin qubit with an optical transition at 737 nm as a communication qubit and one nuclear spin qubit as a memory (*34*). In our implementation, we use both the electron (e_1) and nuclear (n_1) spins at server 1 and the electron spin (e_2) at server 2 as matter-qubit resources. The nanophotonic cavity enables a high-contrast electron spin–dependent reflectance of the SiV-cavity system, and we send microwave (MW) or radio-frequency (RF) pulses to a gold coplanar waveguide to apply high-fidelity single and two-qubit gates on the electron and nuclear spin qubits (Fig. 1A). The above features allow us to generate spin-photon entanglement (*34*) and photon-mediated entanglement between two spins at separate nodes (*33*). Starting with a weak coherent state, we use the presence of a photon in an early ($|0\rangle$) or late ($|1\rangle$) time bin as the photonic qubit (*37*). Universal BQC requires controllable photon measurements in the $X-Y$ plane of the Bloch sphere. To achieve this, the client uses an acousto-optical modulator (AOM) to apply a phase (ϕ) between early and late time bins, followed by a time-delay interferometer (TDI) to interfere both time-bin photons.

Intranode blind gates

We first focus on the 1QBG, which utilizes the z-axis rotation with a hidden angle ϕ ($R_z(\phi)$) as its basic building block. We use the spin-photon gate (SPG) (Fig. 2A) to entangle an electron in an arbitrary initial state, $|\psi\rangle_e = (\alpha|\uparrow\rangle + \beta|\downarrow\rangle)_e$, with a photon ($\gamma$) through spin state–dependent reflectivity (*33*, *34*) as follows:

$$(|0\rangle + |1\rangle)_\gamma(\alpha|\uparrow\rangle + \beta|\downarrow\rangle)_e \xrightarrow{\text{SPG}} (\alpha|0\uparrow\rangle + \beta|1\downarrow\rangle)_{\gamma,e}$$

[1]Department of Physics, Harvard University, Cambridge, MA, USA. [2]Department of Physics and Research Laboratory of Electronics, Massachusetts Institute of Technology, Cambridge, MA, USA. [3]ITAMP, Harvard-Smithsonian Center for Astrophysics, Cambridge, MA, USA. [4]John A. Paulson School of Engineering and Applied Sciences, Harvard University, Cambridge, MA, USA. [5]Department of Physics, ETH Zurich, Zurich, Switzerland. [6]Division of Materials Science & Engineering, Boston University, Boston, MA, USA. [7]Lightsynq Technologies, Brighton, MA, USA. [8]Department of Chemistry and Chemical Biology, Harvard University, Cambridge, MA, USA. ***Corresponding author. Email: azizasuleymanzade@g.harvard.edu (A.S.); lukin@physics.harvard.edu (M.D.L.)** †These authors contributed equally to this work.

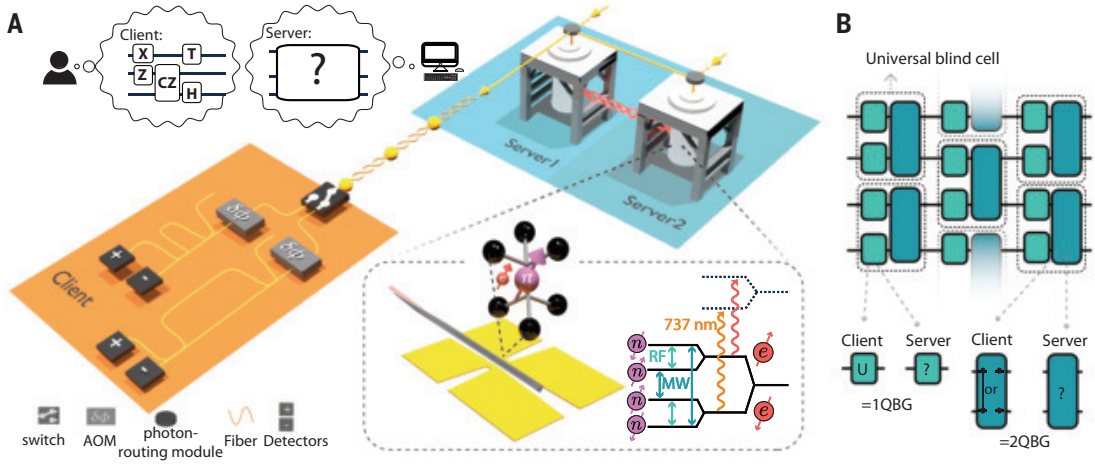

Fig. 1. Distributed BQC with a two-node quantum network with SiVs. (**A**) (Top left) High-level schematic diagram of BQC. (Middle) The client receives photons from the servers and performs measurements. Each server operates a ^{29}SiV inside a nanophotonic cavity within a dilution refrigerator. (Bottom right) The ^{29}SiV energy-level diagram shows the MW and RF transitions in the two-qubit manifold (straight arrows) and spin-conserving optical transitions (wavy arrows). (**B**) BQC circuits are constructed from repeated universal blind cells. A universal blind cell can be implemented from two subunits: 1QBG and 2QBG. 1QBG allows the client to perform an arbitrary gate within the universal single-qubit gate set *U*. 2QBG allows the client to apply either a maximally entangling or a nonentangling gate, such as *CZ* or Identities (*I*).

Due to the inevitable photon loss, this entanglement generation occurs probabilistically with experimental success probability $\eta \sim 10^{-3}$ but is heralded by the photon detection by the client. We implement $R_z(\phi)$ by first performing a SPG at the server, after which the client measures the photon in the $\left|\pm_\phi\right\rangle_\gamma = \left(|0\rangle \pm e^{i\phi}|1\rangle\right)_\gamma / \sqrt{2}$ basis (Fig. 2A). We use $s = 0(1)$ to denote the measurement results $\left|+_\phi\right\rangle_\gamma \left(\left|-_\phi\right\rangle_\gamma\right)$, each occurring with equal probability. By applying the feedback Z^s, the resulting electron state is $\alpha|\uparrow\rangle_e + e^{i\phi}\beta|\downarrow\rangle_e = R_z(\phi)|\psi\rangle_e$, completing the desired *z*-axis rotation on the qubit. This feedback is not applied by the server; instead, the client implements this by adaptively adjusting the measurement phase of subsequent blind gate(s) (*37*). No measurement information or feedback actions are needed at the server side.

Because the client's measurement outcome s is unknown to the servers, they observe a mixed state averaged over $s = 0$ and 1 without any information about ϕ, rendering the operation blind (Fig. 2B). We measure a blind R_z gate fidelity of $94.8 \pm 0.3\%$ (*37*). We characterize the information leakage as the Holevo information χ of the client's operations gained by the servers [see (*37*) for definition]. This is measured by examining the resulting states at the server side over the different operations chosen by the client. For an n-qubit operation, χ ranges from 0 to n bits, with $\chi = 0$ for perfectly blind operations. We find χ to be $0.0045^{+0.018}_{-0.0045}$ bits, far below the 1 bit necessary to fully reveal ϕ.

To implement a universal 1QBG, we apply 3 SPGs interleaved with Hadamard gates, realizing $R_z(\phi_3)R_x(\phi_2)R_z(\phi_1)$ on the spin qubit (Fig. 2C). The adaptive feedback must be carried out in real time for non-Clifford gates, which are necessary for universal operations. This is done by applying the i^{th}-photon blind rotation ϕ'_i, as a function of the previously run outcome s_{i-1} and the desired rotation ϕ_i (*37*). This protocol generates a three-photon linear cluster state with the electron as the fourth qubit, and the client measures the first, second, and third photon in the $\left|\pm_{\phi_1}\right\rangle_\gamma$, $\left|\pm_{\phi'_2}\right\rangle_\gamma$, and $\left|\pm_{\phi'_3}\right\rangle_\gamma$ bases, respectively. This implements an arbitrary single-qubit operation. To demonstrate the universality of this gate, we implement three different 1QBGs: Identity (*I*), Hadamard (*H*), and $TX^{1/2}T$—an arbitrarily designed non-Clifford gate. *T* gate, or the $\pi/4$-phase shift gate, is a non-Clifford gate and essential for universal quantum computation. By applying this gate to $|+i\rangle_e = \frac{1}{\sqrt{2}}\left(|0\rangle_e + i|1\rangle_e\right)$, we observe the resulting state fidelities to be 0.70 ± 0.06, 0.71 ± 0.06, 0.69 ± 0.10, respectively, and χ for these three gates is $0.03^{+0.07}_{-0.03}$ bits (Fig. 2D).

We next implement an intranode 2QBG using e_1 and n_1 at server 1. Crucially, the 2QBG can be either an entangling or nonentangling gate based on the client's measurement, whereas the servers should observe output states independent from this choice. We achieve this with a sequence consisting of local two-qubit gates and an SPG (Fig. 3A). An SPG with the client's measurement phase $\phi = 0\,(\pi/2)$ results in the sequence being $I\left(S_{e_1}S_{n_1}CZ\right)$, a nonentangling (entangling) gate. Here, S is the $\pi/2$-phase shift gate. We emphasize that, by utilizing local matter-qubit operations, we implement this entanglement-hiding gate with fewer probabilistic photon operations compared with all-photonic platforms (*6*, *37*).

We first probe our intranode 2QBG by measuring the gate truth table using $|\uparrow/\downarrow\rangle_{e_1}$ and $|+i/-i\rangle_{n_1}$ or $|+/-\rangle_{n_1}$ as initial input states. Figure 3D (Fig. 3E) shows the probability distribution of resulting output states when the client measures the photon in the $\left|\pm_0\right\rangle_\gamma$ $\left(\left|\pm_{\pi/2}\right\rangle_\gamma\right)$ basis, corresponding to an $I\left(S_{e_1}S_{n_1}CZ\right)$ operation. We then apply the 2QBG to the initial state $|{+}{+}\rangle_{e_1,n_1}$. By applying $I\left(S_{e_1}S_{n_1}CZ\right)$, the client observes a resulting product-state (Bell-state) fidelity of 0.85 ± 0.01 (0.85 ± 0.02). We then continuously tune the entangling degree of the gate by varying ϕ. The client observes a corresponding change of entanglement entropy of the resulting state, whereas the server always observes an entanglement entropy close to 1, which is consistent with the mixed state generated by our protocol (Fig. 3B). The purity of the two-qubit system remains high for the client but stays at ~0.5 for the server (Fig. 3C), indicating that the system is in a coherent quantum state for the client but appears mixed to the server. We characterize χ over $\phi = \{0, \pi/2\}$ to be $0.032^{+0.12}_{-0.032}$ bits, far below the 1 bit required to fully decode the client's choice between entangling and nonentangling gates (complete protocol and error budgets are given in the supplementary materials).

Distributed two-qubit blind gate

To utilize computational resources across different servers (*10*, *14*), we perform the second type of 2QBG—a distributed 2QBG. We use n_1 at server 1 and e_2 at server 2 as computational qubits, while e_1 at server 1

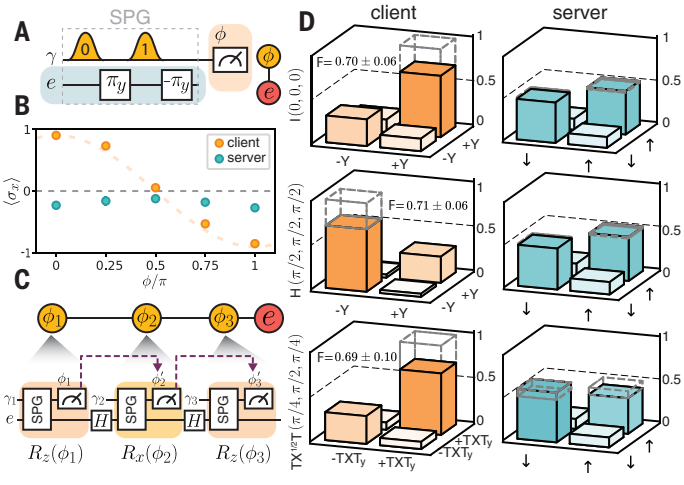

Fig. 2. Single-qubit blind gates. (**A**) $R_z(\phi)$ sequence. (**B**) Measured $\langle\sigma_x\rangle$ of the electron as a function of the rotation angle ϕ set by the client, with the electron initialized at $|+\rangle_e$. (**C**) Universal 1QBG consisting of 3SPGs generates a three-photon linear cluster state with the electron as the fourth qubit. (**D**) By choosing $(\phi_1, \phi_2, \phi_3) = (0, 0, 0)$, $(\pi/2, \pi/2, \pi/2)$, and $(\pi/4, \pi/2, \pi/4)$, we implement Identity, Hadamard, and $TX^{1/2}T$ gates to the electron initialized at $|+i\rangle_e$, respectively. We observe the corresponding fidelities of 0.70 ± 0.06, 0.71 ± 0.06, 0.69 ± 0.10, and χ for the three cases to be $0.03^{+0.07}_{-0.03}$ bits, with the shown measured density matrices. The fidelities are mainly limited by the laser drift noise and can be improved by postselection on the measurements with less laser frequency drift (details provided in table S16 and supplementary materials section 4.5).

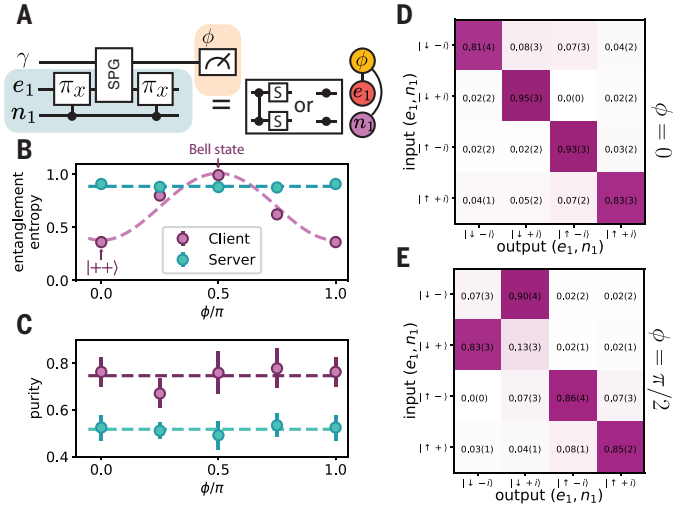

Fig. 3. Intranode two-qubit blind gate. (**A**) Intranode 2QBG sequence. We use e_1 and n_1 as our computational qubits. (Right) The cluster state after applying the intranode 2QBG to $|++\rangle$ (explained in the supplementary materials). (**B**) Entanglement entropy and (**C**) state purity as a function of the photon measurement angle ϕ set by the client. At $\phi = 0(\pi/2)$, we observe a product-state (Bell-state) fidelity of 0.85 ± 0.01 (0.85 ± 0.02), with χ over $\phi = \{0, \pi/2\}$ to be $0.032^{+0.12}_{-0.032}$ bits. (**D** and **E**) show the gate truth tables. Here, $\phi = 0(\pi/2)$ corresponds to the I gate ($S_{e_1} S_{n_1} CZ$ gate). The client observes the average resulting state fidelity of 0.86 ± 0.02 (0.88 ± 0.02) for the I ($S_{e_1} S_{n_1} CZ$) gate.

is an ancilla qubit that always starts at $|+\rangle_{e_1}$ and is measured out at the end (Fig. 4, A and B). The sequence starts with distributing entanglement between e_1 and e_2 over the two-server network, such that this entanglement can be switched on or off secretly by the client. This switchable entanglement is achieved by using a four–time-bin photonic qudit to carve out four combinations of e_1, e_2 states using a specially designed gate: a quantum universal blind entanglement gate (QUBE). For any initial state $(\alpha|\uparrow\rangle + \beta|\downarrow\rangle)_{e_2}$, the QUBE gate results in the state

$$(|0\rangle + |1\rangle + |2\rangle + |3\rangle)_\gamma (|\uparrow\rangle + |\downarrow\rangle)_{e_1} (\alpha|\uparrow\rangle + \beta|\downarrow\rangle)_{e_2}$$
$$\xrightarrow{\text{QUBE}} (\alpha|0\rangle|\uparrow\uparrow\rangle + \beta|1\rangle|\downarrow\downarrow\rangle + \beta|2\rangle|\uparrow\downarrow\rangle + \alpha|3\rangle|\uparrow\downarrow\rangle)_{\gamma, e_1, e_2}$$

where $|0-3\rangle_\gamma$ are four photonic time bins separated by a time difference τ. To turn on (off) the entanglement, the client secretly switches the photon to a TDI with delay time τ (2τ) (Fig. 4D). A short (long) TDI interferes $|0\rangle_\gamma, |1\rangle_\gamma$ or $|2\rangle_\gamma, |3\rangle_\gamma$ ($|0\rangle_\gamma, |2\rangle_\gamma$ or $|1\rangle_\gamma, |3\rangle_\gamma$), which entangles (disentangles) e_1, e_2 without decohering our computational qubits. A local $e_1 - n_1$ gate is then applied to teleport this switchable entanglement to n_1 and e_2, completing a switchable gate, CZ or I (Fig. 4B). The gate is generated with the experimental success probability $\eta \sim 10^{-5}$ and is heralded by single-photon detection by the client.

We first characterize our distributed 2QBG by measuring the population transfer with combinations of $|\uparrow/\downarrow\rangle_{n_1}$ and $|+/-\rangle_{e_2}$ as input states. The client observes an average output-state fidelity of 0.76 ± 0.03 (0.75 ± 0.02) for the CZ (I) operation (Fig. 4E, top). The servers observe two indistinguishable truth tables because the client's choice is hidden from the servers (Fig. 4E, bottom). Through our gate design, the phase of the state observed from the servers is maximally scrambled, making CZ and I indistinguishable to the servers for any arbitrary input state (*37*). We further apply our distributed 2QBG to the initial state $|++\rangle_{n_1 e_2}$. This generates a Bell state (product state) with fidelity 0.72 ± 0.04 (0.70 ± 0.03) when the client applies CZ (I) (Fig. 4C, top). These output states are, however, indistinguishable to the servers (Fig. 4C, bottom), and χ over $\{CZ, I\}$ is 0.12 ± 0.06 bits, far below the 1 bit needed to fully reveal the client's choice. During the measurement, we reject the data if the monitored system parameters drift beyond calibrated thresholds. Without this rejection, the operation is still hidden with $\chi = 0.076 \pm 0.038$ bits (*37*).

Distributed algorithm with blind operations

The above demonstrations complete a universal gate set for matter-based BQC with a distributed quantum computing architecture. We now utilize these ingredients to realize a Deutsch-Jozsa-type algorithm with hidden oracles. We define a function with n inputs f: $\{0,1\}^n \rightarrow \{0,1\}$, with the constraint that the output over all inputs is either a "constant" value or "balanced" values, i.e., half 0, half 1. An unknown party implements an oracle based on f, while a user wants to know whether this oracle is constant or balanced through queries. A classical algorithm requires, in the worst case, $2^{n-1} + 1$ queries. The Deutsch-Jozsa quantum algorithm takes a single oracle query O_f, a quantum operation applied to n computational qubits and one ancilla qubit (*38*).

We implement a Deutsch-Jozsa-type algorithm with four oracles ($O_1 - O_4$; see Fig. 5A) available from the servers. The client chooses an index i and intends to know whether O_i is constant or balanced, without revealing the choice of i to the servers. To implement the above-mentioned task, the server applies the sequence shown in Fig. 5B. The client measures the photon in a basis specific to the desired O_i, generating one of four possible $e_2 - e_1 - n_1$ entangled states (Fig. 5B, bottom) as a resource for her to determine if O_i is constant or balanced (details provided in supplementary materials section 1.6).

Figure 5C shows the client implementing four oracles with an average probability of 0.85 ± 0.03 of correctly determining the constant-or-balanced property. By the algorithm design, the internode entanglement is hidden from the servers. This makes the servers unable to recognize the implementation of O_1 from O_3 and O_2 from O_4, resulting in a 1-bit oracle hiding. This is characterized by measuring the information leakage over $\{O_1, O_3\}$ to be $0.05^{+0.19}_{-0.05}$ bits and $\{O_2, O_4\}$ to be $0.07^{+0.14}_{-0.07}$ bits, both below the 1 bit necessary to fully distinguish between two oracles (Fig. 5D). Here, we measure the classical information leakage because

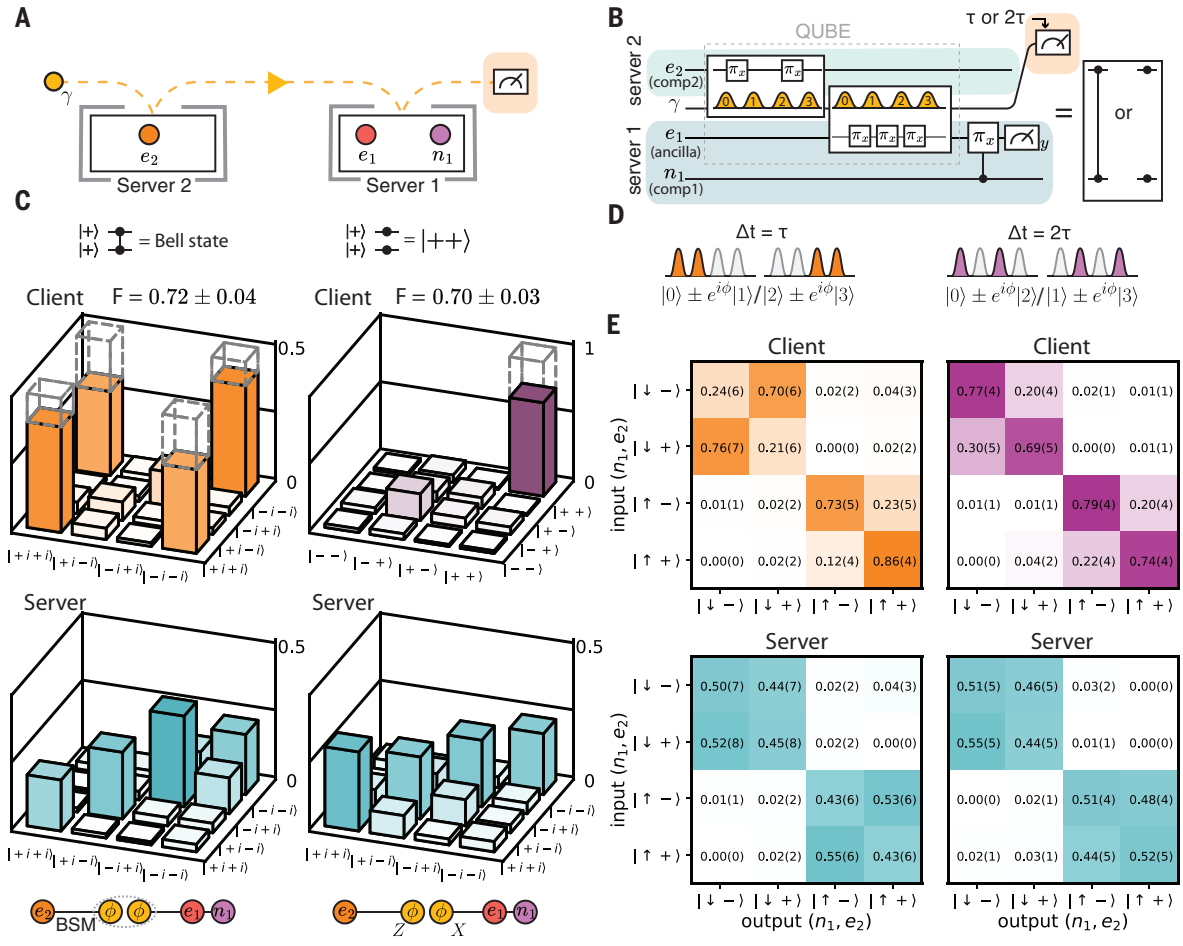

Fig. 4. Distributed two-qubit blind gate. (**A**) Experimental setup. (**B**) Distributed 2QBG sequence. n_1, e_2 are computational qubits, and e_1 acts as an ancilla. (**C**) Density matrix of n_1, e_2 after applying the distributed 2QBG to the initial state $|++\rangle_{n_1,e_2}$. Left (Right) The client observes a Bell-state (product-state) fidelity of 0.72 ± 0.04 (0.70 ± 0.03) with the *CZ* (*I*) operation. The servers observe indistinguishable density matrices over different operations chosen by the client, and χ over $\{CZ, I\}$ is 0.12 ± 0.06 bits. One bit is necessary to fully reveal the client's choice. (Bottom) The left (right) cluster state corresponds to the resulting state after a *CZ*(*I*) operation (explained in the supplementary materials). BSM, Bell-state measurement. (**D**) Left (Right) Interfering $|0\rangle$, $|1\rangle$ or $|2\rangle$, $|3\rangle$ ($|0\rangle$, $|2\rangle$ or $|1\rangle$, $|3\rangle$) with a short (long) TDI entangles (disentangles) e_1, e_2 without causing e_2 to decohere. (**E**) Left (right) column: The gate truth tables for the *CZ* operations as observed by the client and servers. The client observes an average resulting state fidelity of 0.76 ± 0.03 (0.75 ± 0.03) with the *CZ* (*I*) operation.

the output of the algorithm only contains single-basis measurement results (details of system monitoring, postselection, and the relevant information leakage are given in supplementary materials section 4.5). Although in our implementation the traditional quantum advantage is not preserved owing to the probabilistic nature of the QUBE gate, we emphasize that the delegated implementation on the remote servers allows the client to execute oracle queries by simple instructions without knowing the explicit form of the oracle functions, demonstrating the operation in which an oracle-based algorithm can be practically useful.

Discussion and outlook

Our experiments demonstrate key ingredients for universal BQC using matter qubits. We implement universal blind gates on a single qubit and two-qubit blind gates within the same server and distributed over two servers, fulfilling a universal gate set and thereby extending the scope of BQC to matter-based quantum computing systems with a distributed architecture. Distinct from the conventional measurement-based BQC schemes (*6*, *8*, *9*), our implementation utilizes the flexibility of local matter-qubit operations to efficiently realize universal BQC.

To increase the scale and the complexity of the BQC algorithms, the key challenge is associated with the probabilistic gate implementation that is due to the low photon-detection probability (η), corresponding to $\eta \sim 10^{-3}$ and $\eta \sim 10^{-5}$ for the intranode and internode operations, respectively. Deterministic matter-qubit local gates, however, enable efficient blind gate implementation. Notably, our 2QBG implementation requires one photon, as opposed to the five photons needed in all-photonic platforms (*6*, *8*, *37*). For more complex circuits involving multi-photon detection, the running time of algorithms increases exponentially with gate depth (D) as $\sim (1/\eta)^D$. This can be circumvented by using additional ancillary qubit memories, which hold quantum information while communication qubits repeat entanglement attempts until success (*15*, *30*, *39*–*41*) and enable deterministic entanglement generation and deterministic algorithm implementation with the running time scaling linearly with the depth as $\sim D/\eta$. Our demonstrated building blocks can be directly applied to such memory-based architectures (*37*). In our platform, this can be achieved by using weakly coupled ^{13}C spins (*42*) as quantum memories. Such ancillary qubits also enable deterministic internode operations (*39*), which allow scaling up the number of qubits by interconnecting multiple nodes without the exponential cost of the success rate.

Beyond this specific implementation, our methods can apply to other different matter-qubit platforms with matter-photon interfaces.

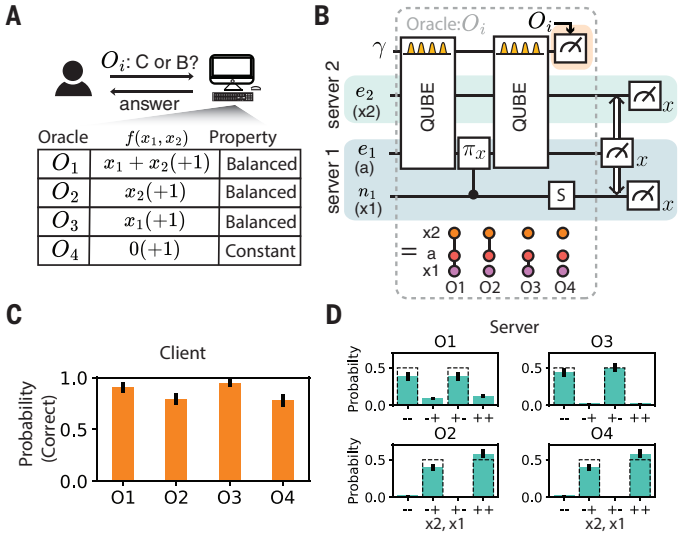

Fig. 5. Distributed algorithm with blind oracles. (**A**) Schematic diagram for Deutch-Jozsa-type algorithms. Four oracles ($O_1 - O_4$) are available from the servers. Their corresponding two-input functions and constant-or-balanced properties are shown in the table. (**B**) Gate sequence for the Deutsch-Jozsa-type algorithm. $x_1(x_2)$ denotes the computational qubit that encodes the first (second) input of the function $f(x)$, where *a* denotes an ancilla qubit. This sequence entangles three matter qubits with an eight–time-bin photonic qudit. Based on the client's photon measurement bases, four possible entangled states are generated, corresponding to four oracles (*37*). (**C**) We obtain a probability of $0.90 \pm 0.05, 0.80 \pm 0.06, 0.94 \pm 0.04$, and 0.78 ± 0.06 of determining the correct outcome for four oracles listed in (A), respectively. (**D**) The server cannot distinguish the implementation of O_1 from O_3 and O_2 from O_4, and we measure the information leakage over $\{O_1, O_3\}$ to be $0.05^{+0.19}_{-0.05}$ bits and $\{O_2, O_4\}$ to be $0.07^{+0.14}_{-0.07}$ bits, respectively. Dash bars indicate the theory expectation.

Platforms like neutral atoms or trapped ions can adopt the demonstrated methods through applying local gates with tens of qubits and transporting them to an optical-access zone for matter-photon entanglement (*30*, *43*). Superconducting qubits can be entangled with microwave photons (*44*) and use cryogenic links (*45*) or microwave-to-optical transduction (*46*) for server-client communication. Lastly, we note that deep-circuit BQC will require substantial reduction in gate error rates, achievable by integrating matter-photon entanglement with error correction (*47*, *48*). In combination with recent experimental advances in quantum error correction (*19*, *21*, *22*, *24*) and error suppression in matter-photon entanglement (*33*, *34*, *49*), our work may pave the way toward eventual realization of fault-tolerant BQC.

REFERENCES AND NOTES

1. J. Preskill, *Quantum* **2**, 79 (2018).
2. A. K. Ekert, *Phys. Rev. Lett.* **67**, 661–663 (1991).
3. H. J. Kimble, *Nature* **453**, 1023–1030 (2008).
4. P. W. Shor, J. Preskill, *Phys. Rev. Lett.* **85**, 441–444 (2000).
5. A. M. Childs, Secure assisted quantum computation. arXiv:quant-ph/0111046 [quant-ph] (2001).
6. A. Broadbent, J. Fitzsimons, E. Kashefi, in *2009 50th Annual IEEE Symposium on Foundations of Computer Science*, 25 to 27 October 2009 (IEEE, 2009), pp. 517–526.
7. P. Arrighi, L. Salvail, *Int. J. Quant. Inf.* **4**, 883–898 (2006).
8. J. F. Fitzsimons, E. Kashefi, *Phys. Rev. A* **96**, 012303 (2017).
9. J. F. Fitzsimons, *NPJ Quantum Inf.* **3**, 23 (2017).
10. B. Polacchi *et al.*, *Nat. Commun.* **14**, 7743 (2023).
11. S. Barz *et al.*, *Science* **335**, 303–308 (2012).
12. S. Barz, J. F. Fitzsimons, E. Kashefi, P. Walther, *Nat. Phys.* **9**, 727–731 (2013).
13. H.-L. Huang *et al.*, *Phys. Rev. Lett.* **119**, 050503 (2017).
14. B. Polacchi *et al.*, Experimental verifiable multi-client blind quantum computing on a Qline architecture. arXiv:2407.09310 [quant-ph] (2024).
15. P. Drmota *et al.*, *Phys. Rev. Lett.* **132**, 150604 (2024).
16. P. Thomas, L. Ruscio, O. Morin, G. Rempe, *Nature* **608**, 677–681 (2022).
17. J. Borregaard *et al.*, *Phys. Rev. X* **10**, 021071 (2020).
18. M. H. Appel *et al.*, *Phys. Rev. Lett.* **128**, 233602 (2022).
19. D. Bluvstein *et al.*, *Nature* **626**, 58–65 (2024).
20. A. G. Radnaev *et al.*, A universal neutral-atom quantum computer with individual optical addressing and non-destructive readout. arXiv:2408.08288 [quant-ph] (2024).
21. R. Acharya *et al.*, *Nature* **614**, 676–681 (2023).
22. R. Acharya *et al.*, Quantum error correction below the surface code threshold. arXiv:2408.13687 [quant-ph] (2024).
23. J. M. Pino *et al.*, *Nature* **592**, 209–213 (2021).
24. C. Ryan-Anderson *et al.*, Implementing Fault-tolerant Entangling Gates on the Five-qubit Code and the Color Code. arXiv:2208.01863 [quant-ph] (2022).
25. S. G. J. Philips *et al.*, *Nature* **609**, 919–924 (2022).
26. M. H. Abobeih *et al.*, *Nature* **606**, 884–889 (2022).
27. R. Debroux *et al.*, *Phys. Rev. X* **11**, 041041 (2021).
28. J. Anders, D. K. L. Oi, E. Kashefi, D. E. Browne, E. Andersson, *Phys. Rev. A* **82**, 020301 (2010).
29. T. Sueki, T. Koshiba, T. Morimae, *Phys. Rev. A* **87**, 060301 (2013).
30. D. Main *et al.*, Distributed Quantum Computing across an Optical Network Link. arXiv:2407.00835 [quant-ph] (2024).
31. S. Daiss *et al.*, *Science* **371**, 614–617 (2021).
32. L. Jiang, J. M. Taylor, A. S. Sørensen, M. D. Lukin, *Phys. Rev. A* **76**, 062323 (2007).
33. C. M. Knaut *et al.*, *Nature* **629**, 573–578 (2024).
34. P.-J. Stas *et al.*, *Science* **378**, 557–560 (2022).
35. M. K. Bhaskar *et al.*, *Nature* **580**, 60–64 (2020).
36. S. Sun *et al.*, *Phys. Rev. Lett.* **121**, 083601 (2018).
37. Materials and methods are available as supplementary material.
38. D. Deutsch, R. Jozsa, *Proc. R. Soc. Lond., Math. Phys. Sci.* **439**, 553–558 (1992).
39. M. Pompili *et al.*, *Science* **372**, 259–264 (2021).
40. K. S. Chou *et al.*, *Nature* **561**, 368–373 (2018).
41. Y. Zhong *et al.*, *Nature* **590**, 571–575 (2021).
42. C. E. Bradley *et al.*, *Phys. Rev. X* **9**, 031045 (2019).
43. T. Đorđević *et al.*, *Science* **373**, 1511–1514 (2021).
44. J. O'Sullivan *et al.*, Deterministic generation of a 20-qubit two-dimensional photonic cluster state. arXiv:2409.06623 [quant-ph] (2024).
45. S. Storz *et al.*, *Nature* **617**, 265–270 (2023).
46. A. Kumar *et al.*, *Nature* **615**, 614–619 (2023).
47. J. Sinclair *et al.*, Fault-tolerant optical interconnects for neutral-atom arrays. arXiv:2408.08955 [quant-ph] (2024).
48. C. A. Pattison, G. Baranes, J. P. B. Ataides, M. D. Lukin, H. Zhou, Fast quantum interconnects via constant-rate entanglement distillation. arXiv:2408.15936 [quant-ph] (2024).
49. B. Grinkemeyer *et al.*, Error-Detected Quantum Operations with Neutral Atoms Mediated by an Optical Cavity. arXiv:2410.10787 [quant-ph] (2024).
50. Y.-C. Wei *et al.*, Universal distributed blind quantum computing with solid-state qubits, version v2, Zenodo (2025); https://doi.org/10.5281/zenodo.14769739.

ACKNOWLEDGMENTS

We thank M. Bhaskar, D. Levonian, D. Sukachev, and M. Sutula for useful discussions and experimental help; E. Kashefi and D. Leichtle for useful discussions on BQC theory; C. De-Eknamkul for support with the tapered-fiber-optical interface; D. Riedel for the support with sample annealing; E. Knyazev, F. A. Arias, and A. A. Armenakas for their insightful discussions and feedback on the manuscript; and J. MacArthur for assistance with electronics. **Funding:** This work was supported by the AWS Center for Quantum Networking, the NSF (grant no. PHY-2012023), NSF Center for Ultracold Atoms, the NSF Engineering Research Center for Quantum Networks (grant no. EEC-1941583), CQN (grant no. EEC-1941583), and NSF QuSeC-TAQS OMA2326787. Devices were fabricated at the Harvard Center for Nanoscale Systems, NSF award no. 2025158. G.B. acknowledges support from the MIT Patrons of Physics Fellows Society. Y.Q.H. acknowledges support from the A*STAR National Science Scholarship G.B. acknowledges support from the MIT Patrons of Physics Fellows Society. Y.Q.H. acknowledges support from the A*STAR National Science Scholarship. F.M. acknowledges support from the NSF through a grant for ITAMP at Harvard University. **Author contributions:** Y.-C.W., P.-J.S., A.S., and G.B. planned the experiment and analyzed the data. G.B., F.M., J.B., and I.W.W. formulated the theory. Y.-C.W., P.J.S., A.S., Y.Q.H., and C.M.K. built the setup and performed the experiment. B.M. and E.N.K. fabricated the devices. All work was supervised by S.F.Y., H.P., M.L., and M.D.L. All authors discussed the results and contributed to the manuscript. Y.-C.W, P.J.S., A.S., and G.B. contributed equally to this work. **Competing interests:** M.D.L. is a cofounder, shareholder, and chief scientist of QuEra Computing. B.M. is a cofounder and chief technology officer of Lightsynq Technologies. J.B. is chief scientist of Lightsynq Technologies. **Data and materials availability:** Data and code can be found on Zenodo (*50*). **License information:** Copyright © 2025 the authors, some rights reserved; exclusive licensee American Association for the Advancement of Science. No claim to original US government works. https://www.science.org/about/science-licenses-journal-article-reuse

SUPPLEMENTARY MATERIALS

science.org/doi/10.1126/science.adu6894
Materials and Methods; Figs. S1 to S25; Tables S1 to S18; References (*51*–*54*)

Submitted 17 November 2024; accepted 14 March 2025

10.1126/science.adu6894

CATALYSIS

Formation of hydrided Pt-Ce-H sites in efficient, selective oxidation catalysts

Ji Yang[1]†, Lorenz J. Falling[2]†, Siyang Yan[3]†, Biluan Zhang[4]†, Pragya Verma[5]†, Luke Daemen[6], Yongqiang Cheng[6], Xiao Zhao[7], Shuchen Zhang[7], Jeng-Lung Chen[8], Bingqing Yao[9], Shengdong Tan[9], Sudong Chae[1], Qian He[9], Slavomir Nemsak[2], Zili Wu[10], David Prendergast[5]*, Yanbing Guo[4]*, Jiaxu Liu[3]*, Miquel Salmeron[7,11]*, Ji Su[1]*

Single-atom site catalysts can improve the rates and selectivity of many catalytic reactions. We have modified Pt_1/CeO_2 single sites by combining them with molecular groups and with oxygen vacancies of the support. The new sites include hydrided (Pt^{2+}-$Ce^{3+}H^{\delta-}$) and hydroxylated (Pt^{2+}-$Ce^{3+}OH$) sites that exhibit higher reactivity and selectivity to previous single sites for several reactions, including a ninefold increase in the reaction rate for carbon monoxide oxidation and a 2.3-fold improvement of propylene selectivity for oxidative dehydrogenation of propane. The atomic structure and reaction steps of these sites were determined with in situ and ex situ spectroscopy techniques and theoretical methods.

Supported metal catalysts have widespread applications in the chemical industry and environmental cleaning (*1*–*5*). Metal-support interactions (MSIs) are usually exploited to modulate catalyst activity (*6*–*10*). Typical MSI effects can lead to metal-support charge transfer, restructuring of metal nanoparticles (NPs), and chemical composition exchange, which provide synergistic properties to control catalysis (*6*, *11*). Generally, the efficiency of MSI reactivity enhancement decays rapidly with increasing metal NP size, with the highest enhancements found in NPs <4 nm in diameter. For single metal atoms, interaction with the support is amplified by the increased number of metal-support bonds (*6*, *12*–*14*).

Single metal atoms can pair with neighboring metal atoms and oxygen vacancy (V_o) sites under MSI effects (*13*, *15*) to form a colocalized active site with synergies that have been shown to attain improved performance for heterogeneous catalysis. For example, colocalized active sites have been reported to facilitate desirable elementary steps, in which the new activation mechanisms provide higher reaction rates and selectivity (*16*) (*17*). Further, the synergy between single Pt atoms, the CeO_2 support, and V_o sites can efficiently help dehydrogenation of large molecular cyclohexane to benzene, outperforming traditional Pt NP catalysts (*13*). Recent studies indicate that the single-atom MSIs have differentiated states and can be finetuned by the size of the support (*18*).

[1]Energy Storage and Distributed Resources Division, Lawrence Berkeley National Laboratory, Berkeley, CA, USA. [2]Advanced Light Source, Lawrence Berkeley National Laboratory, Berkeley, CA, USA. [3]State Key Laboratory of Fine Chemicals, Frontier Science Center for Smart Materials, School of Chemical Engineering, Dalian University of Technology, Dalian, China. [4]College of Chemistry, Central China Normal University, Wuhan, China. [5]The Molecular Foundry, Lawrence Berkeley National Laboratory, Berkeley, CA, USA. [6]Neutron Scattering Division, Oak Ridge National Laboratory, Oak Ridge, TN, USA. [7]Materials Sciences Division, Lawrence Berkeley National Laboratory, Berkeley, CA, USA. [8]National Synchrotron Radiation Research Center, Science-Based Industrial Park, Hsinchu, Taiwan. [9]Department of Materials Science and Engineering, National University of Singapore, Singapore, Singapore. [10]Chemical Sciences Division, Oak Ridge National Laboratory, Oak Ridge, TN, USA. [11]Department of Materials Science and Engineering, University of CA, Berkeley, Berkeley, CA, USA.
***Corresponding author. Email: jisu@lbl.gov (J.S.); mbsalmeron@lbl.gov (M.S.); liujiaxu@dlut.edu.cn (J.L.); guoyanbing@mail.ccnu.edu.cn (Y.G.); dgprendergast@lbl.gov (D.P.)**
†These authors contributed equally to this work.

These findings motivated our study of colocalization, geometry, oxidation states, and new interactions between the constituent atoms and functional groups in adjacent sites. We show that, starting with Pt_1/CeO_2 single sites, we can create new hydrided sites Pt^{2+}-$Ce^{3+}H^{\delta-}$ as well as hydroxylated Pt^{2+}-$Ce^{3+}OH$ pairs which, compared with the original Pt_1/CeO_2 single sites, exhibit nine times higher CO oxidation activity. The active Ce-H hydride and Ce-OH hydroxide species formed only at Pt^{2+}-Ce^{3+} pair sites on the CeO_2 support with proper reduction.

To determine the atomic structure and chemical reactions forming these new sites and their interactions with reactant species, we used an array of in situ and ex situ spectroscopies and theoretical calculations. The critical role of the $H^{\delta-}$ catalytic site in enhanced O_2 activation and catalytic performance is highlighted. Our work demonstrates an easy but overlooked approach to tailoring the catalytic properties of single-atom site catalysts by hydrogenation of active sites. The concept of hydrided sites can be extended to supported metal NP catalysts (*19*–*23*) for many reactions, such as methanol synthesis by CO_2 hydrogenation and others, warranting further study to understand the effects and promises of hydrided sites [with their broader implications detailed in the supplementary materials (SM)].

Active site formation

We prepared single Pt atoms on CeO_2 nanopowder (Pt_1/CeO_2) with a particle sizes <20 nm using the wet synthesis method. Typically, the H_2PtCl_6 precursor was hydroxylated to $[PtCl_4(OH)_2]^{2-}$ in a weakly basic solution (pH of 8) (*24*), and the CeO_2 surface became positively charged as its isoelectric pH value was ~8.7 (see fig. S1) (*25*, *26*). The strong electrostatic adsorption promoted repulsive interactions between Pt ions in solution, which distributed isolated Pt ions on the CeO_2 surface. Further vacuum drying at 200°C helped eliminate solution residues to obtain Pt_1/CeO_2 (fig. S2), which after H_2 reduction at 200°C, enabled integration of the Pt atoms to generate the hydrided-site catalyst.

The interaction between the Pt atoms and CeO_2 matrix during reduction was monitored by the evolution of the Pt 4*f* and Ce 4*d* ambient-pressure x-ray photoelectron spectroscopy (AP-XPS) peaks in 100 mTorr H_2 at increasing temperatures (Fig. 1A). Before H_2 reduction, the Pt 4*f* 7/2 binding energy was 76 eV, which compares well with that of octahedrally coordinated Pt^{4+} in PtO_2 and K_2PtCl_6 (*27*). Cerium in the Ce^{4+} state contributed peaks at 123 and 126 eV, whereas mixed Ce^{3+} and Ce^{4+} contributed peaks between 108 and 120 eV (*28*). Using principal component analysis, we deconvoluted the Ce 4*d* features to quantify the change in oxidation state in a series of Ce 4*d* spectra at temperatures steps from ~60° to ~390°C. As the temperature increased from ~60° to 250°C, Pt^{4+} and Ce^{4+} were gradually reduced, as evidenced by a growing Pt 4*f* doublet with a 7/2 line at lower binding energy of 75 eV and a larger relative contribution of Ce^{3+} between 108 and 120 eV, as well as 107 eV, where Ce^{4+} does not contribute (*28*).

The reduction rate of Pt (Fig. 1A, center panel) was faster at >250°C and reached a plateau at 310°C with ~10% of Pt^{4+} remaining. Although the reduction to metallic Pt could be excluded as shown by the binding energy and symmetric line shape of the Pt 4*f* XPS peak, the final oxidation state remains could not be determined from XPS data alone. A more direct measure of the electron and hole density was obtained from x-ray absorption near-edge structure (XANES) analyses (fig. S3), which indicated that the Pt oxidation state was between +4 and +2 for atomic Pt on CeO_2 nanopowder after H_2 reduction (we denoted the sample after reduction as Pt_1-Ce/CeO_{2-x}) (*29*).

The Pt 4*f* doublet at 75 eV was therefore related to Pt^{2+}. The CeO_2 support reduction was not as rapid and had an onset at ~150°C. The contribution of Ce^{3+} to the XPS peak continued to grow, reaching ~40% at ~390°C, which was ~10% higher than that for the reference CeO_2 sample without Pt. The generation of Ce^{3+} species on Pt_1-Ce/CeO_{2-x} by reduction in H_2 was also confirmed by in situ electron energy loss spectroscopy (EELS) results (figs. S4 and table S1) (*30*). These findings suggested that atomic Pt facilitated the reduction of CeO_2 through the

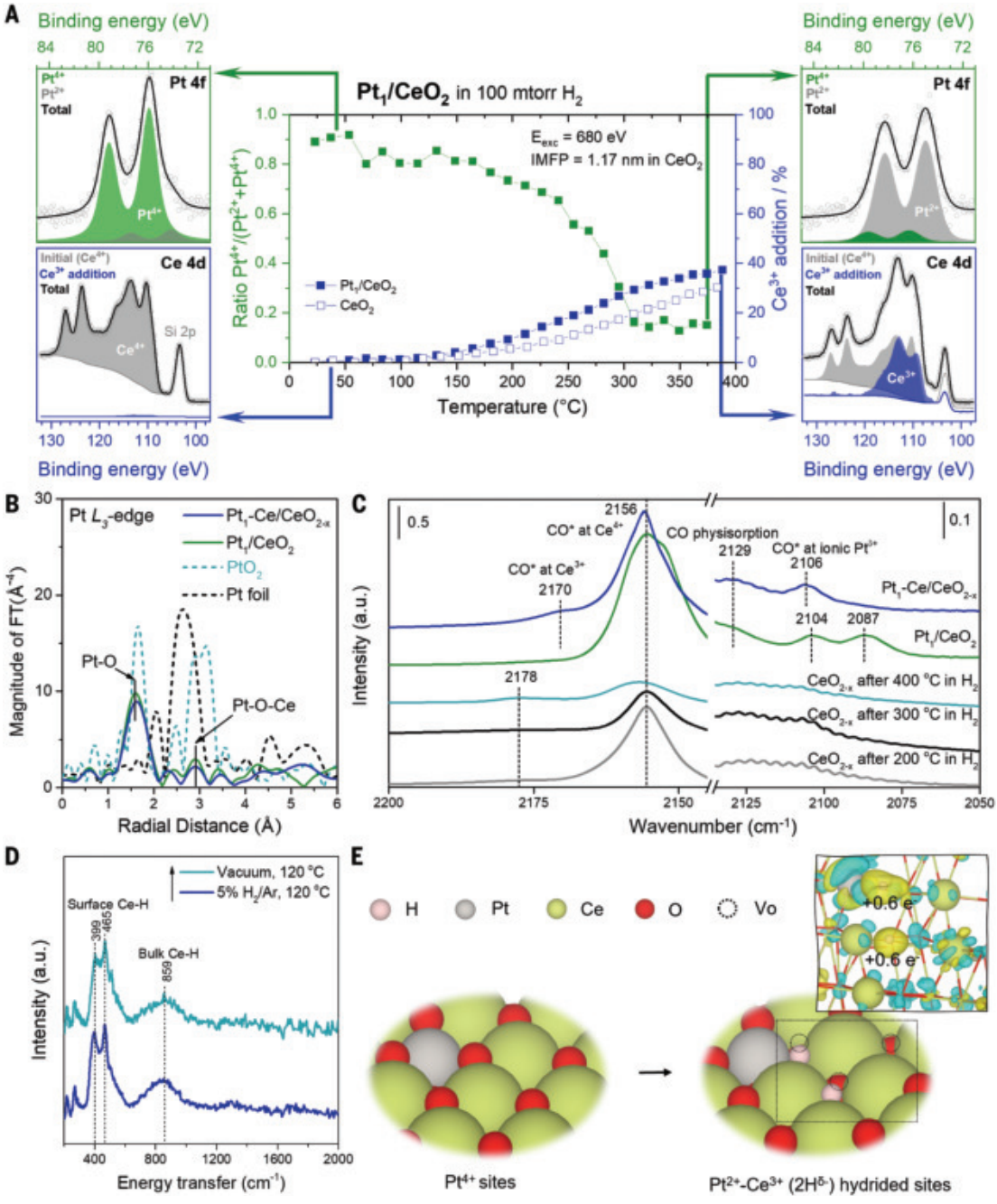

Fig. 1. Formation and structure of hydrided sites Pt^{2+}-Ce^{3+}($H^{\delta-}$). (**A**) APXPS results showing the changes in Pt 4*f* and Ce 4*d* core levels binding energy during formation of the hydrided sites by reaction with H_2 as a function of temperature (middle panel). (**B**) FT-EXAFS spectra of the Pt L_3-edge for Pt_1/CeO_2 and Pt_1-Ce/CeO_{2-x} with reference spectra from Pt foil and PtO_2. (**C**) Dual-beam FTIR spectra at liquid N_2 temperature (77 K) from CO adsorption on Pt_1/CeO_2, Pt_1-Ce/CeO_{2-x} and CeO_{2-x} control samples. (**D**) In situ INS spectra of Pt_1-Ce/CeO_{2-x} collected at 5K with a purge of 5% H_2/Ar at 120°C, followed by evacuation at 120°C. (**E**) DFT models of Pt single sites and hydrided sites Pt^{2+}-Ce^{3+}($H^{\delta-}$), where electron accumulation and depletion are represented by yellow ($\Delta\rho = +1\times10^{-3}$ e bohr^{-3}) and cyan ($\Delta\rho = -1\times10^{-3}$ e bohr^{-3}) colors, respectively.

H atom spillover effect (see SM for a discussion on the ability of ionic Pt sites to dissociate H_2).

Local structure of hydrided sites

Fourier-transform of extended x-ray absorption fine structure (FT-EXAFS) spectra revealed the atomic dispersion of Pt sites for Pt_1/CeO_2 and Pt_1-Ce/CeO_{2-x} (Fig. 1B), as indicated by the absence of the Pt-Pt scattering peak. The strong stabilization of single Pt atoms on CeO_2 was also corroborated by the identification of Pt-O and Pt-O-Ce coordination shells in two samples (Fig. 1B). Additionally, high-resolution high-angle annular dark-field scanning transmission electron microscopy (HAADF-STEM) images and intensity line profiles (fig. S5), confirmed the single-atom state of Pt sites on CeO_2 (see SM for a detailed feasibility analysis of statistical analysis in HAADF-STEM imaging). EXAFS curve-fitting results (fig. S6 and table S2) showed that the Pt-O coordination numbers for Pt_1/CeO_2 and Pt_1-Ce/CeO_{2-x} were 5.9 and 4.2, respectively.

Because of the high sensitivity of the C-O bond stretch mode to the local electronic structure of the adsorption site, we used CO as a probe molecule to characterize the outermost atomic structure of the catalysts. Fourier-transform infrared (FTIR) spectra taken after CO adsorption at

77 K revealed the presence of different Ce and Pt sites (Fig. 1C) corresponding to Pt_1/CeO_2, Pt_1-Ce/CeO_{2-x}, and CeO_{2-x} control samples. Six distinct peaks at 2170, 2156, 2129, and 2106/2104/2087 cm^{-1} were assigned to CO adsorption on Ce^{3+}, Ce^{4+}, and CO physisorption on ionic $Pt^{\delta+}$, and chemisorption (*CO) on ionic $Pt^{\delta+}$, respectively, with different local structures (*14*). The CO adsorption peak on Ce^{3+}, centered at 2170 cm^{-1} in Pt_1-Ce/CeO_{2-x}, was blue-shifted to 2178 cm^{-1} on pure CeO_{2-x} samples, whereas the peak position of CO absorbed on Ce^{4+} remained unchanged. This difference strongly indicated that the Ce^{3+} created in Pt_1-Ce/CeO_{2-x} was chemically different from that in reduced CeO_{2-x}. The lower wave number of the CO peak on Ce^{3+} in Pt_1-Ce/CeO_{2-x} revealed the spatial proximity and electronic interaction between Ce^{3+} and Pt^{2+}.

We also performed in situ inelastic neutron scattering (INS) studies to determine the speciation of H atoms during spillover (Fig. 1D). The strong shoulder peaks at 399 and 465 cm^{-1} and a broad peak at 859 cm^{-1} are observed with the reduction by H_2, which we attributed to Ce-H hydrides on the surface and in the bulk, respectively (*31*). The spectral features remained unchanged after further vacuum treatment at 120°C , indicating that surface Ce-H and bulk Ce-H hydrides were stable and excluding the possibility of surface species such as adsorbed water.

Density functional theory (DFT) calculations were performed to further understand the electronic and geometric structure change of surface sites during H_2 reduction. APXPS, x-ray diffraction (XRD), and EXAFS results (Fig. 1A, fig. S7, and table S2) indicated octahedrally O-coordinated Pt^{4+} of the Pt_1/CeO_2 on the CeO_2 (111) surface, which was used as the starting point in the DFT calculations (left panel in Fig. 1E, and fig. S8). We associated the H_2 reduction process with the creation of V_o. Combined with the above spectroscopic results, our theoretical results (figs. S8 to S11 and table S3) showed that the generation of V_o sites created Pt^{2+}-Ce^{3+} pair sites, with an increased population of adjacent Ce^{3+} created by H from spillover effects (See detailed analysis in fig. S7).

Moreover, we found that the active Ce-H hydrided sites could be formed only at Pt^{2+}-Ce^{3+} pair sites with more than three nearby V_o sites that created an electron-rich surface site. Figure 1E (right panel) shows the formation of 2 Ce-H hydrides (Ce-$H^{\delta-}$) on Pt_1-Ce/CeO_{2-x}_$3V_o$ model after H_2 activation. Bader charge analysis indicated that each H atom gained 0.6 e^- from adjacent Ce^{3+} to form the hydride. On the Pt_1-Ce/CeO_{2-x}_$6V_o$ model surface that had a higher surface electron density than Pt_1-Ce/CeO_{2-x}_$3V_o$ (fig. S12 and table S3), two Ce-$H^{\delta-}$ are also formed with favorable thermodynamics (fig. S12). However, only two lattice OH groups were formed on the Pt_1/CeO_2 and Pt_1-Ce/CeO_{2-x}_$1V_o$ models by bonding with lattice oxygen after H_2 dissociation (fig. S13). Even on the Pt_1-Ce/CeO_{2-x}_$2V_o$ model, only one proton (donating 0.5 e^-) and one $H^{\delta-}$ (gaining 0.2e^-) at Pt^{2+} could be formed (fig. S14 and table S3). These findings supported the formation of hydrided sites Pt^{2+}-Ce^{3+}($H^{\delta-}$) on Pt_1-Ce/CeO_{2-x} nanopowder after H_2 reduction and suggest the importance of retaining electron-enriched surface states to create hydrided sites.

Hydrided site–enhanced surface reactivity

We used CO oxidation to probe the activity of hydrided sites Pt^{2+}-Ce^{3+}($H^{\delta-}$) (Fig. 2, A to C, and figs. S15 to S18). The introduction of Pt atoms on CeO_2 increased the CO oxidation activity (fig. S15). In particular, the temperature at 10% CO conversion (T_{10}) on Pt^{2+}-Ce^{3+}($H^{\delta-}$) hydrided sites in the first run was 40°C lower than in the second and third runs (80°C versus 120°C, respectively; Fig. 2A). This result showed that hydrided sites substantially improved surface reactivity, whereas the active species were likely consumed rather than replenished. However, after 3% H_2 addition, T_{10} could be sustained and CO conversion at 160°C was increased from 33.8 to 100% on Pt^{2+}-Ce^{3+}($H^{\delta-}$) hydrided sites within three runs (Fig. 2A). Figure 2B shows that the turnover frequency (TOF) of CO, O_2, and H_2 at 100°C on Pt^{2+}-Ce^{3+}($H^{\delta-}$) hydrided sites was ~9, ~29, and ~135 times higher, respectively, than that of Pt_1 single sites, indicating a higher and more effective activation of CO, O_2, and H_2. This result was consistent with the favorable kinetics of CO activation by Pt^{2+}-Ce^{3+}($H^{\delta-}$) hydrided sites (fig. S16).

To study the properties of Pt^{2+}-Ce^{3+}($H^{\delta-}$) hydrided sites, we compared CO oxidation performance of the catalyst in the presence of H_2

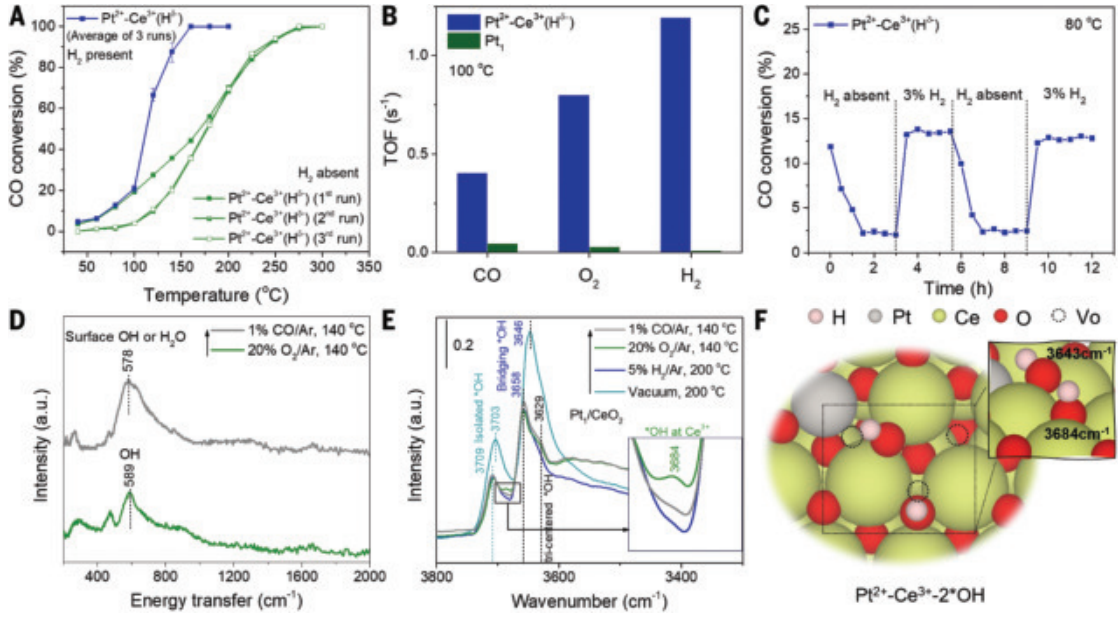

Fig. 2. Catalytic performance of Pt^{2+}-Ce^{3+}($H^{\delta-}$) hydrided-site catalyst and enhanced O_2 activation. (**A**) CO conversion as a function of temperature for Pt^{2+}-Ce^{3+}($H^{\delta-}$) hydrided-site catalyst in the absence and in the presence of H_2 gas. Reaction conditions in the absence of H_2 (H_2 absent): 1% CO + 20% O_2 balanced with argon at weight hourly space velocity (WHSV) of 36,000 mL g^{-1} h^{-1}; Reaction conditions in the presence of 3% H_2 (H_2 present): 1% CO + 20% O_2 + 3% H_2 balanced with argon at WHSV of 36,000 mL g^{-1} h^{-1}. (**B**) Pt site-specific TOF of CO, O_2, and H_2 at 100°C for Pt^{2+}-Ce^{3+}($H^{\delta-}$) hydrided sites and Pt_1 single sites when 3% H_2 was co-fed. (**C**) Effect of H_2 addition on CO conversion for Pt^{2+}-Ce^{3+}($H^{\delta-}$) hydrided-site catalyst. (**D**) In situ INS spectra of Pt^{2+}-Ce^{3+}($H^{\delta-}$) hydrided sites collected at 5K with a purge of 20% O_2/Ar at 140°C, followed by 1% CO/Ar at 140°C. (**E**) In situ dual-beam FTIR spectra of surface OH adsorption on Pt single sites followed by evacuation at 200°C, 5% H_2/Ar at 200°C, 20% O_2/Ar at 140°C, and 1% CO/Ar at 140°C in sequence. (**F**) DFT simulations of O_2 speciation on Pt^{2+}-Ce^{3+}($H^{\delta-}$) hydrided sites.

in different conditions. We found that Pt^{2+}-$Ce^{3+}(H^{\delta-})$ hydrided sites could be passivated in an oxidative environment (fig. S17). Time-on-stream CO oxidation tests indicated that CO conversion on Pt^{2+}-$Ce^{3+}(H^{\delta-})$ hydrided sites decreased from 13.6 to 3.3% within 1.5 hours in the absence of H_2 co-feeding (fig. S17) and then remained unchanged. A constant feed of 3% H_2 sustained the CO conversion at ~13.0% for >4 hours. This process was also reversible (Fig. 2C). By contrast, Pt single sites displayed approximately constant CO conversion of <2% with and without H_2 co-feeding (fig. S18). These results highlight the high sensitivity of Pt^{2+}-$Ce^{3+}(H^{\delta-})$ hydrided sites to H_2 and demonstrate their sustained high surface reactivity in a H_2-containing environment.

We then used the hydrided-site catalyst for CO preferential oxidation (PROX), a promising H_2 purification process providing high-purity H_2 for proton-exchange membrane fuel cells (*32*, *33*). As shown in Fig. 3A, O_2-to-CO_2 selectivity for the Pt^{2+}-$Ce^{3+}(H^{\delta-})$ hydrided-site catalyst could reach 85.5% at 80°C at a CO conversion of 16.9%. The limited CO conversion is the result of insufficient Pt sites (Pt weight loading of 0.044% as determined by inductively coupled plasma-optical emission spectroscopy, shown in table S4). When the Pt weight loading of hydrided-site catalyst was increased to 0.15% (table S5), CO conversion reached >99.9% at 80°C after 24 hours with a weight hourly space velocity (WHSV) of 12,000 mL g^{-1} h^{-1} (Fig. 3B). The high stability of the hydrided sites for CO PROX was further demonstrated by maintaining ~61% CO conversion over 24 hours at an increased WHSV (Fig. S19). The advantages of hydrided-site catalysts in CO PROX reaction compared with other state-of-the-art catalysts (table S6) are detailed in the SM. In addition, the hydrided sites exhibited enhanced propane conversion and markedly higher selectivity for oxidative dehydrogenation of propane (ODP), with the propylene (C_3H_6) selectivity increased by 2.3 times compared with that of Pt single sites (Fig. 3, C and D). Moreover, the Pt sites in hydrided-site catalyst with 0.15% Pt loading maintained atomic dispersion after undergoing CO PROX reaction, or ODP reaction (see HAADF-STEM analysis results in figs. S20 and S21). A comprehensive discussion on the good thermal stability (fig. S22) of the hydrided-site catalyst is provided in the SM. These results indicate that the formation of hydrided sites offers new capabilities for catalyzing other important reactions.

We used INS spectra to study hydride speciation under low-temperature CO oxidation conditions, (Fig. 2D). When Pt^{2+}-$Ce^{3+}(H^{\delta-})$ hydrided sites were exposed to an O_2 atmosphere, the features of Ce-H hydrides (*399*, *465*, and *859* cm^{-1}; Fig. 1D) diminished, and a new band appeared, centered at 589 cm^{-1} (Fig. 2D), which we assigned to hydroxyl groups (OH) through the reaction between Ce-H hydrides and molecular O_2. CO purge generated a broad and intensive band at 578 cm^{-1}, which was caused by water formation generated from $CO + 2OH \rightarrow CO_2 + H_2O$.

In situ FTIR studies were used to determine O_2 speciation (Fig. 2E). Pt_1 single sites (in a vacuum) exhibited two different types of OH adsorption which we identified as isolated OH at Ce^{4+} (*3703* cm^{-1}) and bridging OH (*3646* cm^{-1}) (*31*, *34*, *35*). Subsequent H_2 reductive treatment was applied to in situ generation of Pt^{2+}-$Ce^{3+}(H^{\delta-})$ hydrided sites, where the peak intensity of the OH decreased through reaction with dissociated H species to form water (*31*). O_2 feeding generated a new band at *3684* cm^{-1}, associated with OH bonded at Ce^{3+} (*31*, *36*), whereas isolated and bridging OH peaks remained unchanged. When purging with CO, only the peak of OH on Ce^{3+} at *3684* cm^{-1} disappeared (inset in Fig. 2E), indicating its consumption by CO oxidation and its high reactivity. The products CO_2 and H_2O were detected by mass spectrometry (fig. S23), confirming our conjecture in the INS analysis that H_2O was generated by reaction of CO with reactive OH.

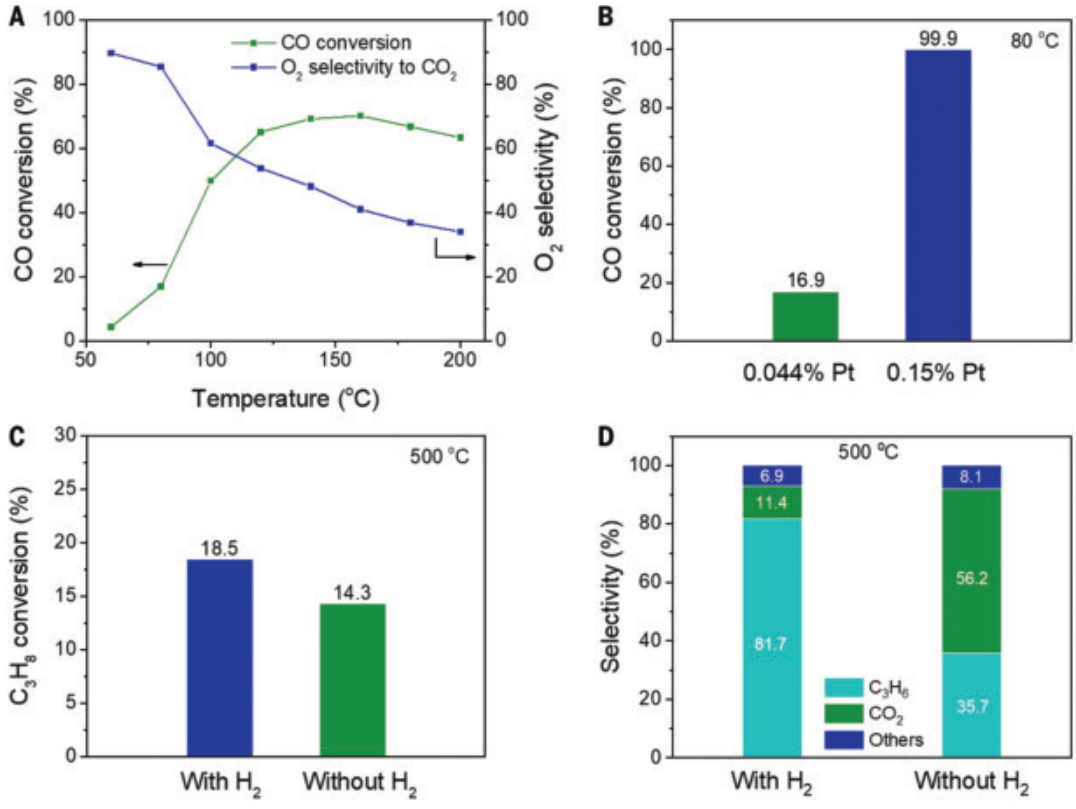

Fig. 3. Expanding the application of Pt^{2+}-$Ce^{3+}(H^{\delta-})$ hydrided-site catalysts to other reactions. (**A**) Activity and selectivity for CO to CO_2 conversion during CO PROX by Pt^{2+}-$Ce^{3+}(H^{\delta-})$ hydrided-site catalyst. Reaction conditions: 1% CO + 1% O_2 + 40% H_2 balanced with argon at WHSV of 36,000 mL g^{-1} h^{-1}. (**B**) Comparison of CO conversion rate under CO PROX conditions of 1% CO + 1% O_2 + 40% H_2 balanced with argon, for two Pt loadings of 0.044% and 0.15%, tested at WHSV of 36,000 and 12,000 mL g^{-1} h^{-1}, respectively. (**C**) Propane (C_3H_8) conversion rate and (**D**) product selectivity for ODP over Pt^{2+}-$Ce^{3+}(H^{\delta-})$ hydrided-site catalysts with/without the participation of H_2. Reaction conditions with H_2 co-feeding: 20% C_3H_8 + 10% O_2 + 20% H_2 + 10% N_2 balanced with helium at WHSV of 24,000 mL g^{-1} h^{-1}; reaction conditions without H_2: 20% C_3H_8 + 10% O_2 + 10% N_2 balanced with helium at WHSV of 24,000 mL g^{-1} h^{-1}.

DFT calculations provided further insight into hydrided-site –controlled O_2 activation. When O_2 was introduced, two OH groups formed on Ce^{3+} (Ce^{3+}-OH) (Fig. 2F). The calculated stretching vibration frequencies of these OH groups were 3684 and 3643 cm^{-1}, in line with our FTIR observations (Fig. 2E). When generating more V_o sites (e.g., $6V_o$) around Pt^{2+}-$Ce^{3+}(H^{\delta-})$ hydrided sites, Ce^{3+}-OH species were also readily formed after arrival and dissociation of O_2 (fig. S24). However, molecular O_2 adsorption and activation preferentially occur at unoccupied V_o sites if hydrided sites were not well-formed on electron-deficient surface sites (fig. S25 and table S3). Our findings indicated that the formation of hydrided sites Pt^{2+}-$Ce^{3+}(H^{\delta-})$ was critical to regulating the O_2 activation pathway.

Hydride-transfer catalysis mechanism

We developed a hydrided-site synergistic mechanism for CO oxidation using DFT calculations (Fig. 4, figs. S26 to S32, and data S1 to S11), with computational methods detailed in the SM. Figure 4A and fig. S26 show four pathways for the formation of hydrided sites Pt^{2+}-$Ce^{3+}(H^{\delta-})$ from H_2 dissociation at Pt sites and subsequent spillover to Ce^{3+} and forming the active Ce-H hydrided site. Depending on the H spillover path, the final structure of the hydride will determine the energy barrier (E_a) for H_2 activation, varying from 0.13 to 0.16 eV (Fig. 4B). The final Pt^{2+}-Ce^{3+} ($H^{\delta-}$) sites serve as highly reactive catalytic sites for CO oxidation (Fig. 4C). The key role of Pt (fig. S27) in forming hydrided sites is detailed in SM. Our DFT calculation results show that the hydrides ($H^{\delta-}$) could be recycled or consumed in each CO oxidation cycle.

In the $H^{\delta-}$ recycling path (upper diagram in Fig. 4C), both two $Ce^{3+}H^{\delta-}$ sites are adjacent to Pt atoms within its first and second coordination sphere (generated from H spillover paths I and II), which activate adsorbed molecular O_2 ([1]) to form two reactive OH ([2]) at the same Ce^{3+} (Ce^{3+}-OH) after overcoming an E_a of 0.29 eV ([TS1]). Once CO is adsorbed at the Pt site ([3]), CO oxidation readily proceeds through the coupling of CO and Ce^{3+}-OH to yield carboxyl (*COOH, [TS2]), which is then decomposed to generate the first CO_2 and return the $H^{\delta-}$ ([4]). This is the rate-determining step (RDS) with an E_a of 0.43 eV ([TS2]). The other Ce^{3+}-OH reacts with another adsorbed CO at the Pt site and undergoes a similar oxidation process ([5]), with an E_a of 0.42 eV ([TS3]). After releasing the second CO_2 and restoring the second $H^{\delta-}$ ([FS]), hydrided-sites Pt^{2+}-Ce^{3+} ($H^{\delta-}$) are recovered for the next catalytic cycle.

The pathway and energy of O_2 activation in the $H^{\delta-}$ consumption path (lower diagram in Fig. 4C) are similar to that of the $H^{\delta-}$ recycling path, the difference being that (i) one of the $Ce^{3+}H^{\delta-}$ sites and the subsequently created Ce^{3+}-OH site are located beyond the second coordination sphere

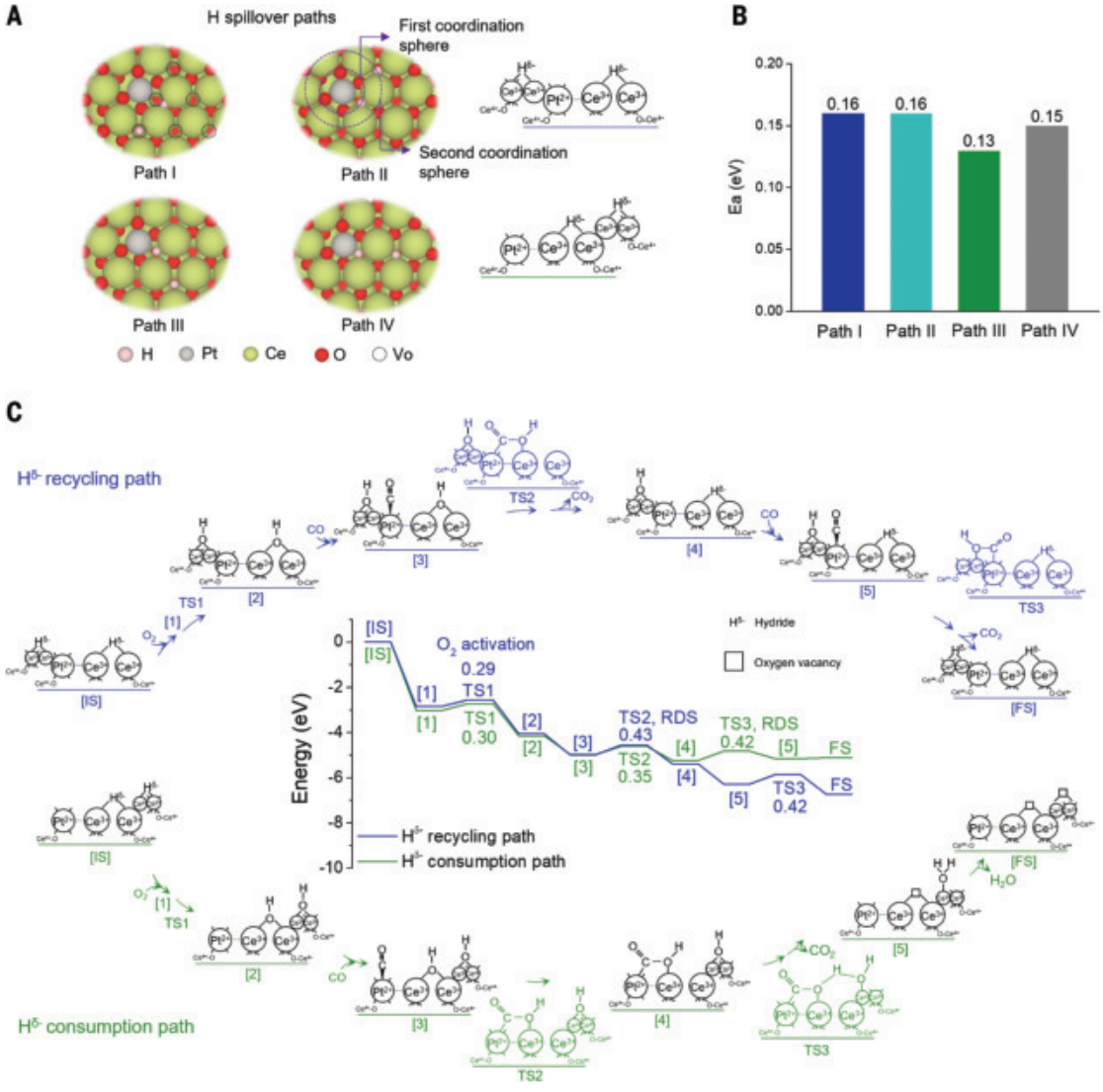

Fig. 4. Hydride transfer-controlled CO oxidation mechanism. (**A**) The hydrogen spillover paths on Pt_1-Ce/CeO_{2-x}_$6V_o$ model after H_2 activation. (**B**) Comparison of calculated energy barrier for four H_2 activation paths. (**C**) Catalytic cycles and potential energy diagram of $H^{\delta-}$-transfer enhanced CO oxidation on Pt^{2+}-$Ce^{3+}(H^{\delta-})$ hydrided sites. IS, TS, and FS represent initial state, transition state, and final state, respectively.

of Pt site (represented by H spillover path III and IV) and (ii) the generated *COOH (by overcoming E_a of 0.35 eV) tends to react with the other Ce^{3+}-OH to release CO_2 and H_2O because of their spatial proximity, which is the RDS with an E_a of 0.42 eV.

We found that two $H^{\delta-}$ transfer pathways for CO oxidation displayed comparable energy barriers for the RDS (0.43 vs 0.42 eV). Considering the molar balance of elements in a catalytic reaction, the $H^{\delta-}$ recycling and consumption path for CO oxidation has O_2-to-CO_2 selectivity of 100 and 50%, respectively. Our CO PROX results (Fig. 3A) showed that Pt^{2+}-Ce^{3+}($H^{\delta-}$) hydrided-site catalyst displayed a O_2-to-CO_2 selectivity of >50% below 120°C, which indicated that both $H^{\delta-}$ recycling and consumption paths were involved in the CO oxidation process. Further DFT calculations revealed that two CO oxidation pathways showed decreasing E_a for the RDS with the increase of surface V_o coverage (fig. S28). In particular, creating a highly electron-rich surface (i.e., more reduced sites) enabled the $H^{\delta-}$ recycling with more favorable kinetics than in the $H^{\delta-}$ consumption path (for example, with 9 V_o, E_a was 0.40 versus 0.43 eV with 9 V_o). These findings demonstrate the strong impact of the (atomic and electronic) structure of hydrided sites Pt^{2+}-Ce^{3+}($H^{\delta-}$) on the CO oxidation mechanism.

In contrast to the high reactivity of Ce^{3+}-OH formed on Pt^{2+}-Ce^{3+}($H^{\delta-}$), the lattice OH groups on the Pt_1 single-site model, formed by the reaction of dissociated H with lattice O, were inactive for CO oxidation (fig. S29). This reaction proceeds through the Mars-van-Krevelen (MvK) mechanism on Pt_1/CeO_2 (fig. S30), where CO was oxidized by surface lattice oxygen (as RDS) with an E_a of 0.70 eV. Theoretical calculations showed that the CO oxidation pathway shifted from the MvK mechanism (0.77 eV) on Pt single sites to a kinetically favorable Langmuir–Hinshelwood mechanism (0.52 eV) on Pt^{2+}-Ce^{3+} sites in the absence of H_2 (figs. S31 and S32). However, their RDS are restricted by the low reactivity of lattice and adsorbed oxygen and sluggish O abstraction by *CO.

Comparatively, with the formation of Pt^{2+}-Ce^{3+}($H^{\delta-}$) hydrided sites, the O_2 activation pathway was fundamentally changed and CO could be readily oxidized to CO_2 by $Ce^{3+}H^{\delta-}$ site-activated Ce^{3+}-OH with a low RDS barrier of ~0.40 eV. This marked decrease of RDS energy barrier explains the excellent CO oxidation activity of Pt^{2+}-Ce^{3+}($H^{\delta-}$) hydrided-site catalyst at low temperatures (Fig. 2, A and B). Moreover, CO oxidation proceeded through the $H^{\delta-}$ recycling path when two $Ce^{3+}H^{\delta-}$ sites were within the first and second coordination sphere of Pt^{2+}, which shifted to a $H^{\delta-}$ consumption path if $H^{\delta-}$ spilled over to a more distant Ce^{3+} site. Our DFT results demonstrate the advantage of Pt^{2+}-Ce^{3+} ($H^{\delta-}$) hydrided sites in CO oxidation and underscore the critical role of proximal atom synergy in multisites to accelerate catalytic reactions. Further, the $H^{\delta-}$ transfer mechanism provides new insights into the role of the $H^{\delta-}$ site in oxidation reactions.

Summary

We demonstrated the formation of Pt^{2+}-Ce^{3+}($H^{\delta-}$) hydrided sites by modification of Pt single-atom sites on CeO_2 with a reaction rate nine times higher for CO oxidation than that of Pt single sites. With the help of APXPS, XANES, EELS, FTIR, and INS characterization, in addition to DFT simulations, we determined the structure and formation mechanism of the new Pt^{2+}-Ce^{3+}($H^{\delta-}$) hydrided sites and CO oxidation mechanism. Our study offers new opportunities for catalyst innovations and new breakthroughs in industrial reactions such as the selective oxidation of short-chain alkanes.

REFERENCES AND NOTES

1. Y. Guo, M. Wang, Q. Zhu, D. Xiao, D. Ma, *Nat. Catal.* **5**, 766–776 (2022).
2. C. Vogt, B. M. Weckhuysen, *Nat. Rev. Chem.* **6**, 89–111 (2022).
3. L. Liu, A. Corma, *Chem. Rev.* **118**, 4981–5079 (2018).
4. P. Munnik, P. E. de Jongh, K. P. de Jong, *Chem. Rev.* **115**, 6687–6718 (2015).
5. S. Mitchell, J. Pérez-Ramírez, *Nat. Rev. Mater.* **6**, 969–985 (2021).
6. T. W. Van Deelen, C. Hernández Mejía, K. P. de Jong, *Nat. Catal.* **2**, 955–970 (2019).
7. S. J. Tauster, S. C. Fung, R. T. K. Baker, J. A. Horsley, *Science* **211**, 1121–1125 (1981).
8. S. J. Tauster, S. C. Fung, *J. Catal.* **55**, 29–35 (1978).
9. F. Tao, M. Salmeron, *Science* **386**, eadq0102 (2024).
10. T. Wang *et al.*, *Science* **386**, 915–920 (2024).
11. P. Wu *et al.*, *Nat. Commun.* **11**, 3042 (2020).
12. L. Chen *et al.*, *J. Am. Chem. Soc.* **141**, 17995–17999 (2019).
13. L. Chen *et al.*, *Nat. Commun.* **13**, 1092 (2022).
14. F. Maurer *et al.*, *Nat. Catal.* **3**, 824–833 (2020).
15. R. Gao *et al.*, *Nat. Energy* **6**, 614–623 (2021).
16. I. Ro *et al.*, *Nature* **609**, 287–292 (2022).
17. L. Zeng *et al.*, *Science* **383**, 998–1004 (2024).
18. V. Muravev *et al.*, *Science* **380**, 1174–1179 (2023).
19. J. C. Duchet *et al.*, *J. Catal.* **198**, 328–337 (2001).
20. O. Pozdnyakova *et al.*, *J. Catal.* **237**, 17–28 (2006).
21. A. Le Valant *et al.*, *J. Catal.* **324**, 41–49 (2015).
22. J. C. Frost, *Nature* **334**, 577–580 (1988).
23. B. Wang *et al.*, *Adv. Mater. Interfaces* **8**, 2002169 (2021).
24. W. A. Spieker *et al.*, *Appl. Catal. A Gen.* **232**, 219–235 (2002).
25. C. W. Neil *et al.*, *Environ. Sci. Nano* **8**, 233–244 (2021).
26. X. Li *et al.*, *Nature* **611**, 284–288 (2022).
27. A. V. Naumkin, A. Kraut-Vass, S. W. Gaarenstroom, C. J. Powell, NIST X-ray Photoelectron Spectroscopy Database, Version 5.0, NIST (2012); https://dx.doi.org/10.18434/T4T88K.
28. M. Baron, O. Bondarehuk, D. Stacchiola, S. Shaikhutdinov, H. J. Freund, *J. Phys. Chem. C* **113**, 6042–6049 (2009).
29. B. Qiao *et al.*, *Nat. Chem.* **3**, 634–641 (2011).
30. J. Bentley *et al.*, *J. Phys. Conf. Ser.* **26**, 69–72 (2006).
31. Z. Wu *et al.*, *J. Am. Chem. Soc.* **139**, 9721–9727 (2017).
32. S. Cao *et al.*, *Sci. Adv.* **6**, eaba3809 (2020).
33. J. Saavedra *et al.*, *Nat. Chem.* **8**, 584–589 (2016).
34. C. Megías-Sayago *et al.*, *ACS Catal.* **8**, 11154–11164 (2018).
35. Q. Dai *et al.*, *Appl. Catal. B Environ.* **168–169**, 141–155 (2015).
36. C. Binet, M. Daturi, J. C. Lavalley, *Catal. Today* **50**, 207–225 (1999).
37. J. Yang *et al.*, Data for: Formation of hydrided Pt-Ce-H sites in efficient, selective oxidation catalysts, Zenodo (2025); https://doi.org/10.5281/zenodo.14954782.

ACKNOWLEDGMENTS

Funding: This work was funded by the following: US Department of Energy (DOE), Office of Science, Office of Basic Energy Sciences, Chemical Sciences, Geosciences, and Biosciences Division, under contract DE-AC02-05CH11231, FWP CH030201 (Catalysis Research Program); Work by J.Y., L.J.F., P.Y., and X.Z. was performed as part of User Projects at the Molecular Foundry of the Lawrence Berkeley National Laboratory under contract DE-AC02-05CH11231. L.J.F. acknowledges support from the Alexander von Humboldt Foundation, Bonn, Germany. P.Y., D.P., and J.S. acknowledge support from the Hydrogen Materials Advanced Research Consortium (HyMARC), established as part of the Energy Materials Network by the US DOE, Office of Energy Efficiency and Renewable Energy, Fuel Cell Technologies Office, under contract DE-AC02-05CH11231. Y.G. acknowledges support from the National Natural Science Foundation of China under grant 22376075 and the Central China Normal University project (CCNU24JCPT017). Z.W. was supported by the US DOE, Office of Science, Office of Basic Energy Sciences, Chemical Sciences, Geosciences, and Biosciences Division, Catalysis Science program. This research used resources of the Advanced Light Source, which is a DOE Office of Science User Facility under contract DE-AC02-05CH11231. The XANES work was supported by National Science and Technology Council of Taiwan under grant NSTC 113-2112-M-213-008. B.Y. and Q.H. acknowledge support from Singapore National Research Foundation under award NRF-NRFF11-2019-0002 and Singapore Low-Carbon Energy Research Funding Initiative hosted under A*STAR (awards U2102d2006; U2305d4003). This research used resources of the National Energy Research Scientific Computing Center, which is supported by the US DOE, Office of Science, under contract DE-AC02-05CH11231. This research used the Lawrencium computational cluster resource provided by the IT Division at the Lawrence Berkeley National Laboratory (supported by US DOE, Office of Science, Office of Basic Energy Sciences, under contract DE-AC02-05CH11231). This research used resources at the Spallation Neutron Source, a DOE Office of Science User Facility operated by the Oak Ridge National Laboratory. **Author contributions:** Conceptualization: J.Y., M.S., J.S. Methodology: J.Y., L.J.F., D.P., Y.G., J.L., M.S., J.S. Investigation: J.Y., L.J.F., S.Y., B.Z., P.V., L.D., Y.C., Z.W., X.Z., S.Z., S.C., J.L.C., B.Y., S.T., Q.H., S.N. Visualization: J.Y., L.J.F., S.Y., B.Z., P.V., L.D., B.Y. Funding acquisition: M.S., J.S., Y.G., D.P., L.J.F., Z.W., Q.H., B.Y. Project administration: J.Y., M.S., J.S. Supervision: J.S., M.S., J.L., Y.G., D.P. Writing – original draft: J.Y., L.J.F., S.Y., B.Z., P.V. Writing – review & editing: J.Y., J.S., M.S., J.L., Y.G., D.P., Z.W. **Competing interests:** Authors declare that they have no competing interests. **Data and materials availability:** All data are available in the main text or the SM, including data S1 to S11, or have been deposited at Zenodo (*37*).

SUPPLEMENTARY MATERIALS

science.org/doi/10.1126/science.adv0735
Materials and Methods; Supplementary Text; Figs. S1 to S32; Tables S1 to S6; References (*38–80*); Data S1 to S11

Submitted 4 December 2024; accepted 12 March 2025; published online 3 April 2025

10.1126/science.adv0735

APPLIED PHYSICS

Geometrically frustrated rose petals

Yafei Zhang, Omri Y. Cohen, Michael Moshe*, Eran Sharon*

Growth and form are deeply interconnected, in a manner often mediated by mechanical instabilities arising from geometric incompatibilities. Although Gauss incompatibility has long been recognized as the source of morphing in naturally growing slender organs, here we show that the growth profile of rose petals remains Gauss compatible. Their distinctive shape emerges from a different type of geometric incompatibility, the Mainardi-Codazzi-Peterson (MCP) incompatibility, which leads to the formation of localized cusps along the petal margins. We validated this mechanism in model disc petals theoretically, computationally, and experimentally. Our study reveals distinct morphological regimes, ranging from smooth edges to cusp-forming configurations, and demonstrates how stress focusing at cusps influences subsequent petal growth. These findings position MCP incompatibility as a generic mechanism for cusp formation in both natural and manmade self-morphing sheets.

Roses, celebrated for their beauty and symbolic significance, have inspired countless works of art and literature owing to their exquisite form (*1*, *2*). However, the mechanism responsible for the distinctive shape of rose petals, or how this mechanism differs from those governing the shapes of other petals and plants, is poorly understood.

Growth in elastic materials can sometimes lead to situations where the material's preferred geometric state, dictated by the growth process, cannot physically exist without distortion. This creates what is known as a geometric incompatibility, where the material necessarily contains residual stresses (*3*). As these stresses accumulate, they can trigger mechanical instabilities that change the shape of the body and redistribute stresses. In thin elastic sheets, a well-known example of this is Gauss incompatibility (*4*, *5*), which has been extensively studied in the context of growth-induced instabilities including the waviness along the edges of leaves (*6*–*11*), petals (*12*), and seed pods (*5*).

A characteristic feature of shaping through Gauss incompatibility is that the emergent shapes and unstable modes are extended, typically manifested as smooth and often periodic patterns (*5*, *13*). In contrast, the gradual formation of cusps along the petal blade, which is so strongly identified with roses, is localized and does not fall within the framework of Gauss incompatibility.

The importance of cusp formation extends beyond aesthetics. It is accepted that mechanical stresses not only lead to mechanical instabilities but can also influence the growth of tissue. This phenomenon has been demonstrated in the apical meristem (*14*), fruit growth (*15*), and developed leaves (*16*, *17*) as well as during fly embryo development (*18*). In this context, stress focusing by spontaneously generated cusps such as those in rose petals could affect the organ's subsequent growth, potentially serving as a morphogenetic mechanism.

Here we show that the dominant mechanical instability that gives rose petals their characteristic shape originates from the Mainardi-Codazzi-Peterson (MCP) incompatibility. This incompatibility (*19*) can be generated by a simple and highly symmetric growth profile similar to that of the petal.

Racah Institute of Physics, The Hebrew University of Jerusalem, Jerusalem, Israel.
*Corresponding author. Email: michael.moshe@mail.huji.ac.il (M.M.); erans@mail.huji.ac.il (E.S.)

Observation and phenomenology

A representative fresh rose (Red Baccara) under study is depicted in Fig. 1. To imitate the natural growth of a single petal, we analyzed a sequence of petals from the same flower, as marked in Fig. 1A. In Fig. 1B, these petals are arranged (left to right) from younger petals (closer to the center of the flower) to mature ones (nearer to the outer layer). We show that the petals undergo a transition in morphology: from smooth sectors with roughly uniform curvature along the petal edge (indicative of younger petals) to polygons with cusps (representative of older petals). The number of sides of the polygons gradually increases as the petals age (see movie S1). Although Fig. 1 presents data from a single flower, we have collected and analyzed ~100 different petals from rose flowers of different species (see materials and methods in the supplementary materials).

A central property of geometrically incompatible slender solids is that the configuration of the entire body does not necessarily realize the preferred (reference) local curvature. Cutting small elements from the material allows it to release strains and reveal the local rest state, that is, the reference curvature. We therefore cut narrow strips along selected directions on the petal. We found that strips that were cut parallel to the petal edge are flat, whereas strips perpendicular to the edge are curved downward (Fig. 1C). This observation indicates that in polar-like coordinates, the reference azimuthal curvature vanishes $\bar{\kappa}_{\theta\theta} = 0$, whereas the reference radial curvature is finite $\bar{\kappa}_{rr} > 0$. Quantitative measurement of $\bar{\kappa}_{rr}$ reveals that it increases during growth, as shown in Fig. 1D.

Geometric frustration and incompatible elasticity

We modeled a petal as an elastic sector within a disc (Fig. 2A). The reference lengths and curvatures, which evolve during growth, are respectively encoded in two geometric quantities: the reference metric $\bar{\mathbf{a}}$ and the reference curvature $\bar{\mathbf{b}}$. The configurations in Fig. 1, B and C, suggest that the reference length corresponds to a flat configuration, whereas the reference curvature corresponds to a radially curved configuration. In a coordinate system (r, θ), with θ parallel to the petal's edge, we have

$$\bar{\mathbf{a}} = \lambda(t)\begin{pmatrix} 1 & 0 \\ 0 & r^2 \end{pmatrix}, \bar{\mathbf{b}} = \begin{pmatrix} \kappa_0(t) & 0 \\ 0 & 0 \end{pmatrix} \quad (1)$$

The time dependence of the expansion factor λ and curvature κ_0 is assumed to be quasi-static, reflecting a slow growth process. Henceforth, we treat these parameters as constants.

More generally, and regardless of the coordinate system in use, geometric frustration occurs when the reference fields $\bar{\mathbf{a}}$ and $\bar{\mathbf{b}}$ cannot be realized simultaneously. For geometric compatibility, $\bar{\mathbf{a}}$ and $\bar{\mathbf{b}}$ must satisfy Gauss's Theorema Egregium and the two MCP equations (*20*). Gauss's theorem states that the reference Gaussian curvatures, $K_{\bar{\mathbf{a}}}$ and $K_{\bar{\mathbf{b}}}$, corresponding to $\bar{\mathbf{a}}$ and $\bar{\mathbf{b}}$, must agree. When $K_{\bar{\mathbf{a}}} \neq K_{\bar{\mathbf{b}}}$, Gauss incompatibility takes place (*20*), which is at the origin of all morphing instabilities observed in naturally growing sheets (*5*, *10*–*13*). The MCP equations guarantee that the vector normal to the surface is well defined (single valued) and can be expressed compactly in index notation as

$$\bar{\nabla}_\alpha \bar{\mathbf{b}}_{\beta\gamma} - \bar{\nabla}_\beta \bar{\mathbf{b}}_{\alpha\gamma} = 0 \quad (2)$$

where $\bar{\nabla}$ denotes the covariant derivative with respect to $\bar{\mathbf{a}}$, and the indices α, β, and so on take values in $\{1, 2\}$ in general or in $\{r, \theta\}$ in the context of the petal (see supplementary text, section 2.1). It was shown that the violation of MCP compatibility conditions leads to mechanical instabilities (MCP morphing) that shape the sheet differently than Gauss morphing (*19*, *21*).

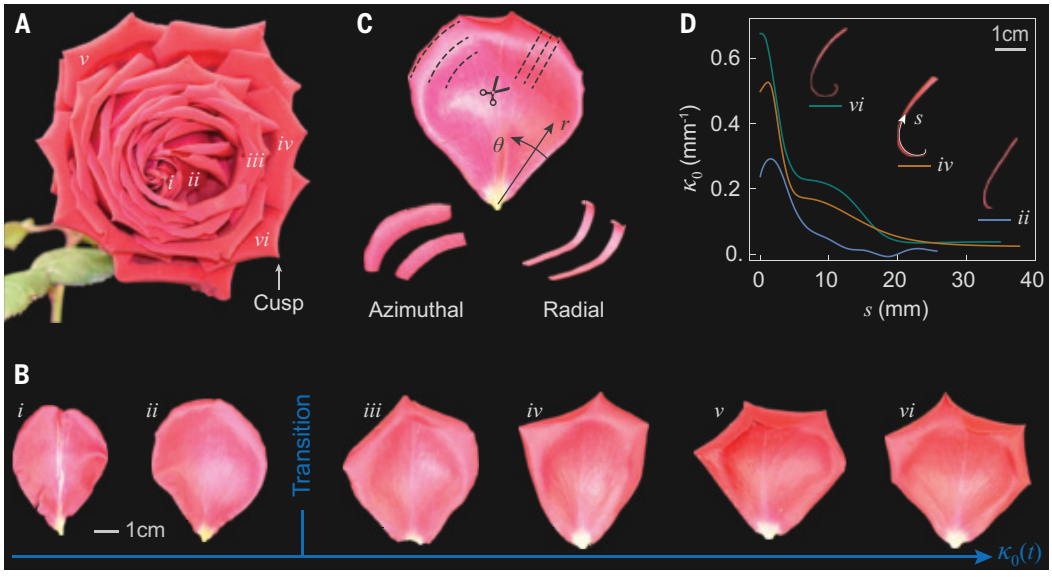

Fig. 1. Morphology and shape morphing in rose petals. (**A**) A typical fresh Red Baccara rose with its characteristic sharp cusps. (**B**) A sequence of petals taken from (A), ordered from central to outer petals, equivalent to ordering from young to old. Young petals are smooth, whereas old petals are polygonal with sharp cusps. (**C**) Strips cut from a petal along the radial and azimuthal directions, respectively. The petal, reminiscent of a sector of a disc, has only nonzero reference curvature $\bar{\kappa}_{rr} = \kappa_0$ along the radial direction. (**D**) Measurements of petal sequence in (B) identify the increased radial curvature during growth.

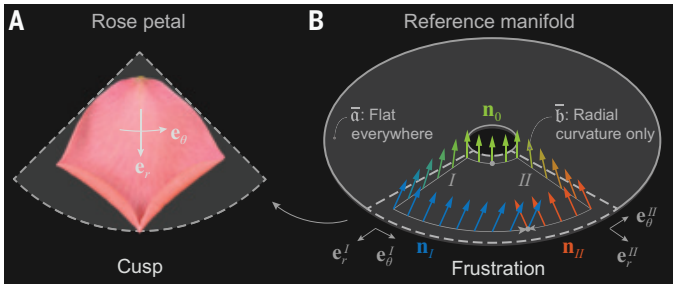

Fig. 2. Geometric illustration of MCP frustration in rose petals. (**A**) Illustration of a typical rose petal modeled as a sector within a disc. (**B**) Sketching MCP frustration of the petal in the reference manifold depicted by $\bar{\mathfrak{a}}$ and $\bar{\mathfrak{b}}$. In the polar basis $\{\mathbf{e}_r, \mathbf{e}_\theta\}$, $\bar{\mathfrak{a}} = \mathbf{I}$ represents an intrinsic flat geometry, while $\bar{\mathfrak{b}} = \kappa_0 \mathbf{e}_r \otimes \mathbf{e}_r$ indicates extrinsic curvature along the radial direction only. Assume that the normal vector at an initial point on the reference manifold is well defined as $\mathbf{n}_0$. Following path 1, translating $\mathbf{n}_0$ along the azimuthal direction is trivial because $\bar{\mathfrak{b}}_{\theta\theta} = 0$, whereas translating along the radial direction introduces a rotation in the $\{\mathbf{n}_0, \mathbf{e}_r^I\}$ plane because $\bar{\mathfrak{b}}_{rr} = \kappa_0$. Accordingly, translation along two paths, 1 and 2, results in two different normals—$\mathbf{n}_1 \neq \mathbf{n}_2$ at the same endpoint—which indicates that a normal vector on this reference manifold cannot be well defined. This violates the MCP constraint and signifies the presence of geometric frustration and cusp formation, resulting in the form of the rose petal shown in (A).

The reference fields modeling a petal in Eq. 1 are Gauss compatible, as $K_{\bar{\mathfrak{a}}} = K_{\bar{\mathfrak{b}}} = 0$. However, they violate the MCP conditions of Eq. 2, with $\bar{\nabla}_r \bar{\mathfrak{b}}_{\theta\theta} - \bar{\nabla}_\theta \bar{\mathfrak{b}}_{r\theta} \neq 0$ (see eq. S11). This raises the hypothesis that the MCP morphing mechanism controls the transition from smooth to polygonal configurations, as shown in Fig. 1. Indeed, the inequality $\bar{\nabla}_r \bar{\mathfrak{b}}_{\theta\theta} \neq \bar{\nabla}_\theta \bar{\mathfrak{b}}_{r\theta}$ indicates that translating the normal along the radial and angular directions induces a noncommutative rotation (see supplementary text, section 2.1). A geometric illustration of this MCP incompatibility is sketched on the reference manifold depicted by $\bar{\mathfrak{a}}$ and $\bar{\mathfrak{b}}$ (Fig. 2B). Assuming that the normal vector at an initial point could be well defined as $\mathbf{n}_0$, evolving $\mathbf{n}_0$ along two different paths according to $\bar{\mathfrak{a}}$ and $\bar{\mathfrak{b}}$ results in two different normals at the same endpoint (Fig. 2B). This paradox implies that the normal vector cannot be defined as a single-valued function on the reference manifold and thus cannot be defined over a smooth surface. Mechanically, this geometric incompatibility induces residual stresses and eventually leads to an instability of the smooth configuration. Through theory, simulation, and experiment, we demonstrate that this instability results in the formation of cusps at the petal edge, as portrayed in Fig. 2A.

Post-instability configurations are analyzed within the theory of non-Euclidean elasticity (*3*). When an elastic sheet is endowed with geometrically incompatible reference fields $\bar{\mathfrak{a}}$ and $\bar{\mathfrak{b}}$, it selects a configuration with compatible $\mathfrak{a}$ and $\mathfrak{b}$ that minimizes an elastic energy, which penalizes metric and curvature discrepancies. Deviations of $\mathfrak{a}$ from $\bar{\mathfrak{a}}$ correspond to stretching energy, and deviations of $\mathfrak{b}$ from $\bar{\mathfrak{b}}$ correspond to bending energy [see eq. S14 and (*3*) for details]. The actual configuration is determined by minimizing the energy with respect to the actual fields $\mathfrak{a}$ and $\mathfrak{b}$.

Shape morphing in disc petals

To test our hypothesis that the MCP instability governs the shaping of the rose petal, we investigated the energy-minimizing configurations of a simplified system that does not include much of the detailed structure of a petal but only its reference geometry. We did this through analytical, numerical, and experimental study. We considered circular domains of radius R_0 and thickness h equipped with the reference fields in Eq. 1, with $\lambda(t) = 1$ and $\kappa_0(t) = \kappa_0$. As in other two-dimensional models of plates or shells, we required $h \ll 1/\kappa_0$ and $h \ll R_0$. We started by studying equilibrium configurations using numerical simulations (see materials and methods). In each simulation, we fixed R_0, h, and κ_0 and performed a numerical minimization of the total elastic energy in eq. S13. The equilibrium configurations are uniquely determined by two dimensionless parameters, $\tilde{\kappa} = \sqrt{h\kappa_0}$ and $\tilde{h} = h/R_0$.

We studied a wide range of parameters, as illustrated in the phase diagram in Fig. 3. By varying $\tilde{\kappa}$ at a given normalized thickness $\tilde{h}$, we found that the resulting stable configurations of the disc petals recover the observed morphological evolution of natural petals (Figs. 1B and 3A). For small values of $\tilde{\kappa}$, smooth axisymmetric configurations are obtained. However, as $\tilde{\kappa}$ is increased, this solution becomes unstable and transitions to a saddle-like configuration. This intermediate configuration further transforms into frustrated polygonal configurations through a

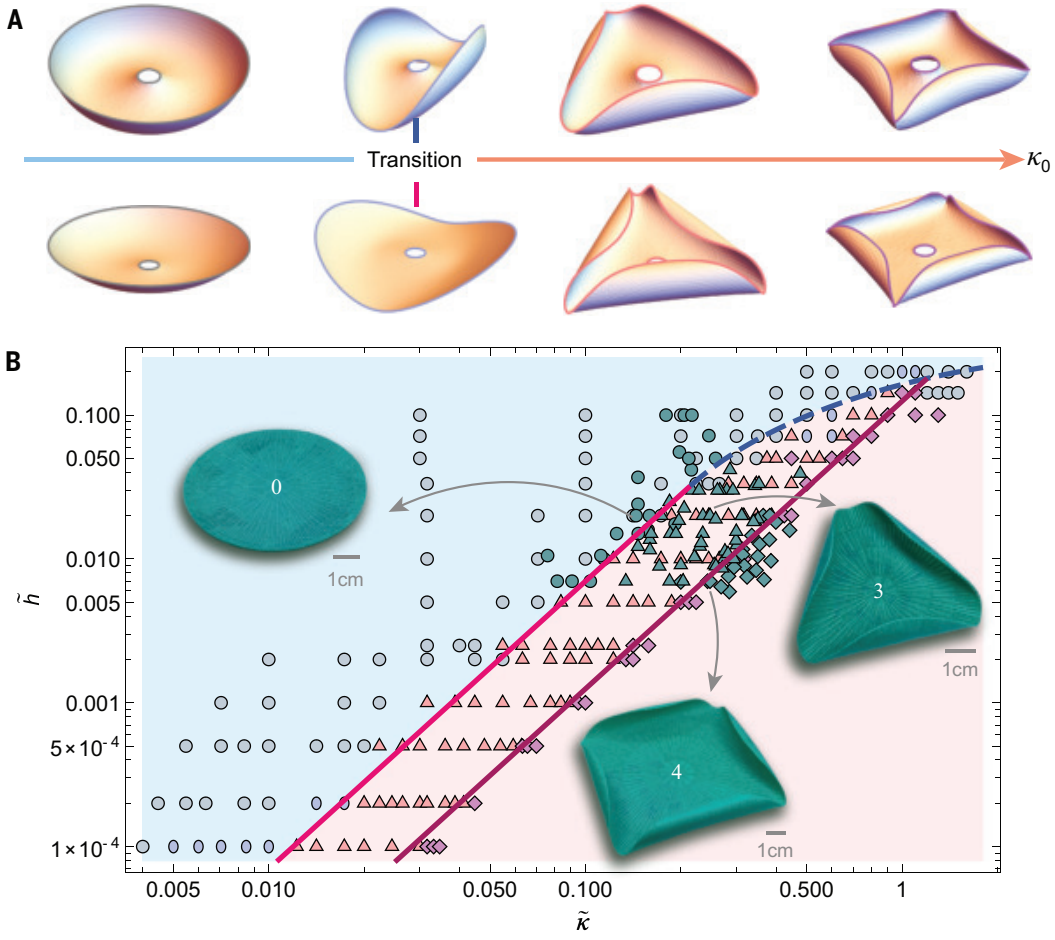

Fig. 3. Shape transition in frustrated disc petals. (**A**) Typical evolution of the disc petal's morphology with increasing radial reference curvature κ_0: Given $\tilde{h} = 0.1$ (first row of configurations) and 0.005 (second row of configurations), increasing κ_0, a disc petal morphs from axisymmetric to saddle-like, triangle, and quadrilateral configurations, corresponding to different markers in (B). The sharpness of the cusps depends on the thickness $\tilde{h}$. (**B**) Phase diagram in the $\tilde{h}$, $\tilde{\kappa}$ plane. Dark green markers denote the experiments, while other color markers indicate the simulations. The shape of the markers represents the configuration (e.g., triangles for three cusps). Clear phases are observed for each shape. Light blue and light pink regimes distinguish the axisymmetric and polygonal configurations, respectively. Equation 5 predicts the scaling of the existing line as $\tilde{h} \sim \tilde{\kappa}^2$, corresponding to a slope of 2 in the diagram. This scaling breaks at large $\tilde{h}$ (dashed curve).

series of instabilities: first into a triangle, then into a quadrilateral, and so on. In each of these shapes, the emergent configuration is considerably affected by the normalized thickness $\tilde{h}$. In the thin limit $\tilde{h} \ll 1$, the Gaussian curvature of the polygonal morphology is close to zero everywhere except for the sharp cusps (fig. S2A). This includes the flat inner region and the piecewise cylindrical outer region (Fig. 3A, the second row of configurations). Conversely, when $\tilde{h}$ is relatively large, regions with nonzero Gaussian curvature extend from the cusp to its surroundings, exhibiting a positive Gaussian curvature (Fig. 3A, the first row of configurations, and fig. S2B). Note that the small hole located in the center of the disc serves the purpose of eliminating the curvature singularities (Fig. 3A). In practice, the reference curvature of rose petals vanishes close to the origin, providing a regularizing mechanism that eliminates this curvature singularity (Fig. 1D, the curvature profile). Neither the hole in the simulation nor the regularized reference curvature in rose petals substantially affects the evolution of the configuration (fig. S1).

The shape morphing of disc petals can be attributed to the interplay between different energy terms. Using $\tilde{\kappa}$ and $\tilde{h}$, we constructed a phase diagram that delineates various morphological regimes (Fig. 3B). Systematic numerical results, indicated by corresponding visual symbols marked in light colors, are depicted in Fig. 3B. The phase diagram reveals two main regimes: the light blue area, of axisymmetric configurations marked by circles, and the light pink area, of symmetry-breaking configurations marked by polygonal symbols such as triangles and squares. To validate our hypothesis and simulations, we conducted a set of experiments using polylactide (PLA), following methods introduced in (*22*). The discs were bilayers with the reference fields in Eq. 1 (see materials and methods and movie S2). In the experiments, h, R_0, and κ_0 were varied. In agreement with the numerical results, the physical discs underwent a set of transitions from circular to polygonal configurations (Fig. 3B, insets). A small number of discs with more than four cusps were generated (fig. S11 and movie S2). These transitions are consistent with the numerical findings. Assembling PLA "petals" together created a structure that is indeed reminiscent of a rose (fig. S12).

To gain insights into the mechanism behind the morphological transitions, we performed a theoretical analysis of the equilibrium configurations and the resulting morphologies. We started by considering the axisymmetric configurations that appear when $\tilde{\kappa}$ is small. In the limiting scenario where $\tilde{\kappa} \ll 1$, the energy density is expanded to the leading order in $\tilde{\kappa}^2$, and an explicit solution is derived (see eq. S25). The total energy associated with this equilibrium configuration scales as

$$\varepsilon_{\mathrm{axi}} \sim Yh^3\kappa_0^2 R_0^2 \tag{3}$$

where Y is the Young's modulus. We find excellent agreement between the theoretical and numerical configurations, as shown in fig. S4.

When $\tilde{\kappa}$ is not small, polygonal configurations are energetically favorable. On the basis of the numerical and experimental findings, we note that an n-gon disc petal exhibits three distinct deformation regions that can be analyzed separately: the outer curved domain, the inner flat domain, and the sharp cusps (fig. S5). The total energy is thus $\varepsilon_{poly} = \varepsilon_{cur}^{bn} + \varepsilon_{flat}^{bn} + \varepsilon_{ch}^{bn}$, where "bn" denotes bending. All three terms correspond to bending energy with total energy

$$\varepsilon_{poly} \sim Yh^3\kappa_0^2 R_0^2 S + Yh^3 C \tag{4}$$

where S and C are both functions of n and ν (see eqs. S36 and S40).

To estimate the onset of shape morphing, we assume that the transition between different morphologies is continuous and that the narrow transition zone can be ignored. Thus, at the transition point from axisymmetric to triangular shape, we equate the energies in Eqs. 3 and 4 with $n = 3$, yielding the condition for the transition. More generally, equating the energies in Eq. 4 for n and $n + 1$ provides the condition for polygon-polygon transitions. We find that, in all cases, at the onset of instability, $\tilde{h} \sim \tilde{\kappa}^2$ (see supplementary text, section 2.5) or, explicitly

$$h / R_0 \sim h\kappa_0 \tag{5}$$

This scaling law can be further elucidated by the method of characteristics (see supplementary text, section 2.6). Our simulation and experimental results confirm this scaling law, as shown in Fig. 3.

Mechanics of the singular cusp

A closer examination of both older rose petals and polygonal disc petals shows that the system deviates from the no-stretching, perfect isometry (Fig. 1B and fig. S13). The cylindrical structures bend into a saddle-like form near the sharp cusps. This deformation relieves the singularity at the cusps, gradually squeezing the cusps out, leading to the characteristic petal shapes (Fig. 1B).

To study the characteristics of the cusp morphology, we initiated the simulations by stabilizing the n-gon disc petal and then increasing the value of κ_0 (see materials and methods). Initially, the edges of the disc petal curve to cylindrical shapes whose generatrices meet outside the domain, as show in Fig. 4A. Upon increasing κ_0, the cylindrical structures extend, and the crossing point of the generatrices approaches the disc domain. This observation suggests that this type of solution is limited by a critical value of κ_0, for which intersections of the generatrices lie exactly on the domain boundary. Beyond this limiting state, the ends of cylinders gradually curve into saddle-like structures. Accordingly, the cusps transition from blunt to relatively sharp, eventually becoming curved. Our simulations faithfully reproduced these phenomena observed in the growing petals (Figs. 1B and 4A and fig. S13).

Introducing negative Gaussian curvature on the outer face of the cylindrical edge (fig. S7) costs stretching energy. However, it allows for a reduction of the bending energy through further rolling of the edges, while keeping the cusp regulated within the plane. Marking the "depth" of the curved edge at its center as w (Fig. 4A), the bending energy scales as $\varepsilon_{bn} \sim Yh^3\left(R_0^2\kappa_0^2 + 1 + R_0 w\kappa_0^2 - w\kappa_0\right)$. The stretching energy can be approximated by two integrations of the Gaussian curvature, which gives $\varepsilon_{st} \sim Yhw^4\kappa_0^2$ (see supplementary text, section 2.7). Additionally, the energy contributed by the cusp scales as $\varepsilon_{ch} \sim Yh^3$. Minimizing the total energy $\varepsilon = n(\varepsilon_{bn} + \varepsilon_{st} + \varepsilon_{ch})$ with respect to w leads to

$$w \sim h^{2/3}\left(\kappa_0 - \kappa_s\right)R_0^{4/3} \tag{6}$$

where κ_s is the critical reference curvature, at which the cusp begins to curve. This scaling relation reveals that the overcurling distance w can increase not only with the increment of reference curvature $\kappa_0 - \kappa_s$ but also with the thickness h, consistent with our simulation results (Fig. 4C and fig. S8). This finding aligns with the physical intuition of petal growth and demonstrates how growing petals spontaneously alleviate stress focusing.

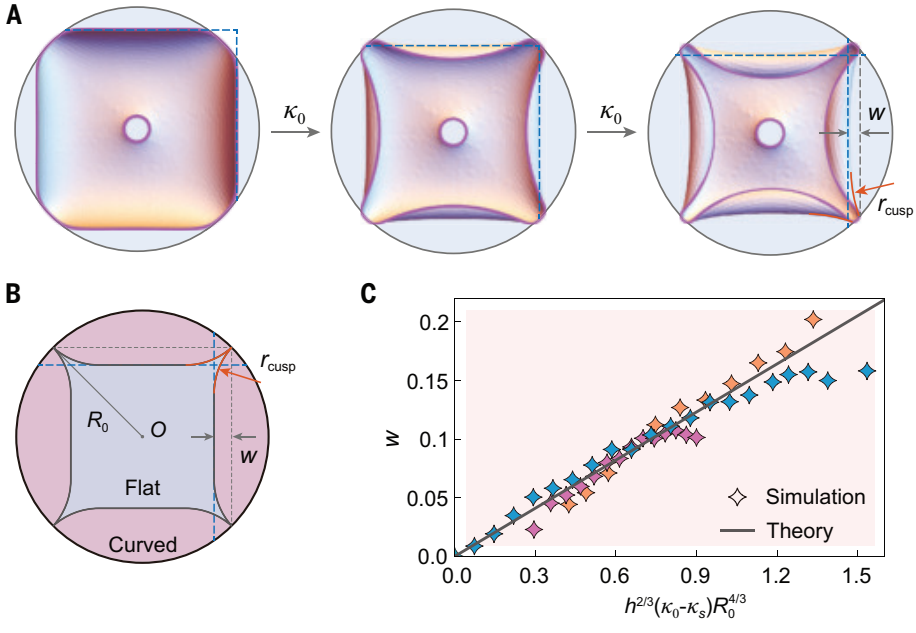

Fig. 4. Morphologies of singular cusps. (**A**) Evolution of cusp morphology as κ_0 increases. The cusps evolve from blunt to relatively sharp and eventually to curved. The expansion of the curved region is indicated by the movement of the cylinder's tangent line (blue dashed line). Simultaneously, the curved cusps are extruded outward, increasing the overcurling distance w. Simulation parameters are set as $\kappa_0 = 5/R_0$, $7.5/R_0$, and $10/R_0$, with $R_0 = 2.5$ and $h = 0.1$. (**B**) Mechanism of cusp formation: The magenta area curls into cylindrical structures with curved ends, while the inner gray region remains flat. The radius of curvature at the curved cusp is denoted as r_{cusp}, and the overcurling distance w is measured from the cusp vertex to the tangent of the curl-flat boundary. (**C**) Scaling of overcurling distance. Equation 6 predicts $w \sim h^{2/3}\left(\kappa_0 - \kappa_s\right)R_0^{4/3}$, which is confirmed by simulations. Color markers correspond to the results when varying κ_0, h, and R_0 independently (fig. S8).

How stress focusing interacts with tissue growth

The observed cusp formation as part of the natural growth of the petal raises the question about possible mechanical feedback: Does the observed stress focusing influence tissue growth? To address this, we investigated the anatomy of petal tissues across different development stages. Specifically, we imaged the petal margins and the geometry of the finest vascular network (Fig. 5 and see materials and methods). Our observations reveal no noticeable disparities in tissue characteristics between young petals without cusps and those immediately after cusp formation: Both exhibit smooth, convex edge profiles (Fig. 5, A and B) and a uniform vascular network. However, in mature petals, where the cusp has been present for several days, concave distortions develop in the cusp region (Fig. 5C). In older petals, the concave morphology becomes more pronounced, and there are indications for distortion and damage to the vascular system at the cusps (Fig. 5D). This effect is evident in many rose varieties, as demonstrated by additional examples in figs. S14 and S15. To verify the

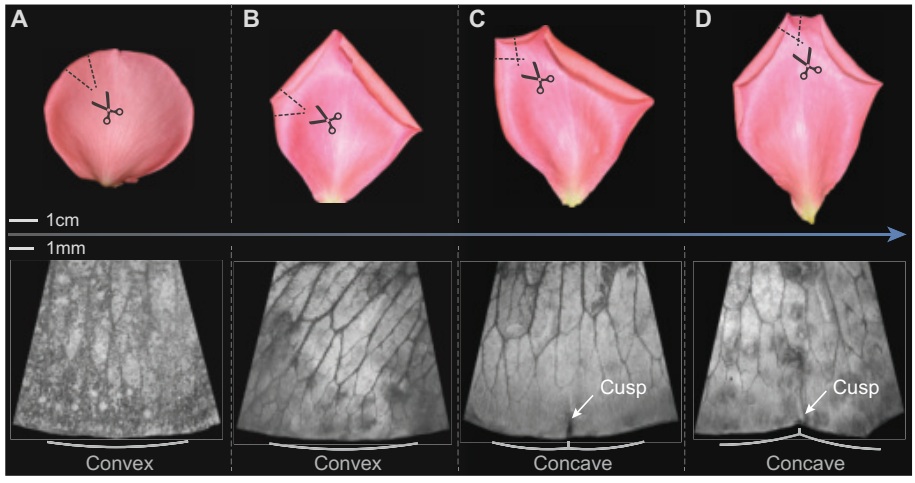

Fig. 5. Stress focusing interacts with tissue growth in rose petals. (Top row) Petal sequence arranged (from left to right) in order of developmental progression. (Bottom row) Corresponding microscopic images of tissue sections from the respective petals in the top row. (**A**) In early development, a young petal displays a smooth and convex edge at the microscopic scale, without stress concentration. (**B**) As the petal matures slightly, the edge near an emerging cusp retains smooth, convex morphology, indicative of minimal stress concentration. (**C**) At a moderate development stage, the petal experiences stress focusing at the cusp, leading to a gradual transition of the tissue edge from convex to concave. (**D**) In fully mature petals, prolonged stress focusing at the cusp results in a pronounced concavity of the tissue edge, illustrating the major impact of mechanical stresses on petal morphology.

direct effect of the cusp on growth, we gently shifted a newly formed cusp on a young petal to an alternative location along the rim, leaving the flower to grow. In line with our expectations, the tissue in the original location of the cusp was normal and the petal edge was convex. In contrast, in the new location of the cusp, the edge had turned concave (fig. S16).

Discussion and conclusions

Our investigation into the geometry and mechanics of rose petals has revealed the fascinating interplay between growth, shape morphing, and stress focusing. We have demonstrated that the characteristic shape of rose petals, with their gradually forming cusps, emerges from the dominant mechanical instability driven by MCP incompatibility. This mechanism represents an example of geometric frustration that leads to stress focusing in living organisms. As such, the work expands the range and type of three-dimensional configurations accessible through self-morphing approaches in synthetic sheets. Specifically, the formation of cusps, which is absolutely impossible through Gauss incompatibility, and the partial control of cusp shape are now feasible and understood.

Furthermore, the characteristic petal shape leads us to study the regularization mechanism of stress at the singular cusp. It is based on the reduction of bending energy by deviation from an isometry. This phenomenon parallels various mechanisms of emergent singularities and their regularization, such as wrinkles, folds, d-cones, minimal ridges, and more (*23*). Such mechanisms that involve a singularity approaching and being smoothed when entering the interior of a domain have been observed in stretched twisted ribbons (*24*), capillary origami (*25*–*27*), and crumpled papers (*28*, *29*). Whereas these studies have shown this mechanism as induced by external loads, the petal's cusp is a realization in a free-standing sheet, as induced by the MCP geometric incompatibility.

Finally, we have presented evidence that stress focusing at the cusps influences the local growth and morphology of petal tissues, providing an example of stress-focusing feedback on growth. Our findings complete a feedback loop between biology, geometry, and mechanics: Highly symmetric growth of a petal induces MCP incompatibility, leading to cusp formation and stress focusing; in turn, this stress focusing further affects local tissue growth.

REFERENCES AND NOTES

1. P.-A. Renoir, *Bouquet of Roses* (c.1890–1900); https://www.wikiart.org/en/pierre-auguste-renoir/bouquet-of-roses-1900.
2. O. Wilde, *The Nightingale and the Rose* (Oxford Univ. Press, 1981).
3. E. Efrati, E. Sharon, R. Kupferman, *J. Mech. Phys. Solids* **57**, 762–775 (2009).
4. Y. Klein, E. Efrati, E. Sharon, *Science* **315**, 1116–1120 (2007).
5. S. Armon, E. Efrati, R. Kupferman, E. Sharon, *Science* **333**, 1726–1730 (2011).
6. U. Nath, B. C. Crawford, R. Carpenter, E. Coen, *Science* **299**, 1404–1407 (2003).
7. E. Sharon, M. Marder, H. L. Swinney, *Am. Sci.* **92**, 254–261 (2004).
8. J. Dervaux, M. Ben Amar, *Phys. Rev. Lett.* **101**, 068101 (2008).
9. C. Huang, Z. Wang, D. Quinn, S. Suresh, K. J. Hsia, *Proc. Natl. Acad. Sci. U.S.A.* **115**, 12359–12364 (2018).
10. F. Xu, C. Fu, Y. Yang, *Phys. Rev. Lett.* **124**, 038003 (2020).
11. M. Ben Amar, F. Jia, *Proc. Natl. Acad. Sci. U.S.A.* **110**, 10525–10530 (2013).
12. H. Liang, L. Mahadevan, *Proc. Natl. Acad. Sci. U.S.A.* **108**, 5516–5521 (2011).
13. H. Liang, L. Mahadevan, *Proc. Natl. Acad. Sci. U.S.A.* **106**, 22049–22054 (2009).
14. O. Hamant *et al.*, *Science* **322**, 1650–1655 (2008).
15. A. Chakrabarti, T. C. Michaels, S. Yin, E. Sun, L. Mahadevan, *Nat. Phys.* **17**, 1125–1129 (2021).
16. Y. Bar-Sinai *et al.*, *PLOS Comput. Biol.* **12**, e1004819 (2016).
17. M. Sahaf, E. Sharon, *J. Exp. Bot.* **67**, 5509–5515 (2016).
18. B. I. Shraiman, *Proc. Natl. Acad. Sci. U.S.A.* **102**, 3318–3323 (2005).
19. E. Siéfert, I. Levin, E. Sharon, *Phys. Rev. X* **11**, 011062 (2021).
20. M. P. Do Carmo, *Differential Geometry of Curves and Surfaces: Revised and Updated* (Courier Dover Publications, ed. 2, 2016).
21. I. Levin, E. Siéfert, E. Sharon, C. Maor, *J. Mech. Phys. Solids* **156**, 104579 (2021).
22. G. Wang *et al.*, in *Proceedings of the 31st Annual ACM Symposium on User Interface Software and Technology* (Association for Computing Machinery, 2018), pp. 623–635.
23. T. A. Witten, *Rev. Mod. Phys.* **79**, 643–675 (2007).
24. J. Chopin, A. Kudrolli, *Phys. Rev. Lett.* **111**, 174302 (2013).
25. C. Py *et al.*, *Phys. Rev. Lett.* **98**, 156103 (2007).
26. T. Jamin, C. Py, E. Falcon, *Phys. Rev. Lett.* **107**, 204503 (2011).
27. J. D. Paulsen *et al.*, *Nat. Mater.* **14**, 1206–1209 (2015).
28. Y. Timounay *et al.*, *Phys. Rev. X* **10**, 021008 (2020).
29. A. Lobkovsky, S. Gentges, H. Li, D. Morse, T. A. Witten, *Science* **270**, 1482–1485 (1995).

ACKNOWLEDGMENTS

Funding: Y.F.Z. is supported by the Israel Academy of Sciences and Humanities and Council for Higher Education Excellence Fellowship Program for International Postdoctoral Researchers. This work was funded by the United States–Israel Binational Science Foundation (grant 2020739) and by the Israel Science Foundation (grants 2437/20 and 1441/19). **Author contributions:** E.S. designed and initiated the research. Y.F.Z. conducted the theoretical, numerical, and experimental studies. M.M. conducted the theoretical and numerical studies. O.Y.C. designed the 3D-printed discs. Y.F.Z., M.M., and E.S. wrote the paper. E.S. and M.M. jointly supervised the work. All authors contributed to the analyses and discussions of the results. **Competing interests:** The authors declare that they have no competing interests. **Data and materials availability:** All data are available in the main text and/or the supplementary materials.

SUPPLEMENTARY MATERIALS

science.org/doi/10.1126/science.adt0672
Materials and Methods; Supplementary Text; Figs. S1 to S16; References (*30*–*32*); Movies S1 and S2

Submitted 10 September 2024; accepted 25 February 2025

10.1126/science.adt0672

EVOLUTIONARY ECOLOGY

Adaptation and gene flow are insufficient to rescue a montane plant under climate change

Jill T. Anderson[1]†*, Megan L. DeMarche[2]†*, Derek A. Denney[2], Ian Breckheimer[3,4], James Santangelo[5], Susana M. Wadgymar[6]

Climate change increasingly drives local population dynamics, shifts geographic distributions, and threatens persistence. Gene flow and rapid adaptation could rescue declining populations yet are seldom integrated into forecasts. We modeled eco-evolutionary dynamics under preindustrial, contemporary, and projected climates using up to 9 years of fitness data from 102,272 transplants (115 source populations) of *Boechera stricta* in five common gardens. Climate change endangers locally adapted populations and reduces genotypic variation in long-term population growth rate, suggesting limited adaptive potential. Upslope migration could stabilize high-elevation populations and preserve low-elevation ecotypes, but unassisted gene flow modeled with genomic data is too spatially restricted. Species distribution models failed to capture current dynamics and likely overestimate persistence under intermediate emissions scenarios, highlighting the importance of modeling evolutionary processes.

Climate change is rapidly shifting the geographic distributions of species (*1*, *2*), owing to changes in local population dynamics, which govern persistence, extirpation, and colonization (*3*). Determining how specific climatic factors causally affect population growth rates across a species' range could enable robust predictions of response to new climates (*3*–*5*). An even bigger, and as yet unmet, challenge, is to incorporate standing genetic variation, rapid adaptation, and gene flow into population models to forecast eco-evolutionary dynamics (*4*, *6*–*9*).

Evolutionary processes have the potential to substantially alter population persistence and distribution under climate change. Widely distributed species with broad climatic tolerances could have a greater potential to survive contemporary climate change than narrowly distributed specialists or species from regions with historically stable climates (*10*–*12*). However, many widespread species consist of mosaics of populations adapted to local conditions (*13*, *14*), and the climatic niche of individuals from a single population may represent only a small proportion of the tolerance of the species. Climate change is expected to increase extinction risks for populations at the warmer range edges of many species (*1*, *2*). However, for locally adapted species, selection imposed by climate change [e.g., (*15*, *16*)] could depress the fitness of local ecotypes (*17*–*21*) throughout the range ("local maladaptation"). Nevertheless, adaptive evolution to new climates could rescue declining populations and enable long-term persistence (*22*) given sufficient within-population genetic variation in climate tolerances ("evolutionary rescue") (*23*, *24*). Similarly, gene flow could enhance population persistence under climate change (*25*) by introducing alleles from populations adapted to new or future conditions ("genetic rescue"). Quantitative genetic field experiments that manipulate climatic factors hold great promise for evaluating the actual roles of eco-evolutionary processes in mitigating extinction risks.

We tested the contributions of local adaptation, migration of pre-adapted ecotypes, and in situ evolutionary rescue to predicted long-term population persistence under climate change in the ecological model species Drummond's rockcress (*Boechera stricta,* Brassicaceae), which is a short-lived perennial species common in montane meadows of North America (*26*) (Fig. 1, A to C, and figs. S1 and S2). High-elevation plants may be particularly susceptible to climate change [e.g., (*27*)] because mountainous ecosystems are subject to high rates of warming (*28*). We identified causal climatic factors that influence performance and characterized the spatial scale of local adaptation by manipulating snowpack and temperature in five common gardens across an elevational gradient around the Rocky Mountain Biological Laboratory (Gothic, Colorado, USA) in experiments using seeds and juvenile plants from inbred maternal lines (hereafter: genotypes). In the "Provenance Trial" experiments, we sampled genotypes that spanned a broad elevational gradient to examine local adaptation under four climate scenarios and quantify the degree of migration that would be necessary to keep pace with climate change. In the "Reciprocal Transplant" experiment, we transplanted genotypes local to each garden to characterize the climate niche and test the potential for in situ evolutionary rescue (*29*). We then leveraged population- and genotype-specific climate responses to develop integral projection models (IPMs) (*30*) capable of evaluating the contributions of evolutionary processes to population growth and persistence. Climatic tolerances are often assessed by comparing occurrence records to macroclimate layers or through short-term laboratory experiments focused on single climatic factors and metrics of performance (e.g., temperature and individual growth) (*31*). Our approach generates more robust assessments by integrating across life history and exposing transplants to complex suites of environments in ecologically realistic field conditions (fig. S3) to uncover the climate conditions in which population growth rate (λ) is positive (the "demographic niche"). Our design overcomes the constraints of space-for-time approaches, in which climatic conditions covary with other environmental factors, such as edaphic characteristics, and captures climates spanning preindustrial to forecasted conditions (Fig. 1 and figs. S1 to S4).

Provenance trial experiment reveals local maladaptation under climate change

To evaluate adaptational lag under climate change, we developed climate-driven stochastic IPMs (*30*), which examined how long-term population growth rates (λ_s) depend on climate as a function of source population elevation. Population growth rate (λ) is the appropriate measure of long-term fitness in constant environments when populations may be growing or declining, and λ_s is the appropriate fitness measure in variable environments (*32*). We transplanted multiple cohorts of 3-month old juveniles (N = 9840 individuals of 199 genotypes from 64 populations, 2013 and 2014) and seeds (N = 64,804 seeds of 285 genotypes from 99 populations, 2014, 2016, and 2018) collected across the elevational range (2499 to 3690 m) into five gardens (table S1). We exposed these individuals of known origin to ambient snowpack and early snow removal to simulate climate change. In two seed cohorts (2016 and 2018), we also examined germination success and seedling survival under snow addition, which reflects recent historical climates (*20*). Additionally, in 2018 and 2020, we factorially manipulated both snow dynamics (ambient versus early snowmelt) and growing season temperature (ambient versus elevated, using open-top chambers, table S2) to capture vital rates under a greater range of climates (N = 8880 juveniles of 96 genotypes from 57 populations, transplanted into four gardens in 2018 and five in 2020). However, snow removals and open-top chambers were not applied at the lowest garden for the 2020 cohort owing to poor performance of transplants in that site in recent years. In all experiments, we left the local vegetation intact and did not modify any other aspects of the environment; thus, transplants experienced the full suite of interacting abiotic and biotic

[1]Department of Genetics and Odum School of Ecology, University of Georgia, Athens, GA, USA. [2]Department of Plant Biology, University of Georgia, Athens, GA, USA. [3]Rocky Mountain Biological Laboratory, Gothic, CO, USA. [4]Western Colorado University, Gunnison, CO, USA. [5]Department of Integrative Biology, University of California, Berkeley, CA, USA. [6]Biology Department, Davidson College, Davidson, NC, USA. ***Corresponding author. Email: jta24@uga.edu (J.T.A.); megan.demarche@uga.edu (M.L.D.)** †These authors contributed equally to this work.

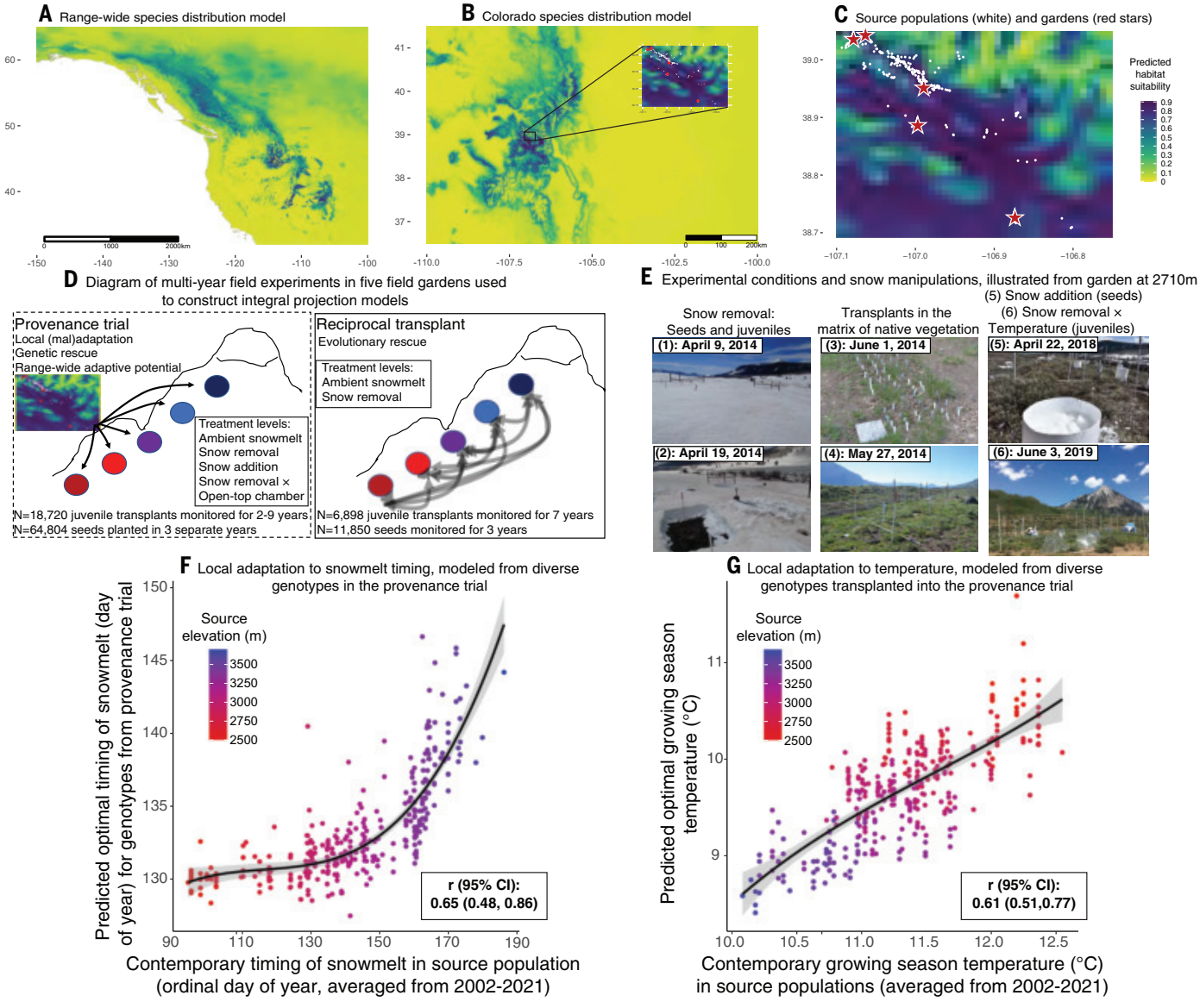

Fig. 1. Distribution and climatic adaptation of *Boechera stricta*. (**A**) Range-wide species distribution model showing regions of high (blue) versus low (yellow) habitat suitability based on correlations of occurrences and recent historical climatic data (1970–2000). Longitude is shown on the *x* axis and latitude on the *y* axis. (**B**) Species distribution model focused on Colorado, with an inset panel showing the locations of all source populations (white circles) and the five common gardens (red stars) used in field experiments. (**C**) Enlarged species distribution map of the source populations and gardens. (**D**) The provenance experiment exposed full siblings from inbred families originating from populations across a broad climatic gradient to variable climates in five experimental gardens. The reciprocal transplant included more genotypes from each garden, transplanted into all gardens. (**E**) Experimental conditions illustrated using images from a low-elevation garden. Photo 1: Immediately before snow removal. Credit: B. Chowdhury. Photo 2: Snow removal blocks were melted out while snow was intact in the control blocks. Credit: B. Chowdhury. Photo 3: Experimental individuals marked with unique identifiers and transplanted into the matrix of natural vegetation. Photo 4: Experimental blocks embedded in natural community, with PVC pipes delineating blocks and data loggers capturing soil moisture and temperature. Photo 5: Snow addition block visible in snow-free garden. Credit: Jillian Gall. Photograph 6: Data collection after establishment of open top chambers. Photos 3, 4, and 6: Credit: J. T. Anderson. (**F**) The optimal timing of snowmelt and (**G**) the optimal growing season temperature for each genotype in the provenance experiment versus the average climatic conditions modeled for each source population from 2002 to 2021, revealing local adaptation to climate (the data are from the Provenance Trial). Data points are colored by source elevation. Correlation coefficients (r) and 95% bias-corrected confidence intervals (CI) are given within each panel.

agents of selection in each garden (Fig. 1, D and E). We examined the entire *B. stricta* life cycle by monitoring seed germination and seedling recruitment of transplanted seeds for 1 year, along with survival, growth, and fecundity of transplanted rosettes from planting through the autumn of 2022.

To construct IPMs, we first analyzed how eight vital rates varied as a function of source elevation and fine-grained spatiotemporal variation in two climatic predictors reflecting energy budgets (average daily growing season temperature) and water availability and growing season timing (snowmelt timing), respectively (table S3 and figs. S5 to S9). These climatic drivers are key determinants of plant fitness at high elevations and latitudes (*33*) and are shifting rapidly with climate change globally (*34*–*36*) and in our study region (fig. S4). We incorporated population- and genotype-specific climate tolerances for each vital rate by testing for interactions between each climate variable and source elevation (as fixed effects), and genotype within population (as random slopes) in

generalized linear mixed models. We used the best-supported models to project λ_s under four climate scenarios: a preindustrial period (1850 to 1879), a contemporary period (2014 to 2022), and an end–21st century period (2071 to 2100) under an intermediate [Representative Concentration Pathway (RCP) 4.5] and a high-emissions pathway (RCP-8.5) based on down-scaled regional projections (*34*, *35*) (fig. S4).

Our models revealed strong local adaptation to climate (Fig. 1, F and G, and fig. S10). Most vital rates exhibited optimal climate conditions that varied significantly with source elevation, indicating that local adaptation to snowmelt and growing season temperature are major drivers of variation in fitness (tables S4 to S11 and figs. S6 to S8). By integrating across vital rates with genotype-specific IPMs, we estimated that each genotype achieved its peak fitness (highest λ) under distinct climates. The optimal snowmelt timing and growing season temperature mirrored the climate of origin (Fig. 1, F and G), reflecting elevational gradients in these climatic variables (figs. S4 and S10). Nevertheless, natural populations are not perfectly adapted to contemporary climates in their home sites. Rather, low-elevation genotypes show enhanced performance under later snowmelt and high-elevation genotypes could benefit from earlier snowmelt, and all genotypes are adapted to cooler temperatures than currently observed at their home sites (Fig. 1, F and G). Advancing snowmelt under climate change (fig. S4) could reduce fitness in low-elevation populations while increasing fitness in high-elevation populations, whereas increasing temperatures could depress fitness across the elevational range.

Local adaptation was most pronounced under preindustrial and contemporary climates, as λ_s (which incorporates realistic interannual climate variation) peaked when source elevations matched the elevation of each garden (Fig. 2A and table S12). Climate change is shifting the adaptive landscape to favor lower-elevation genotypes

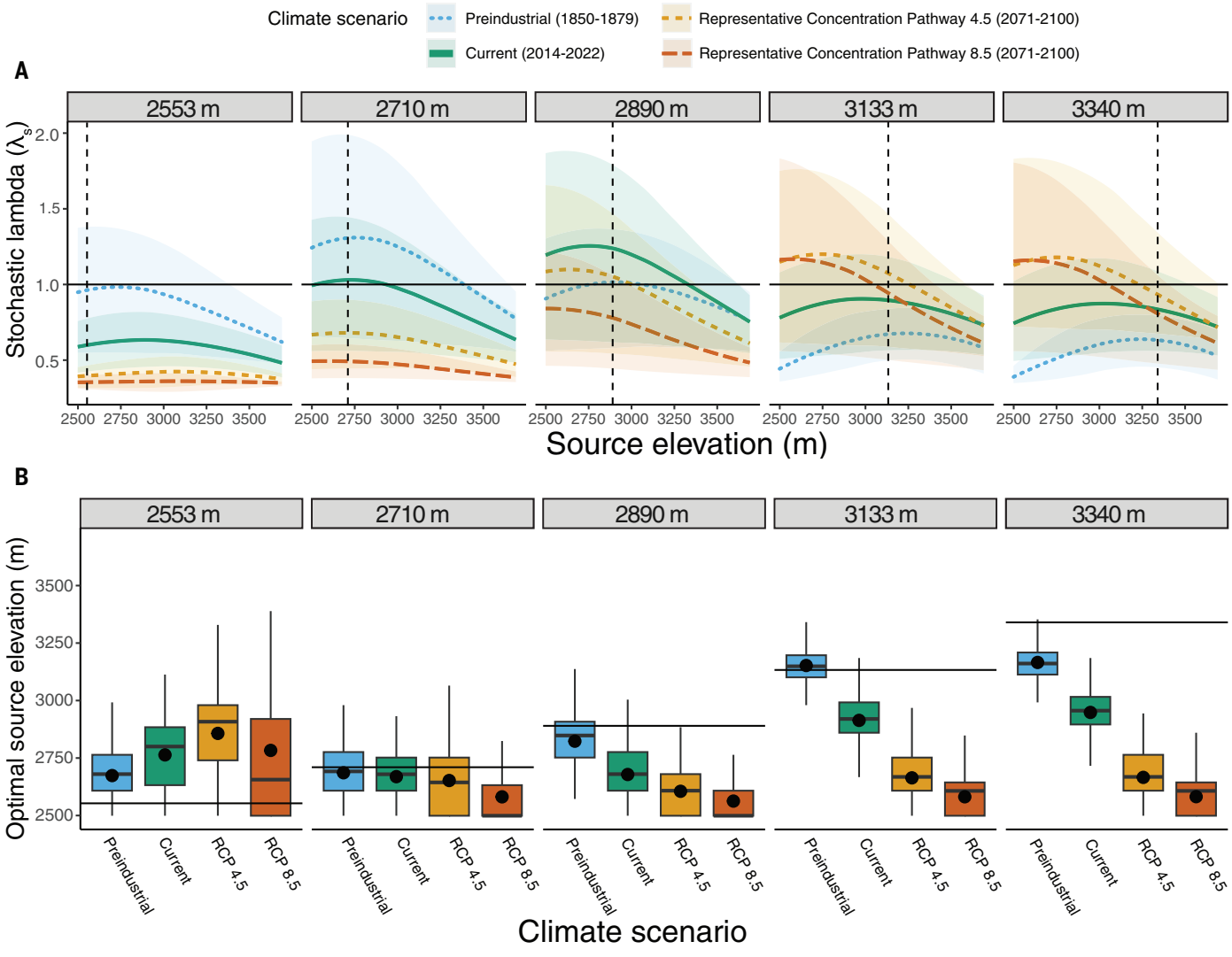

Fig. 2. Climate change disrupts local adaptation. (**A**) Stochastic lambda (λ_s; the geometric mean of λ across 1000 randomly sampled climate conditions for a given scenario), modeled from the Provenance Trial Experiment, varied with source elevation and climate scenario in five common gardens (elevations of the gardens in gray at the top of the panels; source elevations of genotypes on the *x* axis). Horizontal lines reflect $\lambda_s = 1$, at which populations are stable ($\lambda_s > 1$ indicates expanding populations and $\lambda_s < 1$ indicates contracting populations). Dashed vertical lines represent the garden elevation. Panels depict the fitness landscape under preindustrial climates (blue), contemporary climates (green), and end-of-century climates under intermediate emissions (orange) and worst-case emissions (red). Only low-elevation genotypes are predicted to reach $\lambda_s \geq 1$ in future climates in the three highest gardens, whereas all genotypes are predicted to have $\lambda_s << 1$ in future climates at the two lowest gardens. (**B**) The source elevation with the greatest λ_s under each climate scenario in each garden. Horizontal lines reflect the elevation of the garden. Box plots show the mean (circle), median (central line), first and third quartiles (box range), and the largest and smallest values within 1.5× the interquartile range (vertical lines) based on 1000 bootstraps. Under both future climate scenarios, the optimal source elevation is predicted to shift to much lower elevations across all gardens, indicative of local maladaptation.

while depressing the fitness of local genotypes (Fig. 2B and fig. S11). Our models predict significant extinction risks ($\lambda_s < 1$) at low- and even mid-elevation sites under both future climate scenarios (Fig. 2), suggesting substantial elevational range contractions. This prediction accords with our previous models in this system (*20*) and arises from the poor recent performance of transplants in our lowest-elevation garden (*37*). Furthermore, under both future climate scenarios, only low-elevation genotypes achieve $\lambda_s \geq 1$ in the mid-elevation and higher-elevation gardens, demonstrating that local populations are at risk of decline without the influx of migrants from lower elevations. That is, local extinctions may not be confined to marginal populations at the trailing edge of the range. Notably, contemporary high-elevation accessions are predicted to have poor performance ($\lambda_s < 1$) under preindustrial climates (Fig. 2A). Herbarium records in elevations >3200 m in the 1800s (*38*) indicate that high-elevation populations were present at that time. Thus we postulate that colder-adapted genotypes that performed best under preindustrial conditions may have already been lost from high-elevation locales owing to recent climate change.

Upslope gene flow is insufficient to keep pace with climate change

Populations in the historically cooler portion of the range could persist through climate change because of the immigration of genotypes preadapted to elevated temperatures from populations in historically warmer regions (*25*, *39*). Although *B. stricta*, like other species, recolonized high-elevation ecosystems after the retreat of the Pleistocene glaciers (*40*), climate change is likely outpacing recent rates of migration in plants and animals inhabiting mountainous ecosystems (*2*). We leveraged genotype-specific stochastic IPMs to examine how far genotypes would need to migrate to maintain stable local populations under four climate scenarios (Fig. 3A). We compared λ_s of all genotypes in the home site of each source population and calculated the closest genotype that could persist ($\lambda_s \geq 1$) in each climate scenario ("Climate Transfer Analysis").

Little migration is necessary to persist at lower elevations in preindustrial or contemporary climates, as local genotypes generally exhibit stable growth rates ($\lambda_s \geq 1$). However, upslope migration is necessary to maintain high-elevation populations under contemporary climates. Under the two end-of-century climate scenarios, most populations across the species' elevational range are predicted to require migrants from lower elevations to persist (Fig. 3A and tables S12 and S13). Upslope migration could rescue higher-elevation populations while conserving the low-elevation genotypes that are specifically adapted to projected climates.

To evaluate whether rates of upslope gene flow in *B. stricta* would be sufficient to enable population persistence across this elevational gradient, we established three elevational transects across separate mountains and inferred the best-fit long-term demographic models using genomic data (figs. S12 to S15 and table S13). We extracted DNA from 95 accessions across these transects and used an Illumina NextSeq 500 platform to generate low-coverage sequence data (average coverage 2.1×), and fit models using GADMA2 with the "moments" engine (*41*).

Gene flow in this system is spatially restricted, and contemporary levels of gene flow are unlikely to rescue high-elevation populations in the face of climate change. Minimum dispersal distances estimated from IPMs (Fig. 3A) predict that 96.9 m (±73.1, standard deviation) or 138.7 m (±67.8, standard deviation) of upslope migration would be necessary between now and 2071–2100 to maintain stable high-elevation populations in these three transects in the intermediate and worst-case emissions scenarios, respectively (table S13). However, models based on genomic sequence data show no upslope migration in the most recent epoch (Fig. 3B and figs. S12 to S15). This result suggests that natural gene flow alone will not be sufficient to keep pace with rapidly changing climates in this region.

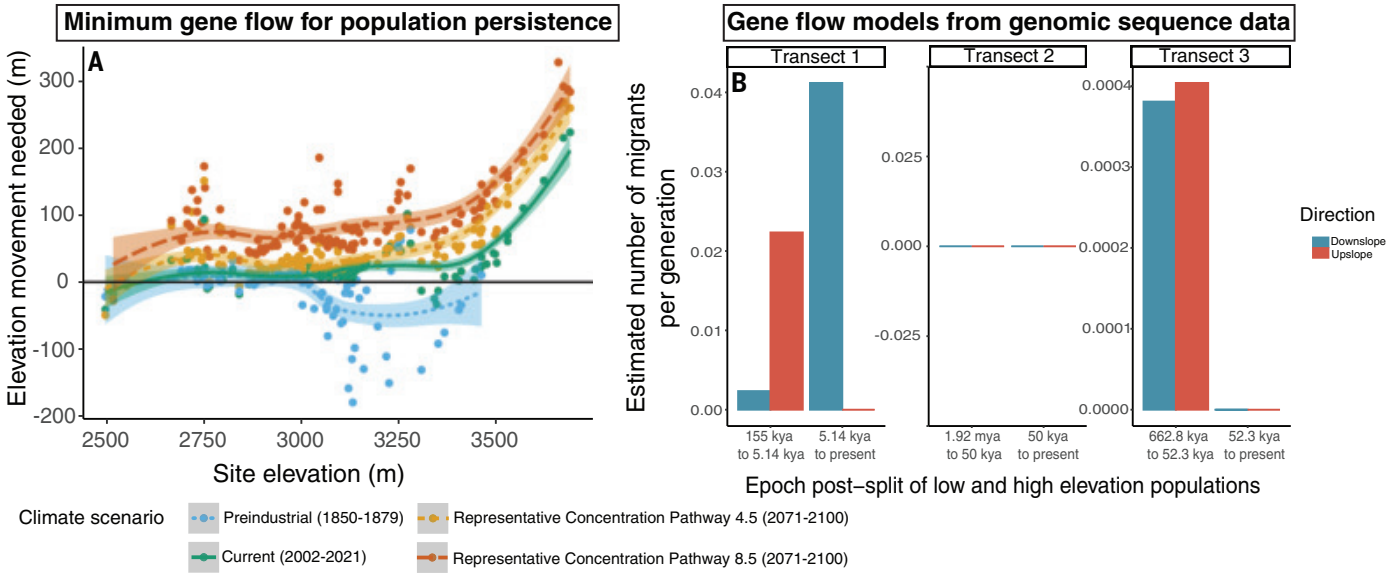

Fig. 3. Gene flow is unlikely to rescue local populations. (**A**) From integral projection models using data from the Provenance Trial Experiment, we calculated the movement necessary to maintain long-term persistence ($\lambda_s \geq 1$) for populations distributed across the elevational gradient under four climate scenarios. Positive values reflect the number of meters of upslope migration required, whereas negative values indicate that downslope migration would be necessary. In preindustrial climates, the highest elevation sites are predicted to have either been inhospitable to any currently available genotype (>3500 m) or to require migrants from even higher elevations to persist (~3000 to 3500 m), indicating a potential loss of the coldest-adapted genotypes from contemporary high-elevation accessions. In contemporary and future climates, IPMs indicate that genotypes from lower-elevation source populations could rescue higher-elevation populations, but our (**B**) genomic models indicate that gene flow is spatially restricted, with no upslope gene flow detected in the most recent epoch in any of the transects. Confidence intervals are so small that they cannot be seen. The population genomic demographic models with the moments engine of GADMA2 (*41*), which uses allele frequency spectrum (AFS) data, supported single ancestral populations that split into low- and high-elevation populations in all three transects (figs. S12 to S15). After this division, the models identified two epochs in each transect with different demographic histories and population sizes. The contemporary time frame is the most relevant to predicting gene flow patterns across current populations.

These results are not surprising, as *B. stricta* is primarily self-pollinating (*42*) and has dehiscent fruits that release gravity-dispersed seeds. In the absence of gene flow, our models predict that climate change could cause the elevational range to contract and could eliminate the low-elevation ecotypes that are best adapted to withstand new climates.

Reciprocal transplant experiment demonstrates limited potential for evolutionary rescue

Rapid adaptation could also allow populations to persist in forecasted climates (*23*, *24*). The rate of in situ adaptation depends on the extent of genetic variance in fitness within populations (*43*). To predict the adaptive potential of populations to climate change, we must consider genetic variance in fitness under projected climates. Some populations likely lack sufficient genetic variation to adapt to climate change (*12*, *44*), whereas others harbor cryptic genetic variation that emerges when exposed to new conditions (*23*, *45*). Environmental change could expose this cryptic genetic variation to selection, potentially hastening adaptive evolution (*23*, *24*). Nevertheless, we still know little about the extent of cryptic genetic variation or its importance in natural populations facing new environments (*45*).

Our provenance trial experiment revealed that range-wide genotypic variance in λ is highest under intermediate to delayed snowmelt timing and low growing-season temperature, with steep declines under projected future climates (Fig. 4A and fig. S16). Correspondingly, range-wide genotypic variance in λ_s is predicted to decline sharply in future climates in low- and mid-elevation sites (Fig. 4C and fig. S17). To evaluate the degree of within-population genotypic variation, we conducted a reciprocal transplant experiment, exposing a larger number of local genotypes to contemporary conditions and early snow removal in all gardens ($N = 11{,}850$ seeds from 124 genotypes, 17 to 30 genotypes per population, transplanted in fall 2015 and censused through fall 2018; $N = 6898$ juvenile rosettes from 122 accessions, 15 to 30 genotypes per population, transplanted in fall 2016 and censused through fall 2022; tables S14 to S15). We tested for interactions between each climate variable and source population (as fixed effects), and genotype within population (as random slopes) in generalized linear mixed models for each vital rate (tables S16) and constructed population- and genotype-specific IPMs to project λ as a function of climate and λ_s in preindustrial, contemporary, and future stochastic climate scenarios.

We found strong support for population and genotypic variation in climate responses in most vital rates in the Reciprocal Transplant

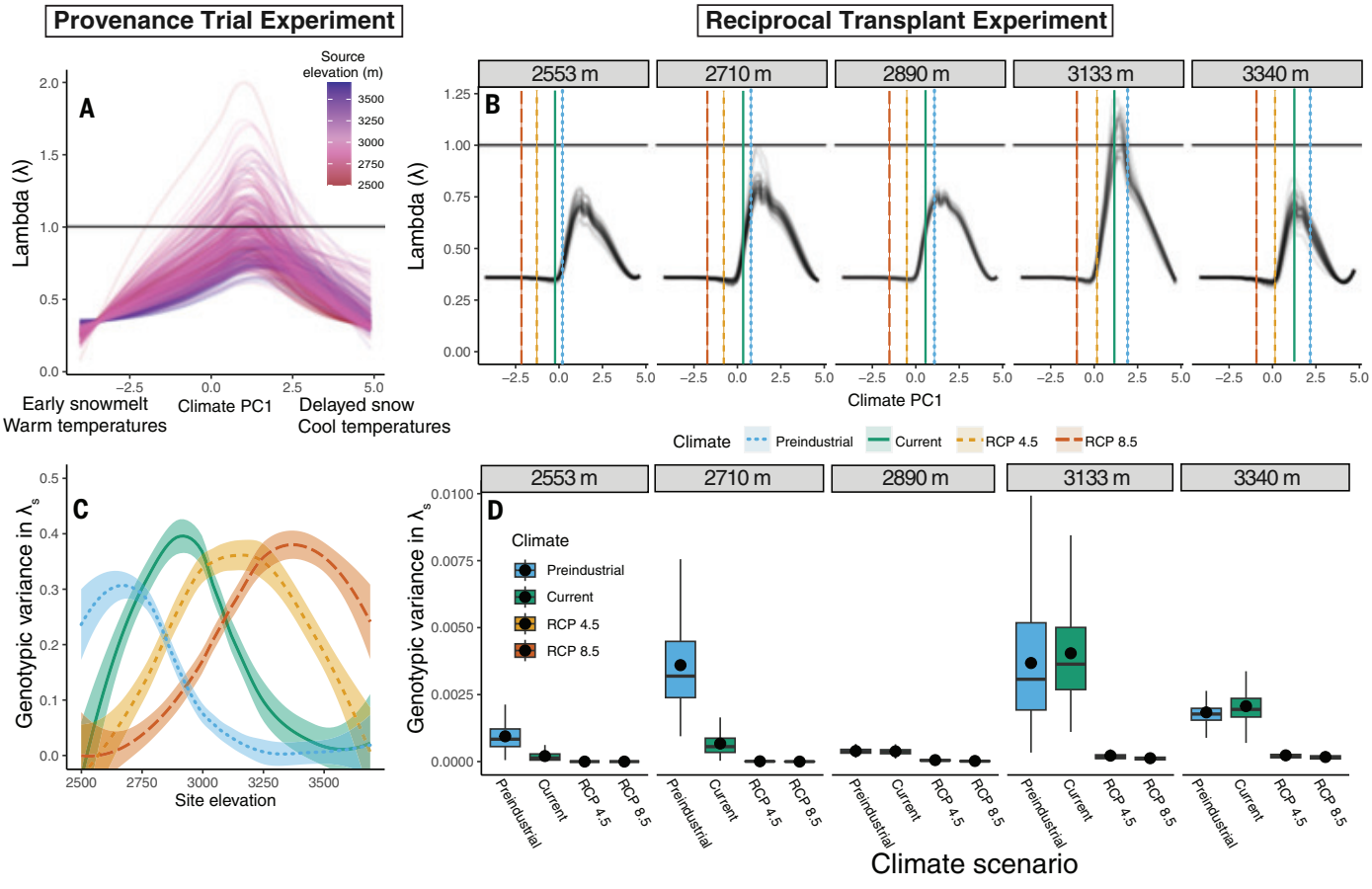

Fig. 4. Climate change reduces adaptive potential. Climatic performance curves for (**A**) all genotypes from the Provenance Trial Experiment and (**B**) local genotypes in each garden from the Reciprocal Transplant Experiment in response to climatic variation. Here, we combine snowmelt timing and growing season temperature in a principal component analysis; figs. S16 (Provenance Trial) and S21 (Reciprocal Transplant Experiment) show separate curves for each climatic variable. Low values of principal component 1 (Climate PC1) represent warm temperatures and early snowmelt and high values reflect cool temperatures and delayed snowmelt. The horizontal line signifies $\lambda = 1$, and vertical lines in (B) indicate local climates under four scenarios. (**C**) Genotypic variance in stochastic lambda (λ_s) across all genotypes of the provenance experiment if they were transplanted into each source location, capturing range-wide adaptive potential, which varies with climate scenario and site elevation. (**D**) Genotypic variance in λ_s for local genotypes from the reciprocal transplant experiment at each garden modeled under four climate scenarios. Box plots depict the mean (circle), median (central line), first and third quartiles (box range), and the largest and smallest values within 1.5× the interquartile range (vertical lines). Limited genotypic variance in λ_s, especially under projected future climates, could restrict adaptation of local populations from standing genetic variation.

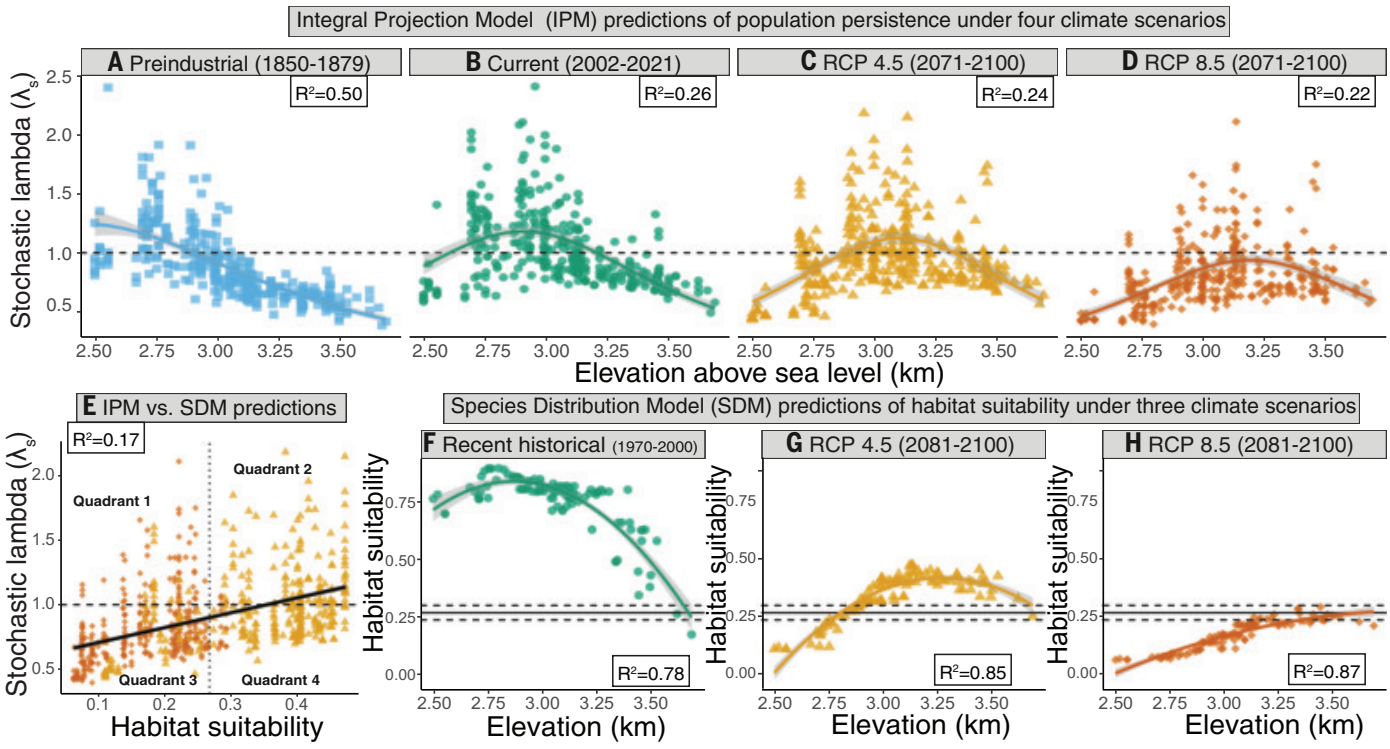

Fig. 5. Integral projection model (IPM) versus ensemble species distribution model (SDM) predictions of population persistence. Predictions of stochastic lambda (λ_s) using data from the Provenance Trial for each source population in its home site under (**A**) preindustrial climates, showing greatest performance of low-elevation populations; (**B**) current climates, revealing contractions at the lower elevational range and expansion at higher elevations, consistent with biogeographic shifts for a diversity of species (*2*); and (**C**) intermediate emissions scenarios, predicting upward shifts in the distribution and (**D**) worst-case emissions scenarios, predicting broad-scale population contractions. (**E**) Contrasts of IPM and SDM predictions under future climate scenarios. The horizontal dashed line shows $\lambda_s = 1$, and the vertical dotted line reflects the habitat suitability threshold for *B. stricta* persistence across 60 models in the ensemble SDM. In quadrants 2 and 3, the two approaches generate similar outcomes. In quadrant 1, IPMs predict persistence whereas SDMs predict extinction. The populations present in quadrant 4 are predicted to persist by SDMs but contract by IPMs. (**F**) SDMs for recent historical climates show high habitat suitability across the elevational range. Discrepancies between (B) and (F) could arise because BioClim data are not available range-wide for current climates (*50*). The habitat suitability threshold and 95% CI are indicated with solid and dashed lines, respectively. SDMs predict (**G**) population loss only at low elevations in the intermediate emissions scenario, and (**H**) large-scale extirpations in the high-emissions scenario.

Experiment (tables S16 to S24 and figs. S18 to S20). Integrating across vital rates in the Reciprocal Transplant Experiment revealed that genotypic variation in λ_s was greatest under preindustrial to contemporary climate conditions (Fig. 4, B and D; fig. S21; and table S25). As the climate shifts toward earlier snowmelt and warmer temperatures, within-population genotypic variation in λ_s diminished to negligible levels for all source populations (Fig. 4D).

By projecting λ_s of populations, allowing for evolution of genotype frequencies, we showed that local adaptive potential is insufficient for evolutionary rescue under future climates (fig. S22 and table S26). These evolutionary IPMs (*46*) evaluate the potential for evolutionary rescue by incorporating genotype as a state variable to allow for realistic changes in genotype frequencies over time driven by differences in their relative fitness. Concordant with thermal performance curves (*47*), genotype-specific climatic niches were often asymmetrical, suggesting that small increases in growing season temperature and accelerations in snowmelt timing will result in steep declines in λ (Fig. 4C and fig. S22). This limited genetic variation under early snowmelt and elevated temperatures suggests that cryptic genetic variation will likely not enable rapid evolution of local *B. stricta* populations to new climates.

Species distribution models could generate unreliable forecasts

Species distribution models (SDMs) are widely used for forecasting distributions under climate change. To evaluate the degree to which SDMs reflect complex population dynamics, we modeled habitat suitability on the basis of bioclimatic parameters from the localities of 156 known *B. stricta* populations in Colorado plus 496 background points, using 30–arc sec resolution environmental variables from WorldClim2.1 (*48*) for near historical (1970–2000) and future climate scenarios (2081–2100; Fig. 1, fig. S2, and table S27).

Ensemble SDMs predict high habitat suitability for Colorado populations that demographic models suggest will contract under the RCP 4.5 climate scenario (Fig. 5E). However, consistent with IPMs (Fig. 5, A to D), the ensemble SDM forecasts population contractions in the lower elevational range (Fig. 5, G and H). Differences in the core assumptions of these approaches could underlie divergent forecasts. Species distribution models estimate the climatic niche for the entire species and predict whether a location is suitable for any accession (*49*). Thus, SDMs assume limited local adaptation and unrestricted migration, whereas IPMs can be constructed to account for local adaptation. Furthermore, SDMs built using near-historical climatic and occurrence data (e.g., from herbarium or museum specimen) may poorly reflect contemporary population dynamics under climate change (*50*), whereas IPMs capture fitness responses to fine-grained environmental variation that is not represented even in the highest-resolution bioclimatic parameters from WorldClim (*48*). Finally, the regressions of habitat suitability from SDMs versus site elevation have substantially higher R-squared values compared with models of stochastic lambdas versus site elevation for the same populations, which could lead researchers to overestimate the predictive power of these models.

Conclusions

Determining the contributions of climatic factors to local adaptation is crucial for forecasting population persistence under future climates, predicting loss of intraspecific genetic diversity, determining whether preadapted ecotypes exist in trailing-edge populations, and drafting informed conservation practices. Here, we show that climate change increases the risk of extinction of locally adapted populations while decreasing adaptive potential and outpacing gene flow, even in a common and widely distributed species.

Gene flow is likely much higher in outcrossing species and those with mixed mating systems, yet even in those systems, it is critical to examine the directionality of gene flow. For example, in the mountains of Norway, asymmetrical downslope gene flow prevails in the self-incompatible *Arabidopsis lyrata* (*51*). Furthermore, syntheses suggest that climate change is outpacing recent rates of upslope migration in plants and animals inhabiting mountainous ecosystems, likely owing to limited dispersal capacity, biotic interactions, and microtopographic variation that generates local thermal refugia (*2*). Assisted gene flow (*52*) may be an efficient strategy for conserving genetic diversity and enhancing persistence of montane species, as long as protocols account for local adaptation to nonclimatic conditions (*53*).

Forecasting approaches that do not account for intraspecific climatic specialization, genetic variation under new climates, and gene flow could miss key avenues for conservation, neglect the importance of assisted gene flow for leading-edge populations, and fail to consider the specific adaptations of trailing-edge ecotypes to future climates. Species distribution models may perform well for highly mobile species with low levels of local adaptation but could generate biased predictions and lead to poor conservation practices for species with locally adapted populations. For example, the demographic models alone suggest that assisted migration could reduce the risk of extinction in future climates. Finally, our models generated markedly different predictions under the two future climate scenarios, highlighting that reductions in greenhouse gas emissions remain a powerful strategy for preserving genetic diversity.

REFERENCES AND NOTES

1. J. Lenoir *et al.*, *Nat. Ecol. Evol.* **4**, 1044–1059 (2020).
2. W.-P. Chan *et al.*, *Nature* **629**, 114–120 (2024).
3. J. Ehrlén, W. F. Morris, *Ecol. Lett.* **18**, 303–314 (2015).
4. J. Gurevitch, G. A. Fox, N. L. Fowler, C. H. Graham, *Q. Rev. Biol.* **91**, 459–485 (2016).
5. C. Merow *et al.*, *Ecography* **37**, 1167–1183 (2014).
6. T. E. X. Miller *et al.*, *Ecology* **101**, e03139 (2020).
7. W. Thuiller *et al.*, *Ecol. Lett.* **16** (Suppl 1), 94–105 (2013).
8. J. R. Lasky, M. B. Hooten, P. B. Adler, *Proc. Biol. Sci.* **287**, 20202219 (2020).
9. A. S. A. Johnston *et al.*, *Proc. Biol. Sci.* **286**, 20191916 (2019).
10. S. N. Sheth, A. L. Angert, *Evolution* **68**, 2917–2931 (2014).
11. K. S. Sheldon, R. B. Huey, M. Kaspari, N. J. Sanders, *Am. Nat.* **191**, 553–565 (2018).
12. V. Kellermann, B. van Heerwaarden, C. M. Sgrò, A. A. Hoffmann, *Science* **325**, 1244–1246 (2009).
13. R. Leimu, M. Fischer, *PLOS ONE* **3**, e4010 (2008).
14. J. Hereford, *Am. Nat.* **173**, 579–588 (2009).
15. D. R. Campbell, J. M. Powers, *Proc. Biol. Sci.* **282**, 20150178 (2015).
16. E. Hamann, A. E. Weis, S. J. Franks, *Evolution* **72**, 2682–2696 (2018).
17. T. Wang, G. A. O'Neill, S. N. Aitken, *Ecol. Appl.* **20**, 153–163 (2010).
18. A. M. Wilczek, M. D. Cooper, T. M. Korves, J. Schmitt, *Proc. Natl. Acad. Sci. U.S.A.* **111**, 7906–7913 (2014).
19. N. J. Kooyers *et al.*, *Am. Nat.* **194**, 541–557 (2019).
20. J. T. Anderson, S. M. Wadgymar, *Ecol. Lett.* **23**, 181–192 (2020).
21. A. J. Gorton, J. W. Benning, P. Tiffin, D. A. Moeller, *Evolution* **76**, 2916–2929 (2022).
22. S. M. Carlson, C. J. Cunningham, P. A. Westley, *Trends Ecol. Evol.* **29**, 521–530 (2014).
23. M. C. Bitter, L. Kapsenberg, J.-P. Gattuso, C. A. Pfister, *Nat. Commun.* **10**, 5821 (2019).
24. J. Zheng, J. L. Payne, A. Wagner, *Science* **365**, 347–353 (2019).
25. M. Bontrager, A. L. Angert, *Evol. Lett.* **3**, 55–68 (2018).
26. I. A. Al-Shehbaz, M. D. Windham, "Boechera" in *Flora of North America North of Mexico*, Flora of North America Editorial Committee, Ed. (Oxford Univ. Press, 2010), pp. 348–412.
27. H. A. Nomoto, J. M. Alexander, *Ecol. Lett.* **24**, 1157–1166 (2021).
28. Mountain Research Initiative, *Nat. Clim. Chang.* **5**, 424–430 (2015).
29. Methods and materials are available as supplementary materials.
30. S. P. P. Ellner, D. Z. Childs, M. Rees, *Data-Driven Modelling of Structured Populations: A Practical Guide to the Integral Projection Model Lecture Notes on Mathematical Modelling in the Life Sciences* (Springer, 2016).
31. R. Wooliver, E. E. Vtipilthorpe, A. M. Wiegmann, S. N. Sheth, *AoB Plants* **14**, plac016 (2022).
32. S. C. Stearns, *Evolution of Life Histories* (Oxford Univ. Press, 1992).
33. D. R. Campbell, *Proc. Natl. Acad. Sci. U.S.A.* **116**, 12901–12906 (2019).
34. V. Masson-Delmotte et al., Eds., *Climate Change 2021: The Physical Science Basis. Contribution of Working Group I to the Sixth Assessment Report of the Intergovernmental Panel on Climate Change* (Cambridge Univ. Press, 2023).
35. A. C. Lute, J. Abatzoglou, T. Link, *Geosci. Model Dev.* **15**, 5045–5071 (2022).
36. C. J. Talsma, K. E. Bennett, V. V. Vesselinov, *Earth Space Sci.* **9**, e2021EA002086 (2022).
37. J. Anderson, M. DeMarche, Boechera stricta climate change dataset, Zenodo (2024); https://doi.org/10.5281/zenodo.14659942.
38. Biodiversity occurrence data published by the Consortium of Intermountain Herbaria (2025); https://intermountainbiota.org/portal (accessed 12 January 2025).
39. A. Hampe, R. J. Petit, *Ecol. Lett.* **8**, 461–467 (2005).
40. C. Kiefer, C. Dobeš, T. F. Sharbel, M. A. Koch, *Mol. Phylogenet. Evol.* **52**, 303–311 (2009).
41. E. Noskova *et al.*, *Gigascience* **12**, giad059 (2022).
42. B.-H. Song, M. J. Clauss, A. Pepper, T. Mitchell-Olds, *Mol. Ecol.* **15**, 357–369 (2006).
43. R. A. Fisher, *The Genetical Theory of Natural Selection* (Oxford Univ. Press, 1930).
44. M. Exposito-Alonso *et al.*, *Science* **377**, 1431–1435 (2022).
45. A. B. Paaby, M. V. Rockman, *Nat. Rev. Genet.* **15**, 247–258 (2014).
46. M. Rees, S. P. Ellner, *Methods Ecol. Evol.* **7**, 157–170 (2016).
47. T. L. Martin, R. B. Huey, *Am. Nat.* **171**, E102–E118 (2008).
48. S. E. Fick, R. J. Hijmans, *Int. J. Climatol.* **37**, 4302–4315 (2017).
49. D. Zurell *et al.*, *Ecography* **43**, 1261–1277 (2020).
50. J. Lee-Yaw, J. McCune, S. Pironon, S. N. Sheth, *Ecography* **2022**, e05877 (2022).
51. T. Hämälä, O. Savolainen, *Mol. Biol. Evol.* **36**, 2557–2571 (2019).
52. S. N. Aitken, M. C. Whitlock, *Annu. Rev. Ecol. Evol. Syst.* **44**, 367–388 (2013).
53. A. Bucharova, *Restor. Ecol.* **25**, 14–18 (2017).

ACKNOWLEDGMENTS

We are grateful for J. Reithel's assistance with logistics for the field experiments. The Rocky Mountain Biological Laboratory, the Crested Butte Land Trust and Estess family allowed us to conduct common garden experiments on their land. We thank the expert backcountry skiers who conducted the snow removals, field researchers for their assistance collecting vital rate data, and greenhouse staff who assisted with growing plants prior to transplanting, including M. Robbins, I. Jameel, S. Day, B. Chowdhury, C. Daws, A. Battiata, C. Boerner, T. Morrison, S. Srivatsan, N. Workman, H. Nagle, M. Boyd, K. Tarner, D. Proudfoot, T. Kilgore, C. Smith, A. Beason, B. Ammon, A. Tiberio, P. Innes, K. Haner, A. Esparza, D. Eldridge, H. Grimess, E. Cheslock, E. Ross, R. MacTavish, A. Bohon, J. Adachi, J. Gall, M. Verner-Crist, M. Manto, and C. Beutler. V Ezenwa, M. Geber, D. Doak, S. Sheth, and B. Schmitz commented on a previous draft, and T. Pendergast assisted with model runs on the cluster, helped with data collection and garden maintenance, and provided feedback on the manuscript. We are grateful for the comments of two anonymous reviewers on a previous draft. B. Chowdhury and J. Gall granted permission to use photographs 1, 2, and 5 in Fig. 1E. **Funding:** Fieldwork and data collection for this study were funded by the National Science Foundation (DEB-1553408 to J.T.A.). A separate award from the National Science Foundation (IOS-2220927 to J.T.A. and M.L.D.) aided in the conceptualization of this study. **Author contributions:** Conceptualization: J.T.A., M.L.D. Methodology: J.T.A., M.L.D., I.B., D.A.D., J.S., S.M.W. Investigation: J.T.A., M.L.D., I.B., D.A.D., J.S., S.M.W. Visualization: J.T.A., M.L.D., D.A.D., J.S. Funding acquisition: J.T.A. Project administration: J.T.A. Supervision: J.T.A. Writing – original draft: J.T.A., M.L.D., I.B., D.A.D., J.S. Writing – review & editing: J.T.A., M.L.D., I.B., D.A.D., J.S., S.M.W. **Competing interests:** The authors declare that they have no competing interests. **Data and materials availability:** Data, code, and output files from the integral projection models are available in Zenodo from reference (*37*). That repository includes data for the provenance trial and reciprocal transplant experiments and code for the vital rate models, integral projection models, associated figures, species distribution models, and code for gene flow models. Genomic data for the gene flow analyses are available at GenBank (BioProject: PRJNA1123727).

SUPPLEMENTARY MATERIALS

science.org/doi/10.1126/science.adr1010
Materials and Methods; Supplementary Text; Figs. S1 to S25; Tables S1 to S27; References (*54*–*146*); MDAR Reproducibility Checklist

Submitted 14 June 2024; accepted 7 March 2025

10.1126/science.adr1010

BIRD DECLINE

North American bird declines are greatest where species are most abundant

Alison Johnston[1,2]*, Amanda D. Rodewald[1,3], Matt Strimas-Mackey[1], Tom Auer[1], Wesley M. Hochachka[1], Andrew N. Stillman[1], Courtney L. Davis[1], Viviana Ruiz-Gutierrez[1], Adriaan M. Dokter[1], Eliot T. Miller[1,4], Orin Robinson[1], Shawn Ligocki[1], Lauren Oldham Jaromczyk[1], Cynthia Crowley[1], Christopher L. Wood[1], Daniel Fink[1]

Efforts to address declines of North American birds have been constrained by limited availability of fine-scale information about population change. By using participatory science data from eBird, we estimated continental population change and relative abundance at 27-kilometer resolution for 495 bird species from 2007 to 2021. Results revealed high and previously undetected spatial heterogeneity in trends; although 75% of species were declining, 97% of species showed separate areas of significantly increasing and decreasing populations. Populations tended to decline most steeply in strongholds where species were most abundant, yet they fared better where species were least abundant. These high-resolution trends improve our ability to understand population dynamics, prioritize recovery efforts, and guide conservation at a time when action is urgently needed.

Bird communities globally are in crisis, with steep declines of many common species (*1*–*3*), and North America is no exception with more than one-quarter of all breeding birds lost since 1970 (*4*). Long-term indicators of population trends from structured monitoring surveys have documented these declines in bird populations over several decades (*4*–*6*). However, charting a pathway to recover populations requires detailed spatial information about population change to identify where populations are most imperiled and the optimal locations for conservation.

Practitioners have long recognized that conservation is most likely to be successful when the scale of information corresponds to the scale of the problem and implementation of actions, which often is on the order of several hectares or square kilometers (*7*). High-resolution estimates of population trends have a number of advantages for conservation: (i) They can be used to detect localized declines that are obscured at coarser resolutions and thus act as an early warning system; (ii) they can help identify causes of declines because many potential drivers are most readily determined at local or landscape scales (*8*–*11*); and (iii) they can inform management, which is typically implemented within sites and local landscapes (*12*, *13*). Access to high-resolution information is especially valuable when resources for conservation are limited, forcing decision-makers to prioritize actions among locations to get the best return on their investments. Unfortunately, even for well-surveyed taxa, such as birds (*5*, *14*), few monitoring programs can provide population trends at both a high resolution and a broad extent (*1*). We combined recent advances in analytical methods with open-source participatory science data to generate high-resolution bird population trends and provide a new opportunity to meet these needs in North America (*15*).

Estimating population trends

In this study, we harnessed participatory science (also known as "citizen science") data to reveal high-resolution patterns of avian population change across North America. We used 36 million checklists from eBird (*16*) collected from 2007 to 2021 to estimate population trends for 495 bird species breeding within North America, Central America, and the Caribbean. Each eBird checklist is a list of all birds observed and identified by a participant at a particular time and place. We estimated species trends as the average percent-per-year rate of change in relative abundance from 2007 to 2021 at a 27×27 km^2 spatial resolution across each species' range. We also produced confidence intervals for the trend estimates for each species within each 27×27 km^2 grid cell (*15*, *17*).

eBird, like most broad-scale participatory science projects, does not have the structured protocols necessary to maintain consistent sampling across space and time. Therefore, to reliably estimate bird population change, it is critical to use a model that separates changes in the bird populations from changes in how people observe birds. Without formally separating these processes, changes to the observation process will bias estimates of bird population trends. To accomplish this separation, we used a causal machine learning trend model designed to control for confounding sources of intra- and interannual variation, including changes in site selection, search effort, and search efficiency (*15*, *18*–*21*). We assessed the reliability of the trend estimates using an extensive suite of spatially explicit simulations for each species. We used these simulations to assess statistical power and error rates and found high power to reliably detect and delineate spatial variation with low error rates for trends at the 27-km spatial resolution for most North American species. In general, statistical performance was stronger (higher power and lower error rates) among trends with larger magnitudes but did not vary with species' relative abundance at the 27-km spatial resolution (*17*). Although we initially modeled trends for 573 species breeding in the region with sufficient data, we only present the results from the 495 deemed to have reliably estimated trends based on results from these species-specific simulations.

The high-resolution trends provide insights into the spatial structure of population dynamics for North American birds. Range-wide population trends indicated population declines for 75% of species and significant population declines for 65% of species. However, there is strong spatial heterogeneity that is invisible when population trends are summarized across species ranges (Fig. 1). Notably, 97% of species experienced both declines and increases in different locations within their ranges, and 67% of species had declines in more than half of their range (Fig. 2). The amount of spatial variation in trends that is obscured by regional summaries is substantial even within smaller Bird Conservation Regions (BCRs) (*22*), which represent regions with similar ecosystems and bird communities (Fig. 1). Specifically, the range of trend estimates at 27-km resolution within a BCR spanned more than 6% per year for most species (e.g., 27-km resolution trends might range from ±3% per year for a species with a BCR-wide stable trend) (fig. S1).

Birds are declining where they are most abundant

Our most concerning finding was that, for the overwhelming majority of species, the strongest rates of decline occurred in areas where populations were most abundant. By using a linear model that accounted for trend uncertainty with weights and modeled spatial autocorrelation with a Gaussian process, we found a negative association between local rates of population change and population abundances for 83% of species (statistically significant for 73% of species; Fig. 3A). For example, Williamson's sapsucker (*Sphyrapicus thyroideus*) is considered

[1]Cornell Lab of Ornithology, 159 Sapsucker Woods Road, Ithaca, NY, USA. [2]Centre for Research into Ecological and Environmental Modelling, School of Mathematics and Statistics, University of St Andrews, St Andrews, UK. [3]Department of Natural Resources and the Environment, Cornell University, Ithaca, NY, USA. [4]American Bird Conservancy, The Plains, VA, USA.
*Corresponding author. Email: alison.johnston@st-andrews.ac.uk

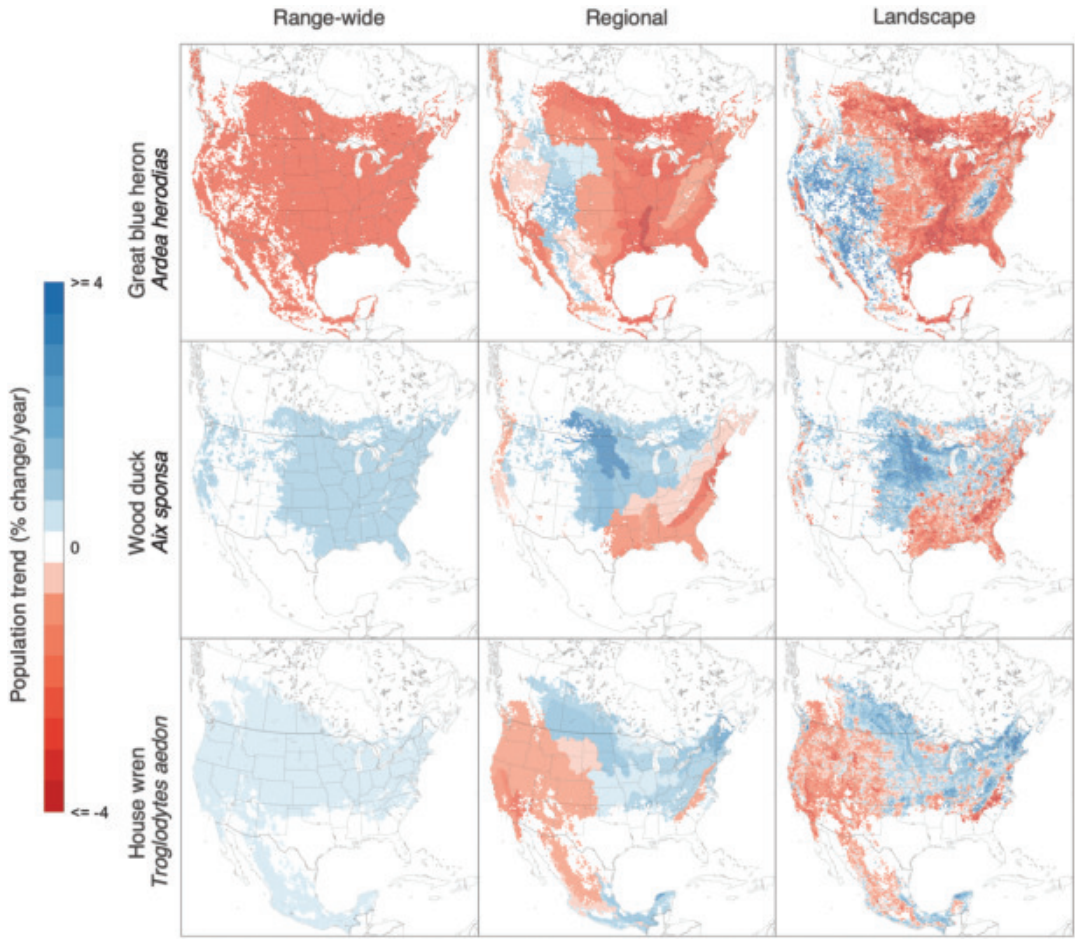

Fig. 1. High trend resolution reveals complexity of population changes from 2007 to 2021. Columns represent range-wide, regional (Bird Conservation Region), and landscape scales (27 × 27 km^2 grid cells). Trends are shown for (rows) the great blue heron (*Ardea herodias*), wood duck (*Aix sponsa*), and house wren (*Troglodytes aedon*). Each map shows the annual percent-per-year rate of change in abundance from 2007 to 2021 as averaged across the whole species' range, within BCRs), or within landscapes. All trends in a row were estimated with the same data and models, with outputs aggregated to the different spatial scales. (https://science.ebird.org/en/status-and-trends/trends-maps)

imperiled or vulnerable in more than half of the states and provinces where it breeds (*4*) and shows declines in remaining strongholds, raising particular concern for its conservation status (Fig. 3A). Positive correlations were evident for 17% of species (significantly positive for 7% of species), such as the yellow-billed cuckoo (*Coccyzus americanus*), whose abundance is increasing in areas where conditions already support high numbers (Fig. 3A). Our study thus builds upon previous alerts of steep declines among the most abundant birds in North America (*4*) and demonstrates that most species are experiencing declines in regions where each species is itself most abundant.

The negative association between local abundance and local population trend was consistent across communities of species breeding in similar habitats. Classifying species into breeding biome communities and calculating average effects over all species within those biomes, we found that every biome was characterized by negative relationships between relative abundance and trends. The strongest negative associations between local relative abundance and local population trends were evident for species breeding in aridlands and grasslands, which had the highest proportions of species with negative associations (87 and 96%, respectively) (Fig. 3B). In only three cases were species' populations within biomes actually increasing at their lowest abundances (positive intercepts on Fig. 3B): aridland, forest, and habitat generalist species. These positive trends suggest that these communities may be able to respond to environmental fluxes with population increases where the species are currently at low abundance or even with colonizations of new locations (Fig. 3B). However, the outlook was less hopeful for grassland, wetland and coast, and Arctic tundra species, which had biome averages with no evidence of population growth in areas of low abundance and stronger declines at higher abundances (Fig. 3B). Taken as a whole, the current weight of evidence points toward a worsening situation for North American birds.

To infer the potential mechanisms of the relationship between abundance and trend in relation to core-periphery population dynamics (*23*), we also explored whether distance to range edge was similarly correlated with local population trend. Consistent with ecological theory (*24*, *25*), most North American birds occur at lower abundance near range edges (*26*) and/or at higher abundance near the centroids of their ranges (*27*). We compared linear mixed models to determine whether variation in species trends was more closely associated with abundance or distance to range edge, the two of which were weakly correlated (median correlation coefficient across species $r = 0.54$). Results showed that both intra- and interspecific variation in trends across space were much better explained by species abundance than by distance to range edge, underscoring the ecological rather than geographical nature of this association (*17*, *23*).

These findings emphasize the need to understand and address the causes of recent declines in species' strongholds. Multiple explanations may account for these negative relationships, and we present several

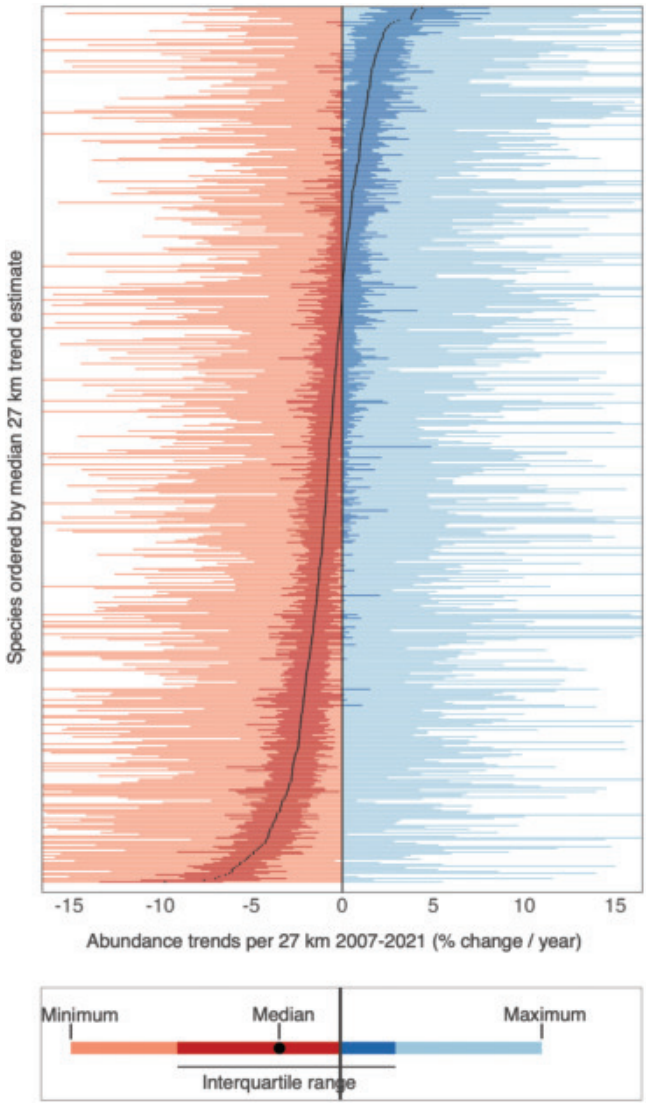

Fig. 2. Most of the 495 species show areas of both increase and decline across their ranges. Each horizontal bar represents a single species, located sequentially in order of their median 27-km resolution trend. The horizontal extent of each bar shows the maximum and minimum of species' 27-km resolution trends across their range. The darker central section of each bar indicates the interquartile range of each species' trends across its range. The median is shown with a black dot. Sixty-seven percent of species have a median trend less than 0 (black dot to the left of the vertical line).

possible interpretations that are not mutually exclusive; indeed, the relevant explanations likely vary across species. First, high-quality sites that could support abundant populations may be more affected by stressors, such as climate change, land conversion, and pollution, than lower-quality sites, where birds are less abundant and may have been previously exposed to any given stressor. Nonequilibrium populations in areas of low abundance also may be less subject to density-dependent mortality and/or reduced breeding success than areas where populations are near carrying capacity (*28*). Secondly, if areas predicted to have higher abundances are characterized by more suitable and/or stable habitats, then birds in those areas may be selected for slower pace-of-life syndrome ("k" selected) owing to differential environmental selection processes (*29*–*31*). This could make these populations less demographically suited to recovery after perturbations. Thirdly, individuals in areas of low abundance (i.e., range edges or nonideal environments) may be adapted to and/or more resilient to marginal, fluctuating, extreme, or unpredictable conditions, as has been shown for other taxonomic groups (*31*–*33*). Individuals adapted to these conditions at distribution edges may be important for population persistence in a changing environment (*32*). However, species and communities are still decreasing in total population size, suggesting that environmental changes (e.g., climate or land conversion) are outpacing the ability of most species to adapt, leading to potentially irreversible declines in their core ranges (*34*–*36*).

Trends among breeding biome communities

The high resolution of the trend estimates allows us to compare range-wide population changes with the proportion of the range experiencing declines. For species with the same population trend, there was high variation in the proportion of the range that was declining (fig. S2). Although 75% of species were declining overall, species declined, on average, across only 60% of their ranges. The proportions of ranges declining were largest for species that breed in Arctic tundra (on average, populations of Arctic-breeding species were declining across 74% of their nonbreeding ranges) and grasslands (70%) but smallest for aridland birds (47%). Declines tended to be worse for species whose trends were estimated during nonbreeding seasons (typically those species that breed further north) (fig. S3). These patterns of decline suggest that biome-level impacts, such as climate change in the Arctic (*37*), are impacting critical breeding habitats for species. These patterns also point toward opportunities for conservation, as almost all declining species have areas where the population is locally increasing (Fig. 2), demonstrating they have potential for increases in some environmental conditions.

Within species' breeding biomes, we discovered patterns of spatial convergence in species' trends that can be used to identify common areas of community declines and increases (Fig. 4). Grassland species were declining strongly within the core of their ranges, though with small pockets of increase in the Upper Midwest and Arid West of the US (Figs. 3B and 4). This is consistent with the broad-scale changes to agricultural practices throughout the distributions of grassland birds (*38*). Most communities tended to have both mean declines and the majority of species declining in the Southeast US, the Mississippi Alluvial Valley, parts of the Upper Midwest, the California Central Valley, and the Pacific Northwest (Fig. 4). By contrast, we found many shared patterns of community increases in the Appalachian and western mountains (Fig. 4), particularly at higher elevations in the southern Appalachians, where many species reach their southern range limits (*39*). Birds associated with aridlands stood out as faring better in Mexico than in the US or Canada. These shared patterns of population change enable us to identify areas of threat and refuge for these communities (*40*). However, some caution in interpretation is required, as these patterns also reflect changes in community composition across space.

Conservation implications

The fine-scale heterogeneity of population change that we describe in this work highlights the geographic variability in conservation urgency. These trends were estimated over a 14-year period, which provides information about recent population changes while being long enough to reliably reflect population change rather than short-term demographic stochasticity (*41*). Therefore, this time period has high value for guiding strategically directed conservation action for current drivers of population change (*9*, *42*). The availability of high-resolution trends makes it possible to inform and direct management interventions to specific landscapes where action is most needed and resources are best invested, whether for individual species or groups of species (*20*, *43*, *44*). As such, we expect that these trends will be useful to international or multisector partnerships, such as the North American Bird Conservation Initiative, government agencies, not-for-profit

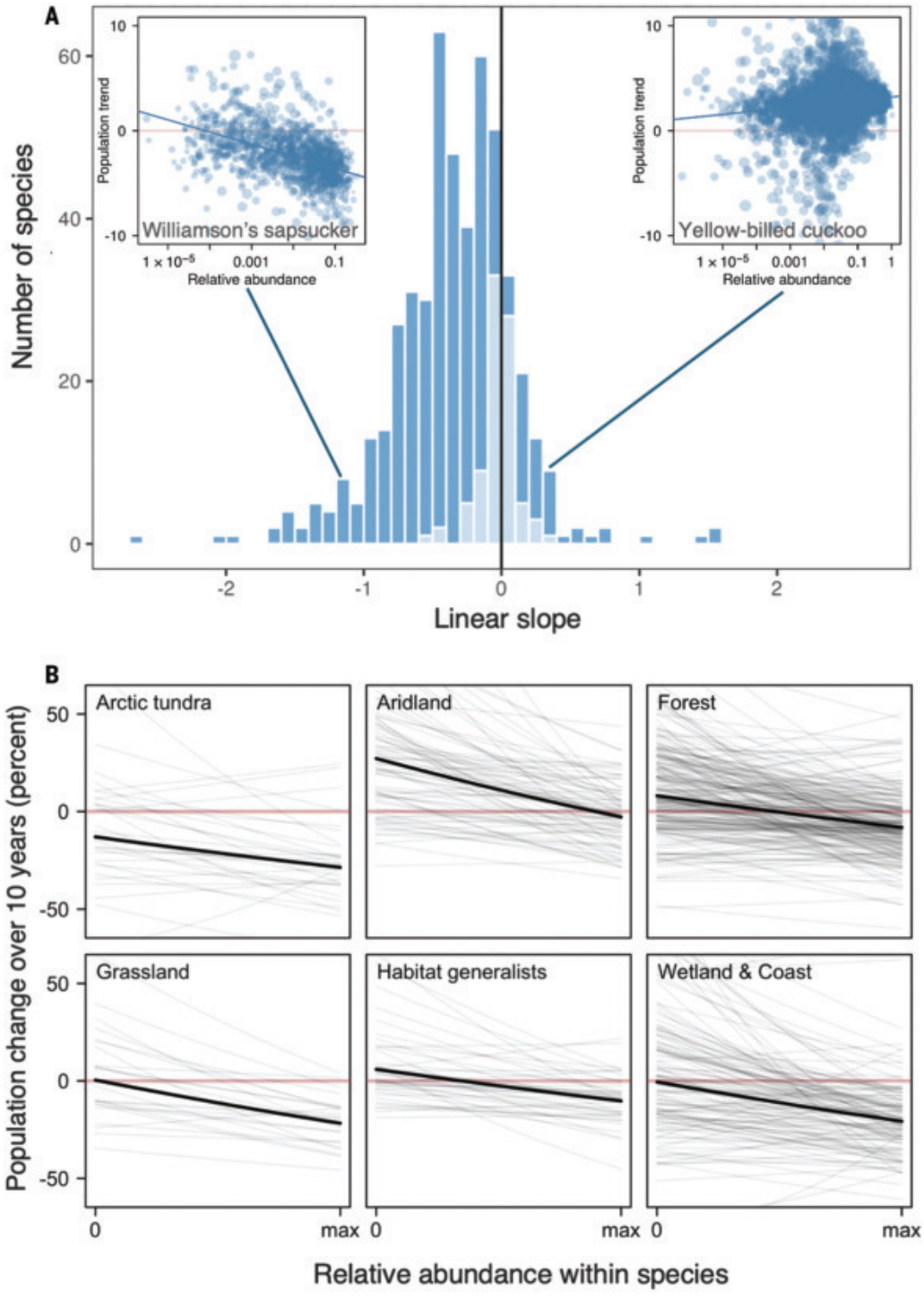

Fig. 3. Most species have a negative correlation between abundance and trend, indicating population declines in areas with highest abundance. (**A**) The histogram shows species-specific slopes of the fitted relationships between relative abundance and trend at 27-km resolution. Example species with negative (Williamson's sapsucker, *Sphyrapicus thyroideus*) and positive (yellow-billed cuckoo, *Coccyzus americanus*) relationships are shown in the insets. The vertical black line indicates a slope of zero or no association between abundance and trend. Eighty-three percent of species have negative slopes (to the left of the zero line), and 73% of species have significantly negative slopes (dark blue to the left of the zero line). (**B**) Most species (thin gray lines) and all community averages of all species breeding in each biome (thick black lines) have negative correlations between population change and abundance at a 27-km resolution. The pale horizontal pink lines indicate zero population change. The models were fit with percent-per-year changes related to $\log_{10}$ abundance, and here we show these trends aggregated to expected population change over a 10-year period. This leads to some nonlinear relationships due to "compound interest" of population changes. Biome effect sizes were calculated as the average of species differences in expected trend (percent per year) between minimum and maximum $\log_{10}$ relative abundance and population trend. These were also aggregated up to estimate 10-year population change, and the average differences in percent population change from minimum to maximum abundance over 10 years within the species in each biome were (in increasing order): Aridlands, −30%; Grassland, −22%; Wetlands and Coast, −20%; Forest, −16%; Habitat Generalist, −16%; and Arctic Tundra, −16%.

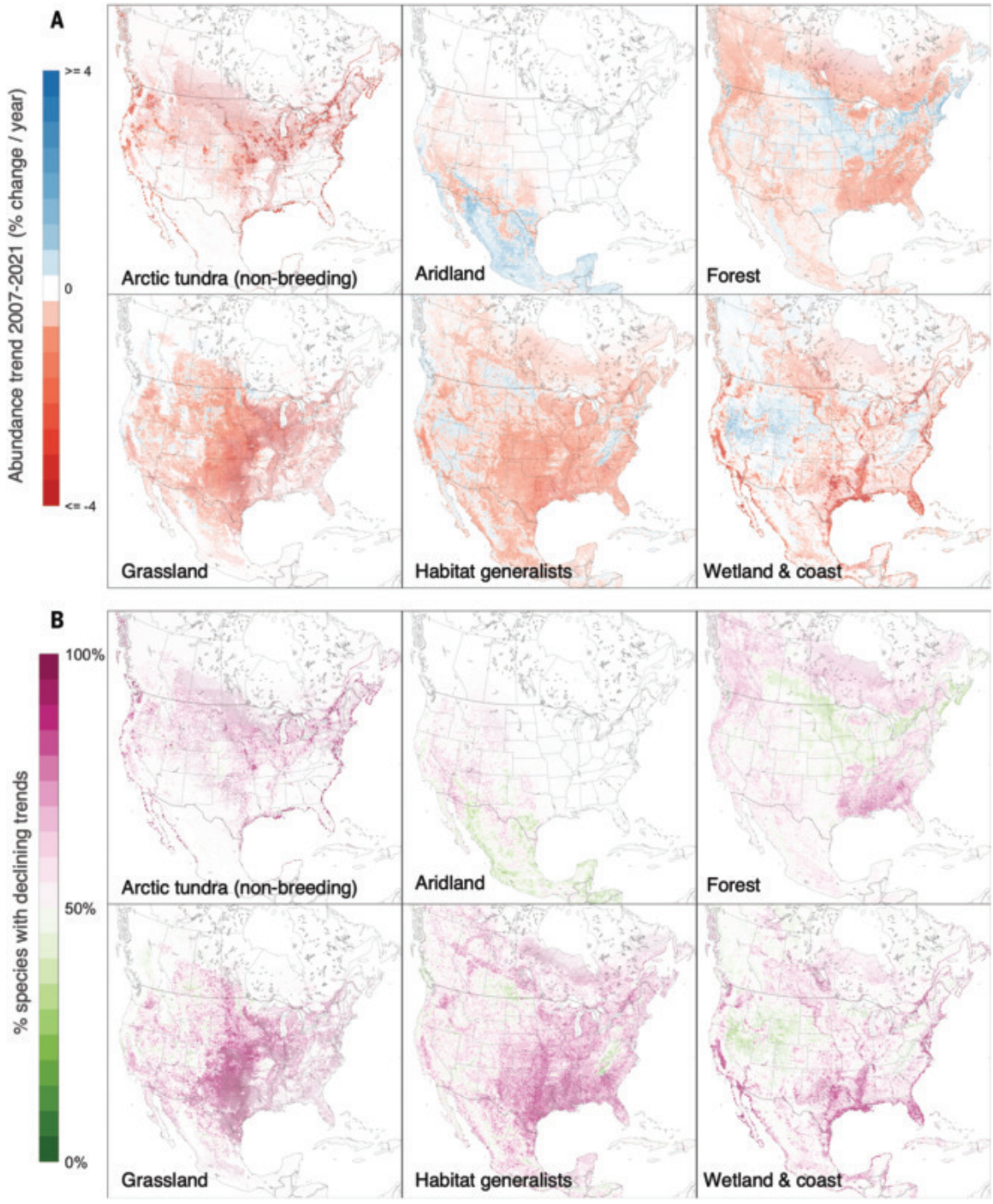

Fig. 4. Landscape-scale patterns of population change were shared among breeding biome communities. (**A**) Red-blue maps show the mean trend (i.e., annual percent-per-year rate of change in abundance) from 2007 to 2021 (red, decline; blue, increase; darker colors indicate stronger trends) within each 27×27 km^2 grid cell averaged across all species in each of six North American breeding biome communities. (**B**) Pink-green maps show the percentage of species within each breeding biome community with declining trends (pink, the majority of species declining; green, the majority of species increasing; darker colors indicate larger majorities). Note that all Arctic tundra species have trends estimated in their nonbreeding season. Despite the heterogeneity among trend maps for individual species, the red-blue and pink-green patterns within community-level trends indicate shared patterns of population change among species within breeding biome communities.

organizations, and the private sector, all of which have limited fiscal and human resources to address a multitude of environmental challenges, including the recovery of North American birds.

This study demonstrates how participatory science data and other broad-scale, observational datasets can be leveraged with promising analytical tools to detect, diagnose, and respond to population changes at ecologically relevant scales. We present high-resolution spatially explicit population trends across a broad geographic extent for most of an entire taxonomic group. The continued expansion of participatory science projects provides opportunities to replicate our approach to trend estimation on other continents and other taxonomic groups. The ability to estimate population trends for hundreds of species at

landscape scales and across an entire continent can advance the ability of scientists, managers, and decision-makers seeking to understand and reverse population declines (*44*). High-resolution trends, in conjunction with other environmental datasets, can also be used to study the associations with other spatially dependent processes (e.g., management actions, resource availability or change) and provide new insights to better understand the drivers of population change.

REFERENCES AND NOTES

1. S. H. M. Butchart *et al.*, *Science* **328**, 1164–1168 (2010).
2. A. S. L. Rodrigues *et al.*, *PLOS ONE* **9**, e113934 (2014).
3. F. Burns *et al.*, *Ecol. Evol.* **11**, 16647–16660 (2021).
4. K. V. Rosenberg *et al.*, *Science* **366**, 120–124 (2019).
5. J. R. Sauer, W. A. Link, J. E. Hines, The North American Breeding Bird Survey, analysis results 1966 - 2019, US Geological Survey (2020); https://doi.org/10.5066/P96A7675.
6. V. Brlík *et al.*, *Sci. Data* **8**, 21 (2021).
7. J. A. Wiens, D. Bachelet, *Conserv. Biol.* **24**, 51–62 (2010).
8. L. A. K. Barnett, E. J. Ward, S. C. Anderson, *Ecography* **44**, 427–439 (2021).
9. D. M. Ethier, N. Koper, T. D. Nudds, *Ecol. Evol.* **7**, 4152–4162 (2017).
10. J. Matthiopoulos *et al.*, *Ecol. Monogr.* **85**, 413–436 (2015).
11. C. A. Morrison *et al.*, *R. Soc. Open Sci.* **9**, 211671 (2022).
12. C. Boyd *et al.*, *Conserv. Lett.* **1**, 37–43 (2008).
13. A. N. Stillman *et al.*, *J. Appl. Ecol.* **60**, 2389–2399 (2023).
14. Pan-European Common Bird Monitoring Scheme, Trends of common birds in Europe (2019); https://pecbms.info/trends-of-common-birds-in-europe-2019-update/.
15. D. Fink *et al.*, *Methods Ecol. Evol.* **14**, 2435–2448 (2023).
16. B. L. Sullivan *et al.*, *Biol. Conserv.* **169**, 31–40 (2014).
17. See supplementary materials and methods.
18. S. Kelling *et al.*, *Bioscience* **69**, 170–179 (2019).
19. A. Johnston, D. Fink, W. M. Hochachka, S. Kelling, *Methods Ecol. Evol.* **9**, 88–97 (2018).
20. D. Fink *et al.*, *Ecol. Appl.* **30**, e02056 (2020).
21. D. Fink *et al.*, eBird Status and Trends, Data Version: 2021 (Cornell Lab of Ornithology, 2022); https://doi.org/10.2173/ebirdst.2021.
22. North American Bird Conservation Initiative, The State of the Birds, United States of America (2022); https://stateofthebirds.org/.
23. J. D. Manthey *et al.*, *Endanger. Species Res.* **26**, 201–208 (2015).
24. J. H. Brown, G. C. Stevens, D. M. Kaufman, *Annu. Rev. Ecol. Syst.* **27**, 597–623 (1996).
25. S. Pironon, J. Villellas, W. F. Morris, D. F. Doak, M. B. García, *Glob. Ecol. Biogeogr.* **24**, 611–620 (2015).
26. P. R. Martin, O. J. Robinson, F. Bonier, *Proc. Biol. Sci.* **291**, 20231760 (2024).
27. L. Osorio-Olvera, C. Yañez-Arenas, E. Martínez-Meyer, A. T. Peterson, *Ecol. Lett.* **23**, 555–564 (2020).
28. I. A. Hanski, M. P. Hassell, R. M. May, *Philos. Trans. R. Soc. Lond. B Biol. Sci.* **330**, 141–150 (1997).
29. J. Wright, G. H. Bolstad, Y. G. Araya-Ajoy, N. J. Dingemanse, *Biol. Rev. Camb. Philos. Soc.* **94**, 230–247 (2019).
30. R. E. Ricklefs, M. Wikelski, *Trends Ecol. Evol.* **17**, 462–468 (2002).
31. A. M. Hämäläinen, A. Guenther, S. C. Patrick, W. Schuett, *Ethology* **127**, 32–44 (2021).
32. E. M. Rehm, P. Olivas, J. Stroud, K. J. Feeley, *Ecol. Evol.* **5**, 4315–4326 (2015).
33. L.-M. Chevin, A. A. Hoffmann, *Philos. Trans. R. Soc. Lond. B Biol. Sci.* **372**, 20160138 (2017).
34. S. Y. Gibson, R. C. Van der Marel, B. M. Starzomski, *Conserv. Biol.* **23**, 1369–1373 (2009).
35. C. S. Rushing, J. A. Royle, D. J. Ziolkowski Jr., K. L. Pardieck, *Proc. Natl. Acad. Sci. U.S.A.* **117**, 12897–12903 (2020).
36. D. Massimino, A. Johnston, J. W. Pearce-Higgins, *Bird Study* **62**, 523–534 (2015).
37. M. Rantanen *et al.*, *Commun. Earth Environ.* **3**, 168 (2022).
38. D. J. T. Douglas *et al.*, *Ibis* **165**, 1107–1128 (2023).
39. S. A. Merker, R. B. Chandler, *Glob. Ecol. Conserv.* **22**, e00915 (2020).
40. G. P. Asner *et al.*, *Proc. Natl. Acad. Sci. U.S.A.* **117**, 33711–33718 (2020).
41. H. S. Wauchope, T. Amano, W. J. Sutherland, A. Johnston, *Methods Ecol. Evol.* **10**, 2067–2078 (2019).
42. M. Cimatti *et al.*, *Divers. Distrib.* **27**, 602–617 (2021).
43. P. J. Stephenson *et al.*, *Biodiversity* **16**, 68–85 (2015).
44. D. Zurell *et al.*, *Ecography* **2022**, ecog.05787 (2022).
45. X. C. Song *et al.*, Practice and Experience in Advanced Research Computing (PEARC '22), 10 to 14 July 2022, Boston, MA, USA (ACM, 2022), article 23.
46. A. Johnston *et al.*, North American bird declines are greatest where species are most abundant, Dryad (2025); https://doi.org/10.5061/dryad.5qfttdzhq.
47. A. Johnston *et al.*, North American bird declines are greatest where species are most abundant, Zenodo (2025); https://doi.org/10.5281/zenodo.14883965.
48. A. Johnston, M. Strimas-Mackey, ali-johnston/2024_trends-abundance-paper: v1.0 Paper submission 2025-02-17, Zenodo (2025); https://doi.org/10.5281/zenodo.14883008.

ACKNOWLEDGMENTS

We are grateful to the many thousands of participants, reviewers, and partner organizations around the world who support and contribute to eBird. We thank the eBird team and the associated engineering teams for their tireless efforts to grow, support, and improve the project. Likewise, none of this work would be possible without the generous support of the Cornell Lab of Ornithology's members, donors, and many staff teams. **Funding:** This work was supported by the Leon Levy Foundation (D.F.), the Wolf Creek Foundation, and the National Science Foundation DBI-1939187 (C.L.W., D.F.). Computing support from the National Science Foundation was provided through CNS-1059284 and CCF-1522054. This work used Bridges2 at Pittsburgh Supercomputing Center and Anvil (*45*) at the Rosen Center for Advanced Computing at Purdue University through allocation DEB200010 (D.F., T.A., S.L., O.R.) from the Advanced Cyberinfrastructure Coordination Ecosystem: Services & Support (ACCESS) program, which is supported by NSF grants 2138259, 2138286, 2138307, 2137603, and 2138296. **Author contributions:** Conceptualization: A.J., A.D.R., D.F.; Methodology: A.J., D.F., T.A., S.L., W.M.H., C.C.; Formal analysis: A.J., M.S.-M., T.A., W.M.H., S.L., D.F.; Visualization: M.S.-M., L.O.J., T.A., A.J., D.F.; Data curation: T.A., M.S.-M., S.L., W.M.H., C.L.W., A.D.R.; Writing – original draft: A.J., A.D.R., D.F.; Writing – review & editing: all authors. **Competing interests:** The authors declare that they have no competing interests. **Data and materials availability:** Data are available at the Dryad (*46*) and Zenodo repositories (*47*). The code to rerun the analyses and create figures from this manuscript is available in a Github release archived at Zenodo (*48*).

SUPPLEMENTARY MATERIALS

science.org/doi/10.1126/science.adn4381
Materials and Methods; Supplementary Text; Figs. S1 to S16; Tables S1 and S2; References (*49–82*)

Submitted 10 December 2023; resubmitted 9 August 2024; accepted 18 March 2025

10.1126/science.adn4381

NEUROSCIENCE

Dimensionality reduction simplifies synaptic partner matching in an olfactory circuit

Cheng Lyu[1,2]†, Zhuoran Li[1,2,3]†, Chuanyun Xu[1,2,3], Kenneth Kin Lam Wong[1,2], David J. Luginbuhl[1,2], Colleen N. McLaughlin[1,2], Qijing Xie[1,2,4]‡, Tongchao Li[1,2]§, Hongjie Li[1,2]¶, Liqun Luo[1,2]*

A navigating axon faces complex choices when selecting postsynaptic partners in a three-dimensional (3D) space. In this work, we discovered a principle that can establish the 3D glomerular map of the fly antennal lobe by reducing the higher dimensionality serially to 1D projections. During development, olfactory receptor neuron (ORN) axons first contact their partner projection neuron dendrites on the spherical surface of the antennal lobe, regardless of whether the adult glomeruli lie near the surface or inside. Along this 2D surface, axons of each ORN type take a specific, arc-shaped trajectory that precisely intersects with their partner dendrites. Altering axon trajectories compromises synaptic partner matching. A 3D search is thus reduced to one dimension, simplifying partner matching.

Proper function of the brain requires precise assembly of neural circuits during development. Serial electron microscopic reconstructions of connectivity patterns from *Caenorhabditis elegans* to mammals (*1*–*5*) have revealed unprecedented precision of neural circuit wiring. Understanding how neural circuits establish such precise synaptic connections is a central goal of neurobiology.

A fundamental open question in synaptic partner selection is how to minimize the choice for a navigating axon. Axon guidance mitigates this problem by guiding an axon to a specific brain region (*6*, *7*). At the appropriate brain region, how does an axon navigate the local three-dimensional (3D) space to find its partners among many non-partners? Some neural circuits reduce this task load by organizing target selection in lower dimensions. For example, retinotopic and layered organization in the vertebrate retina and fly optic lobe enable target selection of some visual neurons to be divided into a 1D search for a specific layer followed by a 2D search for a synaptic partner within that layer (*8*–*10*). Here, even though strictly speaking the targets still occupy a 3D physical space, we can approximate these target selection problems as 1D or 2D because the axon only needs to search in a lower-dimensional space at a given step. But for many brain structures in which synaptic partners appear to be distributed in all three dimensions, an axon would need to code for the correct movement along each of the three axes and for recognizing all potential synaptic partners within that brain region. Are there means to simplify the synaptic partner matching problem? In this work, we illustrate that in the wiring of the olfactory circuit in the fly antennal lobe, the task complexity of synaptic partner searching is effectively reduced from 3D to 1D.

[1]Department of Biology, Stanford University, Stanford, CA, USA. [2]Howard Hughes Medical Institute, Stanford University, Stanford, CA, USA. [3]Biology Graduate Program, Stanford University, Stanford, CA, USA. [4]Neurosciences Graduate Program, Stanford University, Stanford, CA, USA. ***Corresponding author. Email: lluo@stanford.edu** †These authors contributed equally to this work. ‡Present address: Calico Life Sciences LLC, South San Francisco, CA, USA. §Present address: Liangzhu Laboratory, MOE Frontier Science Center for Brain Science and Brain-machine Integration, State Key Laboratory of Brain-machine Intelligence, Zhejiang University, Hangzhou, China. ¶Present address: Huffington Center on Aging, Department of Molecular and Human Genetics, Baylor College of Medicine, Houston, TX, USA.

Projection neuron dendrites extend to the antennal lobe surface during development

In adult *Drosophila*, ~50 types of olfactory receptor neurons (ORNs) synapse with 50 types of projection neurons (PNs) in a one-to-one fashion at 50 discrete glomeruli. Each glomerulus forms a functional unit, and the 50 glomeruli together occupy stereotyped 3D positions in the antennal lobe, with some exposed to the antennal lobe surface and others exclusively interior (Fig. 1, A and B). Previous studies indicate that the assembly of the fly olfactory circuit takes sequential steps. PN dendrites first elaborate and form a coarse map (*11*, *12*). ORN axons then circumnavigate ipsi- and contralateral antennal lobes from ~18 to 32 hours after puparium formation (hours APF) (*13*, *14*). Concomitant with extending toward the contralateral antennal lobe, ORN axons send multiple transient branches in the ipsilateral antennal lobe to search for their partner PN dendrites, and those that contact dendrites of cognate PNs are stabilized (*14*, *15*) (Fig. 1A). However, the strategy that an ORN axon uses to match with partner PN dendrites remains incompletely understood. Does each ORN axon search the entire 3D space and scan through all PN types, or are there ways to reduce the number of PN candidates for each ORN type? We note that in vertebrates, glomeruli are located on the olfactory bulb surface, simplifying target selection of ORN axons to a 2D problem (*16*). Could a similar strategy be used in the developing *Drosophila* antennal lobe?

To address these questions, we began by examining the distribution of PN dendrites during development with single-type resolutions. We generated a collection of genetic drivers that label single PN types across developmental stages (Fig. 1, C to F, and fig. S1) using split-GAL4 (*17*) and Flp/FRT-based intersection strategies (*18*). Using these drivers, we compared the dendritic patterns of single PN types between the adult and the developmental stage when ORN axons start navigating the antennal lobe. We found that PNs that innervate surface and interior glomeruli in the adult antennal lobe (referred to hereafter as adult-surface and adult-interior PNs, respectively) both had parts of their dendrites at the antennal lobe surface during development (Fig. 1, C to F).

Quantitative analyses revealed that the dendritic locations of all PN types at 30 hours APF approximated their future glomerular positions in adults (Fig. 1, G and H, and fig. S1). Furthermore, dendritic distributions along the radius of the antennal lobe confirmed that all four adult-interior PN types we tested extended some of their dendrites to the antennal lobe surface, even though smaller fractions were at the surface compared with the dendritic distribution of the eight adult-surface PN types (Fig. 1I). The surface extension of adult-interior PN dendrites during development likely does not result from cognate ORN and PN interactions, as it was also observed in the same PN types at an earlier developmental stage before ORN axons had reached the antennal lobe (fig. S2). Thus, both adult-surface and adult-interior PNs extend their dendrites to the antennal lobe surface during development (Fig. 1J).

ORN axons take cell type–specific trajectories at the antennal lobe surface during development

To encounter correct partners, each ORN axon should ideally navigate along a trajectory that intersects with cognate PN dendrites. To test this hypothesis, we generated a collection of genetic drivers that label single-type or groups of ORNs across developmental stages (Fig. 2, A and B, and figs. S3 and S4). When viewed from a vertical perspective orthogonal to navigating axons, all ORN axons navigated along the spherical surface of the antennal lobe, regardless of their surface or interior positions in adults (Fig. 2B and fig. S4), in line with previous studies that examined axons in bulk (*13*, *19*).

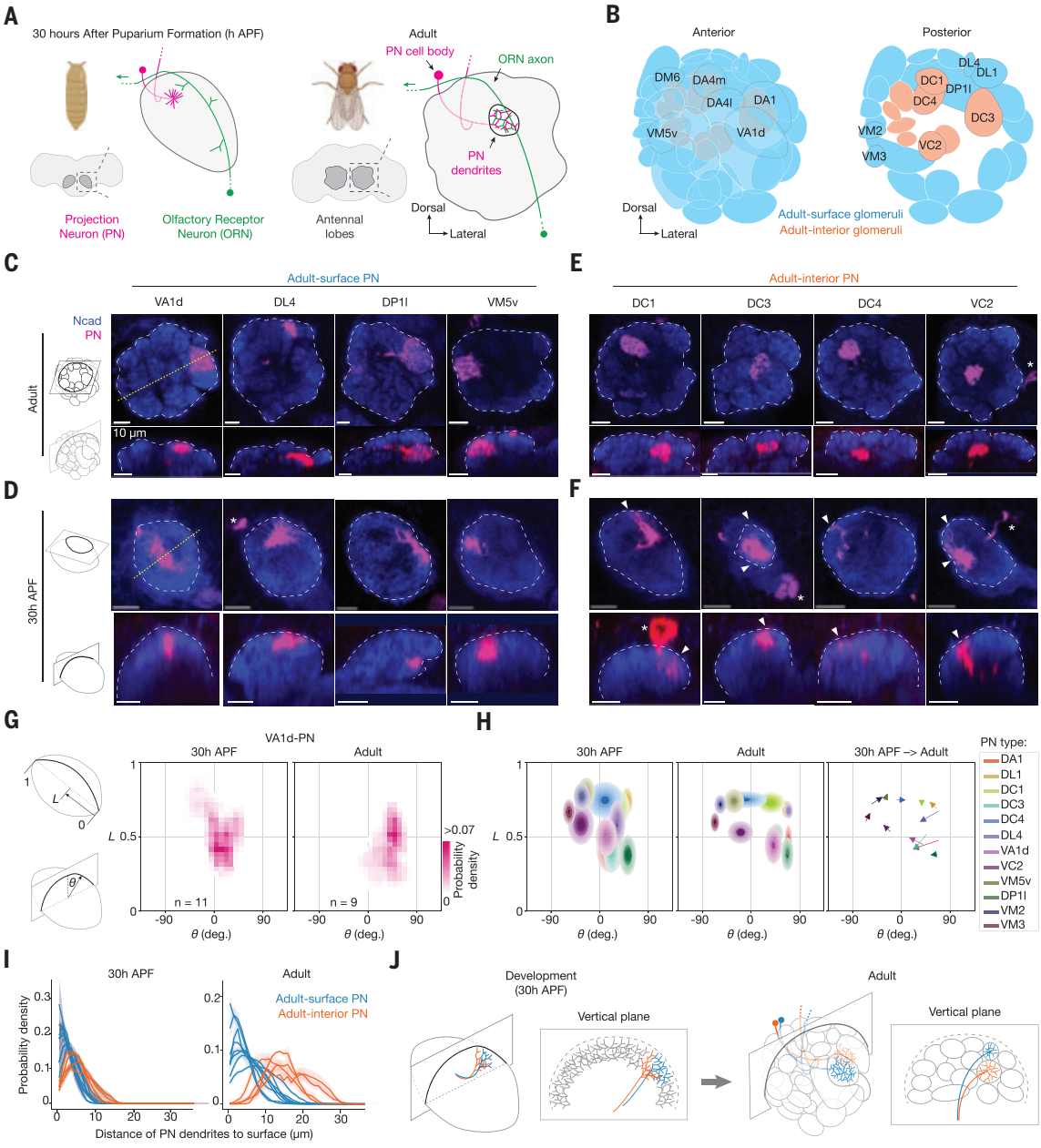

Fig. 1. During development, PN dendrites are exposed to the antennal lobe surface regardless of their position in adults. (**A**) *Drosophila* brain and antennal lobe schematics, at 30 hours APF (left) and in adults (right). Antennal lobes are highlighted in dark gray surrounded by dashed squares and are magnified to the right. At 30 hours APF, PN dendrites (magenta) innervate similar positions as in adults and ORN axons (green) navigate along the surface of the ipsilateral antennal lobe from an entry point at the bottom right toward the midline at the top left (green arrow). In adults, ORNs and PNs establish one-to-one connections in individual glomeruli that form a 3D glomerular map. (**B**) Adult antennal lobe schematic with ~50 glomeruli circled. Cyan represents glomeruli located at the surface of the antennal lobe; orange represents glomeruli located in the interior of the antennal lobe. (**C**) Optical sections showing dendrites of specific adult-surface PN types [magenta, labeled by a membrane-targeted green fluorescent protein (GFP) driven by separate genetic drivers specific to the PN types labeled above] viewed from the horizontal plane (top row) and the vertical plane (bottom row) of the antennal lobe in adults. White dashed lines outline the antennal lobe neuropil stained by the N-cadherin (Ncad) antibody (blue). Yellow dotted lines indicate the intersections with the vertical planes shown below. Vertical planes were reconstructed from 3D image volumes where optical sections were taken horizontally. The top and bottom rows show the same brains. (**D**) Same as (C), but with optical sections from 30 hours APF. (**E** and **F**) Same as (C) and (D), but for adult-interior PN types. In (F), arrowheads indicate PN dendrites extending to the antennal lobe surface; asterisks indicate PN cell bodies. In (C) to (F), scale bars are 10 µm. (**G**) Probability distribution of VA1d-PN dendritic pixels projected onto the antennal lobe surface during development (middle) and in adults (right). The 2D antennal lobe surface is flattened and decomposed into two axes: The *x* axis indicates the angle θ of each vertical plane, and the *y* axis indicates the position *L* along the long axis of the antennal lobe. A schematic definition of θ and *L* is on the left. For all genotypes, $n \geq 6$. (**H**) Probability distribution of dendritic pixels from 12 PN types projected onto the antennal lobe surface. In the left and middle panels, each ellipse corresponds to one PN type, with ellipse centers matching PN-dendrite centroids and ellipse boundaries matching the standard deviations of PN dendrites along the *x* and *y* axes, respectively. In the right panel, arrows represent how each centroid shift from 30 hours APF to adults; the color of the arrow corresponds to the ellipse in the left and middle panels. See fig. S1 for the sample number (*n*) of each group. (**I**) Probability distribution of the shortest distance in 3D space from PN dendritic pixels to the antennal lobe surface during development (left) and in adults (right). Each line represents data from an individual PN type, population mean ± SEM. (**J**) Schematics of two individual PN types during development (left) and in adults (right) viewed from +45° anterior and from a single vertical plane. Note that PN dendrites extend to the antennal lobe surface during development regardless of their surface or interior positions in adults. See table S1 for detailed genotypes.

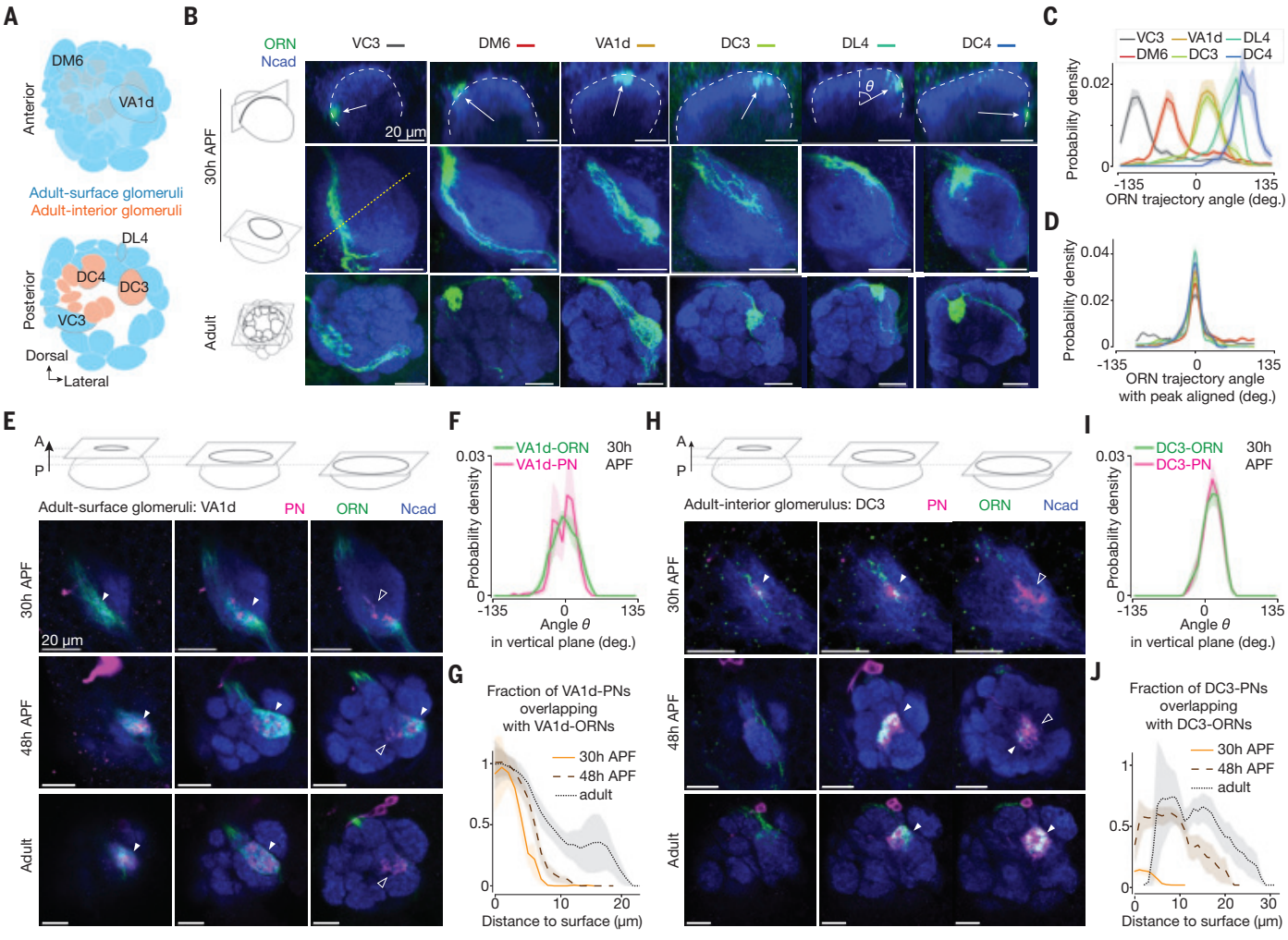

Fig. 2. During development, ORN axons take cell type–specific trajectories and contact cognate PN dendrites first on the antennal lobe surface. (**A**) Adult antennal lobe schematic highlighting six glomeruli, corresponding to the six ORN types shown in (B) to (D). (**B**) Single ORN types (green, labeled by a membrane-targeted GFP driven by separate genetic drivers) at 30 hours APF (top and middle rows, same brains) and in adults (bottom row). Shown in the top row are single optical sections from a vertical plane, with dashed lines outlining the antennal lobe neuropil stained for Ncad (blue). Vertical planes were reconstructed from 3D image volumes where optical sections were taken horizontally. Arrows point from the antennal lobe center to the average positions of ORN axons. Trajectory angle θ is defined in the DL4 panel. Shown in the middle and bottom rows are maximum projections of horizontal optical sections of antennal lobes at 30 hours APF and in adults, respectively. The yellow dotted line indicates the intersection with the vertical plane shown above. (**C**) Probability distribution of the axon's angular position from single-type ORNs at 30 hours APF. Data are population mean ± SEM. For all genotypes, $n \geq 9$. (**D**) Same as (C), but with each data curve aligned to its peak to minimize data variance between brains and more accurately reflect the width of the probability distribution. (**E**) Single optical section showing VA1d-ORNs (green, labeled by membrane-targeted GFP driven by a split-GAL4) and VA1d-PNs [magenta, labeled by membrane-targeted red fluorescent protein (RFP) driven by a split-LexA (*35*)]. Shown from left to right are anterior, middle, and posterior sections from the same brain, respectively. Filled arrowheads indicate examples where ORN axons and PN dendrites overlap; open arrowheads indicate examples where PN dendrites do not overlap with ORN axons. (**F**) Probability distribution of the angular position of VA1d-ORNs and VA1d-PNs. The definition of the angle θ is the same as in (C). Only vertical planes with PN dendrites were analyzed. Data are population mean ± SEM; $n = 9$. (**G**) Fraction of VA1d-PNs overlapping with VA1d-ORNs, as a function of the distance from PN pixels to antennal lobe surface. For a given distance on the *x* axis, a *y* value of 1 means that all the VA1d-PN dendrites within that distance bin match with VA1d-ORN axons. Data are population mean ± SEM. For all time points, $n \geq 8$. (**H** to **J**) Same as (E) to (G), respectively, but with data from DC3-ORNs and DC3-PNs. For all groups, $n = 12$. In (B), (E), and (H), scale bars are 20 μm. See table S1 for detailed genotypes.

Axons of each of the six ORN types we examined took a specific angular trajectory at 30 hours APF (Fig. 2, B to D), consistent with the positioning of their axonal tracts in adults. Some ORN types could have substantial trajectory overlaps, as observed in DC3-ORNs and VA1d-ORNs (specific ORN and PN types are named after the glomeruli they innervate, such as DC3 and VA1d). Axons from complementary ORN groups together covered the entire anterior surface of the antennal lobe (fig. S4). These findings are consistent with PN dendrites extending to specific locations at the antennal lobe surface during development and suggest that partner PN dendrites and ORN axons first meet on the 2D antennal lobe surface.

ORN axons first contact cognate PN dendrites at the antennal lobe surface

To test whether the precise locations of PN dendrites and ORN axons enable future synaptic partners to be near each other, we labeled individual ORN types and their cognate PN types with different markers in the same brain across developmental stages (Fig. 2, E and H). We observed that PN dendrites occupied a narrow angular range coinciding precisely with their cognate ORN axons (Fig. 2, F and I). For an adult-surface glomerulus, VA1d, ORNs first contacted PNs at the antennal lobe surface (Fig. 2, top row of E and orange curve in G) and maintained this into adulthood (Fig. 2, bottom rows

of E and black curves in G). For an adult-interior glomerulus, DC3, even though in adults the matching ORN axons and PN dendrites were interiorly located (Fig. 2, bottom rows of H and black curves in J), ORN axons also first contacted PN dendrites at the antennal lobe surface during development (Fig. 2, top row of H and orange curve in J).

These results suggest a working model in which individual ORN types and their cognate PNs first contact each other at the antennal lobe surface, regardless of their surface or interior positions in adults (Fig. 3A). We previously reported that two cell-surface proteins, Ten-m and Ten-a, instruct synaptic partner matching in adult-surface glomeruli through their matching expression patterns in cognate ORNs and PNs and homophilic attraction (*20*). Overexpressing Ten-m or Ten-a in adult-interior DC3-ORNs also caused mismatching phenotypes (fig. S5), suggesting that similar mechanisms are used for ORN-PN partner matching in adult-interior glomeruli. Because contact between cognate ORN and PN branches during development correlates with higher levels of filamentous actin, leading to stabilization of transient ORN axon branches (*15*), the overlaps we observed between ORN axon branches and PN dendrites at the surface could initiate synaptic partner matching. We further tested this using genetic perturbation experiments, as detailed in the next sections.

Adult-interior PNs leave more dendrites on the surface after missing cognate ORNs

If the surface-located branches from adult-interior PNs are expecting ORN partners during development, then a lack of ORN partners during development may cause these PN branches to stay at the surface, perhaps connecting with other ORN types (Fig. 3, A and B). We tested this hypothesis by genetically altering ORN trajectories in two different adult-interior glomeruli with available reagents (Fig. 3, C to K). Previous studies have shown that Sema-2b (*19*) and Toll-family proteins (*21*) are differentially expressed in ORN axons along the medial-lateral axis orthogonal to the trajectories that ORN axons take to navigate across the antennal lobe surface and also that Sema-2b instructs trajectory choice of ORN axons (*19*). Using genetic drivers that label different ORN types, we confirmed that manipulating Sema-2b and Toll expression could alter ORN trajectories during development (fig. S6). Therefore, in all the genetic perturbation experiments we performed, we rerouted specific ORN axons by combinatorially manipulating Sema-2b and Toll expression in specific ORN types.

In wild-type adults, DC4-ORN axons match DC4-PN dendrites near the center of the antennal lobe (Fig. 3D). After we experimentally rerouted most DC4-ORN axons during development, DC4-PNs no longer matched DC4-ORNs, and a portion of their dendrites remained at the

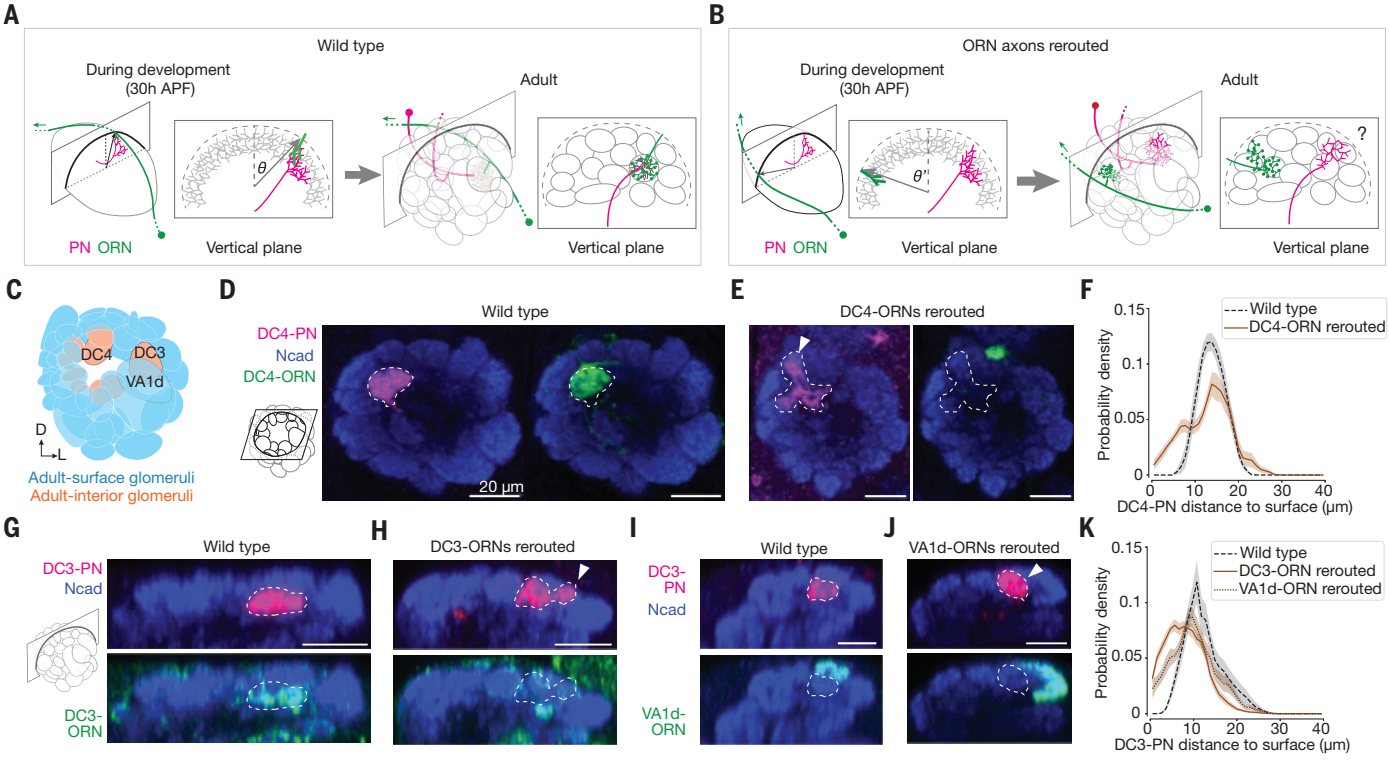

Fig. 3. Dendrites of adult-interior PNs remain at the antennal lobe surface in adults after rerouting cognate ORN axons during development. (**A**) Schematics of the same ORN-PN pair during development (left) and in adults (right). Note that DC3-ORN axons and DC3-PN dendrites are present at the antennal lobe surface during development but not in adults. (**B**) Same as (A), but with ORN axons largely rerouted and missing cognate PNs during development (left). This could lead to adult-interior PNs remaining at the surface in adults (right, indicated by a question mark). (**C**) Adult antennal lobe schematic labeling three glomeruli, corresponding to the three ORN-PN pairs shown in (D) to (J). D, dorsal; L, lateral. Some glomeruli were omitted for visualization clarity. (**D**) Single optical section of DC4-ORNs (green, labeled by membrane-targeted GFP driven by a split-GAL4) and DC4-PNs (magenta, labeled by membrane-targeted RFP driven by a split-LexA) in a wild-type brain. Dashed lines outline the boundaries of PN dendrites. (**E**) Same as (D), but with the trajectory of DC4-ORN axons changed through genetic manipulations (Toll-7 overexpression; fig. S6). The arrowhead indicates DC4-PNs innervating the antennal lobe surface. (**F**) Probability distribution of the distance from DC4-PN dendritic pixels to the antennal lobe surface in 3D space. Data are mean ± SEM. For all genotypes, $n \geq 6$. (**G** and **H**) Same as (D) and (E), but with DC3-ORNs and DC3-PNs shown in a vertical plane and a different genetic manipulation [*Toll-6* and *Toll-7* RNA interference (RNAi); fig. S6]. (**I** and **J**) Same as (G) and (H), but with the trajectory of VA1d-ORNs instead of DC3-ORNs changed through genetic manipulations (*Sema-2b* RNAi and *Toll-7* RNAi; fig. S6). (**K**) Same as (F), but with data from DC3-PNs upon the rerouting of axons from two ORN types. For all genotypes, $n \geq 11$. For (D), (E), and (G) to (J), scale bars are 20 μm. See table S1 for detailed genotypes.

antennal lobe surface in adults (Fig. 3, E and F, and fig. S7). We obtained similar findings for another adult-interior glomerulus, DC3 (Fig. 3, G, H, and K). With DC3-ORNs rerouted, some surface dendrites of DC3-PNs appeared postsynaptic to ORN axons innervating the surface VA1d glomerulus exterior to the DC3 glomerulus (fig. S8). Given that these rerouting experiments involved specific and small perturbations to the olfactory system, the inward movement of adult-interior PN dendrites is not likely to be caused passively by global antennal lobe morphogenesis but rather requires interactions of PN dendrites with their cognate ORN axons.

To examine the nature of the force that drives this inward movement, we genetically rerouted axons of VA1d-ORNs, which target the VA1d glomerulus external to the DC3 glomerulus (Fig. 3, C and I, and fig. S7). This rerouting also caused DC3-PN dendrites to remain at the antennal lobe surface in adults (Fig. 3, J and K, and fig. S7). This nonautonomous effect from manipulating neighboring glomeruli suggests that axons and dendrites of adult-interior ORNs and PNs are pushed inward by neurites from nearby adult-surface glomeruli.

The accuracy of ORN-PN matching correlates with the accuracy of ORN trajectories

Our results thus far suggest a model in which the dimensionality of partner selection for each ORN type can be further reduced from two dimensions to one dimension: Each ORN type only searches for synaptic partners within a 1D narrow stripe near its axon trajectory (fig. S9). To further test this model, we examined how the accuracy of the ORN axon trajectory affects the accuracy of ORN-PN partner matching. If each ORN type only searches within the vicinity of its trajectory, then changing its trajectory should impair ORN-PN partner matching, with the degree of trajectory deviation determining the degree of mismatching. Using genetic drivers that label specific ORN types across developmental stages, we performed genetic manipulations in specific ORN types and altered their trajectories to different degrees in both directions during development. We then labeled cognate ORNs and PNs with distinct markers in the same adult brain and calculated the fraction of ORN axons that overlaps with dendrites of cognate PNs as a measure for the accuracy of ORN-PN partner matching (Fig. 4).

Taking the VA1d-ORNs as an example (Fig. 4, A to D), we used three genetic manipulation strategies that combinatorially manipulated the expression of Sema-2b and the Toll proteins in VA1d-ORNs to alter the ORN trajectories during development to three different distributions deviating from the wild-type distribution (Fig. 4, top row of A, and B and C). In adults, we observed different degrees of mismatching between the VA1d-ORNs and VA1d-PNs (Fig. 4, bottom rows of A, and D). We repeated this type of experiment in three other ORN types and observed similar results (Fig. 4, E to P).

Manipulating the expression of Sema-2b and the Toll proteins may affect not only ORN axon trajectories but also other processes that might influence ORN-PN partner matching. The following evidence suggests that the ORN-PN mismatching we observed is largely due to the change of ORN trajectories. In all cases, the portion of ORNs that mismatched with cognate PNs in adults were likely the portion of ORNs whose axons deviated from the wild-type position during development. For example, a comparison of "Manipulation #1" with "Wild type" (first two columns of Fig. 4A) shows that the VA1d-ORN trajectory partly deviated counterclockwise during development (top row of Fig. 4A); in adults, the VA1d-ORNs that mismatched with VA1d-PNs also moved counterclockwise (appearing to move leftward in the lower rows). The fact that data from all the manipulation conditions followed this trend strongly suggests that synaptic partner matching is most likely due to trajectory changes rather than other effects caused by the change in Sema-2b or Toll protein expression (which presumably happens in all manipulated ORN axons, whether the trajectory is changed or not).

Furthermore, when grouping all the data, we observed a strong positive correlation between the accuracy of ORN axon trajectories during development and the accuracy of ORN-PN matching in adults (Fig. 4Q), indicating that the further ORN axons deviate from their normal positions, the more severe the ORN-PN mismatch that occurs. These data support the model that each ORN axon searches for synaptic partners within a narrow stripe near its axon trajectory on the antennal lobe surface, approximating a 1D space (fig. S9).

Discussion

In this work, we discovered that the repeated use of the dimensionality reduction principle simplifies the synaptic partner matching problem in the assembly of the fly olfactory circuit: For each ORN type, instead of selecting 1 out of 50 PN types in a 3D volume, the ORN only needs to select one out of a few PN types along a 1D trajectory (fig. S9). A linchpin of this work has been the collection of genetic drivers that label many individual PN and ORN types across development. Although single–cell type labeling in the adult fruit fly is becoming routine (*22*, *23*), genetic drivers that consistently label specific cell types across development are more difficult to generate because of the dynamic nature of gene expression throughout development. Our work shows that such drivers, once generated, allow systematic examination of the same neurons at high resolution across development. This led to the discovery of PN dendrite surface extension and the coincidence of partner PN dendrites and ORN axons at the surface, two key bases for our model. These drivers also allowed us to simultaneously manipulate the expression of multiple genes in specific cell populations across development to test the model. Our dataset included glomeruli innervated by ORNs from both antenna and maxillary palp, which reach the antennal lobe at different times (*24*); it also included glomeruli innervated by PNs that contribute to only the adult antennal lobe and to both larval and adult antennal lobes (*25*). Thus, dimensionality reduction likely applies generally to the fly olfactory system. A systematic approach of generating cell type–specific drivers throughout development (*26*) can propel mechanistic understandings of more developmental processes.

In principle, searching for synaptic partners in a lower-dimensional space reduces simultaneous choices at any given time and thus could increase wiring accuracy and robustness. Indeed, some circuits are apparently organized following the dimensionality reduction principle, as exemplified by the distribution of glomeruli on the surface of the vertebrate olfactory bulb. In other circuits where synaptic targets are seemingly distributed in 3D space, as in the fly antennal lobe, the dimensionality reduction principle may nevertheless apply. For example, in the fly optic lobe and vertebrate retina, target selection across different layers often occurs within a 1D columnar structure (*8*, *9*), which, in some cases, is followed by a 2D search of synaptic partners within a specific layer (*10*). Further, axons of a specific retinal ganglion cell type connect with their target in the correct retinotopic position and a specific sublayer in the superior colliculus (*27*, *28*). During development, retinal ganglion cell axons could divide the 3D search task to a 2D retinotopic mapping with a 1D search for a specific sublayer. Lastly, axons of callosal projecting neurons in the mammalian cortex not only target appropriate cortical areas in the contralateral hemisphere but also terminate at specific layers (*29*, *30*). During development, these axons first navigate via the corpus callosum to appropriate cortical areas before ascending to specific layers (*29*, *31*), converting a 3D target-selection problem into sequential 2D and 1D problems. Thus, dimensionality reduction might be a widely used strategy for selecting synaptic partners in developing nervous systems.

What molecular mechanisms might be involved in executing the dimensionality reduction strategy? As is evident from the fly olfactory circuit, a coordinated patterning of pre- and postsynaptic partners is required. First, PNs must target dendrites to type-specific 2D

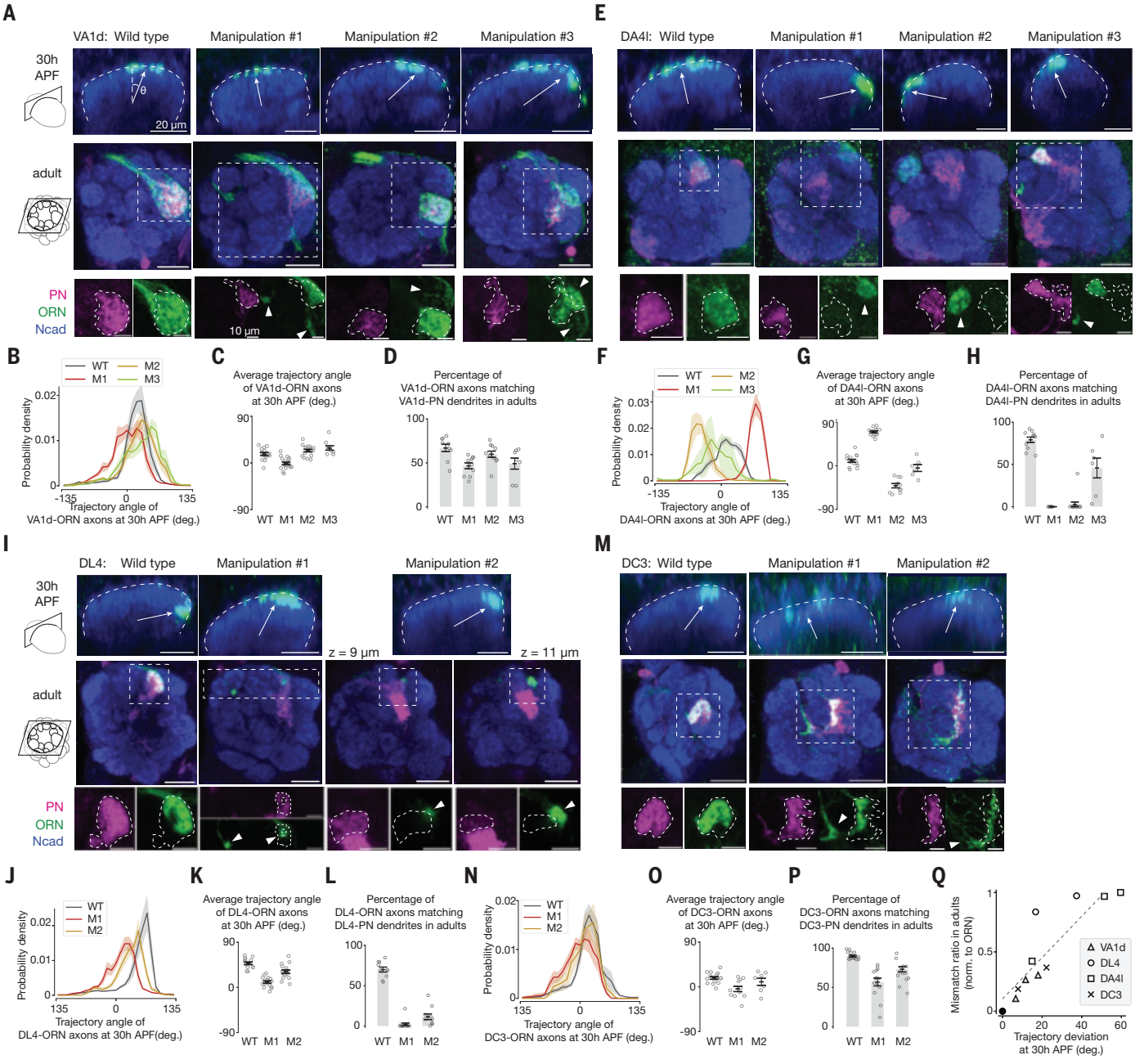

Fig. 4. The accuracy of ORN-PN synaptic partner matching correlates with the accuracy of ORN trajectories. (**A**) Single optical sections showing VA1d-ORN axons from a vertical view during development (top) and horizontal view in adult (middle and bottom). In the top row, dashed lines outline the antennal lobe neuropil. Arrows point from the antennal lobe center to the average positions of ORN axons. Images in the bottom row are magnified views of the regions enclosed by the dashed squares in the middle row. In the bottom row, dashed lines outline the boundary of PN dendrites. Arrowheads indicate ORN axons mismatching with cognate PN dendrites. The three manipulation conditions are (1) *Sema-2b* RNAi, (2) *Toll-7* RNAi, and (3) *Sema-2b* RNAi and *Toll-7* RNAi. (**B**) Probability distribution of the angular position of VA1d-ORN axons in each condition at 30 hours APF. Data are population mean ± SEM. For all genotypes, $n \geq 6$. WT, wild type; M, manipulation condition. (**C**) Average angular position of VA1d-ORN axons in each condition. Data are the same as in (B). Circles indicate the averages of individual antennal lobes; bars indicate the population mean ± SEM. (**D**) Percentage of VA1d-ORN axons overlapping with VA1d-PN dendrites in adults. Circles indicate the average of individual antennal lobes; bars indicate the population mean ± SEM. (**E** to **H**) Same as (A) to (D), respectively, but for DA4l-ORNs and DA4l-PNs. The three manipulation conditions are (1) *Sema-2b* RNAi; (2) *Toll-6* RNAi, *Toll-7* RNAi, and Sema-2b overexpression; and (3) *Toll-6* RNAi and *Toll-7* RNAi. Note that owing to reagent limitations, the ORN signals from the top row result from a combination of three ORN types: DA4l, DA4m, and DC1, all of which take a similar trajectory (fig. S3). (**I** to **L**) Same as (A) to (D), respectively, but for DL4-ORNs and DL4-PNs. The two manipulation conditions are (1) Sema-2b overexpression and (2) *Toll-6* RNAi, *Toll-7* RNAi, and Sema-2b overexpression. (**M** to **P**) Same as (A) to (D), respectively, but for DC3-ORNs and DC3-PNs. The two manipulation conditions are (1) *Toll-7* RNAi and (2) *Toll-7* RNAi and *Sema-2b* RNAi. (**Q**) Percentage of ORN-PN mismatch in adults as a function of the absolute angular changes in ORN axon trajectory at 30 hours APF, with each manipulation condition represented by a data point. Only the population means are shown. The black dot indicates wild type in each ORN type, which is the origin ($x = 0, y = 0$) in the plot by definition. The dashed line indicates the linear fit. The Pearson correlation coefficient is equal to 0.88; $p = 3.6 \times 10^{-4}$. Note that DL4 deviates most from the linear fit; this is likely to be because the DL4 glomerulus is in the middle of the DL4-ORN axon trajectory and is thus more sensitive to trajectory angle changes (than glomeruli located near the ORN axon entry point before axons with different trajectories fully diverge). In (A), (E), (I), and (M), scale bars are 20 μm in the first and second rows and 10 μm in the third row. See table S1 for detailed genotypes.

areas of the antennal lobe surface. Semaphorins and leucine-rich-repeat cell-surface proteins have been shown to instruct global targeting and local segregation of PN dendrites, respectively (*32*–*34*). We do not know what mechanisms ensure that all PN types extend at least part of their dendrites to the antennal lobe surface or what causes PN dendrites and ORN axons that target interior glomeruli to descend after they first contact each other at the surface. Our rerouting experiments suggest that the latter process likely involves competition with neurites from neighboring glomeruli. Second, ORN axons must choose type-specific trajectories according to their types. Sema-2b plays an instructive role (*19*) and we further implicated Toll receptors in this study, but more molecules are likely required to fully specify ORN axon trajectories. Third, along the chosen 1D trajectory, ORN axons must select dendrites from one out of several PN types to form synaptic connections. Homophilic attraction molecules such as teneurins play a role in this process (*15*, *20*), but more molecules are likely involved. We note that the dimensionality reduction strategy also enables combinatorial use of wiring molecules; for example, synaptic partner–matching molecules can be combined with different trajectory-selection molecules so that they can be reused along spatially segregated 1D trajectories. Finally, all of the wiring molecules we have discussed are evolutionarily conserved from invertebrates to mammals, raising the possibility that they also contribute to executing the dimensionality reduction strategy in the wiring of the more complex mammalian brain.

REFERENCES AND NOTES

1. J. G. White, E. Southgate, J. N. Thomson, S. Brenner, *Philos. Trans. R. Soc. London Ser. B* **314**, 1–340 (1986).
2. K. L. Briggman, M. Helmstaedter, W. Denk, *Nature* **471**, 183–188 (2011).
3. S. Loomba *et al.*, *Science* **377**, eabo0924 (2022).
4. P. Schlegel *et al.*, *Nature* **634**, 139–152 (2024).
5. S. Dorkenwald *et al.*, *Nature* **634**, 124–138 (2024).
6. B. J. Dickson, *Science* **298**, 1959–1964 (2002).
7. A. L. Kolodkin, M. Tessier-Lavigne, *Cold Spring Harb. Perspect. Biol.* **3**, a001727–a001727 (2011).
8. J. R. Sanes, S. L. Zipursky, *Neuron* **66**, 15–36 (2010).
9. J. R. Sanes, S. L. Zipursky, *Cell* **181**, 536–556 (2020).
10. E. Agi *et al.*, *Science* **383**, 1084–1092 (2024).
11. G. S. X. E. Jefferis *et al.*, *Development* **131**, 117–130 (2004).
12. K. K. L. Wong *et al.*, *eLife* **12**, e85521 (2023).
13. M. Okumura, T. Kato, M. Miura, T. Chihara, *Genes Cells* **21**, 53–64 (2016).
14. T. Li *et al.*, *Cell* **184**, 5107–5121.e14 (2021).
15. C. Xu *et al.*, *Cell* **187**, 5081–5101.e19 (2024).
16. K. Mori, H. Sakano, *Annu. Rev. Neurosci.* **34**, 467–499 (2011).
17. H. Luan, N. C. Peabody, C. R. Vinson, B. H. White, *Neuron* **52**, 425–436 (2006).
18. K. G. Golic, S. Lindquist, *Cell* **59**, 499–509 (1989).
19. W. J. Joo, L. B. Sweeney, L. Liang, L. Luo, *Neuron* **78**, 673–686 (2013).
20. W. Hong, T. J. Mosca, L. Luo, *Nature* **484**, 201–207 (2012).
21. A. Ward, W. Hong, V. Favaloro, L. Luo, *Neuron* **85**, 1013–1028 (2015).
22. L. Tirian, B. J. Dickson, bioRxiv 198648 [Preprint] (2017); https://doi.org/10.1101/198648.
23. G. W. Meissner *et al.*, *eLife* **12**, e80660 (2023).
24. L. B. Sweeney *et al.*, *Neuron* **53**, 185–200 (2007).
25. E. C. Marin, R. J. Watts, N. K. Tanaka, K. Ito, L. Luo, *Development* **132**, 725–737 (2005).
26. Y. D. Chen *et al.*, *Proc. Natl. Acad. Sci. U.S.A.* **120**, e2307451120 (2023).
27. D. A. Feldheim, D. D. M. O'Leary, *Cold Spring Harb. Perspect. Biol.* **2**, a001768–a001768 (2010).
28. I.-J. Kim, Y. Zhang, M. Meister, J. R. Sanes, *J. Neurosci.* **30**, 1452–1462 (2010).
29. S. P. Wise, E. G. Jones, *J. Comp. Neurol.* **168**, 313–343 (1976).
30. S. Pal, J. W. C. Lim, L. J. Richards, *Curr. Opin. Neurobiol.* **84**, 102837 (2024).
31. J. Zhou *et al.*, *Proc. Natl. Acad. Sci. U.S.A.* **110**, E2714–E2723 (2013).
32. T. Komiyama, L. B. Sweeney, O. Schuldiner, K. C. Garcia, L. Luo, *Cell* **128**, 399–410 (2007).
33. W. Hong *et al.*, *Nat. Neurosci.* **12**, 1542–1550 (2009).
34. L. B. Sweeney *et al.*, *Neuron* **72**, 734–747 (2011).
35. C. Y. Ting *et al.*, *Genetics* **188**, 229–233 (2011).

ACKNOWLEDGMENTS

We thank the labs of G. Rubin, N. Perrimon, Y. Aso, T. Lee, and T. Chihara; the Bloomington *Drosophila* Stock Center, the Vienna *Drosophila* Resource Center, and the Kyoto *Drosophila* Stock Center for fly stocks; H. Dionne and G. Rubin for many enhancer plasmids; K. Shen and H. Deng for their generous help with super-resolution microscopy; and S. Block and J. Luo, as well as members of the Luo laboratory, especially D. Paderick and T. Hindmarsh Sten, for helpful discussions. **Funding:** This work was supported by National Institutes of Health grant R01-DC005982 (to L.L.). C.L. was supported by the Stanford Science Fellows Program. L.L. is a Howard Hughes Medical Institute investigator. **Author contributions:** C.L., Z.L., and L.L. conceived the project. C.L. and Z.L. performed all of the experiments and analyzed the data. C.L., Z.L., and L.L. jointly interpreted the data and decided on new experiments. C.X. and K.K.L.W. assisted in cloning and immunostaining. D.J.L., K.K.L.W., C.N.M., Q.X., T.L., and H.L. assisted in the generation of transgenic flies. C.L., Z.L., and L.L. wrote the paper, with input from all other co-authors. L.L. supervised the work. **Competing interests:** The authors declare that they have no competing interests. **Data and materials availability:** All data are included in the manuscript or the supplementary materials.

SUPPLEMENTARY MATERIALS

science.org/doi/10.1126/science.ads7633
Materials and Methods; Figs. S1 to S9; Table S1; References (*36*–*43*); MDAR Reproducibility Checklist

Submitted 27 August 2024; resubmitted 30 December 2024; accepted 20 February 2025

10.1126/science.ads7633

STRUCTURAL BIOLOGY

Cryo-EM reveals mechanisms of natural RNA multivalency

Liu Wang[1,2]†, Jiahao Xie[3]†, Tao Gong[1]†, Hao Wu[4,5]†, Yifan Tu[6]†, Xin Peng[6]†, Sitong Shang[6]†, Xinyu Jia[1]†, Haiyun Ma[1]†, Jian Zou[1]†, Sheng Xu[4,5]†, Xin Zheng[1,2]†, Dong Zhang[6]†, Yang Liu[7]†, Chong Zhang[1], Yongbo Luo[1], Zirui Huang[1], Bin Shao[1], Binwu Ying[7], Yu Cheng[8], Yingqiang Guo[9], Ying Lai[1], Dingming Huang[1,2], Jianquan Liu[6], Yuquan Wei[1], Siqi Sun[4,5]*, Xuedong Zhou[1,2]*, Zhaoming Su[1]*

Homo-oligomerization of biological macromolecules leads to functional assemblies that are critical to understanding various cellular processes. However, RNA quaternary structures have rarely been reported. Comparative genomics analysis has identified RNA families containing hundreds of sequences that adopt conserved secondary structures and likely fold into complex three-dimensional structures. In this study, we used cryo–electron microscopy (cryo-EM) to determine structures from four RNA families, including ARRPOF and OLE forming dimers and ROOL and GOLLD forming hexameric, octameric, and dodecameric nanostructures, at 2.6- to 4.6-angstrom resolutions. These homo-oligomeric assemblies reveal a plethora of structural motifs that contribute to RNA multivalency, including kissing-loop, palindromic base-pairing, A-stacking, metal ion coordination, pseudoknot, and minor-groove interactions. These results provide the molecular basis of intermolecular interactions driving RNA multivalency with potential functional relevance.

Symmetric assembly in macromolecular complexes frequently underlies the core of biological processes and functions (*1*, *2*). Homo-oligomerization of multiple identical subunits through a network of intermolecular interactions forms higher-order quaternary structures that acquire distinctive features such as increased stability, allosteric regulation, and multivalent and cooperative interactions (*2*). These homomers have been predicted to occur in 50% of proteins (*2*, *3*), forming structures including chaperonins and viral capsids in dihedral and cubic symmetry with a large central cavity as well as cytoskeleton filaments in helical symmetry (*2*). Impairment of homo-oligomerization is implicated in disease (*4*, *5*).

RNAs fold into intricate tertiary structures to play critical regulatory roles in numerous biological processes (*6*). However, although protein homomers are ubiquitous across all life domains, the oligomeric quaternary structures of natural RNA sequences have not been well characterized (*7*, *8*). The predominantly observed RNA multimers are homodimers, enabled primarily by kissing-loop (KL) and complementary (including palindromic) base-pairing interactions and occasionally by tertiary interactions such as minor-groove, A-stacking, and pseudoknot (PK) interactions (*8*). A recent study has also reported the dimerization of large group II introns through such interactions (*9*). Although these structural motifs have been widely used for higher-order assembly in RNA nanotechnology (*10*), the only natural RNA homomer structure consisting of more than two protomers is the φ29 prohead RNA (*11*), which was shown to assemble into a four-membered ring in crystalline conditions (*12*) and a five-membered ring in the context of the φ29 phage packaging motor (*13*). The leading factor that limits our understanding of RNA quaternary interactions is the challenge posed to RNA three-dimensional structure determination, highlighted by orders of magnitude fewer depositions of RNA structures in the Protein Data Bank (PDB) compared with proteins (*14*). This paucity largely prompts the insufficient accuracy of RNA structure predictions in contrast to that of proteins (*15*, *16*).

The RNA families database (Rfam) has classified thousands of RNA families on the basis of multiple sequence alignment (MSA) and covariance models of conserved secondary structures (*17*). Aside from families with well-characterized functions and structures, more RNA families are constantly being discovered by comparative genomic analysis, yet their structures and functions remain mostly unexplored (*18*, *19*). Here, we focus on four RNA families with uncharacterized structures: ARRPOF (area required for replication in a plasmid of *Fusobacterium*), OLE (ornate, large, and extremophilic), ROOL (rumen-originated, ornate, large), and GOLLD (giant, ornate, lake- and Lactobacillales-derived). ARRPOF is predicted to perform functions related to plasmid replication and regulation (*19*), OLE participates in bacterial cell growth under extreme conditions such as cold or alcohol stress (*20*), and ROOL and GOLLD are frequently associated with prophages and reside close to tRNAs either in the chromosomes or plasmids (*21*).

Single-particle cryo–electron microscopy (cryo-EM) has recently emerged as a powerful method to study protein-free RNA structures with heterogeneous conformations and compositions (*22*). We selected sequences from bacteria with characterized functions in ARRPOF, OLE, ROOL, and GOLLD RNA families, which are predicted to form complex tertiary structures, whose functions could be further explored. Cryo-EM structures determined at 2.6- to 4.6-Å resolutions reveal quaternary assemblies of all these RNAs through conserved intermolecular interfaces and elucidate molecular mechanisms of RNA multivalency.

ARRPOF forms a homodimer and adopts two conformations by swapping the 3′ domain

ARRPOF has been shown by comparative genomics analysis to adopt a conserved secondary structure (*19*). The sequence is present in the pKH9 plasmid from *Fusobacterium nucleatum* (*Fnu*) identified in an earlier study, which showed that the truncated plasmids, while still retaining the ARRPOF sequence but lacking a predicted *rep* (replication) gene, could still replicate (*23*), suggesting that ARRPOF might play a role in plasmid replication (*19*). We carried out in vitro transcription, denatured gel purification, and subsequent refolding to prepare RNAs for cryo-EM structure determination (*22*). Cryo-EM reconstructions revealed that the 255-nucleotide (255-nt) *Fnu* ARRPOF assembles into a homodimer and adopts two alternative conformations with swapped 3′ domains, determined at 3.9- and 4.0-Å resolutions (Fig. 1, A and B; fig. S1; and table S1).

ARRPOF adopts eight consecutive paired stems (P1 to P8) from 5′ to 3′ end that form a three-way junction (3WJ) and a four-way junction (4WJ) (Fig. 1C and fig. S2). In conformation 1, the 5′ end starts with two intermolecular complementary base pairings, P9 and P10, with L6 (L denotes loop) and the 5′ leader of the other protomer (Fig. 1, D and E). P10 is followed by the 3WJ and two intramolecular PKs

[1]The State Key Laboratory of Biotherapy, National Clinical Research Center for Geriatrics, West China Hospital; The State Key Laboratory of Oral Diseases, National Clinical Research Center for Oral Diseases, National Center for Stomatology, West China Hospital of Stomatology, Sichuan University, Chengdu, China. [2]Department of Cariology and Endodontics, West China Hospital of Stomatology, Sichuan University, Chengdu, China. [3]Mingle Scope (Chengdu), Chengdu, China. [4]Research Institute of Intelligent Complex Systems, Fudan University, Shanghai, China. [5]Shanghai Artificial Intelligence Laboratory, Shanghai, China. [6]The Key Laboratory for Bio-resources and Eco-environment of Ministry of Education, College of Life Sciences, Sichuan University, Chengdu, China. [7]Department of Laboratory Medicine, West China Hospital, Sichuan University, Chengdu, China. [8]Department of Computer Science and Engineering, The Chinese University of Hong Kong, Shatin, New Territories, Hong Kong, China. [9]Cardiovascular Surgery Research Laboratory, Department of Cardiovascular Surgery, West China Hospital, Sichuan University, Chengdu, China.
***Corresponding author. Email: zsu@wchscu.cn (Z.M.S.); zhouxd@scu.edu.cn (X.D.Z.); siqisun@fudan.edu.cn (S.Q.S.)** †These authors contributed equally to this work.

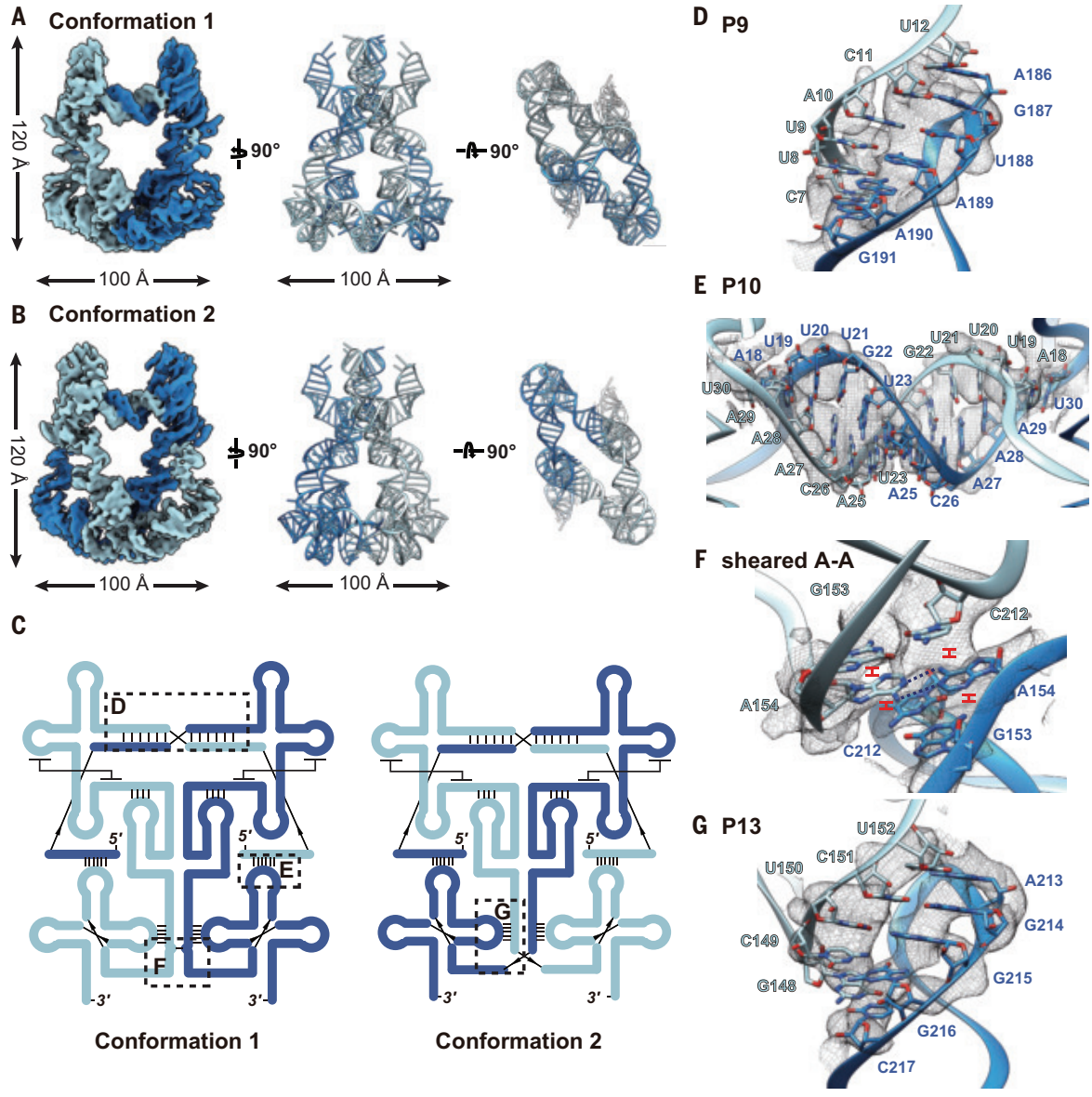

Fig. 1. Cryo-EM structures reveal alternative conformations and intermolecular interfaces of ARRPOF dimer. (**A** and **B**) Overall cryo-EM density maps and models at 5.0σ threshold of conformation 1 (A) and conformation 2 (B) with the 3′ domain P5-P8 swapped to the other side. (**C**) Projected secondary structures in cartoon of conformations 1 and 2 with designated tertiary interactions. (**D** to **G**) Cryo-EM density maps and models of intermolecular interfaces of P9 in both conformations (D), P10 (E), and sheared A-A base pair stacked by P13 from both protomers (F) in conformation 1 and junction-loop interaction P13 in conformation 2 (G), all at 2.0σ threshold.

formed between J3/4 (J denotes a junction between paired regions) and L2 and L4, namely P11 and P12, before reaching P4 (fig. S2, A to C). Following P4 is the intramolecular PK P13 between J4/5 and L7 that stacks on an intermolecular sheared A-A pair (Fig. 1F), after which the remaining 3′ domain consisting of the 4WJ swaps to the opposite side in conformation 2 (movie S1). All tertiary interactions have been found by comparative genomics analysis to be conserved (*19*), including the intermolecular palindromic P10 observed in the cryo-EM structures (fig. S2A). The sheared A-A pair is not conserved, implying that those sequences lacking this A-A pair and adjacent stacking interactions may only adopt conformation 2 (Fig. 1C), in which P9 is intramolecular and P13 is intermolecular (Fig. 1G).

OLE assembles into a homodimer for protein interactions

A recent surge of notable structural and functional studies has demonstrated that OLE RNA binds to proteins and forms ribonucleoprotein (RNP) complexes to participate in a wide range of fundamental processes in bacteria such as cell growth, stress response, and replication (*20*). OLE colocalizes with OapA (OLE-associated protein A) at the cell membrane, whose coding region is located in tandem of *ole* in the gene cluster (*24*). OapB and OapC also directly bind to OLE (*25*, *26*), and impaired OLE RNP function makes bacterial cells more sensitive to unconventional conditions such as cold temperatures, alcohols (*27*), and magnesium ions (*28*).

We determined the 2.6-Å-resolution cryo-EM structure of the OLE (578-nt) dimer from *Clostridium botulinum* (*Cbo*) (Fig. 2A, fig. S3, and table S1), a pathogen known to produce a lethal neurotoxin that causes botulism and muscle paralysis, which has been used in cosmetic dermatology to induce facial muscle paralysis (*29*). The *Cbo* OLE contains 15 conserved paired stems (P1 to P15) (*24*), but the cryo-EM density only accounts for P3 to P9.3, including the preformed protein binding sites for OapA (*24*), OapC (*26*), and ribosomal protein RpsU (*20*) (Fig. 2A).

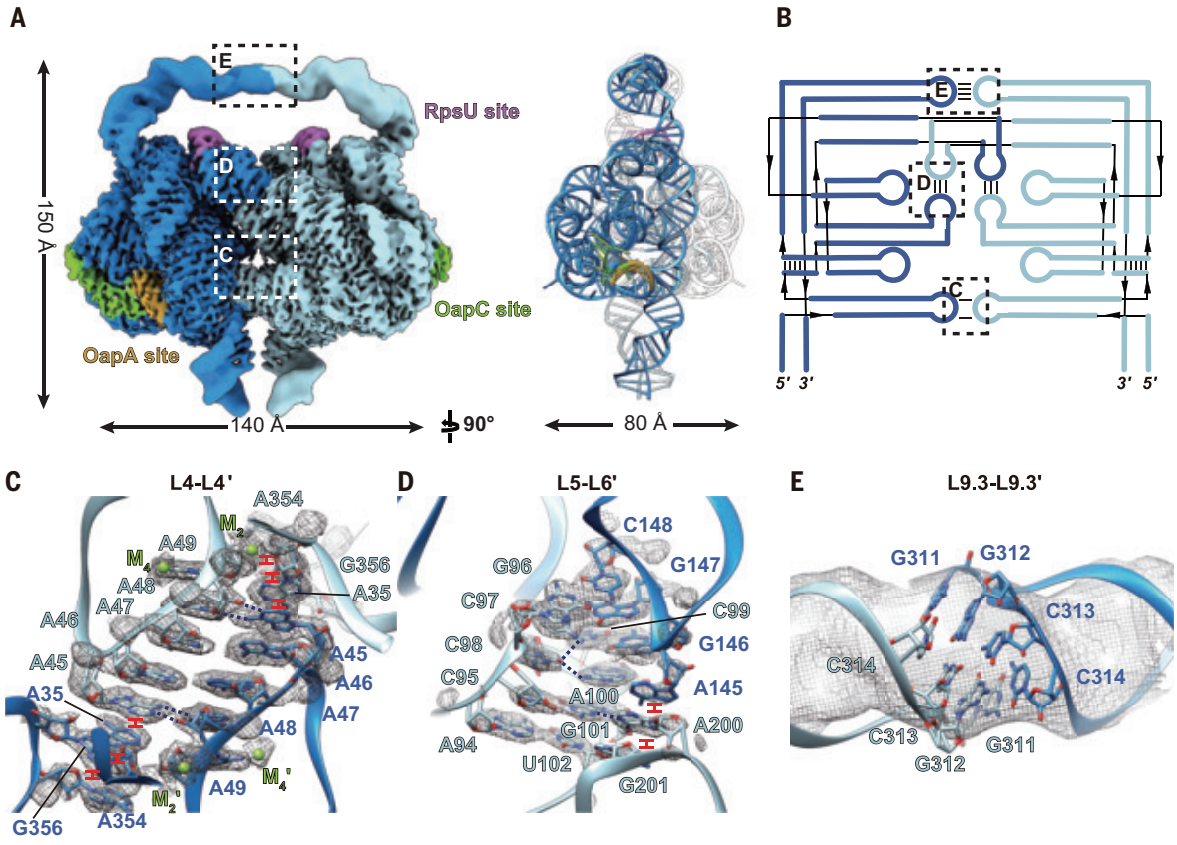

Fig. 2. Cryo-EM structures reveal intermolecular A-stacking and KL interactions of OLE dimer. (**A**) Cryo-EM density map and model of OLE dimer at 3.0σ threshold. (**B**) Projected secondary structure in cartoon with designated intermolecular interactions. (**C** to **E**) Cryo-EM density maps and models of intermolecular interfaces of A-stacking interactions between L4 and L4′ at 1.0σ threshold (C), KL interaction between L5 and L6′ (D), and KL interaction between L9.3 and L9.3′ at 2.0σ threshold (E). Blue dashed lines indicate hydrogen bonds of noncanonical interactions, and red labels indicate stacking.

The P3–P9.3 domain forms an intramolecular PK between J4/5 and J8/9 (fig. S2, D and E) and assembles into a homodimer through three intermolecular interactions (Fig. 2B and movie S2), including the continuous A-stacking and sheared A-A pairs between L4 in each protomer (Fig. 2C) and two KL interactions between L5 and L6 (Fig. 2D) and L9.3 in each protomer (Fig. 2E). Comparative genomics analysis indicates that all intermolecular interactions are highly conserved in primary sequence, suggesting that the dimeric form is likely critical for OLE function. The remaining stems were not resolved owing to high flexibility, which could potentially be stabilized upon binding to OapB as previously reported (*25*).

Cryo-EM reveals multimerization interfaces and different assembly mechanisms of ROOL RNAs

ROOL RNAs are usually associated with bacteriophages and are located close to tRNA genes (*21*), which have been primarily identified in *Lactobacillus* and *Enterococcus*. Recent studies have reported that *Enterococcus faecalis* (*Efa*) strains carrying ROOL in their chromosomes have been found in red tilapia and the international space station (*30*, *31*), whereas megaplasmid-encoded ROOL in *Lactobacillus salivarius* (*Lsa*) had unusually abundant expression levels that exceeded 16*S* ribosomal RNA (rRNA) in the late stationary phase in some strains (*32*).

We observed cage-like particles under cryo-EM directly after in vitro transcription of both *Efa* and *Lsa* ROOL RNAs (figs. S4 and S5), indicating that these RNAs could form quaternary assemblies under native cotranscriptional folding conditions (*22*). Cryo-EM reconstructions of *Efa* ROOL (580-nt) yielded monomer, homotetramer, and dihedral homooctamer at 3.1-, 4.7-, and 3.8-Å resolutions, respectively, whereas the cryo-EM structure of *Lsa* ROOL (526-nt) showed a dihedral homohexamer at 3.1-Å resolution (Fig. 3, A and B; figs. S4 and S5; and table S1). The density of *Efa* ROOL monomer allowed modeling of roughly half of the RNA sequence, suggesting that the remaining unresolved regions are highly dynamic. These dynamic regions are all present in the tetramer and octamer, stabilized by intermolecular interactions in the quaternary structures, allowing modeling of the entire ROOL RNA (fig. S6A). The *Lsa* ROOL monomer from the homohexamer adopts almost identical architecture (fig. S6B) and was modeled by substitution of the *Efa* ROOL sequence.

Both Efa and Lsa ROOL RNAs adopt conserved secondary structures containing 16 paired stems (P1 to P16), five multiway junctions, and four intramolecular tertiary interactions (fig. S6, A and B). The four intramolecular interactions include a tetraloop/tetraloop receptor (TL/TLR) interaction between P2 and L5 (fig. S6C), an A-stacking interaction between L6 and P8 (fig. S6D), and two PKs, between J9/12 and L13 and L13 and P15 (fig. S6, E and F). Five additional intermolecular interactions are observed in both ROOL assemblies (fig. S6, G to K, and movies S3 and S4). Three interfaces are within the same plane of the dihedral assemblies, including two 3-bp (base pair) loop-bulge interactions, between L2 and L13′ and J11/9 and L11′ (the prime symbol denotes the structural motif from the adjacent protomer in the same plane), and one minor-groove interaction, between L12 and P3′ (Fig. 3, E to G). The dihedral complexes are assembled through two interplanar interactions, a minor-groove A-stacking interaction between L14 and P7″ (the double prime symbol denotes the structural motif from the protomer in the opposite plane) and a 4-bp KL between L15 and L15″ (Fig. 3, H and I). Whereas all intermolecular base pairs are conserved, as shown by covariation analysis, interplanar interfaces

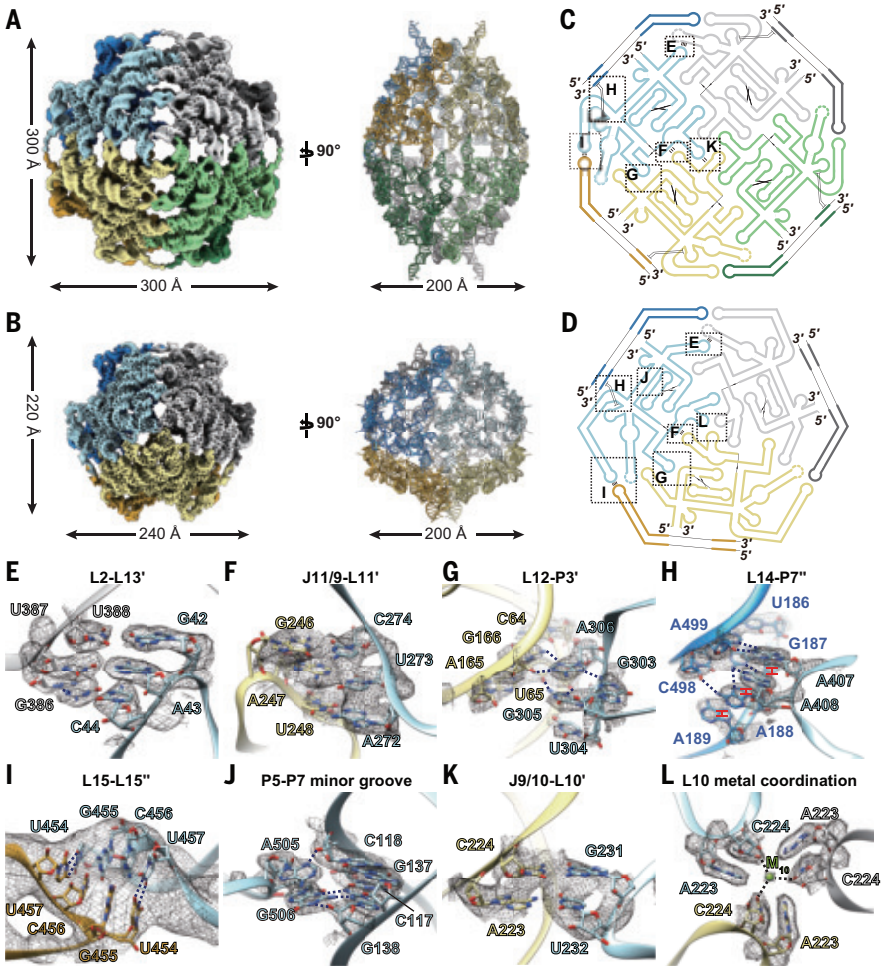

Fig. 3. Cryo-EM structures and intermolecular interfaces of ROOL hexamer and octamer. (**A** and **B**) Overall cryo-EM density maps and architectures of *Efa* ROOL octamer (A) and *Lsa* ROOL hexamer (B) at 4.0σ threshold. (**C** and **D**) Projected secondary structures with designated intermolecular interfaces of *Efa* ROOL octamer (C) and *Lsa* ROOL hexamer (D). (**E** to **I**) Intermolecular interactions in *Lsa* ROOL hexamer, including KL interactions between L2 and L13′ (E) and J11/9 and L11′ at 4.0σ threshold (F), TL/TLR interaction between L12 and P3′ at 1.0σ threshold (G), A-stacking interaction between L14 and P7″ (H), and interplanar KL interaction between L15 and L15″ at 2.0σ threshold (I). (**J**) Intramolecular minor-groove interaction between P5 and P7 observed only in *Lsa* ROOL at 2.0σ threshold. (**K**) KL interaction between J9/10 and L10′ at 2.0σ threshold reveals intraplanar assembly mechanism of *Efa* ROOL. (**L**) Metal ion coordination of three cytidines (C224) in L10s of different protomers at 0.8σ threshold reveals intraplanar assembly mechanism of *Lsa* ROOL. Blue dashed lines indicate hydrogen bonds of noncanonical interactions, and black dashed line indicates metal coordination.

in *Efa* ROOL contain fewer interactions compared with *Lsa* ROOL (fig. S6, J and K), which may result in dissociation of the upper and lower halves of the octamer into tetramers under cryo-EM conditions (fig. S4). Notably, *Lsa* ROOL adopts an extra purine minor-groove interaction between P5 and P7 that is not present in the *Efa* ROOL (Fig. 3J), resulting in a more-compact P2 and P15 that affects assembly stoichiometry (fig. S7, A to D). Moreover, P10 adopts different structures in *Efa* and *Lsa* ROOL RNAs, leading to drastically different intraplanar assembly mechanisms (Fig. 3, C and D, and fig. S7E). The *Efa* ROOL uses four 2-bp KL interactions between J9/10 and L10′ at the apex along the main symmetry axis to assemble the intraplanar tetramer (Fig. 3K), whereas the *Lsa* ROOL presents an interaction right on the main symmetry axis, enabled by metal ion coordination with C224 bases in L10 from all three protomers for homotrimeric assembly (Fig. 3L and table S2). Similar divalent metal ion coordination of cytosines has been previously reported in crystal packing (*33*), and metal ion coordination could also facilitate protein self-assembly (*34*).

Cryo-EM structures of GOLLD RNAs reveal dynamic multimerization

Akin to ROOL, GOLLD RNAs are frequently found near tRNA genes, and their expression levels correlate with bacteriophage packaging in certain bacterial strains (*35*). GOLLD RNAs consist of variable 5′ domains and highly conserved 3′ domains. We prepared two RNA constructs of the full-length (FL, 700-nt) GOLLD and 3′ domain (375-nt) of GOLLD from *Streptococcus agalactiae* (*Sag*) by in vitro transcription, after which we also observed cotranscriptionally folded cage-like particles under cryo-EM. Reconstruction of the GOLLD 3′ domain showed both dihedral homodecamer and dodecamer at 3.6- and 6.1-Å resolutions, with the homodecamer as the major class that contains 12 times more particles than the dodecamer (fig. S8 and table S1). In contrast, the FL GOLLD was reconstructed only as the dihedral homododecamer at 4.6-Å resolution (Fig. 4A and fig. S9).

The FL GOLLD is the largest and most complex RNA structure resolved in this work, containing 25 paired stems (P2–P8 and P10–P27, numbered according to the conserved secondary structure) (*35*), two 4WJs, three 3WJs, and five intramolecular tertiary interactions (fig. S10A). These include two KLs, between L8b and L11 and J24/26 and L27 (P25) (fig. S10, B and C), and three minor-groove interactions, between L5 and P3, P7 and P10, and L27 and P14 (fig. S10, D to F). Additional intermolecular interactions facilitate RNA multimerization (Fig. 4B and movie S5), including four minor-groove interactions, between L3 and P19′, P8 and P11′, L8a and P8a′, and L14 and P21′ (Fig. 4, C to F), and two KL interactions, between L10 and L12′ and L15 and L20′ (intermolecular P16) (Fig. 4, G and H). Together these six intermolecular interfaces assemble the hexameric plane. Another two interplanar interactions, a TL/TLR interaction between L24 and P21″ and a KL between L21 and L21″ (Fig. 4, I and J), complete the dihedral dodecameric nanocage. Intermolecular interfaces involving base pairings show either covariation or sequence conservation (fig. S10A). While the GOLLD 3′ domain multimerization dynamics is likely enabled by the 4WJ formed by P19 to P22 (fig. S11A), the presence of 5′ domain in the FL GOLLD ensures homogeneous assembly through intraplanar interfaces and shape complementarity (fig. S11, B and C), which also allows various assemblies and stoichiometries facilitated by the variable 5′ domains of different GOLLD RNAs (*36*).

Discussion

RNA multivalency has been increasingly recognized to play important roles in biological processes and diseases, such as triggering innate immune responses and driving the formation of pathological condensates and aggregations (*37*). However, the molecular basis behind RNA multimerization remains largely unknown (*8*). Almost all experimentally determined RNA multimers are homodimers with total intermolecular interface areas ranging from 134 to 3143 Å^2 (Fig. 5A). Those with larger interfaces usually contain long complementary base-pairing or

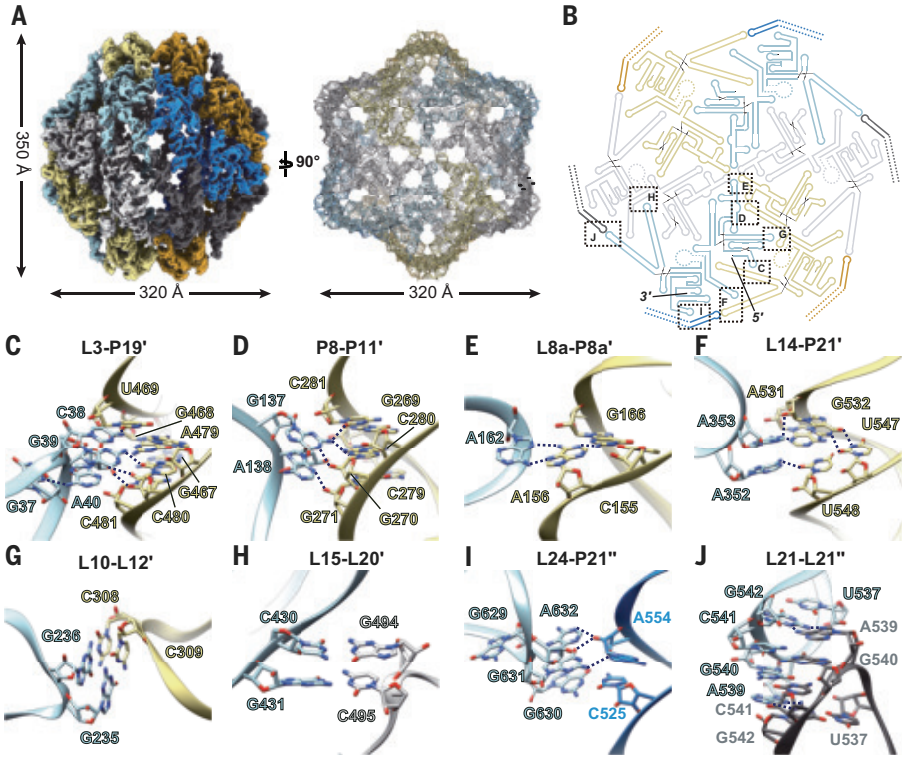

Fig. 4. Cryo-EM structures and intermolecular interfaces of FL GOLLD dodecamer. (**A**) Cryo-EM density map and model of GOLLD dodecamer at 2.0σ threshold. (**B**) Projected secondary structure in cartoon with designated intermolecular interactions. (**C** to **F**) Minor-groove interactions with the adjacent protomer between L3 and P19′ (C), P8 and P11′ (D), L8a and P8a′ (E), and L14 and P21′ (F). (**G** and **H**) KL interactions between L10 and L12′ (G) and L15 and L20′ (intermolecular P16) (H). (**I**) Interplanar TL/TLR interaction between L24 and P21″ in the protomer from the different plane. (**J**) Interplanar KL interaction between L21 and L21″. Blue dashed lines indicate hydrogen bonds of noncanonical interactions.

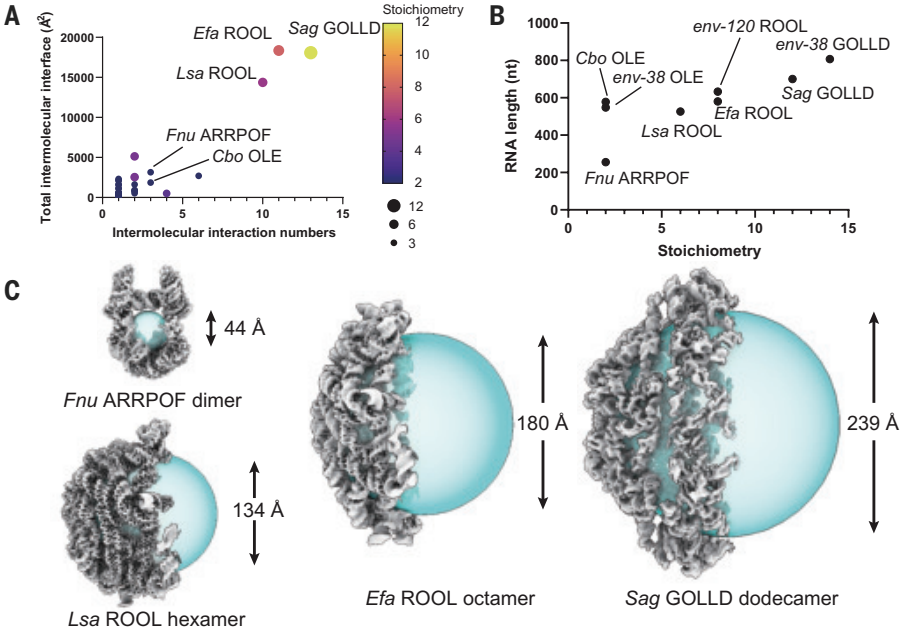

Fig. 5. Correlations between RNA multivalency and numbers of intermolecular interfaces, total interface areas, and RNA lengths. (**A**) Correlation between numbers of intermolecular interfaces, interface areas, and multimer stoichiometry. (**B**) Correlation between RNA length and multimer stoichiometry. (**C**) Central cavities of ARRPOF, ROOL, and GOLLD assemblies.

A-stacking interactions, such as ARRPOF (3143 Å^2) and OLE (1855 Å^2). Proteins also primarily form homodimers, because dimers normally contain fewer intermolecular interfaces and likely emerged earlier in evolution, whereas higher-order multimers require accumulation of mutations for more intermolecular interactions and thus evolved later (Fig. 5A) (*1*). Homomers with dihedral symmetry (D_n) are more prevalent than those with cyclic symmetry (C_n), as observed in this work and a recent independent study of the same RNA families (*36*), because there are potentially multiple evolutionary paths to D_n symmetry, in contrast to the single pathway toward C_n symmetry (*1*).

Within the ROOL and GOLLD families, the dihedral symmetry of the RNA assemblies varies with different sequences and correlates with RNA length; longer RNAs tend to assemble into multimers with higher stoichiometry (Fig. 5B). The 526-nt *Lsa* ROOL assembles into a dihedral homohexamer, whereas the *Efa* and *env-120* ROOL of 580- and 659-nt, respectively, form homooctamers (*36*). The 700-nt *Sag* GOLLD forms a 12-membered dodecamer, and the 833-nt *env-38* GOLLD forms a 14-membered tetradecamer (*36*). The more conserved *Sag* GOLLD 3′ domain of 375 nt could form decameric and dodecameric assemblies and even more heterogeneous states, as observed in cryo-EM two-dimensional averages (fig. S8). Variations in critical structural motifs could lead to multimerization dynamics and drastically different assembly mechanisms within the same RNA family. Superposition of the *Efa* and *Lsa* ROOL monomers reveals that the additional P5-P7 minor-groove interaction only observed in the *Lsa* ROOL induces more-compact P2 and P15 (fig. S7, A to D), whereas the missing P10 facilitates the intraplanar metal ion coordination of three *Lsa* ROOL protomers (Fig. 3L and fig. S7E), which together affect the stoichiometry and symmetry of RNA multivalent assembly. For GOLLD, the 4WJ consisting of P19 to P22 in the 3′ domain allow heterogeneous assemblies (figs. S8 and S11A), whereas its 5′ domain in the FL GOLLD promotes homogeneous quaternary assembly through intermolecular interactions and shape complementarity (fig. S11, B and C).

ROOL and GOLLD assemblies have demonstrated that RNA sequences selected from different bacterial strains can adopt different multimerization states, which may also affect their functions. Although comparative genomics analysis has provided a collection of sequences that adopt conserved secondary structures, selecting proper sequences for structural and functional analyses remains difficult for RNA families such as GOLLD, whose variable 5′ domain can adopt alternative secondary structures in different bacteria (*35*). Alignment of the *Sag* and *env-38* GOLLD sequences to the previously reported conserved secondary structure revealed that *env-38*

GOLLD matched perfectly with the presence of all structural motifs, whereas *Sag* GOLLD contained extra P8a and P8b but lacked part of P7 and P10 as well as the entirety of P9, P11a to P11c, and P21b. Nonetheless, *Sag* GOLLD could still form the quaternary assembly, albeit with different stoichiometry (fig. S12, A to C). Another GOLLD sequence from *Flavobacteriales bacterium* ALC-1 (*Fba*), also retrieved from the Rfam and previous covariation analysis (*17*, *35*), failed to form a rigid tertiary structure that could be experimentally determined, despite exhaustive RNA and cryo-EM sample optimizations (*22*). Comparison between *Fba* and *Sag* GOLLD showed that *Fba* GOLLD is missing L8b-L11, P22, and part of P27 (fig. S12, D and E). While these differences in secondary structures are not apparently related to tertiary structure formations, we explored whether a pretrained contrastive learning language model, fine-tuned by sequences from structured RNA families (CRAFTS), could extract structural features from RNA sequences and retrieve their likelihood of forming tertiary structures within their respective families (fig. S13 and supplementary text, note 1). Although the ARRPOF sequences were clustered on the basis of variations in P4 and P6 and extra nucleotides in P10 (fig. S14, A to C), which may result in steric clash of extended P4 and disruption of P9 with truncated P6 (fig. S14D), the remaining OLE, ROOL, and GOLLD families showed inconclusive sequence consensus variations that require further validations (fig. S15). These observations suggest that general application of such a model across RNA families remains challenging and is primarily limited by the scarcity of RNA structures available in the PDB.

Our cryo-EM structures of ARRPOF, ROOL, and GOLLD RNAs revealed cage-like nanostructures with various central cavities ranging from 44 to 239 Å in diameter (Fig. 5C), which could form under extremely low concentrations (*36*). This might imply that natural RNA homomers can encapsulate macromolecules such as double-stranded DNA during transcription, tRNAs, and even molecules as large as rRNAs. These homomers may function as delivery vehicles or chaperones, possibly representing relics of "the RNA world" (*38*, *39*). In modern organisms, the roles of these homomers have largely been taken over by proteins. Preliminary functional results indicate that ARRPOF dimerization may play critical roles in transcription regulation of the fructose-associated pathway that modulates *Fnu* autoaggregation (supplementary text, note 2, and fig. S16) (*40*). The OLE RNP complex has been recently proposed to participate in multiple pathways essential in cellular processes, equivalent to TOR complexes in eukaryotes (*20*). ROOL and GOLLD are bacterial noncoding RNAs larger than 500 nt that frequently reside in tRNA clusters, whereas other structured RNAs of similar sizes have been characterized to participate in catalytic reactions (*21*, *41*, *42*). Although their possible catalytic functions as large ribozymes await to be tested, the highly symmetrical assembly may enhance RNA stability and potentially allow their movements within cells and across organisms and species as mobile elements (*43*, *44*).

REFERENCES AND NOTES

1. E. D. Levy, E. Boeri Erba, C. V. Robinson, S. A. Teichmann, *Nature* **453**, 1262–1265 (2008).
2. D. S. Goodsell, A. J. Olson, *Annu. Rev. Biophys. Biomol. Struct.* **29**, 105–153 (2000).
3. H. Schweke *et al.*, *Cell* **187**, 999–1010.e15 (2024).
4. C. M. Dobson, *Nature* **426**, 884–890 (2003).
5. T. A. Thibaudeau, R. T. Anderson, D. M. Smith, *Nat. Commun.* **9**, 1097 (2018).
6. L. Statello, C.-J. Guo, L.-L. Chen, M. Huarte, *Nat. Rev. Mol. Cell Biol.* **22**, 96–118 (2021).
7. C. P. Jones, A. R. Ferré-D'Amaré, *Trends Biochem. Sci.* **40**, 211–220 (2015).
8. C. Bou-Nader, J. Zhang, *Molecules* **25**, 2881 (2020).
9. Z.-X. Liu *et al.*, *Science* **383**, eadh4859 (2024).
10. H. Ohno, S. Akamine, H. Saito, *Curr. Opin. Biotechnol.* **58**, 53–61 (2019).
11. P. X. Guo, S. Erickson, D. Anderson, *Science* **236**, 690–694 (1987).
12. F. Ding *et al.*, *Proc. Natl. Acad. Sci. U.S.A.* **108**, 7357–7362 (2011).
13. H. Mao *et al.*, *Cell Rep.* **14**, 2017–2029 (2016).
14. H. Ma, X. Jia, K. Zhang, Z. Su, *Signal Transduct. Target. Ther.* **7**, 58 (2022).
15. R. C. Kretsch *et al.*, *Proteins* **91**, 1600–1615 (2023).
16. F. Bu *et al.*, *Nat. Methods* **22**, 399–411 (2025).
17. N. Ontiveros-Palacios *et al.*, *Nucleic Acids Res.* **53**, D258–D267 (2025).
18. S. Stav *et al.*, *BMC Microbiol.* **19**, 66 (2019).
19. Z. Weinberg *et al.*, *Nucleic Acids Res.* **45**, 10811–10823 (2017).
20. R. R. Breaker, K. A. Harris, S. E. Lyon, F. D. R. Wencker, C. M. Fernando, *Mol. Microbiol.* **120**, 324–340 (2023).
21. K. A. Harris, R. R. Breaker, *Microbiol. Spectr.* **6**, RWR-0005-2017 (2018).
22. X. Chen *et al.*, *Nat. Protoc.* 10.1038/s41596-024-01072-1 (2024).
23. G. Bachrach *et al.*, *Appl. Environ. Microbiol.* **70**, 6957–6962 (2004).
24. E. Puerta-Fernandez, J. E. Barrick, A. Roth, R. R. Breaker, *Proc. Natl. Acad. Sci. U.S.A.* **103**, 19490–19495 (2006).
25. Y. Yang, K. A. Harris, D. L. Widner, R. R. Breaker, *Proc. Natl. Acad. Sci. U.S.A.* **118**, e2020393118 (2021).
26. S. E. Lyon, K. A. Harris, N. B. Odzer, S. G. Wilkins, R. R. Breaker, *J. Biol. Chem.* **298**, 102674 (2022).
27. J. G. Wallace, Z. Zhou, R. R. Breaker, *Nucleic Acids Res.* **40**, 6898–6907 (2012).
28. K. A. Harris, N. B. Odzer, R. R. Breaker, *Mol. Microbiol.* **112**, 1552–1563 (2019).
29. B. M. Lund, M. W. Peck, in *Guide to Foodborne Pathogens*, R. G. Labbé, S. García, Eds. (Wiley, 2013), pp. 91–111.
30. R. Rizkiantino *et al.*, *J. Surv. Fish. Sci.* **7**, 27–42 (2020).
31. N. C. Bryan *et al.*, *Front. Microbiol.* **11**, 515319 (2021).
32. F. J. Cousin *et al.*, *Microb. Genom.* **3**, e000126 (2017).
33. N. Marino, D. Armentano, C. Zanchini, G. De Munno, *CrystEngComm* **16**, 8286–8296 (2014).
34. E. N. Salgado, R. J. Radford, F. A. Tezcan, *Acc. Chem. Res.* **43**, 661–672 (2010).
35. Z. Weinberg, J. Perreault, M. M. Meyer, R. R. Breaker, *Nature* **462**, 656–659 (2009).
36. R. C. Kretsch *et al.*, bioRxiv 2024.12.08.627333 [Preprint] (2024); https://doi.org/10.1101/2024.12.08.627333.
37. G. M. Wadsworth *et al.*, *Mol. Cell* **84**, 3692–3705 (2024).
38. W. Gilbert, *Nature* **319**, 618 (1986).
39. T. R. Cech, *Cold Spring Harb. Perspect. Biol.* **4**, a006742 (2012).
40. X. Zheng *et al.*, *Sci. Adv.* **10**, eado0016 (2024).
41. L. Wang *et al.*, *Nat. Struct. Mol. Biol.* 10.1038/s41594-025-01484-x (2025).
42. A. M. Pyle, *Annu. Rev. Biophys.* **45**, 183–205 (2016).
43. X. Chen, O. Rechavi, *Nat. Rev. Mol. Cell Biol.* **23**, 185–203 (2022).
44. A. M. Jose, *Genesis* **53**, 395–416 (2015).
45. H. Wu *et al.*, Code for CRAFTS model, Zenodo (2025); https://doi.org/10.5281/zenodo.14966520.

ACKNOWLEDGMENTS

We thank members from J. Bujnicki's and S. Glatt's groups for constructive discussions under the 1000 RNAs initiative and S. Y. Huang for RNA modeling suggestions. Cryo-EM data were collected on Can Cong at SKLB West China Cryo-EM Center and processed at SKLB Duyu High Performance Computing Center at West China Hospital. This work was partially supported by the Shanghai Artificial Intelligence Laboratory (S.Q.S.). **Funding:** National Key Research and Development Program of China grant 2022YFC2303700 (Z.M.S.); Natural Science Foundation of China grant 32222040 (Z.M.S.); Natural Science Foundation of China grant 32270120 (X.Z.); and the 1.3.5 Project for Disciplines Excellence of West China Hospital grant ZYYC21006 (Z.M.S.).
Author contributions: Conceptualization: Z.M.S.; RNA and cryo-EM grids preparation: L.W., Y.F.T., X.P., X.Y.J., D.Z., Y.Liu, Z.R.H.; Cryo-EM data collection and processing: L.W., Y.F.T., X.P., X.Y.J., H.Y.M., D.Z., Y.Liu, Y.B.L., Z.R.H.; Generating RNA atomic coordinates: L.W., J.H.X., X.P., S.T.S., X.Y.J., J.Z., Z.M.S.; Bacteria assays: T.G., X.Z., X.D.Z.; Language models: H.W., S.X., Y.C., S.Q.S.; Methodology: L.W., J.H.X., T.G., H.W., C.Z., S.X., Y.Lai, X.Z., B.S., Y.C., S.Q.S., X.D.Z., Z.M.S.; Investigation: L.W., J.H.X., T.G., H.W., X.Z., J.Q.L., S.Q.S., X.D.Z., Z.M.S.; Visualization: L.W., T.G., H.W., Y.F.T., X.P., X.Y.J., H.Y.M., J.Z., S.X.; Funding acquisition: Z.M.S., X.D.Z., S.Q.S.; Project administration: Z.M.S.; Supervision: Z.M.S., X.D.Z., S.Q.S., Y.Q.W., D.M.H., J.Q.L., Y.Q.G., B.W.Y.; Writing – original draft: Z.M.S., X.D.Z., S.Q.S., L.W., T.G., H.W.; Writing – review & editing: L.W., J.H.X., TG.,. H.W., Y.F.T., X.P., S.T.S., X.Y.J., H.Y.M., J.Z., S.X., X.Z., D.Z., Y.Liu, C.Z., Y.B.L., Z.R.H., B.S., B.W.Y., Y.C., Y.Q.G., Y.Lai, D.M.H., J.Q.L., Y.Q.W., S.Q.S., X.D.Z., Z.M.S. All authors contributed to the preparation of the manuscript. **Competing interests:** The authors declare that they have no competing interests.
Data and materials availability: The cryo-EM maps and associated atomic coordinate models have been deposited in the wwPDB OneDep System under the following EMD accession codes and PDB IDs: EMD-62489 and 9KPO for ARRPOF dimer conformation 1, EMD-62487 and 9KPH for ARRPOF dimer conformation 2, EMD-62991 and 9LCR for OLE dimer, EMD-60850 and 9ISV for *Efa* ROOL monomer, EMD-61123 and 9J3R for *Efa* ROOL tetramer, EMD-61125 and 9J3T for *Efa* ROOL octamer, EMD-61189 and 9J6Y for *Lsa* ROOL hexamer, EMD-62721 and 9L0R for FL GOLLD dodecamer, EMD-63218 and 9LMF for GOLLD 3′ domain decamer, and EMD-62724 for GOLLD 3′ domain dodecamer. Code for CRAFTS model and benchmark data are available in Zenodo (*45*). Data for transcriptomics analysis of *Fnu* with ARRPOF overexpression have been deposited in the Gene Expression Omnibus (GEO) of NCBI (BioProject accession number PRJNA1207299). All data are available in the main text or the supplementary materials.

SUPPLEMENTARY MATERIALS

science.org/doi/10.1126/science.adv3451
Materials and Methods; Supplementary Text; Figs. S1 to S16; Tables S1 to S5; References (*46*–*80*); MDAR Reproducibility Checklist; Movies S1 to S5; Data S1 to S3

Submitted 17 December 2024; accepted 4 March 2025; published online 13 March 2025
10.1126/science.adv3451

Cyto-Mine Chroma

Sphere Bio, a leading provider of innovative picodroplet-based microfluidics solutions for functional single cell analysis and isolation, today announced the launch of Cyto-Mine® Chroma and the opening of its Early Access Program. Cyto-Mine Chroma represents the next generation of Sphere Bio's industry-leading Cyto-Mine single-cell analysis platform. The Early Access Program provides an opportunity to be among the first to demo the Cyto-Mine Chroma for faster project timeline completion and improved outcomes across broad applications, including antibody discovery, cell line development, and emerging areas such as cell therapy. Through the program, the Company will collaborate closely with forward-thinking customers to drive innovation and inform the development of future applications and assays on the platform. Offering enhanced capabilities, including multiplexing and greater assay flexibility, Cyto-Mine Chroma has been developed to maximize the efficiency and precision of single-cell functional analysis – enabling tens of millions of cells to be screened in a day. Leveraging a four-color laser and detector system, Cyto-Mine Chroma expands the number of parameters that can be analyzed for each cell in a single assay. This supports the upcoming launch of the Company's first multiplexed assay kit, facilitating multiple readouts within a single experiment, optimizing the throughput and precision of cell selection. By accelerating the early selection of superior candidate cells for downstream expansion or further analysis, overall timelines are reduced from months to weeks, while reducing effort and cost.

Sphere Bio Ltd.
For Info: +44 (0)7365 209 441
www.spherebio.com

PragLife

A customized version of PragLife, Pragmatrix's flagship platform, will now be implemented to support Achieve Clinics' operations end-to-end. PragLife is a robust therapy orchestration platform specifically designed to meet the complex needs of the cell therapy industry. By centralizing operations and ensuring compliance with Chain of Identity (COI) and Chain of Custody (COC) standards, PragLife streamlines workflows, enhances patient safety, and supports operational scalability. Through the elimination of manual processes and optimization of communication, PragLife empowers providers to improve efficiency, reduce errors, and deliver exceptional patient care. The Achieve Clinics Portal by Praglife will enable patients, clinicians, apheresis facilities, cell processing and cryopreservation sites, cold chain logistics providers and cell therapy manufacturers to interface seamlessly. The crux of the Portal lies in its automated integration of critical workflows like scheduling, collection, freezing, and tracking in a 21 CFR Part 11-compliant system capable of data-level auditing. Achieve Clinics' decision to adopt PragLife reflects their dedication to operational excellence and patient-centric innovation. After evaluating several available solutions, PragLife's comprehensive functionality, intuitive interface, and compliance-ready features made it the clear choice.

Pragmatrix Technology
For info: 630-452-8848
www.prag.atrix.com

ReiCell-AAV

ReiThera, a global Contract Development and Manufacturing Organization (CDMO), is highlighting its latest vector platform, ReiCell-AAV, alongside the rest of its comprehensive portfolio at Advanced Therapies 2025 in London. ReiCell-AAV enables scalable production of AAVs, the most common vector used in commercial gene therapies. With three innovative platforms to advance viral vector-based therapies, ReiThera is building on its impressive track record in developing and manufacturing genetic vaccines and gene therapies to meet the evolving needs of the biopharmaceutical industry. ReiThera's ReiCell-AAV platform offers a clonal HEK-293 cell line optimized for scalable AAV vector production. Derived from a well-characterized lineage, ReiCell-AAV enables high-density suspension culture in chemically defined media, ensuring enhanced yield, safety, and regulatory compliance. Tailored for large-scale bioreactor-based production, this platform provides a seamless transition from research to clinical-grade manufacturing, supporting the growing demand for AAV-based gene therapies. ReiCell-AAV joins two other cutting-edge platforms with impressive clinical records. ReiThera's MVA (Modified Vaccinia Ankara) platform provides a robust, validated, and industry-proven technology for genetic vaccine production. ReiThera's GRAd platform leverages a proprietary gorilla adenovirus vector with low seroprevalence in humans, making it an ideal candidate for strong and sustained immune responses in particular for CD8 T-Cell based immunity. With an established GMP manufacturing process and validated quality control measures, ReiThera provides a reliable and scalable solution for vaccine developers worldwide.

ReiThera
For info: +39 06 9977539
www.reithera.com

Ready-to-use hiPSC-derived cells

AMSBIO announces a new range of ready-to-use human induced pluripotent stem cell (hiPSC) -derived cardiomyocytes, hepatocytes, and neurons. Supplied fully differentiated and available in high-purity formats, these ready-to-use cells help accelerate research by streamlining lab workflows, eliminating the need for in-house differentiation and minimizing preparation time. Provided as functionally validated cells, researchers do not need to spend time on in-house validation and can instead apply them directly to their assays without additional steps. This is a major advantage for Contract Research Organizations (CROs) and life science labs who can save time and money on optimization work. Outstanding batch-to-batch consistency ensures that AMSBIO's iPSC-derived cells deliver reliable experimental outcomes every time. These hiPSC-derived cells provide a reliable and physiologically relevant alternative to primary cells and animal models, offering researchers a consistent and scalable source of cells for drug discovery, disease modelling, and toxicity screening. Now part of the Europa Biosite group of companies, AMS Biotechnology (AMSBIO) is recognized as a leading transatlantic company contributing to the acceleration of discovery through the provision of cutting-edge life science technology, products, and services for R&D in the medical, nutrition, cosmetics, and energy industries.

AMS Biotechnology
For info: +44 1235 828200
www.amsbio.com

Electronically submit your new product description or product literature information! Go to www.science.org/about/new-products-section for more information.

Newly offered instrumentation, apparatus, and laboratory materials of interest to researchers in all disciplines in academic, industrial, and governmental organizations are featured in this space. Emphasis is given to purpose, chief characteristics, and availability of products and materials. Endorsement by *Science* or AAAS of any products or materials mentioned is not implied. Additional information may be obtained from the manufacturer or supplier.

Who's the top employer for 2024?

Science 2024 TOP EMPLOYER

Science Careers' annual survey reveals the top companies in biotech & pharma voted on by *Science* readers.

Explore these highly-rated employers in our new interactive experience:
sciencecareers.org/topemployers

Changing plans

Jacqueline Curtis

Friday night a few weeks ago, as I was finally slipping into much needed sleep, my phone buzzed. It was another student whose career plans had been disrupted by recent upheavals in the U.S. research landscape. They asked a question I was all too familiar with: How do I get through this uncertainty to get back to my carefully laid plans? Wrestling with that question had defined my career. Twenty years ago, I had a plan. I was living in Louisiana, completing my Ph.D. in geography, and about to begin law school, planning to combine both specialties to protect human health. It took every ounce of me to study for the LSAT and apply to law school while writing my dissertation and teaching, and it had paid off. Then, on 29 August 2005, Hurricane Katrina made landfall.

You may remember the jarring foreground images, but you probably missed the background: people hurrying in and out of the Emergency Operations Center at all hours, working to map the devastation and answer questions such as where is the flooding, how deep is it, and how can we get these people off this roof? I was one of them. My law school had closed for the foreseeable future. So, when the geography department circulated an email requesting geospatial support, I had said yes. I saw it as a temporary detour, a chance to use my skills to help the community.

But weeks became months and law school had yet to reopen. I returned to the lab where I had been a graduate student, now as a research associate. I felt aimless and disoriented. Mapping environmental change after a disaster many people had already forgotten, I felt I had lost my identity. I stayed in this limbo for about a year, waiting to get through the uncertainty so I could get back to my plans.

Then, during routine field mapping, a woman walked over, looked at my map, and showed me it was incomplete. I was missing the underlying human factors, which I could never have known as an outsider. Although I could map vegetation overgrowth, for example, I had missed how that visible process intersected with the community's varied uses of different areas—as meeting spots, recreation areas, and more. That moment redrew my map, literally and for the rest of my career.

Law school finally reopened, offering me a chance to get back on my original track. But the chance encounter stayed with me. I couldn't deny my new fascination: studying how people can be environmental sensors and developing systems to harness this knowledge. The idea of abandoning my long-held plans scared me. I grieved for my hard work and sacrifices. I cried in sadness and screamed in frustration and ate too much ice cream. Then, I chose the unknown.

I became a research assistant professor. For several years I pivoted between teaching-focused and research-focused appointments, which made it difficult to build momentum. But I did not look back. I got married and had a baby and strapped that baby to my chest while field mapping. Eventually, I became tenure track. Now, I'm an associate professor, doing work I love.

As an academic, I had always talked about the cool science I'm able to do, never about how I got here. But then, that baby grew into a teenager struggling with perfectionism. Teachers advised me to tell my daughter about my own struggles, and the unexpected turns my life had taken. When I finished, she smiled, hugged me, and said hearing about my messy humanness made her feel more normal. I wondered what would happen if I opened up to my colleagues in science?

I said nothing for another year; I'm uncomfortable admitting my struggles. But then a colleague experienced a devastating, life- and career-changing event. She wanted to talk. So, one bitter cold morning, we tucked ourselves into a corner seat of our favorite bakery and I told her about how my plans had changed, too. I was open about how unmoored I had been—professionally, emotionally, financially, intellectually. I spared no detail. She smiled, hugged me, and said it made her feel more normal.

I now start my classes by saying science is a human endeavor, with the uniquely human parts making us stronger—if we let them. My students in turn often share their stories of plans changing because of illnesses, caregiving, traumas, and more. We smile, hug, and carry on—all feeling more normal. □

Jacqueline Curtis is an associate professor at Case Western Reserve University. Send your career story to SciCareerEditor@aaas.org.

ILLUSTRATION: ROBERT NEUBECKER

NOMIS & Science
YOUNG EXPLORER AWARD 2025

Research at the intersection of the social and life sciences

Unconventional. Interdisciplinary. Bold.

The NOMIS & *Science* Young Explorer Award recognizes and rewards early-career M.D., Ph.D., or M.D./Ph.D. scientists who perform research at the intersection of the social and life sciences. Essays written by these bold researchers on their recent work are judged for clarity, scientific quality, creativity, and demonstration of cross-disciplinary approaches to address fundamental questions.

A cash prize of up to USD 15,000 will be awarded to essay winners, and their engaging essays will be published in *Science*. Winners will also be invited to share their work and forward-looking perspective with leading scientists in their respective fields at an award ceremony.

Apply by May 15, 2025
at www.science.org/nomis

NOMIS FOUNDATION
Creating the Spark

Science
AAAS

mRNA-Lipid Nanoparticles

MEMBRANE PROTEIN & ANTIBODY GENERATION BY mRNA-LNP

CAR-T/NK /Macrophage

Monoclonal & Bispecific Antibodies

ACCELERATE YOUR GPCR RESEARCH

Accelerate your therapeutic breakthroughs with ProMab's validated mRNA-LNP delivery platform, tailored for effective and reliable gene delivery across diverse immune cell types. Collaborate with us to harness our expertise in formulation, encapsulation, and scale-up, bringing next-generation therapies closer to reality.

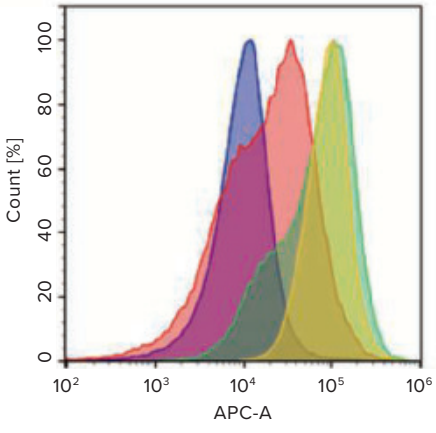

Figure: Flow cytometric analysis of mouse polyclonal antibody binding to HEK293S cells expressing the target GPCR.

HEK293S cells were transfected with GPCR mRNA-LNP and stained with a negative control antibody (blue histogram), an antibody generated by GPCR peptide immunization (red overlay), an antibody generated by full-length GPCR mRNA-LNP immunization (green overlay), and an antibody generated by GPCR ECR mRNA-LNP immunization (yellow histogram). After washing, the cells were stained with a labeled anti-mouse IgG secondary antibody.

All products are for research use only

Discover more | www.promab.com

ProMab Biotechnologies, Inc.
2600 Hilltop Dr, Building B, Richmond, CA 94806
1.866.339.0871 | info@promab.com

To learn more on how to get started with GMP mRNA-LNP Services, scan this QR code.

Visit us at 2025 ASCO Booth # 13141